

**THE DRIVING FORCE DEPENDENCE OF CHARGE
CARRIER DYNAMICS IN DONOR-ACCEPTOR
ORGANIC PHOTOVOLTAIC SYSTEMS USING
OPTICAL AND ELECTRONIC TECHNIQUES**

A thesis submitted in fulfilment of the requirements for the award of the degree

DOCTOR OF PHILOSOPHY

from

UNIVERSITY OF WOLLONGONG

by

**BRENDAN F. WRIGHT
(BACHELOR OF NANOTECHNOLOGY, HONOURS)**

INTELLIGENT POLYMER RESEARCH INSTITUTE

2017

Abstract

The overall objective of this thesis was to quantify the influence of the free energy driving force for electron transfer ΔG_{ET} on electron transfer kinetics and charge generation yield in donor-acceptor organic photovoltaic systems, with the aim of reducing ΔG_{ET} to increase device photovoltage (reduce energy loss) while maintaining high device current (high charge generation yield), thereby maximising solar conversion efficiency.

A novel switched time resolved charge extraction measurement technique was developed, with the first time inclusion of an applied bias. This technique was used to accurately determine the origin of, and systematically quantify charge extraction losses, enabling the attribution of device performance limitations to the underlying loss mechanisms. It was found that over half of photogenerated charge density is lost without an applied bias, significantly impacting the calculation of recombination kinetics and trapping behaviour. The applied bias is also capable of reducing the disparity of results between devices with different active layer thickness, and provides a method for overcoming measurement and material system limitations that would otherwise severely impact accuracy, most effective when investigating systems with short lifetime and slow charge transport.

A series of novel cyclopentadithiophenes based polymer donor materials were used to vary ΔG_{ET} , and a combination of ultrafast transient absorption spectroscopy and applied bias time resolved charge extraction was used to investigate the charge generation yield of optical films and operational photovoltaic devices with respect to the influence of ΔG_{ET} . These transient measurement investigations indicate that ΔG_{ET} should exceed 0.18 eV for the presented donor-acceptor systems, in order to facilitate femtosecond electron transfer with near unity quantum yield, and high charge generation yield. It is however important to minimise ΔG_{ET} , as increases above 0.30 eV do not provide significant improvements in charge generation yield, while significantly reducing device photovoltage. Additionally, charge generation yield appears limited by charge-transfer state recombination rather than electron transfer kinetics.

Importantly, bimolecular recombination was found to exhibit a far greater influence on charge extraction yield than ΔG_{ET} , with bimolecular recombination severely limiting device performance in these donor-acceptor systems. It is therefore necessary to develop methods to suppress bimolecular recombination in the pursuit of more efficient photovoltaic systems. Additionally, the free energy driving force for recombination ΔG_{rec} was observed to influence bimolecular recombination kinetics, and presents an interesting new area for future research.

Although further investigations into the generality of these findings across different material systems can refine our understanding, the primary findings of this thesis contribute to our understanding of the fundamental influences of energetic driving forces in charge carrier generation and recombination processes within donor-acceptor photovoltaic systems. Additionally, the newly

developed charge extraction technique provides the photovoltaic community with a robust and capable methodology for investigating the fundamental processes governing charge carrier transport, extraction, and recombination within photovoltaic systems.

Acknowledgements

Thanks to my supervisors Attila Mozer and Tracey Clarke for invaluable discussion, advice, and guidance throughout the course of my studies, to Andrew Nattestad for guidance and assistance during my earlier years, particularly regarding device fabrication and characterisation techniques, and finally to all those who provided a forum for discussion, feedback, and support.

Certification

I, Brendan F. Wright, declare that this thesis, submitted in fulfilment of the requirements for the award of Doctor of Philosophy, at the Intelligent polymer Research Institute (IPRI), in the Department of Science, Medicine and Health (SMAH), University of Wollongong, is wholly my own work unless otherwise referenced or acknowledged. This document has not been submitted for qualifications at any other academic institution.



Brendan F. Wright
12 November 2017

Table of Contents

Table of Contents	i
List of Figures	iv
List of Tables	x
1 Introduction	1
1.1 Donor-Acceptor Organic Photovoltaics	1
1.1.1 Photoexcitation and Charge Separation	2
1.1.2 Charge Extraction and Bimolecular Recombination	7
1.1.3 Developments in Donor-Acceptor Photovoltaic Device Performance	9
1.2 Charge Photogeneration Processes	11
1.2.1 Theoretical Background of Exciton Dissociation, Electron Transfer, and Charge-Transfer States	12
1.2.2 The Role of Driving Force for Electron Transfer in Charge Carrier Separation	18
1.2.3 Summary of Charge Photogeneration Process Understanding	22
1.3 Charge Transport and Recombination Processes	22
1.3.1 Charge Carrier Transport and Non-Geminate Recombination Mechanisms .	23
1.4 The Study of Charge Photogeneration and Recombination Processes	26
1.4.1 Transient Absorption Spectroscopy	26
1.4.2 Transient Charge Extraction Based Techniques	28
1.5 Thesis Overview	31
1.5.1 Donor-Acceptor Material Systems	32
1.5.2 Ultrafast Transient Absorption Spectroscopy	34
1.5.3 Time Resolved Charge Extraction	35
1.5.4 Applied Bias Time Resolved Charge Extraction	36
1.5.5 Influence of Material Energy Levels in Operational Photovoltaic Devices .	36
2 Experimental Methods	38
2.1 Photovoltaic Film/Device Fabrication and Characterisation	38
2.1.1 Photovoltaic Film/Device Fabrication	38
2.1.2 Steady-State Device Performance	40

2.1.3	Active Layer Thickness Measurement	42
2.1.4	Transmission Electron Microscopy	43
2.1.5	UV-Visible Absorbance Spectroscopy	43
2.2	Transient Optical Measurement Techniques	43
2.2.1	Transient Absorption Spectroscopy	43
2.2.2	Integrated Photoluminescence Spectroscopy	44
2.3	Transient Electronic Measurement Techniques	45
2.3.1	Time Resolved Charge Extraction Measurements	45
2.3.2	Photovoltage Decay Measurements	47
2.3.3	Time Resolved Charge Extraction with an Applied Bias	47
2.3.4	Switched Photoinduced Charge Extraction in Linearly Increasing Voltage .	48
2.3.5	Analysis of Time Resolved Charge Extraction Measurements	49
3	The Influence of Energetic Driving Force on Electron Transfer Kinetics and Charge Generation Yield	51
3.1	Introduction	51
3.1.1	Motivation and Objectives	51
3.1.2	Donor-Acceptor Material Systems	53
3.1.3	Summary of Chapter Objectives	54
3.2	Experimental	54
3.2.1	Film Preparation	54
3.2.2	UV-Visible Absorbance Spectroscopy	55
3.2.3	Transmission Electron Microscopy	55
3.2.4	Transient Absorption Spectroscopy	55
3.2.5	Integrated Photoluminescence Spectroscopy	56
3.3	Results and Discussion	56
3.3.1	Polaron Photogeneration in Donor-Acceptor Blend Film	56
3.3.2	Transient Absorption Spectroscopy	62
3.3.3	Ultrafast Electron Transfer Kinetics and Polaron Generation	67
3.4	Conclusions	85
4	Suitability of a Novel Charge Extraction Technique to Determine Charge Generation Yield, Recombination Kinetics, and Trap State Density Distribution	87
4.1	Introduction	87
4.1.1	Motivation and Objectives	87
4.1.2	Background of Time Resolved Charge Extraction Techniques	88
4.2	Outstanding Issues in Time Resolved Charge Extraction Measurements	92
4.2.1	Influence of Charge Extraction Losses on the Measurement of Charge Density and Recombination Kinetics	92

4.2.2	Measurement of Trap State Density Distribution using Time Resolved Charge Extraction	95
4.2.3	Summary of Outstanding Issues and Chapter Objectives	97
4.3	Experimental	98
4.3.1	Photovoltaic Device Fabrication	98
4.3.2	Steady-State Device Performance	99
4.3.3	Transient Charge Extraction and Photovoltage Decay	100
4.4	Results and Discussion	101
4.4.1	Influence of Laser Excitation Density and Delay Time on Extracted Charge Density	101
4.4.2	Recombination Kinetics and Trap State Density Distribution	111
4.4.3	Excitation Pulse Length	123
4.5	Summary of Results and Discussion	134
4.6	Conclusions	135
5	Applied Bias in Time Resolved Charge Extraction Measurements	137
5.1	Introduction	137
5.1.1	Motivation and Objectives	137
5.1.2	Time Resolved Charge Extraction with an Applied Bias	138
5.2	Outstanding Issues in Time Resolved Charge Extraction Measurements and the Benefits of Incorporating an Applied Bias	139
5.2.1	Charge Carrier Extraction Processes under an Applied Bias	139
5.2.2	Summary of Issues and Chapter Objectives	142
5.3	Experimental	142
5.3.1	Photovoltaic Device Fabrication	142
5.3.2	Transient Applied Bias Charge Extraction and Photovoltage Decay	144
5.4	Results and Discussion	145
5.4.1	Applied Bias in Time Resolved Charge Extraction for Charge Density Measurement	145
5.4.2	The Origins of Increased Charge Extraction with an Applied Bias	154
5.4.3	Distinguishing the Dominant Charge Extraction Loss Mechanism	159
5.4.4	Influence of Extraction Losses on the Measurement of Recombination Kinetics and Trapping	179
5.4.5	Inherent Spatial Separation in Devices with Thin Active Layers Device	183
5.5	Conclusions	186
6	Donor-Acceptor Material Energy Levels and Charge Carrier Generation/Recombination in Photovoltaic Devices	188
6.1	Introduction	188

6.1.1	The Influence of Driving Force for Electron Transfer of Charge Generation Yield	189
6.1.2	The Influence of Driving Force for Electron Transfer on Device Photovoltage	191
6.1.3	The Influence of Driving Force for Recombination on Device Recombination Kinetics	191
6.1.4	Summary of Chapter Objectives	193
6.2	Experimental	194
6.2.1	Photovoltaic Device Fabrication	194
6.2.2	Steady-State Current-Voltage Characterisation	195
6.2.3	Transient Applied Bias Charge Extraction and Photovoltage Decay	196
6.2.4	Photo-CELIV	197
6.3	Results and Discussion	197
6.3.1	Charge Transport and Extraction Behaviour	198
6.3.2	Influence of Driving Force for Electron Transfer on Charge Extraction Yield	204
6.3.3	Influence of Material System Energy Levels on Device Photovoltage	211
6.3.4	Influence of Material System Energy Levels on Recombination Processes	217
6.4	Conclusions	224
7	Conclusions and Outlook	226
References		231
8	Appendix	245

List of Figures

3.4	Integrated photoluminescence spectra of optical films incorporating pristine polymer donors and PCBM blends.	59
3.5	Transmission electron microscopy images of polymer donor films blended with 70 % PCBM.	61
3.6	Transient absorption spectra of pristine polymer donor films at a range of pump-probe excitation delay times.	63
3.7	Transient absorption spectra of polymer donor films blended with 70 % PCBM at a range of pump-probe excitation delay times.	64
3.8	Transient absorption spectra of pristine polymer donor and PCBM blend films illustrating shift in transient peak.	66
3.9	Ultrafast transient absorption transients of pristine and PCBM blend films, illustrating variations in transient decay between polymer donors.	68
3.10	Illustrative diagram of pristine polymer excitation and decay processes	70
3.11	Illustrative diagram of polymer:PCBM blend excitation, decay, and charge separation processes	73
3.12	Illustrative diagram of polymer:PCBM blend excitation, decay, and charge separation processes, including charge-transfer state	74
3.13	Ultrafast transient absorption transients for pristine polymer donor films.	78
3.14	Ultrafast transient absorption transients for polymer donor films blended with 10 % PCBM.	80
3.15	Ultrafast transient absorption transients for polymer donor films blended with 70 % PCBM.	82
3.16	Electron transfer kinetics as a function of driving force for electron transfer	84
4.1	Illustrations of time resolved charge extraction measurement circuit diagram, timing diagram, and example transient response.	91
4.2	Illuminated and dark current-voltage response for a PCDTBT:PCBM device.	102
4.3	Short-circuit current and open-circuit voltage as a function of illumination intensity for a PCDTBT:PCBM device.	104
4.4	Example illuminated and dark charge extraction transients and integral for a PCDTBT:PCBM device.	106
4.5	Illuminated time resolved charge extraction current transients for a PCDTBT:PCBM device at a range of excitation-extraction delays.	107
4.6	Illuminated charge extraction current transients for a PCDTBT:PCBM device at a range of excitation densities for short and long excitation-extraction delays.	109
4.7	Extracted charge density as a function of excitation-extraction delay time at multiple excitation densities for a PCDTBT:PCBM device, including illustration of behavioural regions.	110

4.8	Empirical reaction order as a function of extracted charge density at multiple excitation-extraction delay time for a PCDTBT:PCBM device, including illustration of behavioural regions.	113
4.9	Charge carrier lifetime and bimolecular recombination coefficient as a function of extracted charge density at multiple excitation-extraction delay time for a PCDTBT:PCBM device, including illustration of behavioural regions.	115
4.10	Photovoltage decay transients at multiple excitation-extraction delay time for a PCDTBT:PCBM device, including illustration of behavioural regions.	118
4.11	The dependence of photovoltage on charge density and corresponding slope at multiple excitation densities for a PCDTBT:PCBM device.	120
4.12	Photovoltage as a function of charge carrier lifetime and corresponding slope for a PCDTBT:PCBM device at multiple excitation densities.	122
4.13	Illuminated and dark current-voltage response for a P3HT:PCBM device.	124
4.14	Short-circuit current and open-circuit voltage as a function of illumination intensity for a P3HT:PCBM device.	126
4.15	Charge density decay and charge carrier lifetime as a function of charge density for a P3HT:PCBM device using a short and long excitation laser pulse at multiple excitation densities.	128
4.16	Photovoltage decay transients for a P3HT:PCBM device using a short and long excitation laser pulse at multiple excitation densities.	130
4.17	Photovoltage as a function of charge density and corresponding slope for a P3HT:PCBM device using a short and long excitation laser pulse at multiple excitation densities.	132
5.1	Illustrations of applied bias time resolved charge extraction measurement circuit diagram, timing diagram, and example transient response.	140
5.2	Example charge extraction transients for a P3HT:PCBM device using an applied bias, including response without illumination or applied bias, response when using an applied bias, both with illumination and without, and the subtracted transient.	146
5.3	Illuminated applied bias charge extraction transients for a P3HT:PCBM device at a range of excitation-extraction delay times, including response without illumination.	148
5.4	Illuminated applied bias charge extraction transients for a P3HT:PCBM device at high/low excitation density and short excitation-extraction delay time for a range of applied bias, including illustration of transient peak position shift as a function of applied bias.	149
5.5	Extracted charge as a function of applied bias for a P3HT:PCBM device, covering a range of excitation-extraction delay times and excitation densities.	151
5.6	Charge density decay as a function of excitation-extraction delay time for a P3HT:PCBM device, with both zero and high applied bias at low/high excitation density.	152

5.7	Charge carrier lifetime as a function of extracted charge density for a P3HT:PCBM device, with both zero and high applied bias at low/high excitation density.	153
5.8	Illustrative figure of space charge perturbed charge extraction under an applied bias at high charge density.	156
5.9	Illustrative figure of spatial separation of charge carriers under an applied bias at low charge density.	158
5.10	Charge extraction response transients and integral without illumination for a PCDTBT:PCBM device under a range of applied bias, including fits to model of capacitive charging current.	162
5.11	Charge extraction response transients and integral without illumination for a P3HT:PCBM device under a range of applied bias, including fits to model of capacitive charging current.	163
5.12	Applied bias charge extraction response transients and integral without illumination for a P3HT:PCBM device at various measurement circuit impedances, including fits to model of capacitive charging current.	165
5.13	Charge extraction transients and integral for a P3HT:PCBM device at multiple excitation-extraction delay times, each at a range of measurement circuit impedances.	167
5.14	Charge density decay for a P3HT:PCBM device at a range of measurement circuit impedances.	168
5.15	Applied bias charge extraction response transients and integral without illumination for two P3HT:PCBM devices with different active surface area, including fits to model of capacitive charging current.	170
5.16	Charge extraction transients and integral for two P3HT:PCBM devices with difference active surface area, both at multiple excitation-extraction delay times.	171
5.17	Charge density decay for P3HT:PCBM devices with difference active surface area.	172
5.18	Applied bias charge extraction response transients and integral without illumination for P3HT:PCBM devices with a range of active layer thickness, including fits to model of capacitive charging current.	174
5.19	Illuminated applied bias charge extraction response transients and integral for P3HT:PCBM devices with a range of active layer thickness, at a range of excitation-extraction delay times.	176
5.20	Extracted charge as a function of applied bias for three P3HT:PCBM devices with different active layer thickness covering a range of excitation densities and excitation-extraction delay times.	178
5.21	Extracted charge density as a function of applied bias for three P3HT:PCBM devices with different active layer thickness at short and long excitation-extraction delay times.	179
5.22	Empirical reaction order as a function of charge density for a P3HT:PCBM device with both zero and high applied bias, at both low and high excitation density.	180

5.23 Photovoltage decay transients for a P3HT:PCBM device at a range of excitation densities.	181
5.24 The dependence of photovoltage on charge density for a P3HT:PCBM device, using both zero and high applied bias at high/low excitation densities, including the calculated trap state density distribution as a function of charge density.	182
5.25 Illustrative figure of inherent spatial separation of charge carriers at open circuit in a thin device, relative to a thick device, at an identical low charge density.	184
5.26 Charge density decay, charge carrier lifetime, and empirical reaction order as a function of charge density for P3HT:PCBM devices with a range of active layer thickness.	185
6.1 Molecular structures of cyclopentadithiophene based polymer donors and fullerene acceptor, including molecular energy levels	189
6.2 Molecular structures of cyclopentadithiophene based polymer donors and fullerene acceptor, including molecular energy levels	192
6.3 Dark and illuminated current-voltage response of three photovoltaic devices incorporating different cyclopentadithiophene polymer donors with the PCBM acceptor.	199
6.4 Photoinduced charge extraction in linearly increasing voltage (photo-CELIV) response transients for three cyclopentadithiophene donor and PCBM acceptor blend devices.	200
6.5 Applied bias time resolved charge extraction transients for three cyclopentadithiophene donor and PCBM acceptor blend devices.	202
6.6 Charge extraction yield as a function of the driving force for electron transfer at multiple excitation densities for three cyclopentadithiophene donor and PCBM acceptor blend devices	204
6.7 Charge extraction yield as a function of the driving force for electron transfer at multiple excitation densities for three cyclopentadithiophene donor and PCBM acceptor blend devices	206
6.8 Dark and illuminated current-voltage response of three photovoltaic devices incorporating different cyclopentadithiophene polymer donors with the PCBM acceptor.	207
6.9 UV-Visible absorbance and incident photon to electron conversion efficiency of three photovoltaic devices incorporating different cyclopentadithiophene polymer donors with the PCBM acceptor.	209
6.10 Charge density and photovoltage decay plots for three cyclopentadithiophene polymer donor and PCBM acceptor blend devices.	212
6.11 The dependence of photovoltage on charge density for three cyclopentadithiophene polymer donor and PCBM acceptor blend devices, and the dependence of photovoltage on the material energy level offset for each donor-acceptor material system.	215

6.12 Illustrative figure of the relationship between the density of states, trap state occupancy, and device photovoltage	216
6.13 Molecular structures of additional cyclopentadithiophene based polymer donors and fullerene acceptor, including molecular energy levels	218
6.14 UV-Visible spectra and current-voltage response of five photovoltaic devices incorporating different cyclopentadithiophene polymer donors with the PCBM acceptor.	220
6.15 Charge density decay and the dependence of charge carrier lifetime on charge density for five cyclopentadithiophene polymer donor and PCBM acceptor blend devices	222
6.16 Charge carrier lifetime as a function of driving force for recombination for two high charge densities for each donor-acceptor blend device.	223
 8.1 Ultrafast transient absorption transients of pristine and PCBM blend films, illustrating variations in transient decay between films blends.	246
8.2 Ultrafast transient absorption transients of pristine and PCBM blend films, illustrating variations in transient decay between polymer donors.	247
8.3 Fitting of transient absorption transients using various models	248
8.4 Influence of energetic driving force on recombination kinetics for P1-5 donor blend devices	250
8.5 Influence of energetic driving force on photovoltage and trap density for P1-5 donor blend devices	251

List of Tables

3.1	Kinetics results from fitting transient absorption transients for pristine polymer donor films using the developed models.	79
3.2	Kinetics results from fitting transient absorption transients for polymer donor films blended with 10 % PCBM using the developed models.	79
3.3	Kinetics results from fitting transient absorption transients for polymer donor films blended with 70 % PCBM using the developed models.	81
4.1	Summary of device parameters and steady state performance obtained from illuminated and dark current-voltage response for a PCDTBT:PCBM device.	101
4.2	Summary of device parameters and steady state performance obtained from illuminated and dark current-voltage response for a P3HT:PCBM device.	124
6.1	Summary of device parameters and steady state performance obtained from dark and illuminated current-voltage response of three photovoltaic devices incorporating different cyclopentadithiophene polymer donors with the PCBM acceptor.	208
6.2	Summary of device parameters and steady state performance obtained from dark and illuminated current-voltage response of three photovoltaic devices incorporating different cyclopentadithiophene polymer donors with the PCBM acceptor.	221

Chapter 1

Introduction

The overall objective of this thesis is to quantify the influence of the driving force for electron transfer on electron transfer kinetics and charge generation yield in organic photovoltaic systems, with the motivation of reducing this driving force as a method for increasing device photovoltage (reduce energy losses), while maintaining high device current (high charge generation efficiency). As such, this Introduction Chapter will provide: the requisite background of donor-acceptor organic photovoltaic systems and their development to the present day state-of-the-art (Section 1.1); a more detailed discussion of charge photogeneration processes (Section 1.2) and transport/recombination processes (Section 1.3), with a survey of recent literature developments and outstanding gaps in understanding that have motivated the investigations of this thesis; a brief background of transient measurement techniques used in the investigation of the aforementioned systems and processes (Section 1.4); and finally an overview of the investigations presented within this thesis (Section 1.5).

1.1 Donor-Acceptor Organic Photovoltaics

Organic photovoltaic systems utilise incident solar radiation to generate electronic charges and produce usable power. The absorption of light results in the formation of an excited electron and hole pair, which requires dissociation into free charge carriers, that are then transported through the active layer and are collected at the device electrodes. The number of long-lived, dissociated charge carriers that are collected at the device electrodes determine the device photocurrent, while the electrochemical potential of these charges determine the device photovoltage. A high yield of photo-carrier generation would imply the effective absorption and generation of separated charge carriers, as well as their transport to the device electrodes. Any loss of initially photogenerated charges, during either the separation process or transport through the active layer, represents a loss of potential photocurrent. Similarly, for a high solar power conversion efficiency, the absorption of photons with a given energy should produce a correspondingly high device photovoltage. Any loss in the electrochemical potential of the photogenerated charge carriers during the separation and

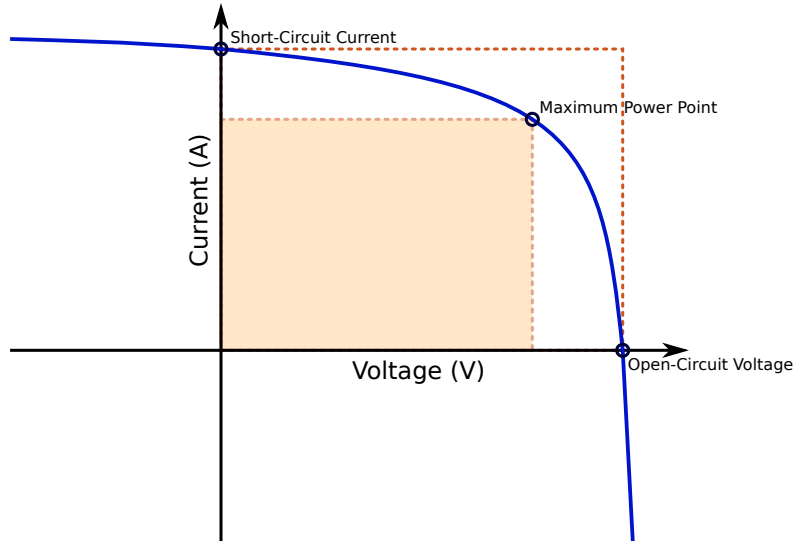


Figure 1.1: Illustration of a photovoltaic device current-voltage response (blue line), with open-circuit voltage, short-circuit current, and maximum power point labelled.

transport processes will reduce the device photovoltage, representing a loss in power output of the photovoltaic device. An efficient organic photovoltaic device therefore requires the separation of photogenerated electron-hole pairs into free charge carriers and transport to the device electrodes, with a high quantum yield and minimal loss of free energy.

Figure 1.1 illustrates an example current-voltage response for a photovoltaic device under illumination. The power conversion efficiency η of a device is obtained under steady state illumination equivalent to that of the sun (AM1.5 spectrum at 100 mW cm^{-2} illumination intensity) where

$$P_{max} = FF J_{SC} V_{OC} \quad (1.1)$$

$$\eta = \frac{FF J_{SC} V_{OC}}{P_{in}} \quad (1.2)$$

where FF is the device fill factor, J_{SC} is the short-circuit current, V_{OC} is the open-circuit voltage, P_{max} is the power obtained at the maximum power point, and P_{in} is the input power (incident radiation). The FF is calculated as the quotient of P_{max} and the product of J_{SC} and V_{OC} , illustrated as the ratio of the two square regions in Figure 1.1.

1.1.1 Photoexcitation and Charge Separation

The efficiency of the photocurrent generation process is strongly related to the proportion of incident photons that are absorbed, which is related to the fraction of light that is absorbed by the active layer. This is in turn determined by the active layer thickness, the absorption spectra of the materials comprising the active layer, and the absorption strength (extinction coefficient) of the materials.¹ The conjugated polymers used in organic photovoltaic systems typically exhibit

high extinction coefficients, however their absorption spectra (related to the optical bandgap of the material) limits the effective coverage of the solar spectrum, thereby limiting the total fraction of solar radiation that can be absorbed and utilised to generate photocurrent. Significant research effort has been targeted towards improving the absorption spectrum of organic donor and acceptor materials. Advances in the design and synthesis of conjugated polymers with tunable optical bandgaps has enables the development of new materials with low bandgaps, as well as increasingly broad or complimentary coverage of the solar spectrum, leading to improvements in device light harvesting capabilities.²⁻⁴

Unlike that of inorganic solid-state semiconductors, primary photoexcitations in conjugated polymers based organic photovoltaic systems do not directly generate free charge carriers, rather yielding the formation of bound electron-hole pairs known as excitons.⁵ These bound electron-hole pairs must overcome their mutual Coulomb attraction, which is inversely proportional to the dielectric constant of the surrounding medium and the inverse of the pair separation distance. The Coulomb capture radius r_c is defined as the distance at which the energy of the Coulomb attraction equals that of the available thermal energy ($k_B T$) such that

$$r_c = \frac{e^2}{4\pi\epsilon_r\epsilon_0 k_B T} \quad (1.3)$$

where e is the charge of an electron, ϵ_0 is the vacuum permittivity, ϵ_r is the dielectric constant of the surrounding materials, T is the temperature, and k_B is Boltzmann constant. Overcoming the initial Coulomb attraction is relatively trivial for conventional inorganic photovoltaics devices, due to the inherently high dielectric constant and highly delocalised nature of the electronic states involved, enabling the effective screening of the Coulomb attraction.⁶ However, in the case of organic photovoltaic systems, which typically exhibit relatively low dielectric constants (on the order of 4, compared to 12 for that of silicon), significant electron-lattice interactions, and more localised electronic states, the Coloumb attraction represents a significant barrier to electron-hole pair dissociation. Without an effective mechanism to dissociate these charge carriers, the photogenerated excitons will undergo radiative or nonradiative decay, with typical lifetimes on the order of 100 ps to 1 ns, thereby severely limiting charge photogeneration efficiency.⁷

Donor-Acceptor Systems for Exciton Dissociation

An early method (ca 1985) that was developed to provide a mechanism for efficient exciton dissociation in organic photovoltaic systems employed the use of a donor and acceptor material in the form of a bilayer device.⁸ This approach utilised a free energy offset at the donor-acceptor material interface, driving exciton dissociation through an energetically favourable electron transfer process from donor to acceptor material, achieved through a relative difference in material energy levels (electron affinities). This process is illustrated in Figure 1.2. The electron transfer process produces an increase in both energetic and spatial separation of the electron-hole pair from that

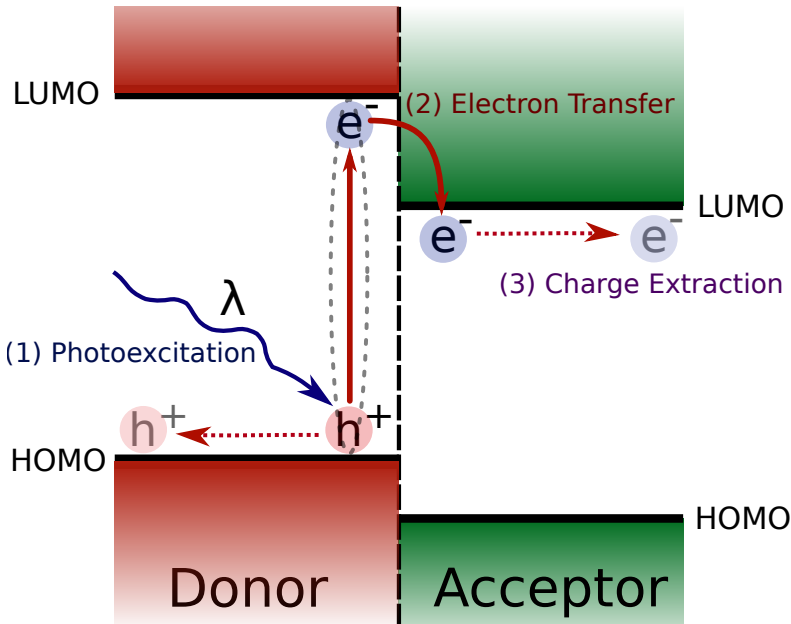


Figure 1.2: Illustration of donor-acceptor concept used in organic photovoltaics. (1) Photoexcitation generates a bound electron-hole pair. (2) Electron transfer occurs from excited donor material to the acceptor material, providing energetic and spatial separation. (3) Charge carriers are extracted through respective material phases.

of the initially photogenerated exciton, enabling the charges to overcome the Coulomb binding potential and dissociate into fully separated states.⁹

Initially photogenerated excitons are neutral species, and must diffuse to a donor-acceptor interface in order to undergo dissociation and generate separated charge carriers. If this diffusion to an interface does not occur within the exciton's lifetime, the exciton will recombine and result in the loss of potential photocurrent. The distance that an exciton will diffuse prior to recombination is known as the diffusion length, and is dependent on the exciton lifetime and rate of diffusion, with typical diffusion lengths on the order of 10 nm.¹⁰⁻¹² In the case of donor-acceptor bilayer device architectures, the requirement of having a donor-acceptor interface within the diffusion length of any exciton photogenerated within the active layer severely limits the active layer thickness. With typical optical absorption depths on the order of 100 nm, while diffusion lengths are closer to 10 nm, this limited active layer thickness drastically reduces the achievable incident photon to charge carrier conversion efficiency.

In order to overcome the active layer thickness limitations of bilayer donor-acceptor photovoltaic devices, the bulk heterojunction active layer was developed, incorporating a bicontinuous interpenetrating network of donor and acceptor materials.¹³ This intimately mixed active layer, featuring tunable donor and acceptor phase segregation and morphology, provides a significant increase in donor-acceptor interfacial area within the active layer. Examples of both bilayer and bulk heterojunction device architectures are presented in Figure 1.3. This active layer morphology

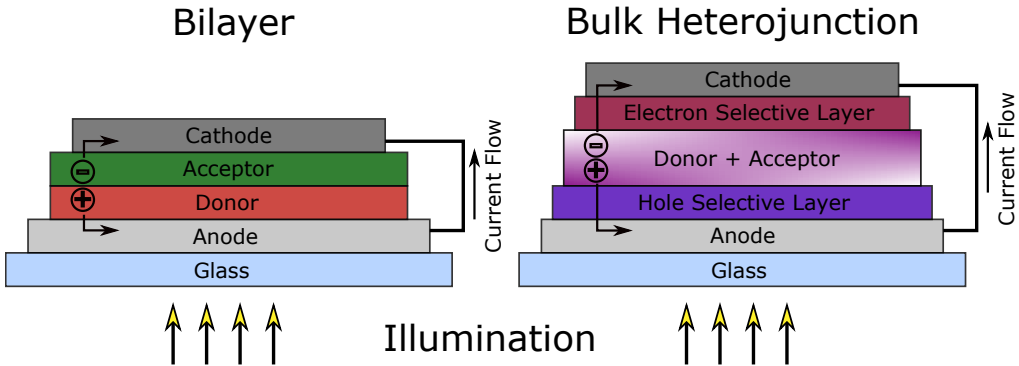


Figure 1.3: Illustration of typical donor-acceptor organic photovoltaic device architectures, including bilayer (left) and bulk heterojunction (right) type active layers. Illumination is performed through a transparent anode deposited on a glass substrate, with active layer residing between anode and cathode. Incident light is absorbed by the active layer materials (donor/acceptor), photogenerating charge carriers which drift to their respective electrodes and are extracted to produce usable power. The bilayer device has separate pure donor and acceptor material layers, whereas the bulk heterojunction features an intimately mixed blend of donor and acceptor materials. Electron and hole selective layers are used to selectively extract the respective charge carriers from the active layer.

can in turn facilitate the diffusion of the vast majority of photogenerated excitons to an interface (within the diffusion length) for dissociation, while also enabling active layer thicknesses better tuned to the absorption profile of the active layer materials. Further, bulk heterojunctions also allow for the formation of effective percolation pathways of respective donor and acceptor material phases, from within the bulk active layer to the device electrodes, thereby facilitating the efficient transport and extraction of separated charge carriers. Electron/hole selective layers are typically employed to selectively extract the desired charge carrier at each device contact, avoiding the recombination of charge carriers at the contact through injection enabled by the blended bulk heterojunction active layer morphology. The efficiency of donor-acceptor bulk-heterojunctions was further enhanced with the use of a methanofullerene (PC_{60}BM) acceptor material, exhibiting significant improvements in charge photogeneration yield over existing polymer-polymer based donor-acceptor systems. The origin of this improvement in charge generation efficiency in systems incorporating a methanofullerene acceptor was found to arise primarily from highly efficient electron transfer at a polymer-fullerene interface, greater than that observed in polymer-polymer systems of the time, and even at very low concentrations.^{14–16}

Charge Transfer and Separation in Donor-Acceptor Systems

The process of electron transfer at a donor-acceptor interface, either through direct excitation at an interface or through exciton diffusion to an interface, does not necessarily directly generate fully dissociated charge carriers. Rather, the small spatial separation of an electron-hole pair between donor and acceptor materials (on the order of 0.5 to 1.0 nm) still presents a Coulomb

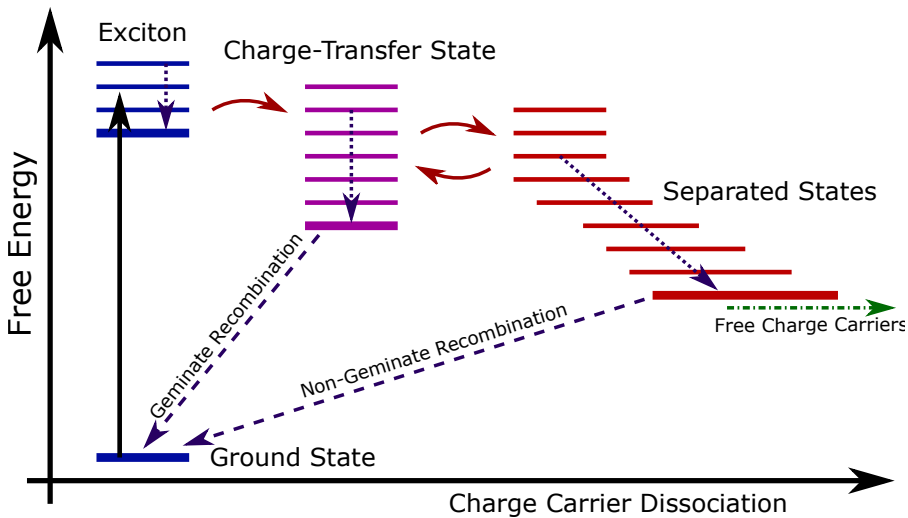


Figure 1.4: Illustration of a simplified state diagram for the charge photogeneration process. Charge photogeneration proceeds through: exciton generation via photoexcitation, electron transfer from donor to acceptor to form a charge-transfer state, followed by further dissociation of this charge-transfer state into free charge carriers. Direct formation of separated states without an intermediate charge-transfer state may also occur, as well as possible reformation of charge-transfer states after the formation of separated states. The primary recombination pathways available after electron transfer are also illustrated, with either geminate recombination of charge-transfer states or non-geminate recombination of separated states to the ground state.

attraction (on the order of 100 to 500 meV), significantly greater than the available thermal energy (on the order of 25.7 meV at 298 K).^{17,18} This can lead to the formation of Coulombically bound interfacial electron-hole pairs, known as charge-transfer states. These partially separated charge-transfer states represent an intermediate separation state between the photogenerated excitons and fully dissociated charge carriers (polymer polaron and PCBM anion), with the hole localised in the donor and the electron in the acceptor. This is again due to the localised electronic states, strong electron-lattice interactions, and low dielectric constants exhibited by these organic materials. An illustration of these charge-transfer states and their role in charge carrier photogeneration is presented in Figure 1.4. Mechanisms to overcome the Coulomb attraction of photogenerated electron-hole pairs (either as excitons or charge-transfer states) with high quantum efficiency and minimal free energy loss is crucial for the development of efficient photovoltaic systems.

The initial electron transfer process from the donor excited state into the acceptor LUMO orbital is facilitated through the use of an energetic driving force, achieved through utilising a suitable energy offset between the LUMO levels of the donor and acceptor materials. Therefore in principle, this energetic driving force sufficiently exceeds the Coulomb binding energy of the exciton, such that the electron transfer process between donor and acceptor is driven at a rate sufficient to favourably compete with the alternative recombination pathways. In addition, this driving force should be sufficient to prevent thermally driven electron transfer back to the initial excited state.

A high driving force will therefore promote efficient electron transfer from donor to acceptor, which can produce a high charge generation efficiency and thereby enable a high device photocurrent. However, the magnitude of this driving force represents a direct loss of free energy, relative to that of the initial photogenerated excited state. The device photovoltage is dependent on the energy difference between the ionisation potential of the donor material and electron affinity of the acceptor material, which can be approximated by the donor HOMO and acceptor LUMO levels, although has also shown to be influenced by the energy of the charge-transfer state.^{17,19–21} An increase in donor-acceptor LUMO-LUMO offset will therefore result in a reduction in achievable device photovoltage. The above explanation therefore suggests an inherent compromise between achieving efficient charge photogeneration and maximising device photovoltage.

1.1.2 Charge Extraction and Bimolecular Recombination

Once photogenerated excitons have been successfully dissociated into fully charge separated states, these free charge carriers must diffuse through the bulk heterojunction active layer to their respective device contacts. In the case of a polymer-PCBM donor-acceptor system, the electrons travels through the PCBM rich phase to the cathode, while the holes travels through the polymer rich phase to the anode. During transport, free charge carriers may travel within the Coulomb capture radius of the opposite charge and undergo bimolecular recombination, either through the reformation of a charge-transfer state or exciton and subsequent radiative decay, or more typically through non-radiative decay pathways to the ground state. Radiative recombination through charge-transfer state reformation followed by intersystem crossing to a triplet state is also a possible pathway, however is far less common and strongly dependent on the energetics of the donor/acceptor system.^{22,23} Thus, charge extraction is in direct competition with bimolecular recombination.

The average distance that charge carriers travel before recombination occurs is the diffusion length, where efficient charge carrier extraction requires diffusion lengths longer than the device active layer thickness.^{24,25} The diffusion length L_D for charge carriers with mobility μ and lifetime τ is described by

$$L_D^2 = \mu\tau \frac{k_B T}{q} \quad (1.4)$$

Diffusion length is therefore proportional to the mobility-lifetime product $\mu\tau$, which is in turn dependent on the material system used and the morphology of the active layer. The recombination probability, and consequently charge extraction efficiency are therefore strongly dependent on charge carrier mobility, lifetime, and the active layer thickness.²⁶ This diffusion process significantly retards the overall recombination kinetics, with dynamics extending out to the millisecond timescale.²⁷ However, this recombination is also a bimolecular process, and as such the probability of recombination increases with increasing charge carrier density, resulting in a reduced charge

carrier lifetime at higher charge densities. This second order process can result in recombination dynamics accelerated to nanoseconds as charge density increases. This is still significantly slower than that of the monomolecular geminate recombination, a first order process with lifetimes typically observed on the picosecond-nanosecond timescale.

The charge carrier lifetime is also strongly influenced by the material system used and morphology of the active layer.^{28–30} An increase in donor-acceptor interfacial area (reduced phase segregation) can increase the probability of bimolecular recombination. The mobility of respective charge carriers is also heavily influenced by the material system used and the morphology of the active layer (phase purity, crystallinity).²⁵ Further, large differences between electron and hole mobilities can impact the recombination probability, where imbalances in charge transport lead to inhomogeneity in the spatial distribution of charge carriers throughout the active layer. The bimolecular recombination of separated charge carriers is a primary loss mechanism in many donor-acceptor systems, resulting in a reduced charge carrier extraction yield, and consequently reduced device photocurrent.

Energetic Disorder and Trapping

Energetic disorder typical of solid-state organic systems produces a broad distribution of electronic states for charge carriers to occupy, leading to a distribution of charge carrier mobilities/lifetimes which participate in recombination to different degrees. In addition to the density of states distribution, localisation of charge carriers into deep trap states can occur during transport, with the spatial and energetic distribution of these trap states dependent on the material system and morphology.³¹ An illustration of this density of states, and the hopping transport and trapping processes, is displayed in Figure 1.5. Occupancy of the trap state distribution results in a reduced average mobility and increased average lifetime for a given charge density, and can reduce the charge extraction efficiency. Additionally, trap state occupancy can influence the recombination mechanism, where localised trap states participate in the recombination of free charge carriers.^{27,32} The degree of influence, and how recombination scales with charge density n at open-circuit is typically characterised through the empirical reaction order δ , where the recombination rate R scales with n such that

$$R \propto n^\delta \quad (1.5)$$

Pure trap free bimolecular recombination would yield a reaction order of 2 (dependent on the concentration of both electrons and holes, therefore second order), while trap state influenced recombination would yield reaction orders above 2, depending on the specific trap state density distribution.^{33,34} A reaction order of approximately 2 is typical of devices with balanced carrier mobilities and only modest bimolecular recombination losses at short circuit, while reaction orders higher than 5 have been reported.^{34–36} The relaxation of charge carriers into a broad density of states distribution, including an exponential tail of trap states, can also lead to a reduction of

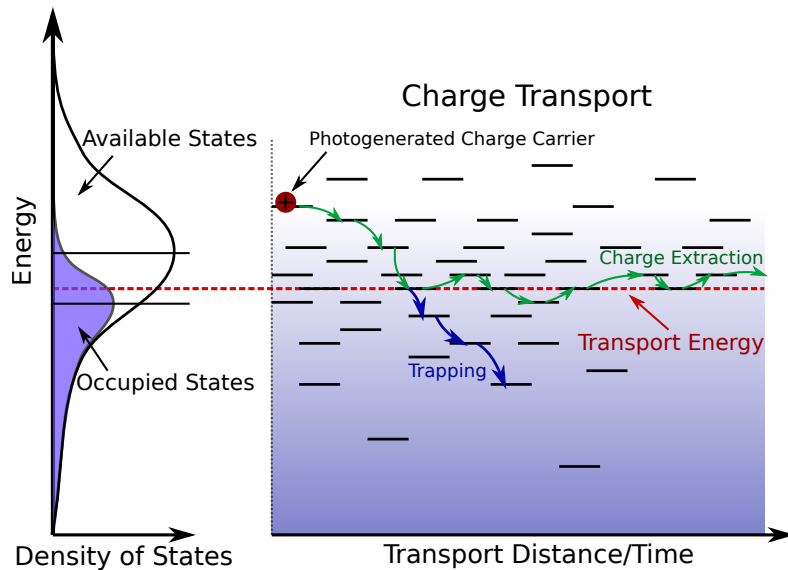


Figure 1.5: Illustration of the density of the states distribution and occupancy with a typical device under steady-state illumination (left), and charge carrier transport by hopping between localised states (right), with energetic relaxation towards a quasi-equilibrium (dependent on thermal energy and disorder), resulting in either continued transport and extraction, or localisation within deep trap states. Steady-state charge carrier transport takes place around the effective transport energy, which depends mainly on the available thermal energy and degree of disorder.

the quasi Fermi levels of respective charge carriers, where not all states are filled and is therefore representative of the effective electrochemical potential of charge carriers within a distribution of energetic states in quasi-equilibrium. As the device photovoltage is directly proportional to the splitting of electron and hole quasi Fermi levels at the device contacts, a reduction in this splitting through trap state occupancy has a direct impact on reducing the maximum achievable device photovoltage.³⁷

1.1.3 Developments in Donor-Acceptor Photovoltaic Device Performance

Significant research and development has been undertaken to better understand the fundamental processes of donor-acceptor organic photovoltaics, as well as the design and development of new material systems, device architectures, and fabrication processes, with state-of-the-art single junction donor-acceptor photovoltaic devices exceeding 12 % solar conversion efficiency.³⁸ Some early (ca 2000-2008) donor materials such as polyphenylene vinylene (PPV) derivatives and poly(3-hexylthiophene) (P3HT) blended with the [6,6]-phenyl-C₆₀-butyric acid methyl ester (PCBM) acceptor yielded reasonably efficient device solar conversion efficiencies η on the order of 2 %, while optimisation of morphology in P3HT:PCBM bulk heterojunctions through annealing resulted in significant further efficiency improvements, η of ~ 3 to 6 %.^{1,3,39} However the large bandgap (around 1.9 eV) of these donor materials limits the solar spectrum absorption coverage, while sub-unity charge photogeneration yields limit the device short-circuit current to under 10 mA cm⁻², and

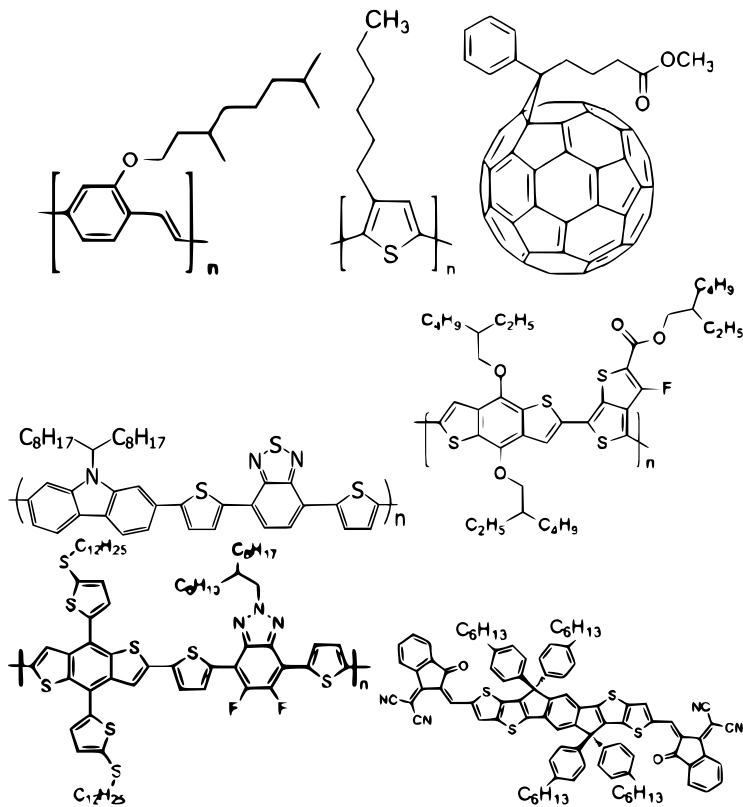


Figure 1.6: The development of organic photovoltaic donor and acceptor materials, illustrating increasing structural complexity over time: (**Top, ca 2000-2008**) MDMO-PPV (left) and P3HT (middle) donors, and the PCBM acceptor (right); (**Middle, ca 2008-2014**) low bandgap, push-pull donors PCDTBT (left) and PTB7 (right); (**Bottom, ca 2017**) J61 donor and ITIC acceptor pair. The top donor-acceptor systems have achieved ~ 3 to 6% device solar conversion efficiency,^{1,3} the middle systems ~ 5 to 9% ,^{40,41} and the bottom system $\sim 11\%.$ ³⁸

a high LUMO-LUMO offset of the donor-acceptor system severely limited the device open-circuit voltage to under 700 mV.

The development of new low bandgap donor materials (ca 2008-2014), featuring internal push-pull character, have yielded significant improvements in device performance, as well as the use of a C₇₀ methanofullerene variant enabling greater absorption coverage within the visible spectrum. Bulk heterojunctions using the PCBM acceptor and polymer donors such as poly[N-9"-hepta-decanyl-2,7-carbazole-alt-5,5-(4',7'-di-2-thienyl-2',1',3'-benzothiadiazole)] (PCDTBT) or polythieno[3,4-b]-thiophene -co-benzodithiophene (PTB7) have resulted in η of ~ 5 to 9% , with improved device fill factors, short-circuit current above 15 mAcm⁻², and open-circuit voltage on the order of 900 mV.^{40,41} These improvements can be attributed to lower energetic losses in driving the charge separation process, as well as achieving charge photogeneration and extraction efficiencies approaching unity.⁴⁰ Additionally, the development of improved active layer processing techniques, introducing solvent additives such as diodoctane, enabled fine tuning of blend morphology and produced up to 3 fold improvements in η .⁴²

The development of organic photovoltaic donor and acceptor materials with increasing structural complexity (as illustrated in Figure 1.6), designed for optimised morphology and donor-acceptor interface energetics have continued to yield improvements in device performance. Cyclopentadithiophene based organic materials have enabled the effective tuning of material energetics to optimise the charge photogeneration process.⁴³ Recently (ca 2016-2017), highly tunable organic systems are enabling the replacement of fullerene acceptors with small organic molecules, achieving η above 11 % with materials such as the J61 donor and ITIC acceptor pair (Figure 1.6, bottom).^{38,44} Further design approaches for improved material systems include the use of high dielectric materials, and the design of increasing on-chain charge delocalisation to stabilise excited states.⁴⁵⁻⁴⁷

Organic Photovoltaic System Design Limited by Fundamental Understanding

Due to the high degree of complexity inherent in these systems, and the interdependence of many parameters in determining overall charge photogeneration efficiency and device performance, a comprehensive understanding of the fundamental processes that govern charge carrier generation, extraction, and recombination has yet to be developed. Despite recent progress, a fundamental understanding of charge photogeneration in donor-acceptor organic photovoltaic systems remains incomplete, and is key to the design and development of improved material systems and enhancements in photovoltaic device performance. In particular, the influence of donor/acceptor material energetics on the photogeneration process, and the role of the driving force for electron transfer on electron transfer kinetics and yield has yet to be clarified.⁴⁸⁻⁵⁰ There exists a need to better understand the relationship between molecular structure and device performance, in order to inform and guide future material system and device design, in the pursuit of enhanced device performance.^{4,49,51} The following Sections 1.2 to 1.4 will detail the current literature understanding of charge photogeneration, extraction, and recombination processes in donor-acceptor organic photovoltaic systems, and highlight the primary gaps in understanding that require investigation, including those that will be addressed within the investigations of this thesis.

1.2 Charge Photogeneration Processes

The previous Section 1.1 presented the general principles of donor-acceptor organic photovoltaic system design, as well as the charge photogeneration, transport, and recombination processes. Significant advancements in device efficiency have been achieved, driven by the continued developments in our understanding of the fundamental processes governing device operation, leading to improvement in material design and device architecture. However as alluded to in the previous section, a number of important aspects regarding the fundamental mechanisms of charge carrier generation and recombination in these systems remain not well understood, or the current understanding is insufficient to adequately explain the expanding set of experimental results within this field. As such, the following sections will present a detailed discussion of the current understanding of these processes (with required background), including recent literature developments and

areas of contention, and identify key areas that require further investigation. The recent progress of research has been rapid, with significant milestones achieved between the start of these thesis investigations and the present day, particularly with regards to the role of charge-transfer states in charge carrier dissociation. The findings of this thesis do however address a number of as yet outstanding gaps in our understanding that are of high importance for the continued development of improved donor-acceptor organic photovoltaic systems. The following discussions will focus primarily on the role of energetic driving forces in charge carrier photogeneration and recombination processes, thereby aligning with the scope and objectives of this thesis.

1.2.1 Theoretical Background of Exciton Dissociation, Electron Transfer, and Charge-Transfer States

Photogenerated Exciton Dissociation

The photoexcitation of conjugated polymers generates a singlet excited state (exciton) where electron and hole remain influenced by a strong Coulomb attraction, due to the low dielectric constant of these materials which are unable to effectively screen the charges, producing a large exciton binding energy significantly greater than the available thermal energy. Excitons must overcome this binding energy in order to dissociate within their lifetime, typically occurring at the interface with an electron acceptor, although this can also occur through interactions with impurities or defects within the polymer phase. In addition to the Coloumbic potential, excitons in conjugated polymers are spatially localised and their formation is accompanied by local relaxation of the surrounding molecular structure, adding to the exciton binding energy. The spatial extent of these deformations are dependent on excited state character and chemical structure of the donor and acceptor materials.

As excitons are electrically neutral species, excitons must diffuse randomly through a Forster-type incoherent energy transfer process to a donor-acceptor interface in order to facilitate efficient dissociation. This diffusion process can be either intramolecular or intermolecular, and usually tends to lower the energy of the exciton through a series of energetically favourable energy transfers within the tail of inhomogeneously broadened density of states. This can also result in localisation within trap sites, such as defects or aggregates, where any further diffusion steps rely on thermal fluctuations. Above bandgap photoexcitation can also yield excitons with excess vibrational energy, which will undergo intramolecular vibrational relaxation during diffusion within 100 fs. The exciton dissociation process can therefore occur from either vibrationally excited or thermally equilibrated, geometrically relaxed excitons.

Exciton binding energy (comprising both Coloumbic potential and structural deformation) and the diffusion length (determined by the rate of diffusion and the exciton lifetime) strongly influence the probability of exciton dissociation, which in turn strongly influences charge generation efficiency. A fundamental understanding of exciton generation, thermalisation, binding energy,

and charge transfer dynamics is therefore crucial for the design of improved donor/acceptor materials. However, the relative influence of excess initial vibrational energy, structural relaxation, and diffusion dynamics on charge carrier dissociation kinetics and yield remains an area of debate, primarily due to difficulty in observing these ultrafast processes. Additionally, difficulty in accurately determining the exciton binding energy and degree of structural deformation in these highly disordered solid-state donor-acceptor blends further obscures understanding of these processes.

Photoinduced Electron Transfer

After diffusion of the photogenerated exciton to a donor-acceptor interface, electron transfer from the photoexcited donor to an electron acceptor will occur, thereby facilitating exciton dissociation and providing both an energetic and spatial separation of charge carriers.⁵² When excitons are generated directly at a donor-acceptor interface (such as where donor and acceptor phases are intimately mixed), electron transfer can occur without the need for diffusion or vibrational relaxation, and has been observed to occur on the femtosecond timescale.

Marcus theory of semi-classical non-adiabatic electron transfer has been successfully applied to electron transfer in a variety of chemical systems, including donor-acceptor organic photovoltaic systems.^{53,54} Non-adiabatic electron transfer theories consider electron transfer as a transition between the potential energy surfaces of the reactant and product states, with electron transfer occurring at the intersection of these surfaces, and electron transfer occurring so rapidly such that effectively no change in nuclear configuration occurs. The electron transfer rate coefficient κ_{ET} is proportional to the electronic coupling of the potential energy surfaces of the product and reactant V and therefore depends on the overlap of electronic wave functions of donor and acceptor. This electron transfer process may also be a thermally activated process.

The activation energy for electron transfer ΔG^A is a function of Gibbs free energy and the reorganisation energy, and takes the form

$$\Delta G^A = \frac{(\lambda + \Delta G_{ET})^2}{4\lambda} \quad (1.6)$$

where ΔG_{ET} is the free-energy offset between products and reactants, and λ is the reorganisation energy required to bring the reactants and surrounding medium to the equilibrium geometry of product state, comprising both intramolecular (vibrational changes in nuclear geometry occurring upon electron transfer) and intermolecular (polarisation of the local environment to stabilise the product state after electron transfer) contributions. This process is illustrated in Figure 1.7. If the electronic coupling V is relatively weak, splitting of the potential energy surfaces is small relative to $k_B T$ and electron transfer occurs non-adiabatically, as is the case considered herein. Therefore, non-adiabatic electron transfer theories predict that κ_{ET} depends on both ΔG_{ET} and V where

$$\kappa_{ET} = \frac{2\pi V^2}{\hbar\sqrt{4\pi\lambda kT}} \exp \frac{-(\lambda + \Delta G_{ET})^2}{4\lambda kT} \quad (1.7)$$

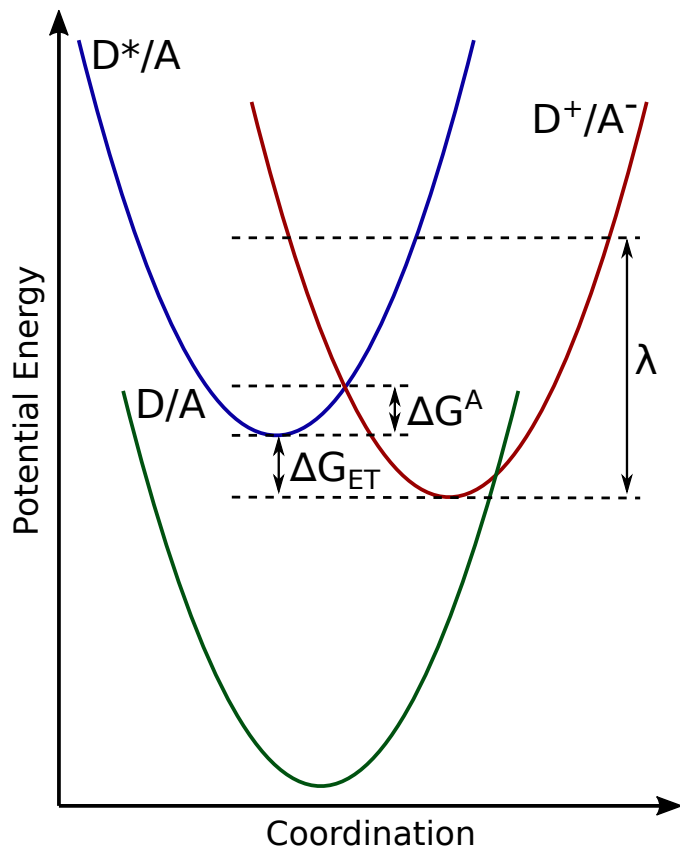


Figure 1.7: Illustration of potential energy surfaces of a donor-acceptor system (the donor D and acceptor A), with the ground state D/A. The photoexcited donor D*/A undergoes electron transfer to yield a positive donor and negative acceptor D⁺/A⁻, where ΔG^A is the energy barrier for reaction, ΔG_{ET} is the energy difference between the product and reactant surface minima, and λ is the reorganisation energy required to bring the reactants and surrounding medium to the equilibrium geometry of product state.

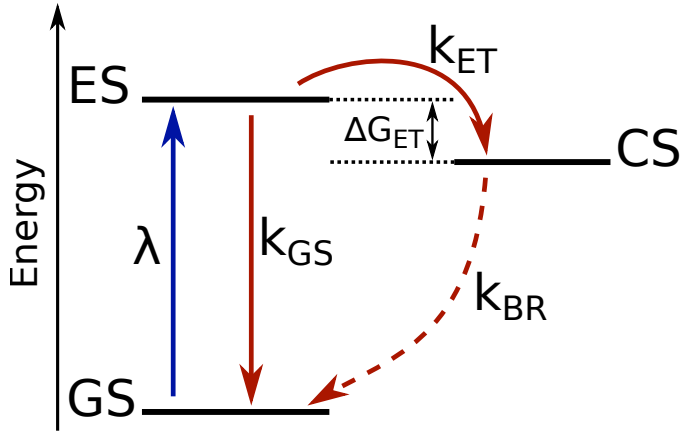


Figure 1.8: Illustration of the kinetic competition in a donor-acceptor system between electron transfer κ_{ET} between excited state (ES) and charge separated state (CS) and geminate recombination κ_{GS} to the ground state (GS). The bimolecular recombination pathway (κ_{BR}) and free energy driving force for electron transfer ΔG_{ET} are also illustrated.

As can be observed from Equation 1.7, an increase in ΔG_{ET} increases κ_{ET} until the point at which ΔG_{ET} is equal to λ , and the reaction has no activation barrier. Beyond this point, any further increase in ΔG_{ET} results in a reduction of κ_{ET} , known as the Marcus inverted region.^{55–57} For an efficient donor-acceptor system, the ΔG_{ET} should be sufficiently large such that κ_{ET} dominates, producing a high quantum yield for electron transfer, and therefore high charge carrier generation. However, the magnitude of ΔG_{ET} must be balanced with the desire for a high device photovoltage, which is proportional to the splitting energy of electron and hole quasi Fermi levels. Any increase in ΔG_{ET} will result in a free energy loss and consequently a reduction of device photovoltage. An illustration of this system is presented in Figure 1.8. From the point of view of maximising both the splitting energy of electron and hole quasi Fermi levels (proportional to V_{OC}) and κ_{ET} , the ΔG_{ET} should be sufficient such that the κ_{ET} is at least to two to three orders of magnitude faster than the excited state decay process to the ground state (κ_{GS}).⁴⁸

Assuming homogeneous reaction kinetics, a kinetic competition between electron transfer and ground state decay pathways predicts that the quantum yield for electron transfer QY_{ET} is of the form

$$QY_{ET} = \frac{\kappa_{ET}}{\kappa_{ET} + \kappa_{GS}} \quad (1.8)$$

Photoinduced charge transfer reactions in solid state donor-acceptor photovoltaic blends however typically do not follow homogeneous reaction kinetics. The calculation of QY_{ET} is not so straightforward, due to a large degree of dispersion arising from the inherent disorder of organic semiconductors. The above semi-classical treatment of electron transfer kinetics, treating electronic coupling quantum mechanically and nuclear motion classically, can be modified to better represent the broad density of states present in condensed phase systems such as those encountered

in organic semiconductors, or further to treat nuclear motion quantum mechanically.⁵⁸

The degree of influence of each electronic coupling, reorganisation energy, and free energy driving force for electron transfer on the eventual yield of charge carrier dissociation remains uncertain to date. The absolute magnitude of driving force required to achieve a high yield of charge carrier dissociation, and thereby efficient charge generation, as well as the degree of variability/transferability in this influence between donor-acceptor material systems remains unclarified. This is of primary importance for the design of donor-acceptor systems, where an excess of energetic driving force above that required to produce efficient charge dissociation represents a direct loss of device photovoltage, with estimates for optimal driving force ranging from 100 to 500 meV.^{17, 21, 59–61}

Charge-Transfer State Dissociation

The previous section highlighted the importance of an energetic driving force for electron transfer in facilitating efficient exciton dissociation at a donor-acceptor interface, based on a consideration of non-adiabatic electron transfer theory for organic photovoltaic systems. However, electron transfer does not always lead directly to the formation of fully separated charge carriers, but rather can lead to the formation of intermediate Coulombically bound charge-transfer states with binding energies on the order of 0.3 eV.¹⁷ This would imply that efficient electron transfer does not necessarily imply efficient charge carrier dissociation. The important role that charge-transfer states play in the dissociation of charge carriers has become increasingly apparent recently, and will be further discussed below.^{62, 63}

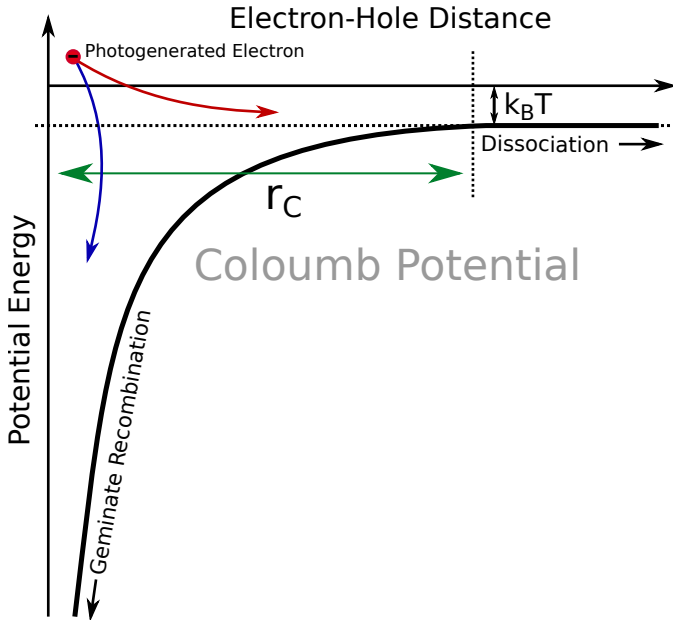


Figure 1.9: Illustration of the Coulomb potential mediating charge-transfer state dissociation. An initially thermally excited photogenerated electron undergoes thermal relaxation through rapid motion to arrive a final distance from the localised hole. If this distance is greater than the Coulomb capture radius r_C , the charge carriers are considered dissociated, otherwise the charge carriers undergo geminate recombination.

Onsager's theory of charge dissociation has been widely used to quantitatively describe the geminate recombination of charge-transfer states.⁶⁴ This theory proposes that photoexcitation generates a localised hole and an excited electron with excess thermal energy. The electron subsequently undergoes thermal relaxation through rapid motion to arrive a final distance from the localised hole (the thermalisation length), yielding a charge-transfer state. The competition between charge-transfer state dissociation into free charge carriers and recombination to the ground state is dependent on the magnitude of the Coulombic attraction. The Coulomb capture radius r_c is defined as the distance at which the energy of the Coulomb attraction equals that of the thermal energy ($k_B T$) such that

$$r_c = \frac{e^2}{4\pi\epsilon_r\epsilon_0 k_B T} \quad (1.9)$$

where e is the charge of an electron, ϵ_0 is the permittivity of vacuum, and ϵ_r is the dielectric constant of the surrounding materials. The charge carriers are considered fully separated if the thermalisation length exceeds r_c , otherwise the probability of dissociation versus the probability of geminate recombination is determined by the thermalisation length relative to r_c , as well as the available thermal energy $k_B T$. This process is illustrated in Figure 1.9. Equation 1.9 emphasises the importance of the dielectric constant of the active layer materials, where the typically low dielectric constants of polymer donors yield large r_c such that dissociation probability without a donor-acceptor interface is low.

Onsager's theory has since been modified by Braun et al to incorporate a finite lifetime for the charge-transfer state, and to better model the experimentally observed thermalisation lengths of condensed phase systems, such as those found in organic photovoltaics.⁶⁵ This modification uses the product of two decay processes for charge-transfer state dissociation probability P , with separate rate constants for dissociation k_d and geminate recombination to the ground state k_r , and a charge-transfer state lifetime τ_{CT} such that

$$P = \frac{k_d}{k_f + k_d} = k_d \tau_{CT} \quad (1.10)$$

Importantly, this new form treats the charge-transfer dissociation process as reversible, where multiple attempts to dissociate may occur during the charge-transfer state lifetime and the charge-transfer state can be regenerated from the partially dissociated charges. Additionally, a distribution of charge-transfer separation distances is expected for these disordered materials, and can be incorporated into this model in order to more accurately reflects the experimentally observed thermalisation lengths.⁶⁴

While models based on Onsager theory have proven effective in modelling experimental results of charge-transfer state dissociation in a variety of systems, significant deficiencies still exist in accurately predicting charge photogeneration yields.^{9,16} These models do not include explicit consideration of the high reorganisation energies expected for typical donor-acceptor systems as in Marcus's non-adiabatic electron transfer theory. Significant difficulty also exists in obtaining reliable estimates for thermalisation and Coulomb capture lengths in organic photovoltaic blends, as well as other important parameters such as interfacial dipoles which further complicate the application of these models for the prediction of charge-transfer state dissociation kinetics and yield.

1.2.2 The Role of Driving Force for Electron Transfer in Charge Carrier Separation

The previous section provided an overview of typically used exciton dissociation, electron transfer, and charge-transfer state theories, and highlighted a number of gaps in understanding, in particular the role of driving force for electron transfer ΔG_{ET} in charge carrier generation/separation processes. Is there a fundamental energy loss requirement for efficient charge dissociation? Is a material energy level offset required to produce a driving force? Or does interface morphology determine the driving force? Can excess vibrational energy drive efficient charge dissociation? And can thermally relaxed charge-transfer states be efficiently dissociated? Or are charge-transfer states primarily a loss mechanism? What role does quantum coherence and delocalisation play in exciton dissociation? Most importantly, can all of the above questions be addressed by a single model, based on a fundamental understanding of charge photogeneration, capable of predicting charge generation kinetics and yield for any donor-acceptor system? And could this be used to inform the design of new donor-acceptor material systems? Addressing these outstanding issues is

crucial to the continued improvement of organic photovoltaic systems. The following section will present a survey and discussion of recent literature developments regarding the energetics of charge carrier dissociation processes, the role of charge-transfer states and excess vibrational energy, and most recently the role of quantum coherence and ultrafast delocalisation in charge photogeneration.

Free Energy Driving Force and Material Energy Levels

It was until recently, generally accepted that an energetic driving force (ΔG_{ET}) was simply required in order to overcome the charge-transfer state binding energy (coulomb potential on the order of 0.3 to 0.5 eV) and produce efficient charge separation.^{17, 21, 59–61} This understanding was related to the required energy for stabilising the charge-transfer state during dissociation, and therefore necessarily lost during the charge separation process.^{21, 66, 67} However multiple studies in recent years have found efficient electron transfer and charge separation with ΔG_{ET} of 0.1 eV or below.^{60, 67–69} This implies that the charge photogeneration process is more complicated than the simple interpretation outlined above. Results from transient absorption and photoluminescence quenching studies of donor-acceptor systems with ΔG_{ET} of ~0.1 eV have reported charge generation yields as high as 80 %.^{60, 69} Further, an increase in the magnitude of donor-acceptor LUMO offset ($\propto \Delta G_{ET}$) has repeatedly been shown by groups including Ohkita et al and Coffey et al to produce an increase in charge separation yield, with the degree of this relationship dependent on the donor-acceptor system used.^{32, 61, 68, 70, 71}

Photoluminescence quenching has been used to investigate the influence of material system energetics (ΔG_{ET}) on charge photogeneration yield, where electron transfer from donor to acceptor results in accelerated exciton decay and altered photoluminescence. Observing the photoluminescence quenching resulting after variation of the ionisation potential of polymer donors blended with the PCBM acceptor has indicated that the initial electron transfer process may not be the limiting factor in the charge photogeneration process.³² However, multiple studies have indicated that photoluminescence quenching is not a reliable indicator for the formation of dissociated charge carriers in donor-acceptor photovoltaic blends. Systems that exhibit very high photoluminescence quenching do not necessarily result in a high yield of separated charge carriers, as determined through transient absorption estimates of the polymer polaron yield. Feier et al used a combination of time-resolved microwave conductivity (TRMC), time-resolved photoluminescence (TRPL), and ultrafast transient absorption spectroscopy to obtain charge separation yields during variation of PCBM concentration and phase aggregation. This study found almost complete exciton quenching at low PCBM concentrations (sub-picosecond electron transfer), while charge separation yields were still quite low, with the dissociation of charge-transfer states post electron transfer again assigned as the primary driver in charge carrier dissociation.⁷²

The influence of free energy driving force for electron transfer on charge generation yield has been investigated by a number of groups, typically varied through the use of different donor-acceptor

systems with relative differences in energy levels (for example, a fixed donor polymer and series of fullerene adducts), and indicate that this driving force plays a fundamental role in charge carrier dissociation.^{62,71,73,74}

Interface Morphology and Electronic Coupling

The local electronic environment of the donor-acceptor interface has additionally been shown to influence the value of ΔG_{ET} due to molecular orientation and donor-acceptor domain crystallinity, and therefore determining the actual ΔG_{ET} within a donor-acceptor blend at the interface is not so straight forward.^{75,76} Improvements to charge-transfer state dissociation of a donor-acceptor system, through thermal annealing or increasing PCBM concentration, have been interpreted as an indication that charge-transfer state dissociation plays a key role in the photogeneration of fully separated charge carriers.¹⁹ Recent investigations by Ayzner et al, Feier et al, and Higashino et al, using a range of theoretical/computational methods, time-resolved microwave conductivity, time-resolved photoluminescence, and transient absorption spectroscopy have confirmed that molecular orientation and electronic coupling at the donor-acceptor interface can strongly influence both charge carrier dissociation rate and yield.^{72,77,78}

Excess Initial Excited State Vibrational Energy

In addition to the above discussion of the driving force in terms of the inherent donor-acceptor LUMO-LUMO offset, the excess thermal energy of the initial exciton has been proposed as another primary mechanism for efficient charge carrier dissociation in systems with a low ΔG_{ET} .⁷⁹ Thermally excited excitons generated through above bandgap excitations, or thermally excited charge-transfer states produced through non-equilibrium electron transfer with sufficient energetic driving force, have both been suggested to strongly influence the dissociation of excitons or charge-transfer states into free charge carriers.

The excess thermal energy available prior to relaxation may result in ultrafast thermalisation of charge carriers to beyond the Coulomb capture radius, thereby directly yielding free charge carriers, with the amount of excess thermal energy determining dissociation efficiency. Multiple studies suggest that the generation of excitons with excess thermal energy through above bandgap excitation of the donor material is sufficient to directly yield free charges, without the requirement of significant ΔG_{ET} .⁷⁹⁻⁸¹ Bakulin et al and other suggest that ΔG_{ET} provides the requisite excess thermal energy for efficient charge separation, by facilitating the formation of thermally excited charge-transfer states which are required for charge separation.^{9,32,82-84} However, direct excitation of relaxed charge-transfer states has been achieved through ultrafast two-pulse excitation measurements using below bandgap excitation, yielding charge-transfer state dissociation without a loss in internal quantum efficiency, relative to above bandgap excitation, and requiring no ΔG_{ET} .⁶³

Excess thermal energy of excited states appears to have an influence on charge carrier dissociation, while thermally relaxed charge-transfer states likely representing a loss pathway, as they are less likely to dissociate prior to geminate recombination. As such, the charge photogeneration yield is expected to be independent of the kinetics for geminate recombination of relaxed charge-transfer states, with kinetic competition between thermalisation and dissociation key to the efficient generation of fully dissociated charge carriers. The thermal relaxation of charge-transfer states has been shown to be slow relative to the initial electron transfer, and may partially explain efficient ultrafast charge separation, where direct dissociation of thermally excited exciton is kinetically favourable relative to charge-transfer state relaxation.⁸⁵

Quantum Coherence and Exciton Delocalisation

Investigations undertaken by a number of groups including Zhang et al,¹¹ Heiber et al,¹² Li et al,⁸⁶ and Dimitrov et al⁷⁰ have attempted to illucidate the mechanisms of exciton generation, diffusion, and dissociation through combined experimental (ultrafast transient absorption and time resolved fluorescence) and computational modelling of various donor-acceptor systems. In particular, these investigations have sought to determine the influence of exciton delocalisation on dissociation probability and kinetics, yielding conflicting conclusions on whether exciton delocalisation is an important factor in charge separation efficiency. Further, investigations into the role of exciton diffusion and exciton-exciton annihilation (internal charge transfer) kinetics have been performed, indicating that differences in process kinetics on the picosecond timescale may not influence charge generation.^{10,11,86,87} Rather, ultrafast charge carrier dissociation appears to be the primary determinant of efficient charge separation in these systems. The role of charge carrier mobility and fullerene domain size were also investigated, and found to impact the initial kinetics of exciton diffusion.

Recently, numerous groups have undertaken studies that suggest quantum coherence is key in triggering charge delocalisation and transfer in donor-acceptor systems.^{46,88–96} Initially generated high energy, highly delocalised excitons sample a large volume with high mobility on the femtosecond timescale prior to relaxation, coupling to highly delocalised charge-transfer states that are well separated prior to thermalisation. This in turn leads to highly efficient charge carrier dissociation on sub-picosecond timescales. Charge photogeneration accounted for by these unrelaxed excitons is substantially faster than predicted for simple exciton diffusion.⁹⁷ Guan et al have further shown that the relaxation of thermally excited charge-transfer states does not reduce their delocalisation character, thereby still allowing dissociation of charges even when relaxed.⁹⁸ Therefore, the role of thermally excited charge-transfer states in efficient charge carrier dissociation is still an area of controversy.

1.2.3 Summary of Charge Photogeneration Process Understanding

From the above discussions, it is clear that the charge photogeneration process is highly complex, and involves many interdependent parameters that vary between donor-acceptor material system. Significant progress has been achieved recently in elucidating the fundamental processes underlying exciton dissociation, charge carrier separation, and the role of ΔG_{ET} therein. However, the relative importance of the above identified factors including ΔG_{ET} , excess thermal energy, and excited state delocalisation, as well as their relative influence on charge photogeneration remains to a large extend unresolved, owing primarily to limited experimental data and difficulty in investigating these ultrafast processes (with short-lived transient species). Much of the current understanding is based on rather indirect investigation of processes, or based on correlations that are either qualitative in nature, or lack clear evidence of a causal relationship between charge photogeneration processes and photocurrent generation.

The design and development of new donor and acceptor material systems with optimised nanoscale morphology and energetics is key to the continued improvement of organic photovoltaic device performance. Of primary importance is the required magnitude of ΔG_{ET} , corresponding to the donor-acceptor material energy level offset. Any excess of ΔG_{ET} , above that required to produce efficient charge dissociation, represents a direct loss of device photovoltage. Optimisation of this balance between charge generation (device photocurrent) and device photovoltage (free energy loss) is a primary motivation for the investigations of this thesis. Therefore, the primary objective of this thesis is to quantitatively determine the influence of driving force for electron transfer on electron transfer kinetics and charge separation yield within donor-acceptor organic photovoltaic systems, and is addressed within the investigations of Chapters 3 and 6.

1.3 Charge Transport and Recombination Processes

The previous Section 1.2 identified a number of outstanding gaps in our understanding of charge carrier generation processes. Similarly, there remain key areas in our current understanding of charge transport and recombination processes that are yet to be clarified. Some of these uncertainties were mentioned in Section 1.1, however a more detailed discussion is presented within this section, expanding on the current state of understanding with regards to charge carrier transport and non-geminate (bimolecular) recombination processes in organic photovoltaic systems. The bimolecular recombination of separated charge carriers is a primary loss mechanism in many donor-acceptor systems, resulting in a reduced charge carrier extraction yield, and consequently reduced device photocurrent.^{28,99} As such, a fundamental understanding of transport and recombination processes is crucial for the design and development of new organic photovoltaic systems and device architectures.

1.3.1 Charge Carrier Transport and Non-Geminate Recombination Mechanisms

After the initial photoexcitation and generation of fully charge-separate states, the charge carriers drift within the active layer until they reach a device contact and are extracted, or enter the Coulomb capture radius of an opposite charge carrier and undergo non-geminate recombination, typically at the donor-acceptor interface. The charge carrier diffusion length L_D , and therefore recombination probability is proportional to the charge carrier mobility-lifetime product $\mu\tau$, which is in turn dependent on the material system used and the morphology of the active layer. As such, charge carrier transport and non-geminate recombination processes are strongly correlated, and a fundamental understanding of both processes is required to effectively control charge carrier extraction losses and thereby optimise photovoltaic device performance. Numerous donor-acceptor photovoltaic systems have been found to exhibit charge generation yields approaching unity, such as the PCDTBT polymer donor blended with fullerene based acceptors, with the predominant loss mechanism attributed to bimolecular recombination processes, heavily influenced by the degree of trapping during transport/extraction.^{40, 100, 101}

$$L_D^2 = \mu\tau \frac{k_B T}{q} \quad (1.11)$$

The above understanding of the bimolecular recombination process, arising from the century old Langevin model, has proven useful in modelling the recombination behaviour of photogenerated charge carriers in donor-acceptor organic photovoltaic systems. However the simplicity of this model also presents a number of shortcomings. For example, the Langevin model does not include the possibility of stable charge-transfer state formation/reformation (equilibrium), which has been recently suggested to play a significant role in these systems.¹⁰² A range of alternative models and more recent understanding are presented and discussed in detail below.

Owing to a lack of long-range order (molecular alignment and orbital wavefunction overlap) in typical solution-processed organic photovoltaic blends, charge transport predominately takes place through hopping between localized states, rather than band transport found in crystalline semiconductors, resulting in comparatively very slow charge transport (low carrier mobilities). This process of hopping transport comprises a combination of tunnelling between localised states (dependent on wave functions correspondence), and thermal activation. Additionally, the high disorder and energetic distortions of molecular structure lead to significant trapping of charge carriers. The photogenerated charge density thermalises to below the centre of the density of states distribution, with charge transport occurring through hopping processes around the transport energy. Charge carriers below this energy remain immobile (trapped within the density of states tail) and do not contribute to conductivity (see illustrative Figure 1.5). The transport energy is dependent on the available thermal energy, and as such, increasing the temperature increases the number of accessible states for mobile charge carriers.³¹

Due to the hopping nature of charge transport in these systems, the bimolecular recombination process cannot be adequately described by a classical band-band or Shockley-Read-Hall processes (electron-phonon coupling and energy exchange, non-radiative recombination through deep traps).^{31,103} As the recombination process involves the recombination of one electron and one hole, the recombination rate R is proportional to the concentration of electrons n and holes p where

$$R = k_{rec}np \propto k_{rec}n^\delta \quad (1.12)$$

where k_{rec} is the recombination proportionality constant. Where only photogenerated charge carriers are considered (with a uniform spatial distribution and therefore concentration), $n \approx p$ with a reaction order $\delta = 2$. The empirical reaction order of the recombination reaction δ can be experimentally determined from the decay of charge density,^{34,104} where α is obtained from the power law $n \propto t^{-\alpha}$ and therefore

$$\alpha = -\frac{d\ln(n(t))}{d\ln(t)} \quad (1.13)$$

$$\delta = \alpha^{-1} + 1 \quad (1.14)$$

This reaction order describes how the charge carrier recombination rate scales with charge carrier density, and incorporates all measured charge carriers, including both free carriers and those within the distribution of trap states, and is therefore dependent on trap state occupancy and charge density.

Langevin-based models of charge carrier recombination are commonly employed to describe the recombination behaviour of photovoltaic devices, a solely diffusion limited treatment where recombination is a certainty every time an electron and hole meet, such that determination of k_{rec} can be approximated with β_L through

$$\beta_L = \frac{q(\mu_n + \mu_p)}{\epsilon} \quad (1.15)$$

where μ_n and μ_p are the mobilities of electrons and holes respectively, q the charge of an electron, and ϵ the dielectric constant of the transport medium.¹⁰² However Langevin-type recombination mechanisms have proven unable to fully explain recombination behaviour, over-predicting the measured recombination rates, and a material system and temperature-dependent empirical factor (β/β_L) is commonly used to adjust for observations of non-Langevin recombination behaviour in numerous high efficiency donor-acceptor blends.^{28,102,105–107} The bimolecular recombination coefficient β (k_{rec} when $\delta = 2$), takes the form

$$\frac{dn}{dt} = -\beta n^2 \quad (1.16)$$

where both τ and β can be experimentally determined through

$$\tau = \frac{1}{n\beta} = -n(t) \left[\frac{dn(t)}{dt} \right]^{-1} \quad (1.17)$$

$$\beta = \frac{dn}{dt} n^{-2} \quad (1.18)$$

Several models have been proposed to explain the observation of non-Langevin recombination, predominately focused on the role of disorder and trapping in recombination processes, while film nanomorphology is known to play a crucial role in charge transport and recombination behaviour (physical separation of charge carriers in respective material domains).^{108–110} One such recent study by Burke et al suggests that free charge carriers are in fact in equilibrium with charge-transfer states, where the formation and dissociation of these states can better account for the observed recombination probability of charge carriers, as well as the observed temperature dependence of open-circuit voltage.¹⁰² Recent investigations by Oosterhout et al have indicated that the current understanding of bimolecular recombination processes are lacking with regards to the origin of dark carriers and the precise nature of the trap states, both found to influence recombination.¹¹¹ They surmise that it is presently unclear how these factors can be accounted for when targeting a specific chemical or solid-state structure for improved photovoltaic system design.

The current uncertainty regarding the exact mechanisms of non-geminate recombination mechanisms in state-of-the-art donor-acceptor photovoltaic devices limits the continued development of these systems. As such, clarification of these processes through the development of new models, improved experimental techniques for the study of charge carrier generation/recombination, and quantification of transport/extraction and recombination losses in photovoltaic devices are areas of high importance. Consequently, these uncertainties represent primary motivations for the charge extraction based investigations of Chapters 4 and 5, with the objectives of quantifying and identifying the origins of extraction losses, developing improved investigative techniques, and improving the understanding of charge carrier transport/trapping and recombination processes in donor-acceptor photovoltaic systems.

Donor-Acceptor Material Energy Levels and Non-Geminate Recombination Kinetics

The existence of the Marcus inverted region has been confirmed for a number of donor-acceptor systems regarding charge separation processes, and suggests that at ΔG_{ET} significantly greater than the reorganisation energy between reactant and product states (on the order of 0.4 eV)⁷⁴ should limit the rate of electron transfer kinetics.^{55–57,66} As such, it is unlikely that the energetic offsets between donor HOMO and acceptor LUMO typically observed in organic photovoltaic systems (greater than 1.0 eV) could influence the kinetics of charge-transfer state non-geminate recombination. However the recent study by Burke et al¹⁰² regarding free carrier/charge-transfer state equilibrium better accounting for observed charge carrier recombination probabilities may further imply that charge-transfer state binding energy could play a role in bimolecular recombination

kinetics, and therefore be influenced by the material energy levels of donor and acceptor. Further, due to the time resolution limitations of the time-resolved microwave conductivity technique employed by Coffey et al,⁷¹ those results obtained regarding the driving force dependence of charge generation yield may include not only geminate recombination, but also possibly a component of non-geminate, charge-transfer state mediated recombination.

Any energetic dependence of non-geminate recombination kinetics would be expected to have a significant dependence on charge density, where diffusion mediated bimolecular recombination at low charge densities would dominate recombination kinetics. At sufficiently high charge densities however, where a significant portion of charge carriers are spatially confined to the donor-acceptor interface, it is possible that the energetics of material energy levels or charge-transfer states could influence bimolecular recombination kinetics. Literature studies addressing this concept in organic photovoltaic systems are very limited to date, providing little experimental basis for conclusive determination, and therefore warrant further investigation. As such, investigations into the influence of material energy levels on non-geminate recombination kinetics are presented in Chapter 6.

1.4 The Study of Charge Photogeneration and Recombination Processes

A wide variety of experimental techniques have been developed and applied to the study of charge photogeneration and device operation in organic donor-acceptor systems. While characterisation of photovoltaic devices using steady-state illumination provides information on the operation of material and device designs under real-world conditions, they are limited in their ability to investigate and provide insight into the fundamental processes. Transient measurements have been extensively employed to investigate charge generation and recombination processes, including optical techniques such as transient absorption capable of observing ultrafast processes of transient excited states, and charge extraction based techniques to obtain information of separated charge carrier generation and extraction yield, as well as recombination dynamics and trapping behaviour of operational photovoltaic devices. A wide range of steady-state, frequency domain measurement techniques have also been employed for the investigation of charge carrier transport and recombination processes in photovoltaics, including electrochemical impedance spectroscopy (EIS) and intensity modulated photocurrent/photovoltage (IMPS/IMPV).^{112–114} A combination of various approaches helps to confirm the attribution of experimental observations to the underlying processes, and can compensate for the weakness each respective measurement.¹⁰⁴

1.4.1 Transient Absorption Spectroscopy

Transient absorption spectroscopy employs a purely optical approach to the investigation of transient excited species within donor-acceptor blend films. A white light probe source is used for illumination, with filters and a monochromator used to select the desired probe measurement

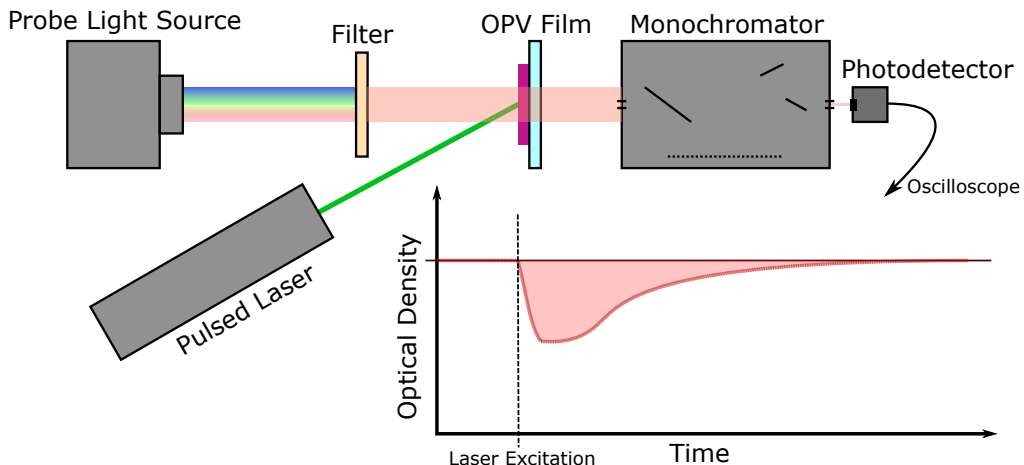


Figure 1.10: Illustration of transient absorption spectroscopy (TAS) experimental setup. A white light probe source is used for constant illumination, with filters and a monochromator used to select the desired probe measurement wavelength. The probe light is shone through the organic photovoltaic film (OPV) and changes in transmission are monitored using a photodetector. A pulsed laser is used to photoexcite the OPV film and generate transient species. Absorption of the probe light by transient species at the select wavelength is monitored over time.

wavelength within the UV-Visible to near-IR range. The probe light is shone through the organic photovoltaic film, and changes in transmission are monitored using a photodetector and oscilloscope. A pulsed laser (short pulse width, short wavelength) is used to photoexcite the film and generate transient excited species. Absorption of the probe light by these photogenerated transient species at the selected probe wavelength is monitored over time. It is also possible to monitor the inverse process, where the bleaching and recovery of ground-state (UV-Visible) absorbance is monitored (kinetics and yield) through the use of appropriate probe wavelength and photodetector. This operational setup is illustrated in Figure 1.10. This technique enables the measurement of excited state spectra through systematic variation of probe wavelength, and can be used to identify transient species, relating extinction coefficients and absorption cross-section with spectral response. The temporal decay of these transient signals is also monitored, providing a measure of transient species decay kinetics, as well as enabling the inference of charge transfer processes and estimation of charge generation yield.

As this experimental approach involves a solely optical investigation of transient species, the time resolution of these kinetics measurement is primarily limited by the pulse width of the excitation laser, thereby enabling the investigation of ultrafast (femtosecond) processes. For this reason, ultrafast transient absorption measurements are used to investigate the driving force dependence of charge carrier generation processes (electron transfer, charge separation) in Chapter 3. However, there exists inherent ambiguity in using optical techniques for investigation of these material systems, relying on the accurate assignment of transient species absorption, while the possible coexistence of multiple transient species at a given probe wavelength can lead to complexity in

interpretation of results. Additionally, these measurements may probe populations of transient species, such as polymer polarons, that are not extractable in a typical photovoltaic device (unable to differentiate between mobile or trapped charge carriers), and therefore quantitative assignment of charge generation yields and recombination kinetics can be difficult. Observations obtained using transient absorption can benefit from additional charge extraction based techniques, capable of investigating charge generation and recombination processes in operational devices. For this reason, transient charge extraction measurements are thoroughly characterised (Chapters 4 and 5), improved through the incorporation of an applied bias (Chapter 5), and utilised (Chapter 6) to compliment the ultrafast transient absorption studies of Chapter 3.

1.4.2 Transient Charge Extraction Based Techniques

Transient charge extraction based measurement techniques involve the measurement of extractable charge density in operational photovoltaic devices, and can therefore provide a quantitative measure of charge generation/extraction yields and bimolecular recombination kinetics. Complimenting these measurements with tandem electronic measurements of transient device photovoltage can further provide information on the density of trap states.

In transient charge extraction measurements, an operational photovoltaic device (with contacts) is connected to an external measurement circuit which incorporates a load (measurement impedance) and oscilloscope. A pulsed laser is then used to photogenerate charge carrier within the device active layer. The device photovoltage can be directly measured as a potential across the device contacts at open-circuit, where a high measurement circuit impedance used to inhibit current flow from the device to the external circuit, and thereby providing a measure of the photovoltage due to the photogenerated charge density. This potential can also be monitored as a function of time after photoexcitation, such as in the photovoltage decay technique. Short-circuiting the measurement circuit across a known small measurement impedance enables the flow of current through the external circuit. Due to the internal potential of the photogenerated charge density, charge carriers are extracted at the device contacts. Monitoring this external current flow provides a direct measure of extractable charge carriers, where integrating extraction current over the required extraction time yields the total photogenerated charge density within the device at the time of extraction. The application of an externally applied reverse bias during this charge extraction process can also be used to facilitate improved charge extraction, as well as provide information on charge carrier transport behaviour (mobility). Variation of the laser pulse excitation density will alter the initially photogenerated charge density, thereby enabling the measurement of photovoltage, and the corresponding internal charge density at a range of charge densities.

Introducing a delay time between the photoexcitation pulse and charge extraction measurement, such as in time resolved charge extraction utilising an nanosecond FET switch to switch rapidly between open circuit and short circuit conditions, enables the measurement of internal charge den-

sity after a known time that the device is held at open-circuit without illumination. Where the decay in internal charge density is due solely to bimolecular recombination, this approach yields a direct measurement of charge carriers that survived recombination and therefore bimolecular recombination kinetics (charge carrier lifetime, reaction order, bimolecular recombination coefficient) as a function of photogenerated charge density.^{104,115} Further combining these results with transient photovoltage decay measurements under identical conditions can be used to obtain the charge density dependence of photovoltage and charge carrier lifetime, and can be further used to investigate the device trap state density distribution and infer donor/acceptor material energy levels.³⁴

Time resolved charge extraction measurements provide a method to quantitatively determine the charge generation yield in operational photovoltaic devices, as well as provide insights into charge carrier transport, recombination, and trapping behaviour. As such, transient charge extraction measurements are used throughout the investigations of this thesis (Chapters 4, 5, and 6). Further details of the time resolved charge extraction measurement technique setup, operational procedures, and methodology used for analysis of results are provided in Chapter 2, Section 2.3.

Inherent Limitations of Charge Extraction Measurements

Inherent to these electronic measurement techniques however are temporal limitations, imposed either by measurement circuit response limitations, or by the time required for extraction of device internal charge density. This limits the time resolution of these measurement techniques to observation of processes on the nanosecond timescale or slower. Additionally, these charge extraction based measurements rely on the assumption that the extracted charge is representative of the device internal charge density, such that no recombination occurs during the extraction measurement. Regarding the degree of recombination during extraction, the loss fraction for P3HT:PCBM based bulk heterojunction organic photovoltaics has been estimated to be less than 10 percent.¹¹⁶ However, for other BHJ solar cells exhibiting faster recombination, slow transport, or using thick active layers, charge extraction times could be comparable to, or longer than the charge carrier recombination lifetime, leading to a much more significant underestimation of charge density. Furthermore, space-charging effects (build up of charge carriers causing screening of internal electric field) occurring during extraction could limit the rate of charge carrier sweep out, leading to further recombination during extraction. These recombination losses during charge extraction introduce error into the measured charge density dependence of photovoltage and charge carrier lifetime, and it is non-trivial to quantify extraction losses in typical charge extraction measurements.

To date, transient charge extraction measurement limitations and recombination losses during extraction have not been systematically quantified for donor-acceptor photovoltaic systems, with the influence of these effects on the calculation of charge density, bimolecular recombination kinetics, and trap state density distribution remaining an unresolved issue. A primary objective of this

thesis is therefore to quantify extraction losses in time resolved charge extraction measurements, and investigate the influence of these losses on the measurement of charge density, recombination kinetics, and trapping behaviour in photovoltaic devices (Chapters 4 and 5).

Background of Transient Charge Extraction Techniques

The study of recombination kinetics and material energy levels has been previously performed using a switched charge extraction technique for dye-sensitized solar cells (DSSCs),¹¹⁵ and was subsequently applied for bulk heterojunction organic photovoltaic devices.¹¹⁶ Charge extraction techniques using an externally applied reverse bias have also been extensively used to determine charge carrier transport and recombination kinetics in photovoltaic devices. Photoinduced charge extraction by linearly increasing voltage (Photo-CELIV) and bias amplified charge extraction (BACE) techniques involve the application of a reverse-bias potential (linearly increasing for Photo-CELIV, constant for BACE) to facilitate charge extraction.^{104, 117, 118} The amount of extracted charge in BACE measurements is greater than that extracted at short circuit (without an applied bias), as accelerated charge transport during extraction competes with recombination, and is therefore better at obtaining the device internal charge density by reducing charge extraction losses.

Typically for Photo-CELIV and BACE measurements, a forward bias is applied to the device prior to illumination to compensate for the device photovoltage, and is maintained during the delay time until the application of the reverse-bias.¹¹⁷ This produces a major limitation for charge carrier lifetime measurements. The open-circuit voltage during the delay time constantly decays due to charge recombination, but the applied forward bias is constant, and therefore results in charge injection. This complicates transient analysis and requires assumptions for the determination of the charge carrier lifetime due solely to photogenerated charge.¹¹⁹ Furthermore, the photogenerated charge distribution in bulk heterojunction solar cells at open-circuit condition may not be homogeneous, and change with charge density.^{120, 121} The application of a constant forward bias during the delay time may change the charge distribution, and therefore alter recombination kinetics compared to that under open-circuit conditions. The open-circuit corrected charge carrier extraction technique was developed by Baumann and Dyakonov et al as a method to overcome the problem of constant forward bias during the delay time in Photo-CELIV and BACE measurements.¹²² The open-circuit voltage decay is measured, and this same voltage signal is applied as the forward bias during delay time, maintaining open-circuit conditions without injection. The widespread adoption of this technical measurement procedure is however hindered by its practical complexity.

Alternatively, charge recombination lifetime can be obtained through transient photovoltage decay measurements.^{24, 104} The photovoltage decay is analysed based on the assumption that the voltage scales with charge density, and that the charge density decreases only due to recombination. However if charge density is not homogeneous, changes in charge density are caused by both

recombination and transport through the active layer, requiring a more complicated analysis. Charge extraction or transient photocurrent measurements (TPC) are however still required to obtain lifetime as a function of charge density.²⁴ As TPC measures the transient photocurrent induced by a pulsed light at short-circuit conditions, the integrated charges may be underestimated due to charge recombination. The BACE technique could be employed to avoid recombination during extraction, however the issues with maintaining open-circuit condition during delay time remain.

A charge extraction technique is therefore required, that avoids the complicated analysis and assumptions needed to overcome the experimental difficulty in maintaining open-circuit condition during delay time, while achieving accelerated charge extraction (through an applied reverse bias) and thereby minimize charge recombination losses during extraction. A primary objective of this thesis is therefore to develop an improved time resolved charge extraction measurement technique through inclusion of an applied bias during charge extraction (Chapter 5). This technique is thoroughly characterised and used in subsequent investigations of extraction losses, as well as the investigations of the influence of material energy levels on charge generation yield, device photovoltage, and bimolecular recombination kinetics (Chapter 6).

1.5 Thesis Overview

The overall objective of this thesis is to quantify the influence of the driving force for electron transfer on electron transfer kinetics and charge generation yield in organic photovoltaic systems, with the motivation of reducing this driving force as a method for increasing device photovoltage (reduce energy losses), while maintaining high device current (high charge generation/separation efficiency and yield). This will further provide a greater understanding of charge photogeneration processes in these photovoltaic systems, to better reconcile material systems design and charge photogeneration behaviour with the performance of operational photovoltaic devices, and thereby provide improved design principals for the development of new donor-acceptor systems and device architectures.

The following main objectives are therefore investigated within this thesis:

- Determine the influence of the driving force for electron transfer on electron transfer kinetics and charge generation yield in donor-acceptor systems using ultrafast transient absorption measurements.
- Develop an improved transient charge extraction measurement technique for the investigation of charge generation yield and recombination kinetics in donor-acceptor organic photovoltaic devices.
- Determine the origin of, and quantify the influence of charge extraction losses on the measurement of charge density, recombination kinetics, and trapping behaviour in transient charge

extraction measurements.

- Quantify the influence of donor-acceptor material system energy levels on charge extraction yield, device photovoltage, and recombination kinetics in operational photovoltaic devices using transient charge extraction.

Details of the methodology adopted to investigate the above objectives, and the primary outcomes of these investigations are outlined in the following sections.

1.5.1 Donor-Acceptor Material Systems

A series of bridgehead imine substituted cyclopentadithiophenes based polymer donor materials developed by Azouley and Bazan et al have shown promise for use in reasonably efficient low-bandgap photovoltaic devices, with solar conversion efficiencies exceeding 3 % for optimised devices incorporating these donor polymers blended with the PCBM acceptor.⁴³ Beyond the photovoltaic performance of these donor-acceptor systems, this series of polymer donors provides a unique opportunity to systematically investigate the influence of material system energetics on charge photogeneration processes, which has to date proven experimentally difficult. The molecular structure of push-pull copolymers incorporating an aryl (Ar) imine substituent at the bridgehead position of 4H-cyclopenta[2,1-b:3,4-b']dithiophene (CPDT) can be used to systematically influence the highest occupied/lowest unoccupied (HOMO/LUMO) energies of the polymer while keeping the backbone structure intact.⁴³

This polymer donor series can therefore be used to provide a series of donor-acceptor systems with engineered variation in the driving force for electron transfer ΔG_{ET} . Modification of the Ar substituent with progressively electron withdrawing substituents, Ar = p-C₆H₁₃ (P1), p-C(CF₃)₂OC₈H₁₇ (P2), and C₆F₅ (P3), provides a set of donor materials with nearly identical band gaps (~1.5 eV) and progressively reduced LUMO energies (-3.73, -4.00, and -4.12 eV for P1, P2, and P3, respectively), as displayed in Figure 1.11. These low bandgap polymer donor materials were synthesised by, and obtained from Jason Azoulay and Guillermo Bazan (The Center for Polymers and Organic Solids, University of California, Santa Barbara, USA). All device fabrication and optimisation was however performed by the doctoral candidate locally (Intelligent Polymer Research Institute, University of Wollongong, Australia). The values of E_{HOMO}/E_{HOMO} and ΔG_{ET} were obtained through cyclic voltammetry of drop-cast films as detailed in the paper by Bazan et. al.⁴³ Bazan et. al. have also published additional literature discussing the electrochemical considerations for determining the absolute frontier orbital energy levels (HOMO/LUMO) of conjugated polymers, with a specific focus on organic photovoltaic materials such as those used herein.¹²³ It is noted that although formal potentials can be correlated with E_{HOMO}/E_{HOMO} , the error margin on these energy levels is likely on the order of ± 0.1 eV. It is therefore reasonable to assume the error associated with ΔG_{ET} is also on the order of ± 0.1 eV. However this is for an absolute value of free energy. Where a series of comparable donor polymers are measured under

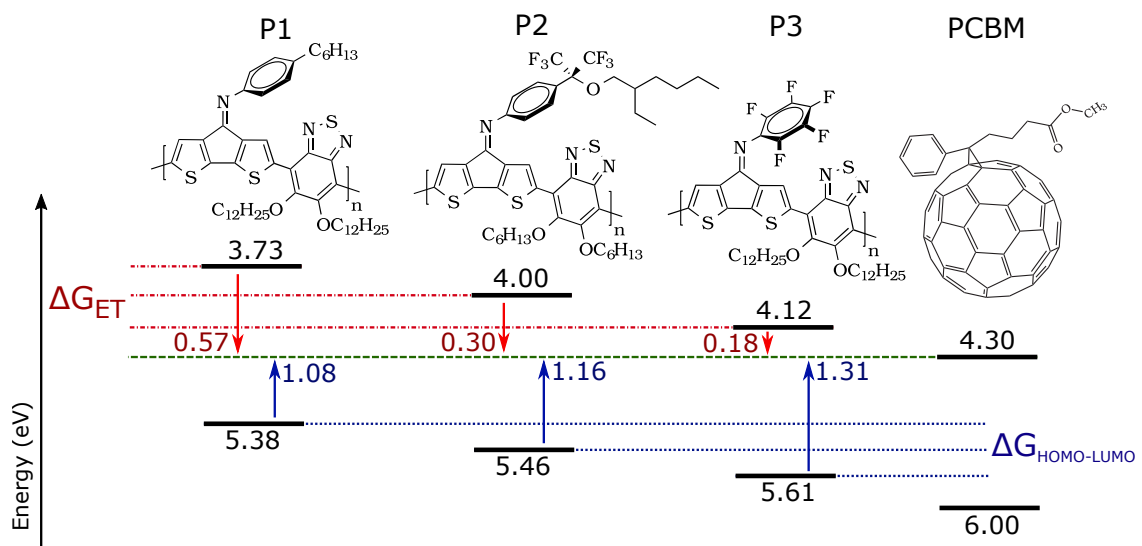


Figure 1.11: Molecular structures of cyclopentadithiophene based polymer donors (P1, P2, and P3) and the fullerene based acceptor (PCBM). Shown are the highest occupied molecular orbital energy level (E_{HOMO}) calculated from the onset of oxidation, and the lowest unoccupied molecular orbital energy level (E_{LUMO}) calculated from the onset of reduction (obtained using cyclic voltammetry), with a comparison of the electrochemical band gaps and LUMO offsets of the donors relative to the PCBM acceptor (E vs vacuum). Also displayed are the driving force for electron transfer (ΔG_{ET}), and the free energy offset between donor polymer E_{HOMO} and PCBM acceptor E_{LUMO} ($\Delta G_{HOMO-LUMO}$).

identical conditions as those presented herein, the relative error in ΔG_{ET} between donors is likely lower than 0.1 eV. The specific donors were selected with ΔG_{ET} relative to the PCBM acceptor of 0.57, 0.30, and 0.18 eV for P1, P2, and P3, respectively. Importantly, these donor polymers also exhibit similar solubility, morphology, processability, and sufficiently red-shifted main absorption bands relative to PCBM absorption, enabling selective photoexcitation of the donor phase in photovoltaic blends.

While active layer morphology can influence the energetics of the donor-acceptor interface through phase crystallinity, reorganisation energy, charge screening, and delocalisation, the use of similar polymer donor blend systems with comparable morphology should minimise the relative influence of these effects. The influence of morphology on charge generation and recombination is not the focus of this thesis, but rather the influence of donor-acceptor system energetics on these fundamental processes. The impact of morphology on charge transport, extraction, and trapping also presented a significant issue in the use of charge extraction measurement techniques in obtaining a measure of internal photogenerated charge density. As such, the development and characterisation of an applied bias charge extraction technique was critical to the successful investigation of these polymer donor systems, thereby circumventing the morphological extraction limitations (Chapter 5). Additionally, in the ultrafast transient charge photogeneration studies (Chapter 3), the use of low PCBM loadings in addition to more typical photovoltaic device loading for the transient absorption films was used to investigate exciton quenching without influencing the morphology of active layer blend.

1.5.2 Ultrafast Transient Absorption Spectroscopy

The experimental approach adopted for the investigation of the charge photogeneration processes in donor-acceptor systems outlined in the previous section centred around the use of ultrafast (femtosecond) transient absorption spectroscopy, capable of directly monitoring electron transfer kinetics and excited state decay. The collaborative nature of the investigations involving femtosecond transient absorption spectroscopy for the studies of the P1/P2/P3 polymer systems requires an explanation of the exact role of the candidate. Due to the advanced nature of equipment and operational expertise required to achieve the requisite ultrafast time resolution, the transient absorption measurements (setup, operation, and data acquisition) were performed in Tsukuba by Kenji Sunahara (Graduate School of Pure and Applied Sciences, University of Tsukuba, Japan), Akihiro Furube (National Institute of Advanced Industrial Science and Technology, Japan), and Attila Mozer (Intelligent Polymer Research Institute, University of Wollongong, Australia). The transient absorption film samples were prepared by Andrew Nattestad (Intelligent Polymer Research Institute, University of Wollongong, Australia). The candidate's role was to analyse the raw data, and to develop models for the interpretation of results. This work was crucial in obtaining more than a basic qualitative understanding of the underlying charge photogeneration processes, with assignment and quantification of kinetics and yield for the multiple underlying components of each transient

at the various measurement conditions. These activities represent the majority of work invested in these ultrafast transient absorption investigations, including processing/normalising of datasets, and the development of appropriate models and custom fitting/analysis routines. Consequently, the candidate was tasked with the primary responsibility of writing the published manuscript.⁵⁰

The results of these investigations are presented in Chapter 3, and indicate that ΔG_{ET} of 0.18 eV is not sufficient to yield ultrafast charge generation, while driving forces above this value exhibited near-unity electron transfer yield on the femtosecond timescale. Additionally, no increase in electron transfer kinetics or estimated charge generation yield was found with an increase in ΔG_{ET} from 0.30 to 0.57 eV, where the initial charge generation yield appears limited by charge-transfer state recombination, rather than the electron transfer kinetics. Picosecond non-geminate recombination was also observed in the donor-acceptor system with ΔG_{ET} of 0.30 eV, indicating that bimolecular recombination may limit the extractable photocurrent in this system.

1.5.3 Time Resolved Charge Extraction

The optical studies of Chapter 3 provided information on the kinetics of electron transfer and an estimate of charge generation yield. However these results alone are insufficient to provide conclusive insights into overall charge generation efficiency, and can benefit from additional charge extraction based techniques, capable of quantitatively determining the charge generation yield in operational photovoltaic devices, as well as providing insights into charge carrier transport, recombination, and trapping behaviour. For this reason, transient charge extraction measurements were assessed for use in further investigations of the influence of ΔG_{ET} on charge generation yield, non-geminate recombination kinetics, and trapping behaviour in operational photovoltaic devices incorporating the cyclopentadithiophene based polymer donors, thereby complimenting the ultrafast transient absorption studies of Chapter 3. The suitability of a relatively novel charge extraction technique incorporating a nanosecond switch is investigated in Chapter 4, including an assessment of measurement limitations and their impact on the calculation of charge density, recombination kinetics, and trap state density distribution. These investigations were performed using the PCDTBT:PCBM and P3HT:PCBM donor-acceptor material systems, both of which have been extensively studied in literature and provide benchmark systems for the investigation of charge extraction measurement limitations. These material systems also provide complimentary device behaviour, and are therefore used to expand the coverage of measurement conditions that can be investigated. The results obtained through these investigations identified fundamental limitations in the time domain of this technique. However, this technique successfully yielded values for charge density, recombination kinetics, and trap state density distribution that compare well with literature reports, and proved capable of monitoring these parameters over a wide range of charge densities.

During the course of assessing the time resolved charge extraction techniques, significant extraction losses were identified, leading to inaccuracy of results under certain measurement conditions, with up to an estimated five fold underestimation of charge density and five fold overestimation of charge carrier lifetime. As such, additional investigations were performed to identify the origins of the observed extraction losses, and to quantify the influence of these losses on the measurement of charge density, recombination kinetics, and trapping behaviour in photovoltaic devices (Chapters 4 and 5).

1.5.4 Applied Bias Time Resolved Charge Extraction

In order to overcome the observed charge extraction losses, particularly that of recombination losses during the extraction process, the development of an improved time resolved charge extraction measurement technique was undertaken, through the first time inclusion of an applied bias during charge extraction (Chapter 5). The capabilities and limitations of the developed technique are thoroughly characterised for a range of measurement conditions (excitation density, magnitude of applied reverse bias, measurement circuit impedance) and device parameters (donor-acceptor material system, active layer thickness and surface area). These investigations are further used to accurately determine the origin of, and systematically quantify the observed extraction losses, enabling the attribution of the operational device performance limitations to the underlying loss mechanisms.

The results of these investigations indicate that upwards of 50 % of photogenerated charge density is not measured, and therefore lost without the application of an applied reverse bias in time resolved charge extraction under certain measurement conditions, which in turn significantly impacts the calculation of recombination kinetics and trap state density distribution, as well as the apparent charge density dependence of these parameters. Additionally, the applied bias is capable of reducing the observed disparity in measurement results obtained for comparable devices with differences in active layer thickness. These findings facilitated the development of improved measurement and analysis techniques, and provide an improved understanding of charge carrier transport/trapping and recombination processes in donor-acceptor photovoltaic devices. These outcomes were then utilised in the investigations of material energy level influence on charge generation yield, device photovoltage, and bimolecular recombination kinetics (Chapter 6).

1.5.5 Influence of Material Energy Levels in Operational Photovoltaic Devices

Investigations were then performed in Chapter 6 to quantify the influence of ΔG_{ET} on charge generation yield, with additional objectives to investigate the influence of ΔG_{rec} on device photovoltage and recombination processes. This is achieved using the newly developed applied bias time resolved charge extraction technique, and photovoltaic devices incorporating the cyclopentadithiophenes based polymer donors, providing complimentary results to the purely optical studies of

Chapter 3. Poor charge transport and extraction behaviour was identified in these donor-acceptor systems, and was found to strongly influence photovoltaic device performance. Use of the developed applied bias charge extraction technique did however enable the effective investigation of charge carrier dynamics, overcoming these extraction limitations.

The measured charge extraction yields indicate that ΔG_{ET} of 0.18 eV results in less than one third that of donor-acceptor systems with ΔG_{ET} of 0.30 eV or above, while increasing ΔG_{ET} above 0.30 eV does not yield a significant further increase in charge generation yield. Increasing ΔG_{ET} does however result in a reduction in device V_{OC} for a given charge density, further resulting in a net loss in overall device efficiency. For a given ΔG_{ET} , increasing the donor material bandgap and therefore ΔG_{rec} can increase the device V_{OC} , without sacrificing charge generation yield. However, increasing ΔG_{rec} was observed to increase bimolecular recombination kinetics at high charge densities, and is the first time that this has been observed experimentally. Further, nanosecond bimolecular recombination was found to have a greater influence on device extraction yield than any variation in ΔG_{ET} , indicating that these recombination processes are crucial in determining the overall photovoltaic device performance.

The primary findings of Chapters 3 and 6 regarding the influence of driving force for electron transfer on charge generation kinetics and yield have been published in the Journal of Physical Chemistry C.⁵⁰ The primary findings of Chapters 4 and 5 regarding the first time introduction of an applied bias in time resolved charge extraction measurements, and the elucidation and quantification of extraction losses have been published in Advanced Energy Materials.¹²⁴

Chapter 2

Experimental Methods

2.1 Photovoltaic Film/Device Fabrication and Characterisation

2.1.1 Photovoltaic Film/Device Fabrication

The architecture used for all fabricated photovoltaic devices was consistent, and of the form ITO anode / PEDOT:PSS hole selective layer / polymer(donor-acceptor blend) active layer (bulk heterojunction) / TiO_x electron selective layer / Aluminium cathode. The electron/hole selective interlayers are used in this device architecture to ensure sufficiently blocking contacts (good diode behaviour) when used in applied bias charge extraction measurements. The cyclopentadithiophene based polymer donor films used in the photoluminescence and transient absorption studies were prepared by Andrew Nattestad (Intelligent Polymer Research Institute, University of Wollongong, Australia). The film preparation/deposition procedures and parameters are identical to that of the device fabrication procedures outline below (performed by the candidate) for the cyclopentadithiophene based polymer donor devices, only deposited on a plain glass substrate and excluding the use of electron/hole selective layers and cathode deposition.

Active Layer Polymer(Blend) Solution Preparation

The active layer blend solutions are prepared with parameters depending on donor-acceptor materials used. Slight variations to solution concentrations and deposition parameters were used where variation of active layer thickness was required. All materials used in the preparation/fabrication of photovoltaic devices are from Sigma-Aldrich unless otherwise specified. The poly[N-9"-hepta-decanyl-2,7-carbazole-alt-5,5-(4',7'-di-2-thienyl-2',1',3'-benzothiadiazole)] (PCDTBT) (Solaris, SOL4280, 68-85Dka, electronic grade) and [6,6]-phenyl-C₆₀-butyric acid methyl ester (PCBM) (Solaris, SOL5061A, 99.5 % purity) (1:4) blend solution was prepared by dissolution in o-dichlorobenzene at 20 mg mL⁻¹ and stirring at 120 C° for 20 hours under an Ar atmosphere. The poly(3-hexylthiophene-2,5-diyl) (P3HT) (LumTec., LT-S909, 45Dka, electronic grade, 93 % regioregular) and PCBM (5:4) blend

solution was prepared by dissolution in chlorobenzene at 50 mg mL⁻¹ and stirring at 80 C° for 20 hours under an Ar atmosphere. For the cyclopentadithiophene based polymer donor/blend solutions, each donor:PCBM (1:4) blend solution was prepared by dissolution in o-dichlorobenzene at 20 mg mL⁻¹ and stirring at 120 C° for 30 hours under an Ar atmosphere. These solutions were then filtered through a 0.45 µm PTFE filter to remove undissolved donor material after cooling to room temperature.

Please note that a ratio of 1:4 (25 %) polymer to PCBM is used within the cyclopentadithiophene based blend devices used in the studies of Chapter 6, typically yielding a PCBM concentration of approx. 70-80 %. A PCBM concentration of 70 % is however used for the blend film studies of Chapter 3. The small difference in blend concentration (on order of 5-10 %) is not expected to, and therefore has been assumed to not influence any behaviour of the material system. A direct comparison between the results obtained in Chapters 3 and 6 is therefore performed without further reference to, or direct consideration of this small difference in active layer PCBM blend concentration.

Glass/ITO Substrate Preparation

Pre-patterned Indium Tin Oxide (ITO) coated glass slides (LumTec., 90 nm thick ITO, variable active pixel area, typical conductivity of 15 Ω cm⁻², above 85 % transmission at 550 nm) are used for the transparent device anode, as well as providing a rigid substrate. The substrates are cleaned by 15 min under sonication in surfactant/H₂O, followed by two subsequent 5 min sonication rinses in H₂O, and 15 min under sonication each in acetone and isopropanol, prior to a 20 min UV-ozone treatment. This ensures a clean, particulate free substrate and improves wettability for solution/active layer deposition.

PEDOT:PSS Hole Selective Interlayer

The cleaned substrates are coated with the poly(3,4-ethylenedioxythiophene):poly(styrenesulfonate) (PEDOT:PSS) hole selective layer, using 0.5 wt % PEDOT:PSS solution (Heraeus Clevios Al 4083) diluted 1:1 in isopropanol. The PEDOT:PSS solution is filtered through a 0.45 µm PVDF filter to remove any particulates prior to dilution, and maintained under stirring. The layer is then deposited using spin coating (Laurell WS-560HZ-15NPP) at 5000 rpm for 30 s, followed by annealing in air at 140 C° for 20 min.

Active Layer Deposition

Directly prior to deposition of the active layer, the active layer polymer(blend) solutions are cooled to room temperature. For the P3HT and PCDTBT based devices, the polymer(blend) solutions were spin-coated in air onto the prepared substrate at between 1500 and 5000 rpm, for times ranging from 90 to 240 s, depending on the active layer thickness required. For the cyclopentadithiophene based polymer donor/blend devices, the polymer(blend) solutions were

doctor-bladed (Erichsen Coatmaster 509 MC) in air onto the substrate at between 13 and 15 mm s⁻¹, with a hotplate (Prazitherm PZ35, high stability) temperature of 75 C° and drying times ranging from 5 to 30 s (depending on polymer donor).

TiO_x Electron Selective Interlayer

To produce the amorphous titanium oxide (TiO_x) electron selective interfacial layer, a titanium oxide sol-gel precursor solution is first prepared. Titanium diisopropoxide bis(acetonate) (75 % isopropanol, Sigma-Aldrich) (1.0 mL) is added to isopropanol (8.0 mL) while stirring. Then 0.5 mL of glacial acetic acid is added, followed by 0.5 mL of deionized water. This solution is then heated to, and maintained at 60 C°, and is left stirring for 24 hours. This prepared precursor solution is diluted (1:10) into isopropanol prior to deposition onto the device active layer. TiO_x layer deposition is performed directly after active layer deposition (and any required active layer solvent drying time) using spin coating at 5000 rpm for 30 s, and is left to hydrolyze in air for 20 min (or under heating where the active layer requires annealing).

Cathode Deposition and Device Sealing

Aluminium (Al) is then evaporated under vacuum through a mask of defined device active area (0.095 cm⁻² unless otherwise stated), to produce a cathode thickness on the order of 100 nm. A ramp in evaporation rate is used to ensure good contact with the active layer (initial 5 nm at 0.5 Å s⁻¹, following 50 nm at 1.5 Å s⁻¹, final ~ 50 nm at 2.5+ Å s⁻¹). The deposition chamber is left to cool down for 30 minutes before returning to atmospheric pressure. These devices were then sealed under an inert Ar atmosphere using a cover glass slide and UV-curable epoxy (Ossila, E131), manually cured using a handheld UV gun. Effort is made to ensure that no epoxy is in contact with the device active layer, and that no significant UV illumination is incident on the device active area. Finally, a metal contact is soldered (ultrasonic) onto the exposed anode/cathode contact regions for increased durability during measurement.

2.1.2 Steady-State Device Performance

Current-voltage (*JV*) measurements are performed to assess steady-state device performance, and characterise a number of important device parameters including open circuit voltage *V_{OC}*, short-circuit current *J_{SC}*, fill factor *FF*, solar conversion efficiency η , series resistance *R_S*, and shunt resistance *R_{Sh}*, using known parameters for device area *A* and device thickness *d*. The solar simulator and measurement system used (TriSol Solar Simulator, IV16-L, PV Measurements Inc.) comprises components for variable electronic load and data acquisition (Keithley 2400, PVM QEX10), and a white light source (constant illumination, 1.5 air mass global solar spectrum) calibrated using a standard silicon diode to 1 sun equivalent (100 mW cm⁻²). The photovoltaic device is held under illumination at a range of constant applied potentials (*V*), from forward to reverse bias, and the extracted current density (*J*) is measured, to produce a *JV* response plot. A dark measurement (without illumination) is also performed across the range of measured

applied potentials. Further, the illumination intensity can be varied below 1 sun through the use of reflective neutral density filters, thereby obtaining *JV* response at a range of steady-state current densities.

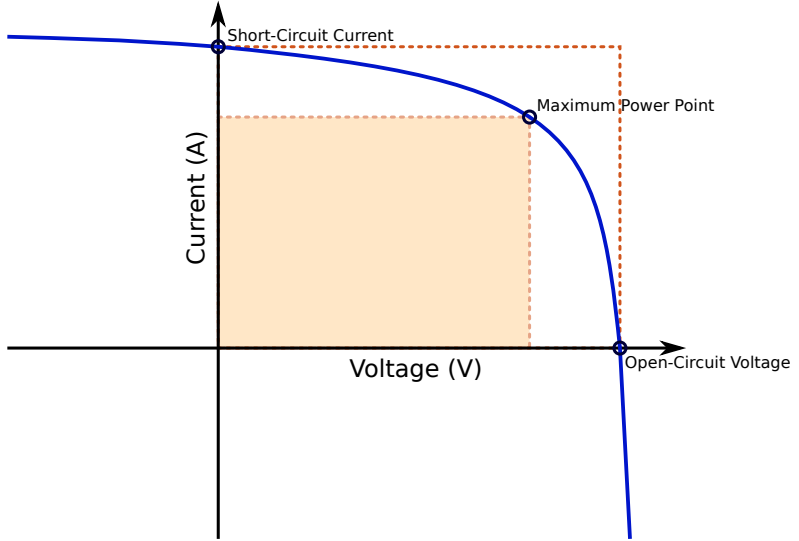


Figure 2.1: Illustration of a photovoltaic device current-voltage response (blue line), with open-circuit voltage, short-circuit current, and maximum power point labelled.

Figure 2.1 illustrates an example current-voltage response for a photovoltaic device under illumination. J_{SC} and V_{OC} are obtained directly as the *JV* response intersection with the voltage and current density axis respectively. The FF is calculated as the quotient of P_{max} and the product of J_{SC} and V_{OC} , illustrated as the ratio of the two square regions in Figure 2.1. The power conversion efficiency η of a device can then be obtained using

$$P_{max} = FF J_{SC} V_{OC} \quad (2.1)$$

$$\eta = \frac{FF J_{SC} V_{OC}}{P_{in}} \quad (2.2)$$

where P_{max} is the power obtained at the maximum power point, and P_{in} is the input power (incident radiation). The series and shunt resistance are then calculated for each device, using the slope of the dark *JV* plot about 1 V and 0 V respectively.³⁵

Further analysis of these measurement results can be performed to obtain the empirical reaction order δ' and diode ideality factor n'_{id} , and can be compared to those obtained through transient measurement and analysis. The δ' can be calculated from the dependence of short circuit current J_{SC} on illumination intensity ϕ using the relations^{34,125}

$$\ln(J_{SC}) = -\alpha' \ln(\phi) \quad (2.3)$$

$$\delta' = \alpha'^{-1} + 1 \quad (2.4)$$

The n'_{id} can be calculated from the dependence of open circuit voltage V_{OC} on ϕ using the relation^{125,126}

$$V_{OC} = n'_{id} \ln(\phi) \quad (2.5)$$

with n'_{id} in units of $k_B T q^{-1}$, where k_B is the Boltzmann constant, T is the temperature, and q is the charge of an electron.

2.1.3 Active Layer Thickness Measurement

Photovoltaic device active layer thickness is determined through the average thickness as measured by stylus and optical profilometry (Veeco Dektak 150, Veeco Wyko NT9100). After all device investigative measurements are complete, the glass cover slip is removed and device active layer is scratched at multiple regions adjacent to the device active pixel (for optical films, thickness was determined in the region used for excitation/probe in transient absorption), and through the Al coated pixel. The scratch results in a relative depth to the glass/ITO layer (the high hardness of ITO resists deformation or removal), incorporating the thickness of the active layer as well as both PEDOT:PSS and TiOx layers (calibrated and determined separately during device fabrication, typically found to be consistent within 5 nm for PEDOT:PSS and 10 nm for TiOx layers respectively). The thickness of the aluminium cathode layer is determined during evaporation through the use of a quartz crystal resonance detector (also calibrated separately using optical/stylus profilometry, found to be accurate to within 5 nm after calibration for substrate relative distance from evaporation source).

The total height of all layer relative to the ITO/Glass substrate is measured, and each respective layer (Al, PEDOT:PSS, TiOx) thickness subtracted, leaving a calculated active layer thickness corresponding solely to the device bulk heterojunction. An average is obtained for 4 scratches (multiple device regions), used to obtain a final active layer thickness for each device. The error in active layer thickness calculation is on the order of 30 nm, however typically the practical error is observed to be significantly lower, with accurate/consistent determination within a single fabrication set of devices (error closer to 15 nm). As the relative thickness of devices is most important for the investigations within this thesis, and variation in other subtracted layers is comparable for devices within a fabrication set, the relative error is reduced. Additionally, these direct measurements of active layer thickness can be compared with those obtained through calculation using charge extraction or electrochemical impedance measurements using known device parameters through

$$d = \frac{\epsilon \epsilon_0 A}{C} \quad (2.6)$$

where d is the calculated active layer thickness, A is the device surface area, ϵ is the dielectric constant of the active layer, ϵ_0 is the permittivity of free space, and C is the measured device capacitance. This can help to ensure the accuracy of measured values with respect to the average over the entire pixel area (electronic measurements).

2.1.4 Transmission Electron Microscopy

Polymer:PCBM blend solutions for each respective polymer donor were prepared by dissolution in o-dichlorobenzene at 20 mg mL^{-1} and stirring at 120 C° for 20 h under an Ar atmosphere. Glass substrates were cleaned by 15 min sonication in surfactant/ H_2O , two subsequent 5 min sonication rinses in H_2O , and 15 min sonication each in acetone and isopropanol prior to 20 min UV-ozone treatment. Spin coating was used to deposit a 50 nm thick PEDOT:PSS layer onto the substrate at 5000 rpm for 30 s. The blend solutions were doctor-bladed onto the PEDOT:PSS layer in air, at 75 C° using a $500 \mu\text{m}$ blade height at a typical rate of 20 mm s^{-1} , to obtain a blend film thickness on the order of 100 nm. The PEDOT:PSS layer was then selectively dissolved in distilled water, with the floated polymer blend film transferred to a transmission electron microscopy (TEM) copper grid. Samples were dried in a vacuum for 2 hours prior to TEM measurements to remove adsorbed water and oxygen. Imaging was then performed (JEOL JEM-2011 TEM, 0.16 nm spatial resolution) to obtain microscopy images at varying magnifications (total field-of-view from 2 to 5 μm), with a resolution on the order of 5 nm.

2.1.5 UV-Visible Absorbance Spectroscopy

UV-Visible absorbance spectroscopy was performed in transmission mode on all pristine and blend films (Shimadzu UV-1800 Spectrophotometer), with a reference device without the active bulk heterojunction layer (but including PEDOT:PSS and TiO_x layers) also recorded, which is subtracted from the spectral response. Typical spectra were recorded from 300 to 1000 nm.

2.2 Transient Optical Measurement Techniques

2.2.1 Transient Absorption Spectroscopy

Nanosecond Transient Absorption of Photovoltaic Devices

Transient absorption measurements were performed through an optically transparent region of the fabricated photovoltaic devices (no Al top electrode), directly adjacent to the active device area. Charge carriers are photogenerated using a laser pulse (532 nm, 6 ns pulse width, Spectra Physics Quanta Ray Lab 170), with incident excitation density varied using reflective neutral density filters from 100 down to $0.1 \mu\text{J cm}^{-2}$. The change in probe (Xenon flashlamp, stable white light) sample transmission as a function of time after excitation is measured through a monochromator, using a photoreciever (Femto, HCA-S-200M-IN) and an oscilloscope (DPO4000 Series, Tektronix). Each decay transient is recorded as an integrated average of 512 individual

measurements to obtain acceptable transient signal-to-noise, as well as to account for any pulse-to-pulse variation in excitation density. The probe wavelength is varied using a combination of longpass and bandpass optical filters, prior to selective transmission through the spectrometer. The probe illumination intensity is altered for each wavelength to optimise signal response, and to avoid saturation of the photoreceiver.

Ultrafast Transient Absorption

For sub-nanosecond transient absorption (TA) measurements (spectra), samples were photoexcited using a 150 ps laser pulse at 532 nm (Ekspla, SL311, repetition rate 10 Hz), while a microsecond flashlamp (Hamamatsu, L4642) and monochromator were used as the probe light. The change in the transmission of the samples was monitored using Si (New Focus, 1601) and InGaAs (New Focus, 1611) photoreceivers and a digital oscilloscope (LeCroy, 6200A) with a time resolution of 400 ps. Femtosecond TA measurements (kinetics) were performed using a Ti:Al₂O₃ laser (Spectra-Physics, Hurricane) and regenerative amplifier (Coherent RegA9000) as a light source. The output from the regenerative amplifier (180 fs pulse width, repetition rate of 10 kHz) was separated into two beams for the excitation of two optical parametric amplifiers (OPAs; Coherent OPA9400 and OPA9800), used as pump and probe light pulses. The delay time of the probe pulse relative to the pump pulse was adjusted by changing the path length of the pump pulse using an optical delay stage, and provided a temporal resolution of 250 fs.¹²⁷

Due to the advanced nature of equipment and operational expertise required to achieve the requisite ultrafast time resolution, these TA measurements (setup, operation, and data acquisition) were performed by Kenji Sunahara (Graduate School of Pure and Applied Sciences, University of Tsukuba, Japan), Akihiro Furube (National Institute of Advanced Industrial Science and Technology, Japan), and Attila Mozer (Intelligent Polymer Research Institute, University of Wollongong, Australia).

2.2.2 Integrated Photoluminescence Spectroscopy

Integrated photoluminescence was detected using a streak camera (Hamamatsu, StreakScope C4334, 50 ps time resolution) equipped with a monochromator, with 532 nm laser pulses (Ekspla, SL311, repetition rate 10 Hz) used to photoexcite the film. The photoluminescence emission spectra was recorded from 650 to 950 nm, integrated over 1 ns post excitation, with a temporal resolution of 30 ps.

These photoluminescence measurements were performed by Kenji Sunahara (Graduate School of Pure and Applied Sciences, University of Tsukuba, Japan) and Akihiro Furube (National Institute of Advanced Industrial Science and Technology, Japan), in tandem with the ultrafast transient absorption measurements (see previous section) to ensure consistency of results and reduce any variation/degradation of films between measurements.

2.3 Transient Electronic Measurement Techniques

2.3.1 Time Resolved Charge Extraction Measurements

The time resolved charge extraction (TRCE) measurement utilises a nanosecond FET switch (SR-05, Asama Lab) to switch rapidly between open circuit and short circuit conditions. A circuit diagram (top) and timing diagram (bottom) are presented in Figure 2.2 to illustrate the set-up and operation of TRCE measurements. The switch is capable to switching from an internal impedance R_{SW} of $2.2\text{ M}\Omega$ to less than $1\text{ }\Omega$ in under 100 ns. A high switch impedance is used to maintain open circuit rather than a true open circuit (infinitely large impedance) to protect the switch. A photovoltaic device (OPV) is connected in series with the switch, and charge carriers are generated using a laser pulse for photoexcitation (532 nm, 6 ns pulse width, Spectra Physics Quanta Ray Lab 170; or during long pulse measurements a 641 nm, variable pulse width, Nation Instruments Coherent CUBE continuous wave). A variable delay time T_{del} is imposed between stopping laser illumination T_0 and switching T_{SW} using a delay generator, during which time the device is held at open circuit, and charge carriers are left to recombine. Upon switching, the device is short circuited and an extraction transient is measured across the variable measurement impedance R_M ($50\text{ }\Omega$ unless otherwise stated) using an oscilloscope (DPO4000 Series, Tektronix).

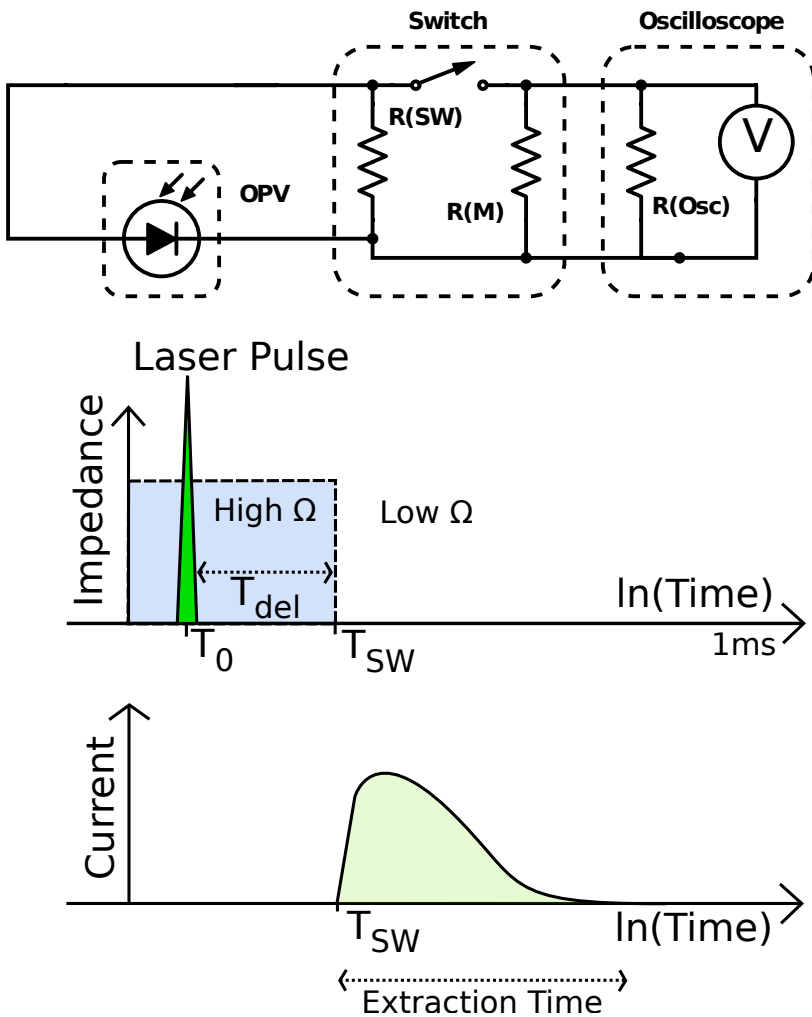


Figure 2.2: Top: Time resolved charge extraction circuit diagram, illustrating the organic photovoltaic device (OPV), FET switch with internal high impedance resistor R_{SW} and measurement resistance R_M , and oscilloscope with internal resistance R_{Osc} . Bottom: Timing diagram for operation of extraction measurements, illustrating the laser excitation pulse at T_0 , high initial circuit impedance ($M\Omega$) switching to low ($< 1 \Omega$) at T_{SW} , variable delay time T_{del} , and an illustration of an extraction current transient as a function of extraction time.

Each extraction transient is recorded as an average of 50 individual measurements, per set of conditions, to minimise noise and account for any variability in laser excitation. All transients presented herein are displayed with an 80 ns shift for illustration purposes, such that switching occurs at 80 ns as presented in figures. Unless otherwise specified, the characteristic switch response has been subtracted from all transients, recorded individually for each set of measurements, as well as the dark (no laser illumination) transient response. The transient voltage response is measured as a function of extraction time, and converted to extracted current using the known measurement resistance. The total extracted charge is obtained through integrating the current transient response over time. The extracted charge is obtained at a range of delay times to yield

the decay of extracted charge as a function of delay time, with laser illumination also varied.

2.3.2 Photovoltage Decay Measurements

Photovoltage decay measurements are performed to obtain the open circuit potential at the device contacts as a function of time that the photovoltaic device is held at open circuit after laser illumination is stopped. Variation of excitation density is also used to alter the initial charge density. These measurements are performed using a laser excitation source (532 nm, 6 ns pulse width, Spectra Physics Quanta Ray Lab 170; OR for long pulse measurements a 641 nm, variable pulse width, Nation Instruments Coherent CUBE continuous wave), with the photovoltaic device connected in series with the oscilloscope high impedance of $1.0\text{ M}\Omega$ to maintain open circuit. The photovoltage decay transients are then recorded using the oscilloscope (DPO4000 Series, Tektronix), from the time of stopping laser excitation until complete decay of photovoltage.

2.3.3 Time Resolved Charge Extraction with an Applied Bias

The time resolved charge extraction (TRCE) measurement utilising a nanosecond high impedance FET switch (Section 2.3.1), is modified through the addition of the ability to apply a reverse bias during charge extraction measurement. This facilitates improved charge extraction under the applied bias, relative to standard operation which relies solely on the device's built in potential to drive charge extraction. In concert with switching at T_{SW} , a reverse bias square pulse potential is applied across the device contacts (through the FET switch) using a function generator (WF1974 Wave Factory Multifunction Generator, NF Corp.). The pulse length of the applied reverse bias was maintained for 1 ms, well beyond typical extraction times on the order of $50\text{ }\mu\text{s}$. A circuit diagram (top) and timing diagram (bottom) are presented in Figure 2.3 to illustrate the set-up and operation of the novel applied bias TRCE measurement. In the course of measurements, the magnitude of the applied reverse bias can be varied in addition to both delay time and excitation density.

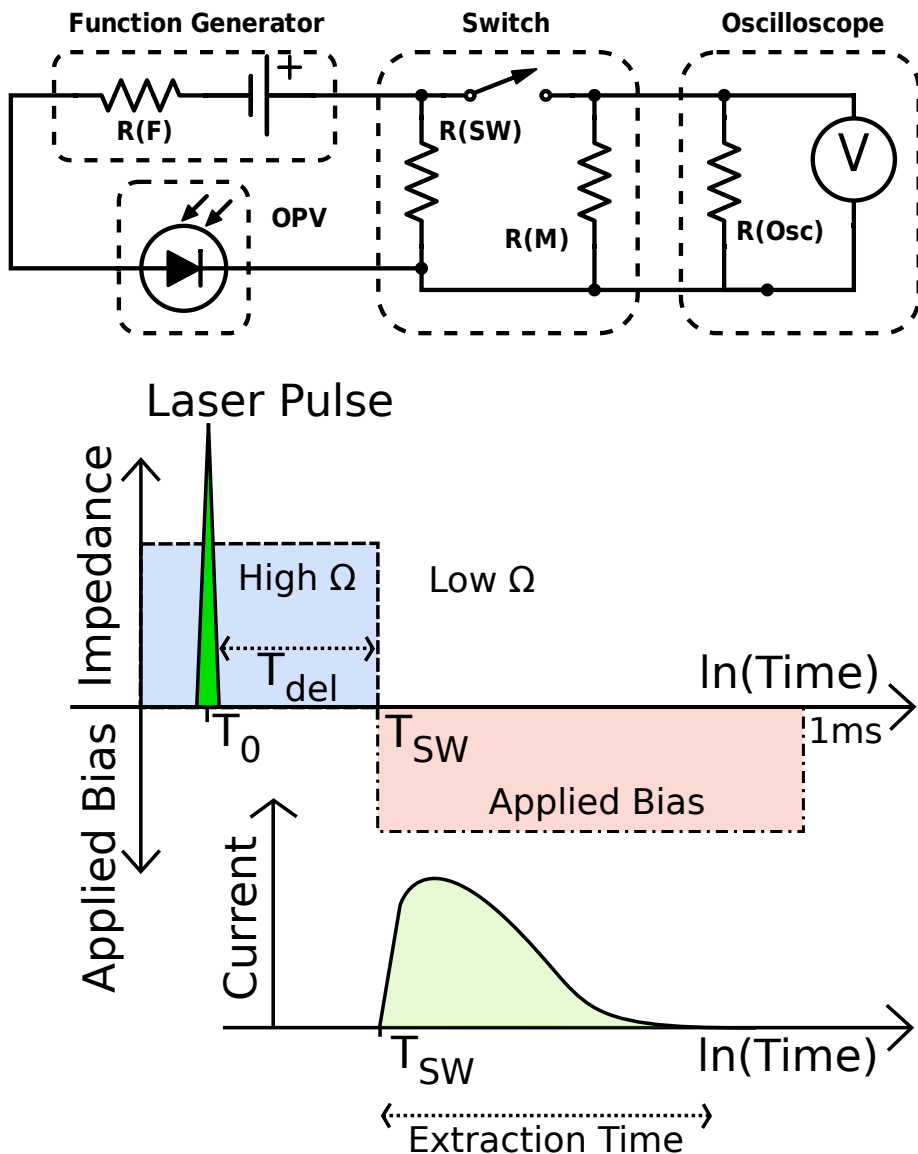


Figure 2.3: Top: Time resolved charge extraction circuit diagram featuring an applied bias, illustrating the organic photovoltaic device (OPV), FET switch with internal high impedance resistor R_{SW} and measurement resistance R_M , oscilloscope with internal resistance R_{Osc} and potentiometer V , and function generator with internal impedance R_F and variable potential. Bottom: Timing diagram for operation of extraction measurements, illustrating the laser excitation pulse at T_0 , high initial circuit impedance ($M\Omega$, blue region) switching to low ($< 1 \Omega$, white region) at T_{SW} , variable delay time T_{del} , variable reverse bias applied at T_{WS} , and an illustration of an extraction current transient as a function of extraction time.

2.3.4 Switched Photoinduced Charge Extraction in Linearly Increasing Voltage

Photoinduced charge extraction in linearly increasing voltage (photo-CELIV) measurements are performed using the FET switch and applied bias TRCE measurement setup as illustrated in

Figure 2.3, however with minor operational differences. The applied bias is a linearly increasing reverse bias voltage ramp, rather than the square pulse used in applied bias TRCE measurements. Additionally, a 2 μ s delay is used between switching and voltage ramp application to separate the CELIV transient and characteristic switch opening response. The use of a switch in photo-CELIV measurements is also a relatively recent modification to the traditional measurement operation (Clarke, Mozer et al,¹⁰⁴ ca 2015), and has similar advantages to that of the TRCE measurement, overcoming the significant leakage of charge density when using an excitation-extraction delay without the need for an offset to be applied for the extended duration of excitation-extraction delay time. A reverse bias offset voltage is applied to the device in time with switching, in order to maintain open circuit conditions (oppose the internal potential V_{OC}) and minimise the leakage of charge density during the 2 μ s delay prior to application of the voltage ramp. The magnitude of the required offset is determined by the device internal potential (proportional to the V_{OC}), however varies as a function of internal charge density, and consequently changes with delay time and excitation density. The offset is manually adjusted such that the extraction current stabilises at zero within the 2 μ s delay time prior to voltage ramp application (and is typically on the order of 600 to 800 mV).

2.3.5 Analysis of Time Resolved Charge Extraction Measurements

The excitation-extraction delay time is the time that the photovoltaic device is held at open circuit after laser illumination is stopped. The measured extracted charge can be correlated with the devices internal photogenerated charge density n , and is calculated using the extracted charge and known device volume (device contact surface area and active layer thickness). The decay of charge density over time is governed by electron-hole recombination occurring in the device. The empirical reaction order of the recombination reaction δ can be calculated from the measured charge density decay,^{34,104} where α is obtained from the power law $n \propto t^{-\alpha}$ and therefore

$$\alpha = -\frac{d\ln(n(t))}{d\ln(t)} \quad (2.7)$$

$$\delta(n) = \alpha(n)^{-1} + 1 \quad (2.8)$$

This reaction order describes how the charge carrier recombination rate scales with charge carrier density, and incorporates all measured charge carriers, including both free carriers and those within the distribution of trap states, and is therefore dependent on trap state occupancy and charge density.

The charge carrier lifetime τ and bimolecular recombination coefficient β can be calculated as a function of charge density n , where

$$\tau(n) = -n(t)[\frac{dn(t)}{dt}]^{-1} \quad (2.9)$$

$$\beta(n) = \frac{dn(t)}{dt} n(t)^{-2} \quad (2.10)$$

Measured photovoltage decay transients are combined with the measured charge density decay obtained through TRCE measurements, to yield a plot of the dependence of photovoltage on charge density. The slope of this plot m is obtained through

$$n = n_0 \exp\left[\frac{qV_{OC}}{mk_B T}\right] \quad (2.11)$$

where n_0 is the initial charge density, V_{OC} is the open circuit voltage (photovoltage), q is the elementary charge, k_B is the Boltzmann constant, and T is the absolute temperature. As the photovoltage is proportional to the Fermi level splitting across the device contacts, the rate of increase in photovoltage with charge density provides information on the trap state density distribution. Calculation of the characteristic exponential slope (in units of eV) of the trap state density distribution E_{ch} is performed through the approximation³⁴

$$E_{ch} = \frac{mk_B T}{2} \quad (2.12)$$

and provides a measure of the density and distribution of trap states within the device active layer.

The measured photovoltage decay transients are also combined with the charge carrier lifetime (calculated with the TRCE measurements of charge density decay, and Equation 2.9), to yield a plot of the dependence of photovoltage on lifetime. The slope of this plot v is obtained through,

$$\tau = \tau_0 \exp\left[\frac{-qV_{OC}}{vk_B T}\right] \quad (2.13)$$

where τ_0 is the initial lifetime.

Using the values of m and v obtained through the above correlations (Equations 2.11 and 2.13), the value of diode ideality factor n_{id} and empirical reaction order δ can be calculated through³⁴

$$\delta = \frac{m}{n_{id}} \quad (2.14)$$

$$n_{id} = (v^{-1} + m^{-1})^{-1} \quad (2.15)$$

which can further be compared to values calculated using steady-state measurements.

Chapter 3

The Influence of Energetic Driving Force on Electron Transfer Kinetics and Charge Generation Yield

3.1 Introduction

3.1.1 Motivation and Objectives

A fundamental understanding of charge photogeneration in donor-acceptor systems is key to the design of improved materials and device architectures for use in organic photovoltaics, enabling further improvements in device efficiency. A key step in the charge photogeneration process is photoinduced electron transfer from a photoexcited donor to an electron acceptor, which is in competition with excited-state decay to the ground state. Nonadiabatic electron transfer theories predict that the rate of photoinduced electron transfer between donor and acceptor is dependent on the driving force for electron transfer ΔG_{ET} (free-energy offset between donor LUMO and acceptor LUMO, refer to Chapter 1, Section 1.2). This driving force should be sufficiently large such that the rate for electron transfer dominates, producing a high quantum yield for photoinduced electron transfer, and therefore high charge carrier generation. However, the magnitude of driving force must be balanced with the desire for a high device open-circuit voltage, which is proportional to the splitting energy of electron and hole quasi Fermi levels, and therefore any increase in driving force will result in a reduction (loss) of photovoltage.

It was until recently, generally accepted that an energetic driving force (ΔG_{ET}) was simply required in order to overcome the charge-transfer state binding energy (coulomb potential on the

order of 0.3 to 0.5 eV) and produce efficient charge separation.^{17, 21, 59–61} This understanding was related to the required energy for stabilising the charge-transfer state during dissociation, and therefore necessarily lost during the charge separation process.^{21, 66, 67} However multiple studies in recent years have found efficient electron transfer and charge separation with ΔG_{ET} of 0.1 eV or below.^{60, 67–69} This implies that the charge photogeneration process is more complicated than the simple interpretation outlined above. Results from transient absorption and photoluminescence quenching studies of donor-acceptor systems with ΔG_{ET} of \sim 0.1 eV have reported charge generation yields as high as 80 %.^{60, 69} Further, an increase in the magnitude of donor-acceptor LUMO offset ($\propto \Delta G_{ET}$) has repeatedly been shown by groups including Ohkita et al and Coffey et al to produce an increase in charge separation yield, with the degree of this relationship dependent on the donor-acceptor system used.^{32, 61, 68, 70, 71} Photoluminescence quenching has been used to investigate the influence of material system energetics (ΔG_{ET}) on charge photogeneration yield, where electron transfer from donor to acceptor results in accelerated exciton decay, producing a reduction in photoluminescence and shorter lifetime. Observing the photoluminescence quenching resulting from variation of the ionisation potential of polymer donors blended with the PCBM acceptor has indicated that the initial electron transfer process may not be the limiting factor in the charge photogeneration process's.³²

The influence of ΔG_{ET} on charge generation yield has been investigated by a number of groups, typically varied through the use of different donor-acceptor systems with relative differences in energy levels (for example, a fixed donor polymer and series of fullerene adducts), and indicate that this driving force plays a fundamental role in charge carrier dissociation.^{62, 71, 73, 74} However, the charge photogeneration process is highly complex, and involves many interdependent parameters that vary between donor-acceptor material system. Significant progress has been achieved recently in elucidating the fundamental processes underlying exciton dissociation, charge carrier separation, and the role of ΔG_{ET} therein. However, the importance of ΔG_{ET} in charge photogeneration remains unresolved, owing primarily to limited experimental data and difficulty in investigating these ultrafast processes.

The design and development of new donor and acceptor material systems with optimised nanoscale morphology and energetics is key to the continued improvement of organic photovoltaic device performance. Of primary importance is the required magnitude of ΔG_{ET} , corresponding to the donor-acceptor material energy level offset. Any excess of ΔG_{ET} , above that required to produce efficient charge dissociation, represents a direct loss of device photovoltage. Optimisation of this balance between charge generation (device photocurrent) and device photovoltage (free energy loss), and thereby photovoltaic device performance is a primary motivation for the investigations of this thesis. Therefore, the primary objective of this thesis and this chapter is to quantitatively determine the influence of ΔG_{ET} on electron transfer kinetics and charge separation yield within donor-acceptor organic photovoltaic systems.

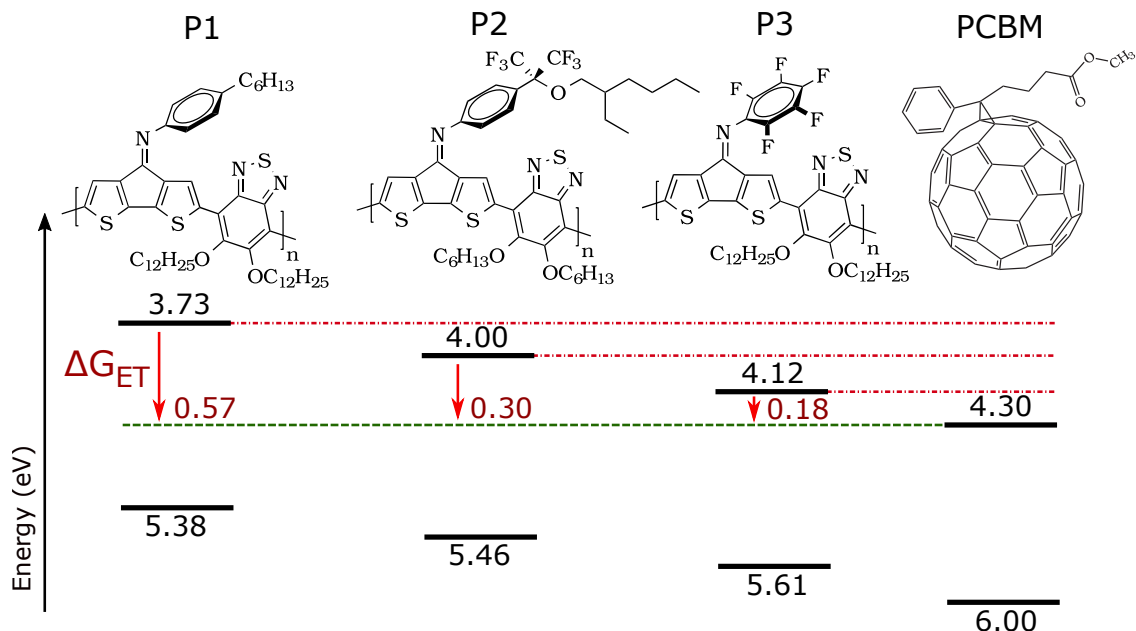


Figure 3.1: Molecular structures of cyclopentadithiophene based polymer donors (P1, P2, and P3) and the fullerene based acceptor (PCBM). Shown are the highest occupied molecular orbital energy level (E_{HOMO}) calculated from the onset of oxidation, and the lowest unoccupied molecular orbital energy level (E_{LUMO}) calculated from the onset of reduction, with comparison of the electrochemical band gaps and LUMO offsets of the donors relative to the PCBM acceptor (E vs vacuum). Also displayed is the driving force for electron transfer (ΔG_{ET}).

3.1.2 Donor-Acceptor Material Systems

The molecular structure of push-pull copolymers incorporating an aryl (Ar) imine substituent at the bridgehead position of 4H-cyclopenta[2,1-b:3,4-b']dithiophene (CPDT) can be used to systematically influence the highest occupied/lowest unoccupied (HOMO/LUMO) energies of the polymer while keeping the backbone structure intact.⁴³ A unique series of polymer donors provides the opportunity to systematically investigate the influence of material system energetics on charge photogeneration processes, which has to date proven experimentally difficult. This polymer donor series (displayed in Figure 3.1) is used to provide a series of donor-acceptor systems with engineered variation in ΔG_{ET} and nearly identical band gaps (~ 1.5 eV). These specific donors were selected with ΔG_{ET} relative to the PCBM acceptor of 0.57, 0.30, and 0.18 eV for P1, P2, and P3, respectively. Importantly, these donor polymers also exhibit similar solubility, morphology, processability, and sufficiently red-shifted main absorption bands relative to PCBM absorption, enabling selective photoexcitation of the donor phase in photovoltaic blends. These low bandgap polymer donor materials were synthesised by, and obtained from Jason Azoulay and Guillermo Bazan (The Center for Polymers and Organic Solids, University of California, Santa Barbara, USA). All device fabrication and optimisation was however performed by the doctoral candidate locally (Intelligent Polymer Research Institute, University of Wollongong, Australia).

While active layer morphology can influence the energetics of the donor-acceptor interface through phase crystallinity, reorganisation energy, charge screening, and delocalisation, the use of similar polymer donors blend systems with comparable morphology should minimise the relative influence of these effects. The influence of morphology on charge generation and recombination is not the focus of this thesis, but rather the influence of donor-acceptor system energetics on these fundamental processes. Furthermore, 10 % PCBM blend films are used in this study in order to isolate the impact of incorporating the PCBM donor material, and observe the charge photogeneration behaviour with respect to variations in energetic driving forces, rather than any variations in blend morphology. This enables the investigation of blend films with morphology comparable to that of the pristine films, for use in photoluminescence and transient absorption measurements presented within this chapter. A higher 70 % PCBM concentration is used to provide an active layer with donor-acceptor ratio more comparable to those typically used in efficient photovoltaic devices, and ensure a high degree of exciton quenching.

3.1.3 Summary of Chapter Objectives

The investigations presented within this chapter are undertaken to address outstanding questions regarding to the influence donor-acceptor material energy levels on the charge photogeneration process. The chapter objective is as follows:

1. Determine the influence of ΔG_{ET} on electron transfer kinetics and charge generation yield for a series of donor-acceptor systems with relative variations in ΔG_{ET} , through the use of photoluminescence and ultrafast transient absorption spectroscopy on films of pristine donor and blended with the PCBM acceptor.

A relatively novel low-bandgap polymer series is utilised, providing polymer donors with a range of energetic offsets relative to the PCBM acceptor material, yielding ΔG_{ET} from 0.18 to 0.57 eV, with the likely result of both efficient and inefficient charge photogeneration. The primary experimental technique adopted for the investigation of the charge photogeneration processes in these donor-acceptor systems is that of ultrafast (femtosecond) transient absorption spectroscopy, capable of directly monitoring electron transfer kinetics and excited state decay.

3.2 Experimental

3.2.1 Film Preparation

Pristine polymer and PCBM blend films for each polymer donor species and PCBM concentration (10 and 70 %) were fabricated. Polymer donor/blend solutions were prepared by dissolution in o-dichlorobenzene at 20 mg mL⁻¹ and stirring at 120 C° for 30 hours under an Ar atmosphere. These solutions were then filtered through a 0.45 μ m PTFE filter to remove undissolved donor material after cooling to room temperature. Glass slides substrates are cleaned by 15 min under

sonication in surfactant/H₂O, followed by two subsequent 5 min sonication rinses in H₂O, and 15 min under sonication each in acetone and isopropanol, prior to a 20 min UV-ozone treatment. This ensures a clean, particulate free substrate and improves wettability for solution/active layer deposition. The polymer(blend) solutions were then doctor-bladed (Erichsen Coatmaster 509 MC) in air onto the substrate at between 13 and 15 mm s⁻¹, with a hotplate (Prazitherm PZ35, high stability) temperature of 75 C° and drying times ranging from 5 to 30 s (depending on polymer donor). The films were then sealed under an inert Ar atmosphere using a cover glass slide and UV-curable epoxy (Ossila, E131), manually cured using a handheld UV gun. Effort is made to ensure that no epoxy is in contact with the device active layer, and that no significant UV illumination is incident on the device active area.

3.2.2 UV-Visible Absorbance Spectroscopy

UV-Visible absorbance spectroscopy was performed in transmission mode on all pristine and blend films (Shimadzu UV-1800 Spectrophotometer), with a reference device without the active bulk heterojunction layer (but including PEDOT:PSS and TiO_x layers) also recorded, which is subtracted from the spectral response. Typical spectra were recorded from 300 to 1000 nm.

3.2.3 Transmission Electron Microscopy

Polymer:PCBM blend solutions for each respective polymer donor were prepared by dissolution in o-dichlorobenzene at 20 mg mL⁻¹ and stirring at 120 C° for 20 h under an Ar atmosphere. Glass substrates were cleaned by 15 min sonication in surfactant/H₂O, two subsequent 5 min sonication rinses in H₂O, and 15 min sonication each in acetone and isopropanol prior to 20 min UV-ozone treatment. Spin coating was used to deposit a 50 nm thick PEDOT:PSS layer onto the substrate at 5000 rpm for 30 s. The blend solutions were doctor-bladed onto the PEDOT:PSS layer in air, at 75 C° using a 500 μm blade height at a typical rate of 20 mm s⁻¹, to obtain a blend film thickness on the order of 100 nm. The PEDOT:PSS layer was then selectively dissolved in distilled water, with the floated polymer blend film transferred to a transmission electron microscopy (TEM) copper grid. Samples were dried in a vacuum for 2 hours prior to TEM measurements to remove adsorbed water and oxygen. Imaging was then performed (JEOL JEM-2011 TEM, 0.16 nm spatial resolution) to obtain microscopy images at varying magnifications (total field-of-view from 2 to 5 μm), with a resolution on the order of 5 nm. The above procedures and measurements were performed by the candidate.

3.2.4 Transient Absorption Spectroscopy

For sub-nanosecond transient absorption (TA) measurements (spectra), samples were photoexcited using a 150 ps laser pulse at 532 nm (Ekspla, SL311, repetition rate 10 Hz), while a microsecond flashlamp (Hamamatsu, L4642) and monochromator were used as the probe light. The change in the transmission of the samples was monitored using Si (New Focus, 1601) and InGaAs

(New Focus, 1611) photoreceivers and a digital oscilloscope (LeCroy, 6200A) with a time resolution of 400 ps. Femtosecond TA measurements (kinetics) were performed using a Ti:Al₂O₃ laser (Spectra-Physics, Hurricane) and regenerative amplifier (Coherent RegA9000) as a light source. The output from the regenerative amplifier (180 fs pulse width, repetition rate of 10 kHz) was separated into two beams for the excitation of two optical parametric amplifiers (OPAs; Coherent OPA9400 and OPA9800), used as pump and probe light pulses. The delay time of the probe pulse relative to the pump pulse was adjusted by changing the path length of the pump pulse using an optical delay stage, and provided a temporal resolution of 250 fs.¹²⁷

3.2.5 Integrated Photoluminescence Spectroscopy

Integrated photoluminescence was detected using a streak camera (Hamamatsu, StreakScope C4334, 50 ps time resolution) equipped with a monochromator, with 532 nm laser pulses (Ekspla, SL311, repetition rate 10 Hz) used to photoexcite the film. The photoluminescence emission spectra was recorded from 650 to 950 nm, integrated over 1 ns post excitation, with a temporal resolution of 30 ps.

3.3 Results and Discussion

3.3.1 Polaron Photogeneration in Donor-Acceptor Blend Film

Polymer films were fabricated incorporating the donor polymers P1, P2, and P3 (see Figure 3.1), including films of the pristine donor materials and films blended with the PCBM acceptor material at both 10 and 70 % PCBM concentrations, yielding three distinct donor-acceptor systems for investigation. All of the films were fabricated with a layer thickness of between 160 and 180 nm, ensuring sufficient absorption at the 532 nm excitation wavelength, while still at a thickness comparable to those used in photovoltaic devices. These films represent the active bulk heterojunction layer within organic photovoltaic devices, and are used within the chapter to study charge photogeneration processes of these donor-acceptor systems, and the influence of material system energetics on these processes.

Ground-State Absorbance

UV-Visible absorbance spectroscopy was performed to obtain the ground-state absorbance of pristine donor and PCBM blend films, to be used in further spectroscopic measurements. The spectra for each P1, P2, and P3 films are displayed in Figure 3.3, including pristine donors, and both 10 % and 70 % PCBM blend films. The spectra have been normalised for the absorbance at 700 nm (polymer donor peak) for ease of comparison. The pristine donors exhibit peak ground state absorption between 680 and 720 nm, with no absorption above 900 nm. Upon addition of 70 % PCBM to the donor films, all donors exhibit characteristic PCBM absorption below 450 nm. Note that all 10 % PCBM blend spectra are not significantly disturbed from that of the

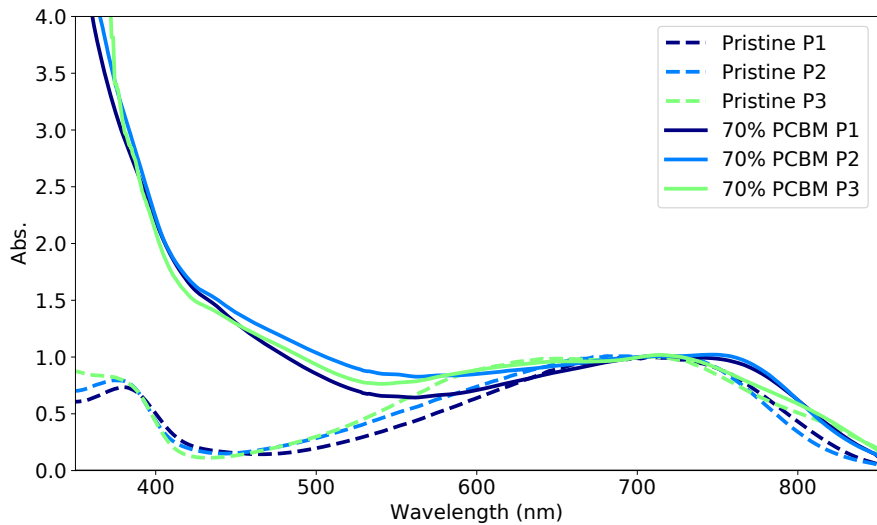


Figure 3.2: UV-Visible spectra of optical films incorporating each pristine polymer donor (broken line) and blended with 70 % PCB M acceptor (solid line), illustrating the large PCB M absorption component below 450 nm.

pristine donor spectra, indicating that these blend films are not significantly different from that of the pristine donor films, with polymer absorption still dominating. A shift in absorption towards longer wavelengths is observed for all polymer donors at the higher 70 % PCB M concentration (Figure 3.2), indicating a significant interaction and influence of the PCB M acceptor material phase on the polymer donor phase. Additionally, a large absorption component is observed about 400 nm, corresponding to the PCB M material absorption.

Photoluminescence Quenching

Photoluminescence spectroscopy was employed to study the exciton quenching behaviour of polymer donor films upon inclusion of the PCB M acceptor, where photoinduced electron transfer is expected to proceed from the photoexcited polymer donor to PCB M acceptor. Photoexcitation of the polymer donors at 532 nm is used to generate the initial exciton population, which will then undergo decay to the ground state. This ground state decay will result in photoluminescence, with the emission monitored over time as a function of both wavelength and intensity (up to 1 ns post excitation with a 50 ps time resolution). The integrated emission intensity is presented as a function of wavelength (emission spectra) in Figure 3.4 for each of the polymer donor films (top: P1, middle: P2, bottom: P3), including pristine donor, 10 % PCB M, and 70 % PCB M blends. Note that the plot for the P3 films (bottom) uses a different scale for the photoluminescence intensity axis, due to the lower emission relative to P1 or P2 films. The units of displayed photoluminescence intensity are counts (c.), and have been corrected for absorbance at the excitation wavelength.

All polymer donors exhibit weak photoluminescence, with peak emission at 850, 840, and 865 nm for P1, P2, and P3 respectively. The peak pristine emission for the P3 film (80 c.) is observed

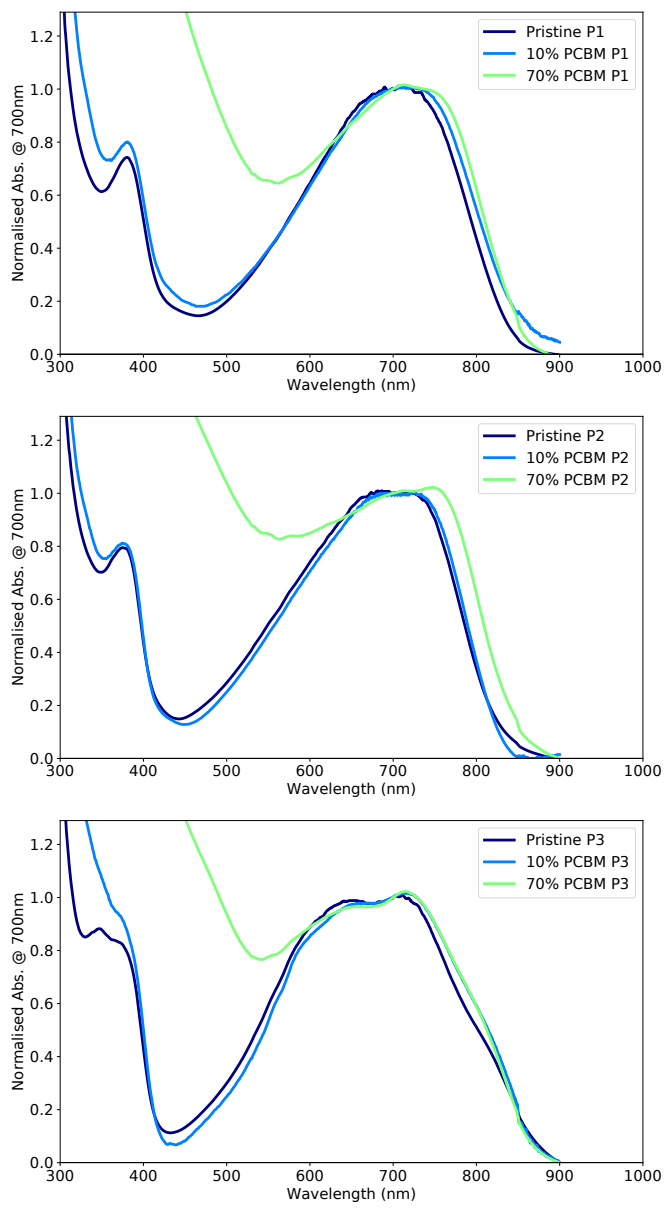


Figure 3.3: UV-Visible spectra of optical films incorporating P1 (top), P3 (middle), and P6 (bottom) polymer donors, including pristine donor, and both 10 % and 70 % PCBM acceptor blend films.

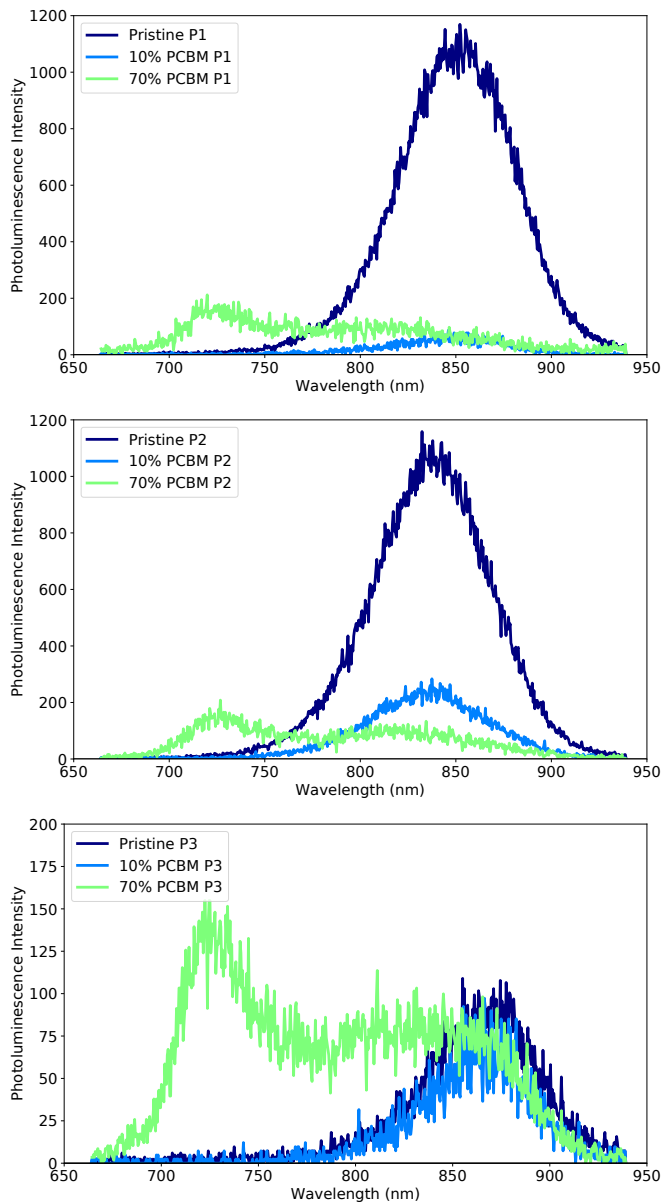


Figure 3.4: Integrated photoluminescence spectra of pristine donor films, and both 10 % and 70 % PCB M blend films (as labelled) for P1 (top), P2 (middle), and P3 (bottom) polymer donors. Photoexcitation of the films was performed using a pulsed laser at a wavelength of 532 nm. Note the different scale for the intensity axis of the P3 plot.

to be significantly lower than either P1 (1100 c.) or P2 (1050 c.) films. Upon addition of 10 % PCBM to the donor films, P1 and P2 exhibit reductions in photoluminescence of 94 % and 78 % respectively. The P3 blend film however shows no resolvable change in photoluminescence intensity. Further, the 70 % blends exhibit a greater reduction in photoluminescence intensity for the P1 and P2 films, to less than 5 % of their respective pristine film intensity. Again however, the P3 film shows no resolvable reduction in photoluminescence intensity. All of the 70 % blend films exhibit a characteristic PCBM photoluminescence spectrum dominating with peaks at 725 and 815 nm.

These results indicate that both P1 and P2 donors exhibit significant photoluminescence quenching upon addition of as little as 10 % PCBM to the pristine donor film, while the P3 donor does not exhibit any resolvable quenching, with the 70 % PCBM film donor emission spectra remaining identical to that of the pristine donor film. There is therefore no indication that this P3 donor-acceptor system undergoes efficient photoinduced electron transfer. Although photoluminescence quenching is a strong indication of electron transfer in donor-acceptor systems, photoluminescence yields do not necessarily correlate to the charge separation efficiency of the system. This technique is only capable of monitoring radiative decay processes. Based on the very poor photoluminescence exhibited by these polymer films, it is likely that the majority of exciton decay occurs through non-radiative processes, and therefore these results alone cannot be used determine charge separation yield. Additional measurement techniques are required (such as transient absorption) to fully investigate the exciton decay and electron transfer dynamics, and will be presented in Sections 3.3.2 and 3.3.3.

The difference between material E_{HOMO} and E_{LUMO} energy levels can provide an approximation of the absorption bandgap and photoluminescence peak position of the polymer donor species. Due to a broad distribution of energetic states around either E_{HOMO} or E_{LUMO} in a condensed phase film (significant energetic disorder), as well as the influence of optically active trap states within the energetic bandgap between E_{HOMO} and E_{LUMO} , the measured energetic bandgap is typically larger than the peak absorption as measured. For example, the P1 donor material has a bandgap energy of 1.65 eV. Although the UV-Visible absorption spectra shows a peak at around 700 nm, significant absorption can be observed down to 900 nm, corresponding to optical energies of 1.77 and 1.38 eV respectively. Photoluminescence represents exciton decay from the singlet excited state to the ground state (approximately the E_{HOMO} - E_{LUMO} bandgap), however is also influenced by energetic distribution and trap states. As such, a broad photoluminescence spectrum is observed with a peak around 850 nm (1.46 eV). This may explain why the absorption and emission spectral peaks of each donor species do not directly correlate with the measured energetic bandgaps, arising from differences in energetic disorder and trap state density distribution between donor films.

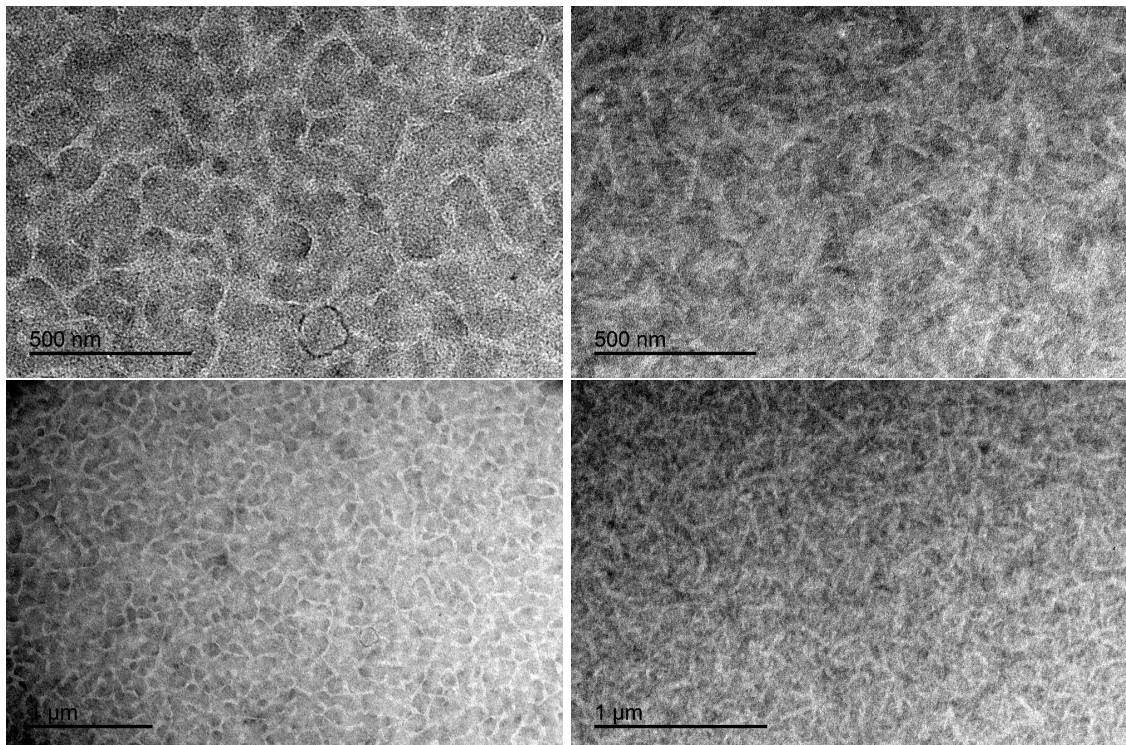


Figure 3.5: Transmission electron microscopy images of 70 % PCBM blend films incorporating P2 (left) and P3 (right) at two magnifications (inset scale bar displayed). The two material phases (polymer donor and PCBM acceptor rich regions) are visibly identifiable by distinct transmission intensity (dark PCBM domains, light interpenetrating polymer donor matrix).

Variations in Blend Film Morphology

Transmission electron microscopy (TEM) was performed to study the nanoscale blend morphology of these donor-acceptor blend films, in order to characterise any significant morphological differences between donor-acceptor systems that could possibly account for differences in charge photogeneration behaviour (such as that observed in the exciton quenching study). The P2 and P3 blend films (70 % PCBM) were chosen for investigation, as these two donor polymers exhibit either a high degree of photoluminescence quenching (P2) or no observable change in photoluminescence (P3) upon addition of PCBM. TEM images can be used to directly characterise thin film morphology and phase separation, as the two material phases (polymer donor and PCBM acceptor rich regions) are visibly identifiable by distinct transmission intensity (darker PCBM domains, lighter interpenetrating polymer donor matrix).^{40,41,128} The measured films are on the order of 100 nm in thickness, and prepared identically to those used in the optical measurements presented within this chapter.

The TEM images displayed in Figure 3.5 show P2 (left) and P3 (right) 70 % PCBM blends at two levels of magnification. Both films show PCBM domains (darker regions) with a diameter on the order of 100 nm, and exhibit similar domain size distribution from the nanometer to micrometer scale. The P2 blend films were observed to exhibit significant exciton quenching while the P3 blend

films were not (indicative of a lack of electron transfer), as indicated by the photoluminescence results presented in the previous section. It is possible that this behaviour could result from a significant difference in donor-acceptor blend phase segregation and corresponding differences in interfacial area. However the similar domain size and degree of respective blend phase mixing observed herein implies that this is likely not the primary factor behind the difference in observed quenching behaviour between P2 and P3 blend films. Although the P3 polymer donor phase appears slightly more crystalline than that of the P2 polymer donor phase, both film morphologies are sufficiently similar such that a meaningful comparison of charge photogeneration behaviour can be made.

3.3.2 Transient Absorption Spectroscopy

To further probe the excited state kinetics of these donor-acceptor systems, transient absorption spectroscopy was performed to obtain an excited state spectrum of each polymer donor, both pristine and 70 % PCBM blend films, as well as decay kinetics on the picosecond to nanosecond timescale. Due to the differing absorption coefficients of transient species, and possible overlap of multiple species with unknown discrete spectra, an accurate deconvolution is not possible. A phenomenological treatment is however possible, with the results and discussion presented below. The excited state transient absorption spectra can be used to assign the photogenerated transient species, based on an analysis of spectral distribution and decay behaviour. This information is used as the foundation of further detailed kinetics studies that directly probe the specific transient species, presented in Section 3.3.3. A pump wavelength of 532 nm ($10 \mu\text{J cm}^{-2}$ excitation density) was used to photoexcite the films, with pump-probe excitation delay times up to 100 ns (sub-nanosecond time resolution), covering probe absorption wavelengths from the tail of ground-state bleaching (900 nm), into the near infra-red (1600 nm). The initial peak change in optical density ΔOD (proportional to the photogenerated transient population) was observed within 700 ps post excitation for all polymer donor films.

Pristine Donor Film Transient Absorption

The transient absorption spectra for the pristine donor films of P1, P2, and P3 are displayed in Figure 3.6, at pump-probe excitation delay times of 700 ps (top), 3 ns (middle), and 70 ns (bottom). The spectra of each donor film exhibit a single broad absorption transient centred about 1350 nm, with peak ΔOD at each delay comparable between donors. The single broad transient signal observed in each pristine polymer donor film exhibits significant decay in peak ΔOD on the nanosecond timescale, with a reduction in ΔOD on the order of 50 % between 700 ps and 3 ns post excitation. This transient signal is attributed to excitation of the polymer singlet excited state (exciton), and is the only resolvable species in the pristine film transients. This assignment is consistent with transient absorption studies of similar low bandgap push-pull polymer donors, with exciton absorption towards 1350 nm.^{41, 129–131}

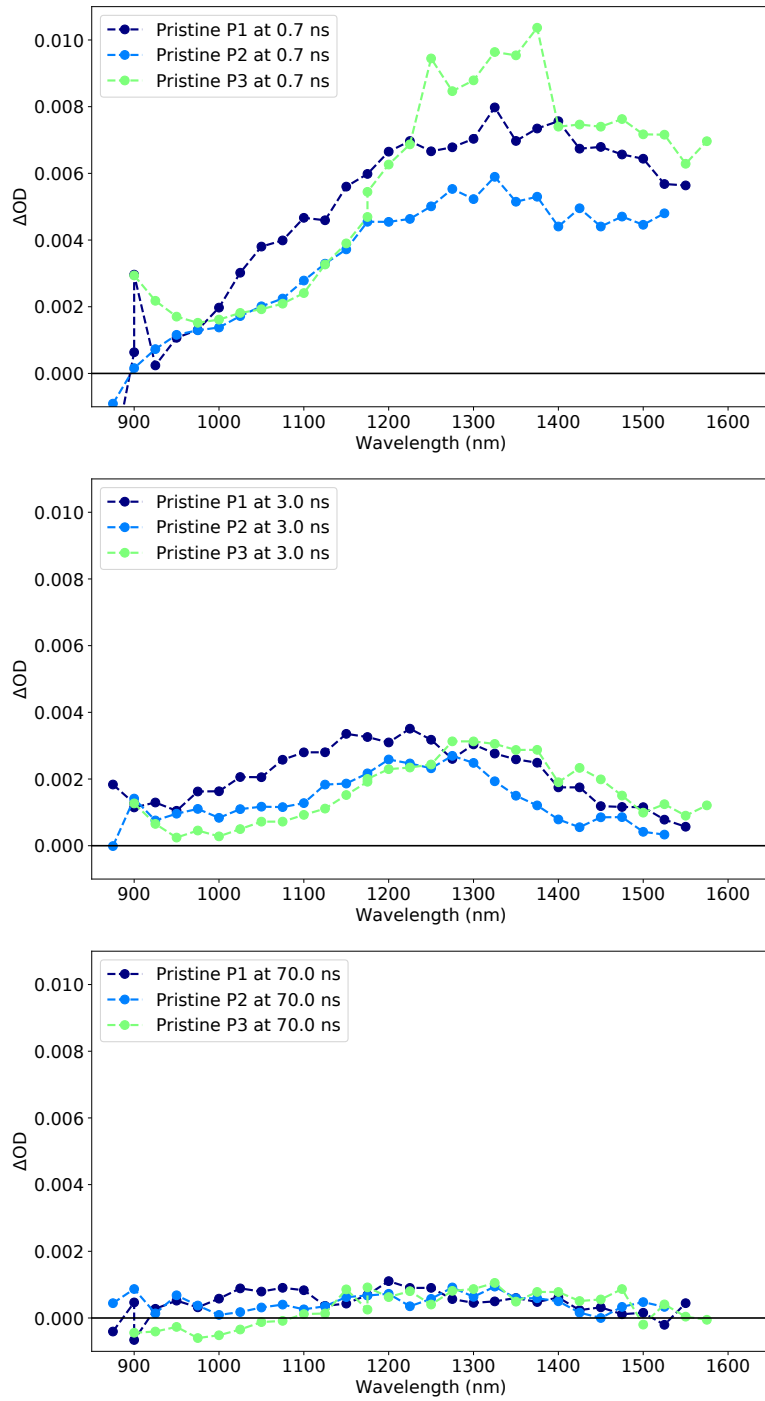


Figure 3.6: Transient absorption spectra of pristine polymer donor films at a range of pump-probe excitation delay times, from picosecond to nanosecond (as labelled), showing the change in optical density as a function of probe wavelength. An excitation wavelength of 532 nm was used, with an excitation density of $10 \mu J \text{ cm}^{-2}$.

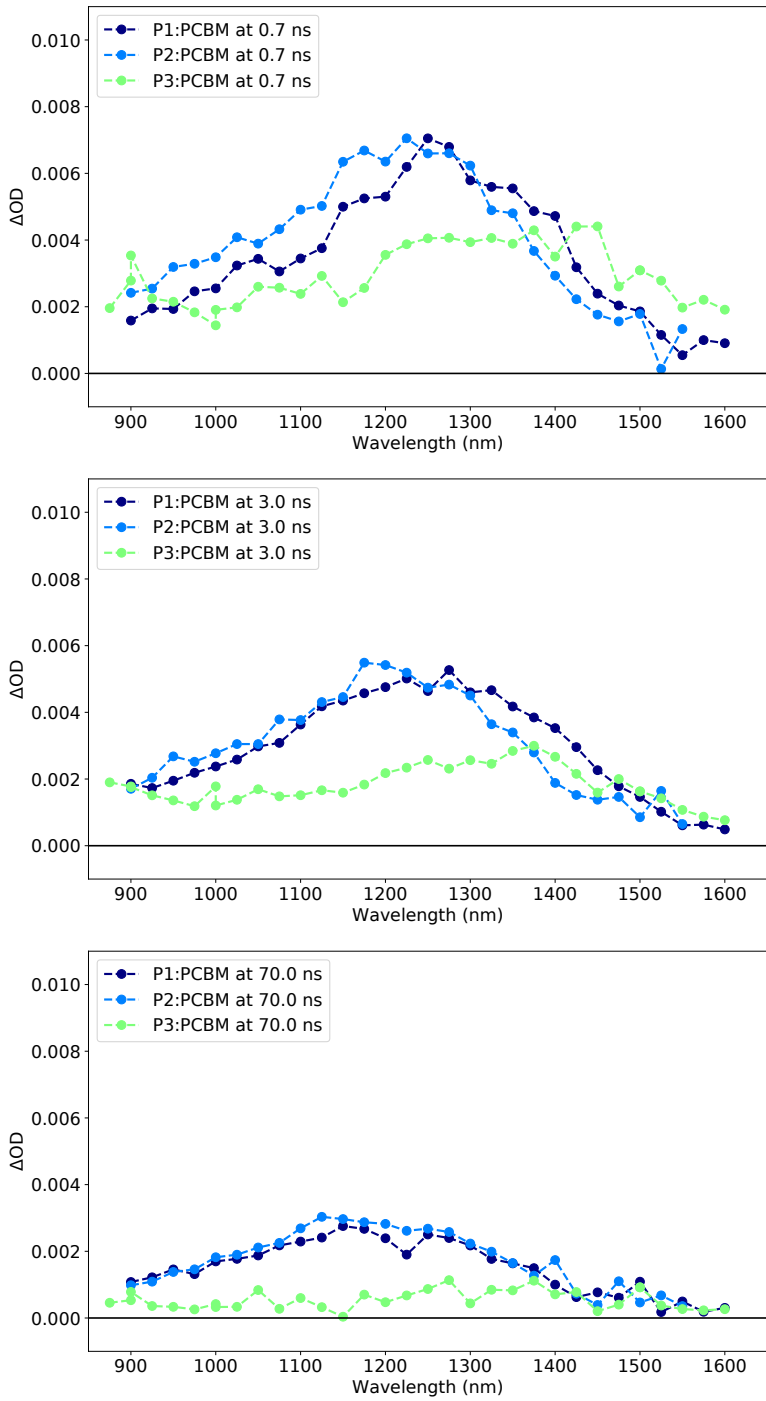


Figure 3.7: Transient absorption spectra of 70 % PCBM blend films at a range of pump-probe excitation delay times, from picosecond to nanosecond (as labelled), showing the change in optical density as a function of probe wavelength. An excitation wavelength of 532 nm was used, with an excitation density of $10 \mu Jcm^{-2}$

PCBM Blend Film Transient Absorption

The transient absorption spectra for the 70 % PCBM blend films of P1, P2, and P3 are displayed in Figure 3.7, at pump-probe excitation delay times of 700 ps (top), 3 ns (middle), and 70 ns (bottom). The blend film spectra show a single broad absorption transient at 700 ps delay time, however the peak centre has shifted from the 1350 nm observed in the pristine films to between 1150 and 1250 nm for both P1 and P2. The P3 blend film transient peak however remains centred about 1350 nm, comparable to the pristine transient spectra. This observed shift in transient spectra is illustrated in Figure 3.8.

Both P1 and P2 blend films exhibit a reduction in transient decay at 1350 nm, with 3-fold greater peak ΔOD at 70 ns post-excitation in the blend films, relative to pristine. This slower decay relative to the observed exciton signal decay is indicative of the formation of a long-lived transient species. This is attributed to the formation of polymer charge separated states (polarons), consistent with similar cyclopentadithiophene based polymer donors exhibiting a polaron absorption centred about 1300 nm.^{41,129} The PCBM anion is known to exhibit a sharp transient absorption peak about 1070 nm, and therefore cannot account for the observed polaron transients.^{14,132} The transient decay at 1350 nm for the P3 blend film is comparable to that of the pristine film, with a 50 % reduction by 3 ns, and 90 % reduction by 70 ns, relative to that at 700 ps. As P3 does not exhibit an observable change in transient decay kinetics, or shift in transient peak position comparable to either P1 or P2 blend films, there is no indication that polaron generation has occurred.

The 700 ps pristine film transients for P1 and P2 exhibit peak ΔOD at 1350 nm, that continues to beyond 1500 nm. The blend films however exhibit a peak at 1250 nm, followed by a 90 % decline in ΔOD by 1500 nm. This indicates that the vast majority of the blend transient corresponds to a polaron population, with possibly only a minor exciton population remaining. Therefore by 700 ps, the majority of photogenerated excitons have undergone electron transfer to yield polarons. The P3 blend film transient signal at 1500 nm however is only 15 % lower than the 1350 nm peak, indicating the presence of a significant remaining exciton population.

To summarise the above findings from sub-nanosecond transient absorption measurements, the pristine films of each polymer donor display an exciton transient signal that exhibits a 90 % decay prior to 70 ns. The addition of 70 % PCBM to the polymer donor films yields a shift in transient peak and extension of transient lifetime for both P1 and P2 systems, with only 30 % decay in transient signal by 70 ns indicating the formation of polymer polarons through photoinduced electron transfer between polymer donor and PCBM acceptor. The 70 % PCBM blends of P3 exhibit transient spectra and decay kinetics comparable to the pristine film, indicating the majority of photogenerated excitons do not undergo electron transfer, and therefore displays severely reduced polaron formation relative to either P1 or P2 blend films.

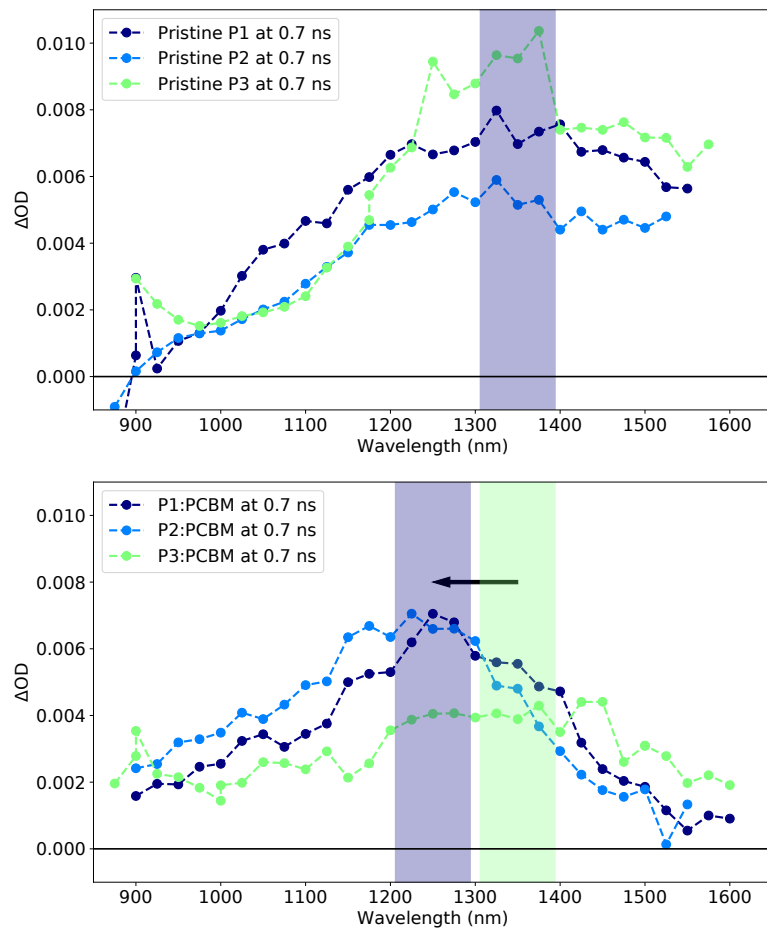


Figure 3.8: Transient absorption spectra of pristine polymer donor (top) and 70 % PCBM blend (bottom) films at 700 ps post excitation, showing the change in optical density as a function of probe wavelength. Coloured bars are used to illustrate the broad spectral peak of the transients, with an arrow indicating a shift in peak position between the pristine and blend films.

3.3.3 Ultrafast Electron Transfer Kinetics and Polaron Generation

With the objective of understanding the influence of donor-acceptor energetics (driving force for electron transfer) on the kinetics of photoinduced electron transfer and yield in these donor-acceptor systems, detailed ultrafast transient absorption measurements were performed on pristine, 10 %, and 70 % PCBM blend films. These transient kinetics measurements were performed at individual probe wavelengths, with transient signal decay monitored over the range of 5×10^{-13} to 5×10^{-10} s with a time resolution of 2.5×10^{-13} s (250 femtoseconds). Based on the analysis of nanosecond transient absorption spectra presented in section 3.3.2, photoinduced electron transfer (quenching of exciton signal) was monitored using a probe wavelength of 1400 nm, where exciton absorption is significantly stronger than polaron absorption. The bleaching (recovery) of ground-state absorption was also monitored at 800 nm (740 nm for the 70 % blend films), in order to study the generation yield of long-lived polaron species. Detailed transient measurements are performed for each of the polymer donor species, including pristine, 10 %, and 70 % PCBM blend films, to obtain ground-state and excited-state kinetics information. The pristine films are used as a reference for polymer donor exciton generation and decay kinetics. The 70 % PCBM blend films are used to ensure efficient charge separation, and provide a blend film comparable to those used in operational photovoltaic devices. The 10 % PCBM blend films are used to introduce exciton quenching without disturbing the morphology from that of the pristine polymer donor films (as indicated by the ground-state absorption in Section 3.3.1).

A selection of transients are displayed in Figure 3.9 showing the picosecond excited-state kinetics for P2 pristine and PCBM blend films (top), and the 10 % PCBM blend films for each polymer donor (bottom). Distinct differences in transient behaviour are observed, both between PCBM concentrations for a single polymer donor, and between respective polymer donors at a single PCBM concentration. The measured transient responses (ΔOD), and their behaviour as a function of time are dependent on multiple interrelated generation and recombination processes, with the nature and degree of each observed to strongly depend on both PCBM concentration and polymer donor species. Based on a qualitative analysis of the transients presented in Figure 3.9, clear behavioural trends can be observed. While the excited state transient of the pristine P2 donor film exhibits complete decay on the order of 100 ps, the introduction of increasing concentrations of PCBM results in much faster decay kinetics, as well as the appearance of a long-lived transient. This would likely indicate the ultrafast quenching of photogenerated excitons through electron transfer from donor polymer to PCBM acceptor, with a corresponding formation of long-lived polarons. Further, a comparison of excited state decay upon the inclusion of 10 % PCBM (Figure 3.9, bottom) indicates very different behaviour between donor-acceptor systems, where both P1 and P2 blend film appear to exhibit ultrafast electron transfer and the formation of polarons. The P3 blend film however exhibits a slower decay with no long-lived transient, indicative of exciton decay rather than electron transfer. A relative difference is also observed between the magnitude of long-lived transient signal displayed by the P1 and P2 blend films approaching the

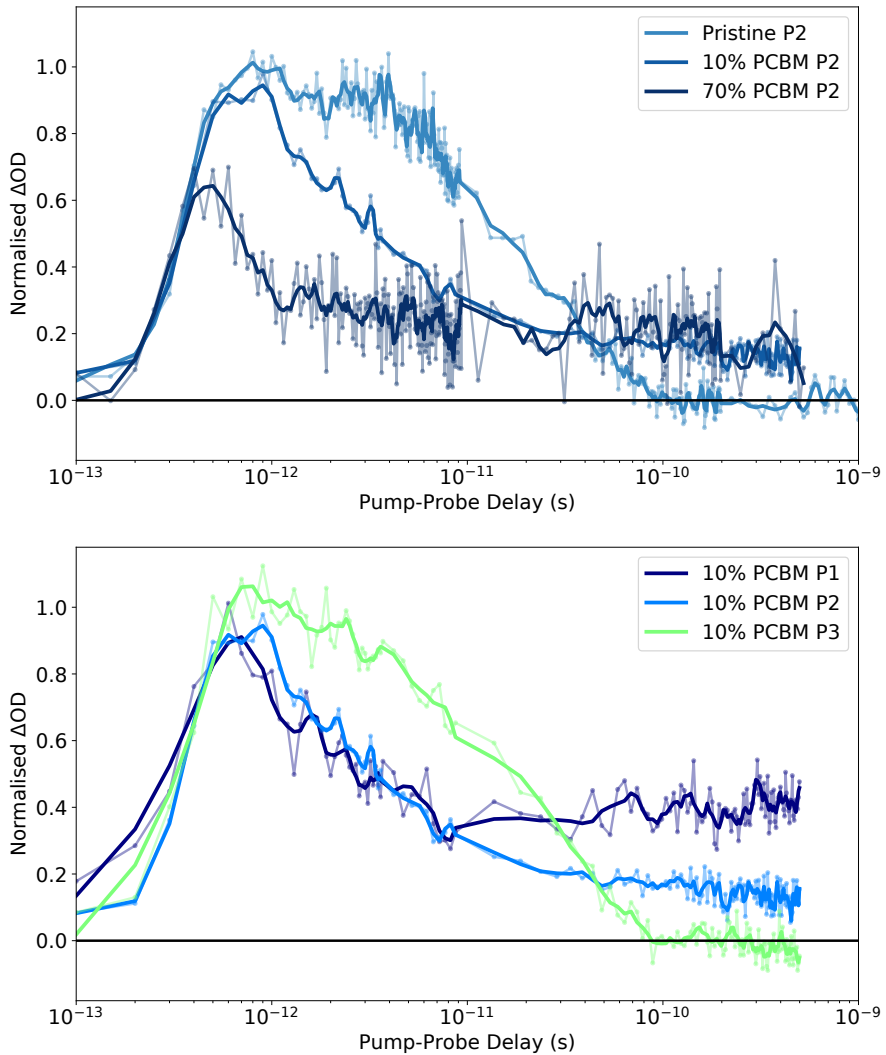


Figure 3.9: Transient absorption transients (change in optical density over time) using a 532 nm excitation and 1400 nm probe wavelength, at an $7 \mu\text{J cm}^{-2}$ excitation density. **Top:** transients obtained for the P2 polymer donor films, including pristine, 10 %, and 70 % PCBM blends. **Bottom:** transients obtained for each polymer donor 10 % PCBM blend film. All transients display both raw data and smoothed plot.

nanosecond timescale. These distinct behaviours exhibited by respective donor-acceptor systems indicate a dependence of charge photogeneration processes (both kinetics and yield) on the driving force for electron transfer ΔG_{ET} . Additional plots are presented in the Appendix (Figures 8.1 and 8.2) covering the full range of excited state decay kinetics as a function of each polymer donor and film PCBM concentration.

A simple analysis of this raw data is insufficient to produce the required quantitative determination of electron transfer kinetics and charge generation yield. Due to the complexity of these transients, and the underlying processes under investigation, a model is required to extract useful quantitative information from the various ground-state and excited-state transients. This is crucial for obtaining more than a basic qualitative understanding of the underlying charge photogeneration processes under observation, and represents the majority of effort spent on these ultrafast transient absorption studies. Therefore, extensive development and testing was performed to produce models for accurately and reliably fitting these transients under a range of measurement conditions, as well as processing/normalising the raw datasets, and developing custom fitting/analysis routines. The details of model development are presented in the following section, and a detailed analysis is presented for the observed electron transfer kinetics and yield with respect to the influence of driving force for electron transfer.

Note that as previously mentioned, due to the advanced nature of equipment and operational expertise required to achieve the requisite ultrafast time resolution, the transient absorption measurements (setup, operation, and data acquisition) were performed in Tsukuba by Kenji Sunahara (Graduate School of Pure and Applied Sciences, University of Tsukuba, Japan), Akihiro Furube (National Institute of Advanced Industrial Science and Technology, Japan), and Attila Mozer (Intelligent Polymer Research Institute, University of Wollongong, Australia). The candidate's role was to analyse the raw data and to develop models for the interpretation of results.

Photogeneration Processes and Model Development

In this section, a model is developed for fitting the measured ultrafast transient absorption transients, in order to extract a quantitative understanding of the kinetics of photoinduced electron transfer k_{ET} , the quantum yield of the electron transfer process QY_{ET} , and the polaron generation yield N_{CS} (post electron transfer, less any charge-transfer state losses). This investigation also highlights the different behaviours observed between the respective donor-acceptor systems, and therefore includes an analysis of the influence of the driving force for electron transfer ΔG_{ET} , and the influence of PCBM concentration in these blend films. The ultrafast transient absorption kinetics measurements were obtained at select probe wavelengths, chosen to monitor both excited-state (ES) and ground-state (GS) kinetics on the picosecond timescale. The resulting transients monitor exciton formation and decay, electron transfer from donor to acceptor, and the formation of polarons (or charge-transfer states), as well as the recombination of these transient species.

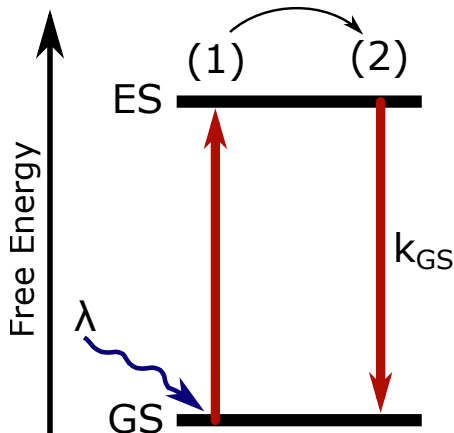


Figure 3.10: Illustrative diagram of pristine polymer excitation and decay processes. (1) Photoexcitation of the donor polymer to the singlet excited state (exciton). (2) Decay of the photogenerated exciton to the ground state with rate k_{GS} .

Fitting of the transients to mathematical models enables the deconvolution of individual transient components (and thereby the discrete underlying processes), and subsequent calculation of process kinetics including electron transfer and transient species decay lifetimes. Through the choice of an appropriate model, a quantitative understanding of the physical processes underpinning these measurement results is possible. A discussion of expected processes and the development of a functional model for fitting the measured transients is presented below.

Firstly, the processes involved in photoexcitation of the pristine polymer donor films are expected to include excitation of the polymer donor from the GS to an ES (polymer excitons), with fast thermalisation (energetic relaxation) to the lowest vibrational state of the singlet excited state, and eventual decay of these excitons to the GS. The photoexcitation and exciton thermalisation processes are assumed to be faster than the time resolution of the measurement (within a few picoseconds),⁸⁶ and are therefore not included in the transient model. The ES transient measurements should monitor the exciton population, with transient signal decay corresponding to the decay of this exciton population. The GS bleaching transient measurements monitor the reduction of GS absorption due to the generation of transient species. Upon decay of transient species back to the GS, a recovery of GS absorption is observed (with total recovery indicating no remaining transient species). As exciton generation and decay are the only processes expected for the pristine films, the GS bleaching transient should mirror that of the ES transient behaviour, with the decay of excitons exhibiting comparable kinetics. Decay of the exciton species from an ES to the GS is a monomolecular process and should therefore exhibit a mono-exponential decay, with a lifetime dependent on polymer donor excited state character and film morphology, and will be representative of the kinetics of this decay process. Stretched exponential decay terms were trialled to model the expected distribution of decay lifetimes typical of these disordered systems, with both Gaussian and non-linear lifetime distributions.^{133,134} This resulted in an improved fit to pristine

transients, however introduced greater complexity in the interpretation of resultant decay lifetimes with an additional distribution coefficient. Without additional experimental measurements of such an energetic distribution for comparison, this approach was therefore abandoned. Final modelling of the exciton decay process was performed with a single exponential decay term, and yielded a reasonable fit for all pristine donor film transients at both ES and GS probe wavelengths, with a range of decay lifetimes obtained. The model is illustrated in Figure 3.10, with radiative decay to the GS (k_{GS}) representing to sole decay process observable in the transients at either ES or GS probe wavelengths.

The transients obtained for PCBM blend films displayed a number of additional components to that observed for the pristine films, beyond solely exciton decay to the GS. Addition of PCBM to form a donor-acceptor system is expected to induce electron transfer from donor to acceptor, with quenching of the photogenerated exciton population and spatial separation of electron and hole to form long-lived polymer polarons. Electron transfer should result in a reduction in the exciton population and a corresponding generation of a polaron population, where monitoring the transient decay will yield the kinetics of this electron transfer process. Based on the spectrum presented in Figure 3.8, the generated polaron population is also expected to be somewhat visible at the ES transient probe wavelength. Therefore the ES transient should exhibit components of both exciton signal decay and polaron signal rise, as is observed in the obtained transients for PCBM blend films. An exponential decay term is used to model and therefore measure the kinetics for this electron transfer process in the ES transients. As the polarons are also produced through this electron transfer, an identical exponential rise term is used to model the transient signal rise representing the polaron population. Initially, separate exponential decay lifetimes were used to model the exciton decay due to electron transfer, and the polaron generation resulting from electron transfer, as it is possible that intermediate charge-transfer states may influence or delay polaron generation, and thereby produce different decay/rise kinetics. However fitting with separate lifetimes was unable to resolve any significant difference in kinetics between the two observed processes (due in part to the fast kinetics approaching the measurement time resolution). Therefore a single lifetime was used for both exciton exponential decay and polaron exponential rise components. As discussed previously, the energetic disorder in these systems will lead to a broad distribution of energies for the generated polarons, and therefore a distribution of generation and relaxation kinetics is expected. The calculated kinetics of electron transfer and polaron generation processes represent an average of this distribution.

The magnitude of polaron signal observed post electron transfer is related to the population of generated polarons, however as neither the relative absorption of exciton nor polaron species are known, determining the exact yield of the electron transfer process is not possible from these measurements. However, analysis of the magnitude of the long-lived polaron signal relative to the initial transient peak, and a comparison of this measure between donor-acceptor systems or PCBM concentrations can provide qualitative insights into the electron transfer yield. Additionally,

as the GS transients monitor all ES transitions to the GS, an approximate measure of long-lived species (assumed to be predominately polarons) can be obtained and compared to the initial GS bleaching signal, and provides an estimate of polaron generation yield. This is still however an approximation, as it cannot account for any electron transfer occurring within the time resolution of the measurement, resulting in uncertainty as to the initial exciton population. Analysis of this approximate yield between donor-acceptor systems and PCBM concentrations can still provide insights into the polaron generation yield.

There may be a component of exciton decay to the GS observable in the blend film transients that exhibits electron transfer, more likely in the 10 % PCBM blends where a larger proportion of excitons will be generated deep within the pristine phase, far enough from a donor-acceptor interface such that electron transfer will not occur. It was however observed during fitting that for films which exhibit electron transfer, no resolvable exciton decay to the GS was observed, such that only the electron transfer and polaron rise components were required to fit the transients. A similar behaviour was observed in the GS transients where no decay component with a lifetime comparable to that of exciton decay to the GS was observed, consistent with the ES transient behaviour. This implies that, where electron transfer is observed, a near unity quantum yield of electron transfer is obtained without any direct exciton decay to the GS.

A slow, power-law decay was observed in both ES and GS transients for P2 PCBM blend films post electron transfer, indicating the presence of non-geminate (bimolecular) recombination of the photogenerated polaron species. Therefore, a power-law decay term was required to fit both ES and GS transients, thereby modelling the observed bimolecular recombination process. The power-law decay was coupled to the polaron component of either ES or GS transient models (representing a decay of the polaron population), which reduces to solely polaron generation (long-lived transient signal) where no recombination component was observed. The updated model, incorporating the expected behaviours of both pristine and PCBM blend films is illustrated in Figure 3.10, including exciton decay to the GS, as well as the additional electron transfer process (k_{ET}), and both polaron generation and bimolecular recombination (k_{BR}). In addition to any exciton decay to the GS, the electron transfer process will be observable at the ES probe wavelength as a decay of exciton signal and generation of polaron signal, as well as any decay in polaron signal due to bimolecular recombination. The GS probe wavelength transient will only exhibit components of either exciton decay to the GS or bimolecular recombination.

The observation of an additional decay component in GS bleaching transients of both P1 and P2 PCBM blend films, with kinetics different to that of the electron transfer process, and not observed in ES transients required further updates to the developed model. The kinetics of this decay are slower than the corresponding ES electron transfer kinetics, however still much faster than exciton decay to the GS. It is possible that the electron transfer process does not directly result in the formation of polarons (sufficiently spatial separated and energetically relaxed), but

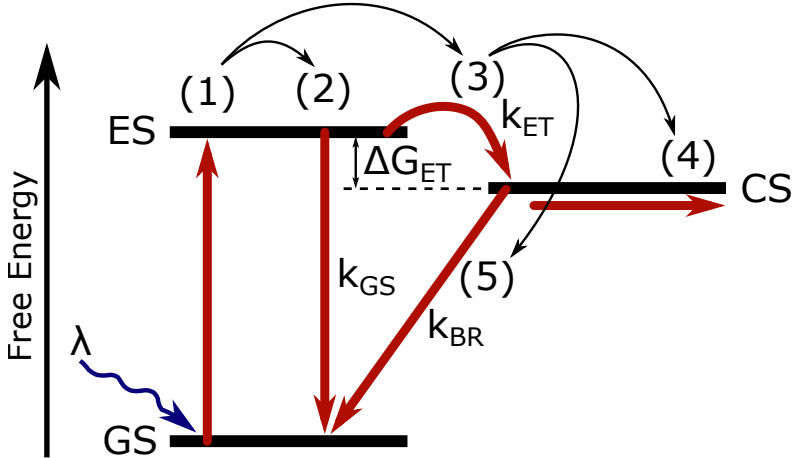


Figure 3.11: Illustrative diagram of polymer:PCBM blend excitation, decay, and charge separation processes. (1) Photoexcitation of the donor polymer to a singlet excited state (exciton). (2) Decay of the exciton to the ground state with rate k_{GS} . (3) Electron transfer from excited donor to PCBM acceptor with rate k_{ET} . (4) Dissociation of separated charge carriers. (5) Bimolecular recombination of separated charges with rate k_{BR} . The driving force for electron transfer ΔG_{ET} is also displayed.

rather may result in the formation of coloumbically bound/trapped charges near a donor-acceptor interface, known as charge-transfer states. These transient species do not have sufficient energy to further spatially separate and form polarons, and therefore undergo recombination to the GS post electron transfer, with kinetics distinct from that of the electron transfer process, resulting in a recovery of GS absorption. An exponential decay term is incorporated to model the charge-transfer state decay process observed in the GS transients, in addition to the exciton decay and polaron generation processes. The lifetime of this decay component is used to obtain a measure of charge-transfer state decay kinetics. The transient signals representing charge-transfer state formation and decay processes are likely indistinguishable from that of the polaron signal, or may not be resolvable at the ES probe wavelength (the absorption profile of these species unknown). However an approximate measure of charge-transfer state formation can be obtained through the recovery of GS absorption attributed to this charge-transfer state decay, relative to the magnitude of remaining polaron transient signal.

Final Model and Transient Fitting Procedure

Based on the above discussion of the observed underlying physical processes, the following models were used for final fitting and analysis of all ES (Equation 3.1) and GS (Equation 3.2) transients presented herein. All of the processes underlying these models are illustrated in Figure 3.12.

$$\Delta OD(t)_{ES} = N_1 \exp\left(\frac{-t}{\tau_1}\right) + N_2 \exp\left(\frac{-t}{\tau_2}\right) + N_3 t^{-\alpha} \left(1 - \exp\left(\frac{-t}{\tau_2}\right)\right) \quad (3.1)$$

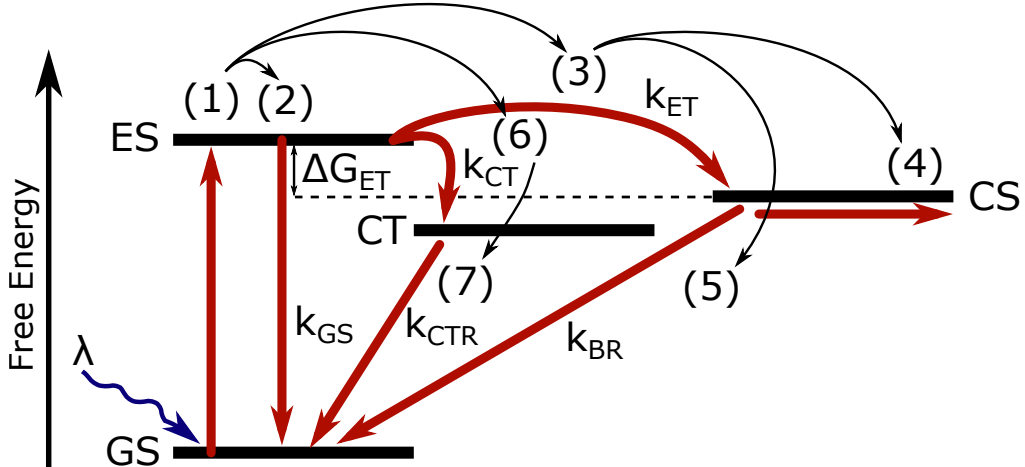


Figure 3.12: Illustrative diagram of polymer:PCBM blend excitation, decay, and charge separation processes, including charge-transfer state. (1) Photoexcitation of the donor polymer to a singlet excited state (exciton). (2) Decay of the exciton to the ground state with rate k_{GS} . (3) Electron transfer from excited donor to PCBM acceptor with rate k_{ET} . (4) Dissociation of separated charge carriers. (5) Bimolecular recombination of separated charges with rate k_{BR} . (6) Charge-transfer state formation with rate k_{CT} . (7) Charge-transfer state geminate recombination with rate k_{CTR} . The driving force for electron transfer ΔG_{ET} is also displayed. The possibility of charge-transfer state dissociation has been excluded from the model used for fitting, as this process is not resolvable within the excited-state transients obtained.

$$\Delta OD(t)_{GS} = -N'_1 \exp\left(\frac{-t}{\tau'_1}\right) - N'_2 \exp\left(\frac{-t}{\tau'_2}\right) - N'_3 t^{-\alpha'} \left(1 - \exp\left(\frac{-t}{\tau'_2}\right)\right) \quad (3.2)$$

Both GS and ES models are functionally similar, however the processes underlying each functional component are not, and therefore coefficients have been labelled separately to aid in understanding during the following analysis. Each model contains a combination of three exponential decays, one of which is coupled with a power law decay. The decay lifetimes of each of these exponential decay terms represent the kinetics of the associated physical processes. The models are used to fit the respective transients from the initial peak ΔOD (a pump-probe delay time on the order of 500 ps) and onwards. The initial transient rise is not modelled as the exciton photogeneration process occurs within the time resolution of the measurement (faster than 250 fs).

In the ES model (Equation 3.1) the functional terms represent exciton decay to the GS (N_1 and τ_1), exciton decay due to electron transfer (N_2 and τ_2), and corresponding rise in polaron signal post electron transfer (N_3 and τ_2) to a plateau. In the case of solely exciton decay to the GS, N_1 is non-zero whilst both N_2 and N_3 are zero. In the case where electron transfer is observed (with no exciton decay component), N_1 is zero whilst both N_2 and N_3 are non-zero. Non-geminate recombination of polarons post electron transfer is modelled with a power law (N_3 and α) coupled to the polaron rise term, as this is known to be a bimolecular process. Where pure

bimolecular recombination is present, an α of 1 is expected corresponding to a reaction order of 2. In the limit that α is zero, no recombination component is observed and the power law term is nullified, resulting in solely exponential rise to a plateau. Note that the decay lifetime (τ_2) for the exciton decay term in the presence of electron transfer (N_2), and that of the polaron term (N_3) are identical. This simplification is used as the exciton decay process that dominates during electron transfer is assumed to predominately result in the direct generation of polarons. It is possible that intermediate charge-transfer state generation occurs, resulting in a slight delay in polaron generation, and either a slower lifetime or broader distribution of lifetimes. No such transient component was however observed at the 1400 nm probe wavelength, while fitting with separate lifetimes generally led to convergence at two identical lifetimes, and it is therefore reasonable to assume a single lifetime is sufficient to model both processes.

The GS model (Equation 3.2) differs from the ES model in that the N'_2 decay corresponds to charge-transfer state recombination post electron transfer, rather than an exciton decay process (of which no component is observed), as the GS recovery can only monitor recombination processes to the GS. The N'_3 rise term is used to model the remaining polaron population post electron transfer, with a rise used to limit the early time influence of this term when α' is non-zero and bimolecular recombination is observed. When α' is zero this is functionally equivalent to fitting with a single exponential decay (N'_2) and a constant (N'_3). Again for simplicity both terms N'_2 and N'_3 share a single lifetime (τ'_2). The N_1 and N'_1 terms in the ES and GS model respectively represent the same underlying process of exciton decay to the ground state, and therefore both τ_1 and τ'_1 should be comparable. This is also true of the bimolecular recombination process, with the power law decay terms α and α' expected to be comparable. The converged parameters of the fitting routine with standard error are used to extract kinetics (lifetime) information for each transient component, presented in the following analysis along with the final fitted transients. Additional details of transient fitting, including the use of simplified models and presentation of goodness-of-fit values for each, are available in the Appendix (Figure 8.3).

Issues were encountered when attempting to fit or de-convolute multiple terms when a single component dominated the transient response, leading to increasingly large errors in the fit parameters of all components. This is further complicated by the low signal-to-noise of these measurements, the fitting of exponential functions to linearly sampled data, and the multiple sampling windows used in the majority of these measurements (necessitated by the measurement setup). To ensure accurate convergence without the requirement of parameter boundary constraints, minority components were removed when they exhibited no significant influence on the resultant fitting parameters of the dominant component. This was achieved by fixing the value of N_2 and N_3 at zero for the case of solely exciton decay to the GS; fixing the value of N_1 and α to zero for the observation of electron transfer without bimolecular recombination; and fixing solely N_1 to zero for the case of both electron transfer and bimolecular recombination. The fitting routine used for all transients utilised a constrained sequential least-squares minimisation function. Initial values

were assigned for all parameters based on progressive optimisation, with final fitting parameters yielding reliable convergence without the use of boundary restraints. Prior to fitting, transients were subjected to a Savitzky-Golay filter to improve convergence, however care was taken to ensure no influence of edge/boundary effects was observed when using this local smoothing algorithm.

Transient Fitting and Analysis

Ultrafast transient absorption measurements were performed on each of the pristine donor polymer films, as well as both 10 % and 70 % PCBM blends. A laser pump excitation wavelength of 532 nm was used to photogenerate transient species, with an excitation density of $7 \mu\text{J cm}^{-2}$. Transient fitting was performed using the developed models (Equations 3.1 and 3.2), and a detailed analysis of transient behaviour is presented below, including the assignment of the underlying processes for each film, the calculation of kinetics for these processes, and a comparison of the observed differences between donor-acceptor systems. The ES measurements were performed using a 1400 nm probe wavelength, and provide a measure of the photogenerated transient populations of both excitons and polarons. These results are used to monitor the kinetics of exciton decay and electron transfer, as well as polaron generation and recombination, providing a direct measure of k_{ET} and an approximation of QY_{ET} . The GS measurements were performed using 800 and 740 nm probe wavelengths, and provide a measure of the bleaching of GS absorption, representing the total generated population of excited transient species. This can therefore be used to observe the recombination of various ES transient species to the GS, as well as provide an approximate polaron generation yield N_{CS} .

Due to the coexistence of absorption by both excitons and polarons at the 1400 nm probe wavelength, each with unknown absorption coefficient, neither the absolute or relative population density, nor absorption cross section can be calculated from this data. Therefore the exact charge generation yields cannot be accurately determined. These results do however provide a relative measure of charge generation yield between donor-acceptor systems at multiple PCBM concentrations. The spectral distribution and absorption coefficient of any generated charge-transfer states is also unknown at 1400 nm, and therefore cannot be accurately monitored. All of the presented transients have been normalized to the response at a 300 fs pump-probe delay (initial peak), rather than using absolute ΔOD . This is done for ease of behavioural comparison between the various donors-acceptor systems and PCBM blend concentrations.

Exciton generation in ultrafast transient absorption measurements can be influenced by higher order processes at sufficiently high excitation densities, which can in turn obscure meaningful observation of transient kinetics. In order to verify that no higher order processes were present in the transient absorption kinetics measurements, the influence of pump laser (532 nm) excitation density on photogeneration of the exciton population was tested. A non-linear dependence of exciton generation on excitation density is expected where higher order processes are present. Ultrafast

transient absorption kinetics measurements were performed on P1 and P3 pristine films using a probe wavelength of 1400 nm, with excitation densities ranging from 3 to 15 $\mu\text{J cm}^{-2}$. Pristine films were used to monitor the initial exciton generation, removing any influence of the exciton quenching observed in the blend films which may obscure determination of initial exciton generation. The exciton decay transients (not shown) exhibit an initial ΔOD dependent on excitation density, which decays to zero on the order of 100 ps. These transients exhibit a good fit to a monoexponential decay, representing solely exciton decay to the ground state. A linear dependence of initial exciton generation on pump excitation density is observed for both donors up to 15 $\mu\text{J cm}^{-2}$, indicating that kinetics measurements are performed without the presence of higher order exciton generation processes within the excitation pulse. Therefore all further ultrafast transient absorption measurements were performed using an excitation density of 7 $\mu\text{J cm}^{-2}$.

Pristine Donor Films

Figure 3.13 displays the ES (top) and GS bleaching (bottom) transients for the pristine films of each donor polymer. Table 3.1 shows the resultant lifetimes from fitting. All pristine transients were adequately fitted with a single exponential (N_1) suggesting that they can be attributed to a single transient species, the polymer exciton. The ES decay lifetimes τ_1 of 49, 23, and 15 ps for P1, P2, and P3 respectively compare well with the corresponding GS bleaching lifetimes τ'_1 of 44, 26, and 21 ps. This suggests that exciton decay to the GS is monitored accurately and without any resolvable electron transfer in the pristine films. The relative differences in observed exciton decay lifetime between the polymer donors can be attributed to differences in structure and excited-state character. For example, a study by Guo and Huang et al⁴⁶ using dithiophene based low-bandgap push-pull donor polymers have shown that variation of side chain substituents can result in changes to pristine polymer film crystallinity, interchain interaction, and excited-state character, yielding shifts in exciton decay lifetimes within the range of 10 to 50 ps. Alternately, non-radiative decay pathways may also contribute to the observed variation.

Blend Films - 10 % PCBM

Figure 3.14 displays the ES (top) and GS recovery (bottom) transients for the 10 % PCBM blend films of each donor. Table 3.2 shows the resultant lifetimes from fitting. The ES transient for the P1 film is fitted using both an exponential decay (N_2) and exponential rise (N_2) with τ_2 of 1.4 ps. This decay lifetime is approximately 40 times faster than that of the pristine film (τ_1 of 49 ps). The observation of a long-lived transient signal is indicative of the formation of a population of long-lived transient species, the polymer polaron. The complete lack of any slower decay component (N_1) is consistent with the majority of excitons undergoing electron transfer. The GS bleaching transient for the P1 film mirrors the ES transient behaviour, with τ'_2 of 0.8 ps and a long-lived residual signal. In this case, τ'_2 is attributed to the recombination of charge-transfer states to the GS, generated through the electron transfer process. The ES and GS transients of P2 show similar behaviour to that of the P1 film, with τ_2 of 2.1 ps and τ'_2 of 1.6 ps, and also exhibit a long-lived

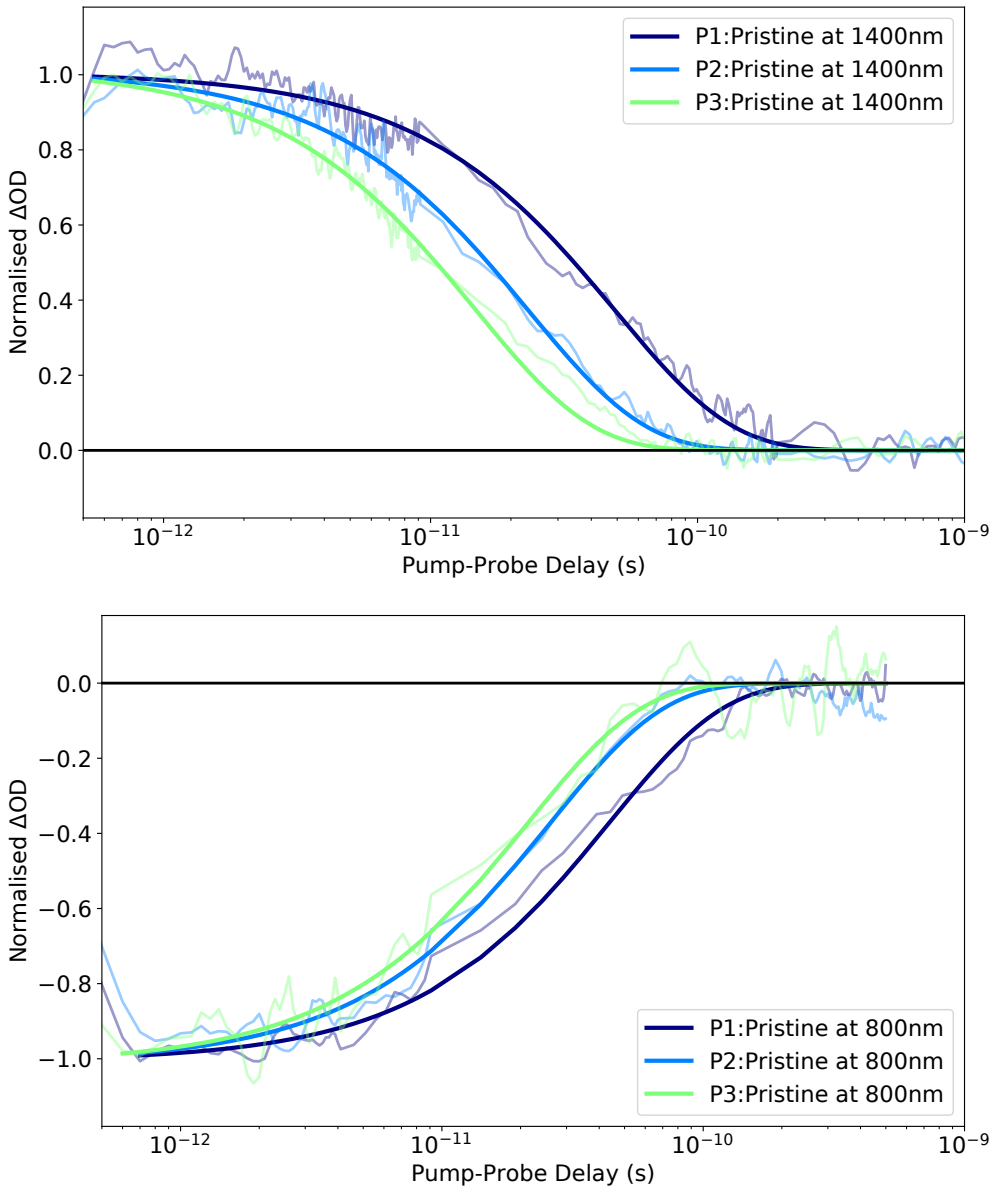


Figure 3.13: Ultrafast transient absorption transients for pristine films of P1, P2, and P3 donor polymers at 1400 nm (top) and 800 nm (bottom) probe wavelengths, using a 532 nm pump wavelength at an excitation density of $7 \mu\text{J cm}^{-2}$. Fitting of each transient is also displayed (solid line).

Table 3.1: Kinetics results (lifetime τ and corresponding rate k) from transient fitting (Figure 3.13) with the developed models (Equations 3.1 and 3.2) for pristine films of P1, P2, and P3 at 1400 nm (excited state) and 800 nm (ground state bleaching) probe wavelengths.

ES (1400nm)		τ_1 (ps)	τ_2 (ps)	k^{GS} (Ts)	k^{ET} (Ts)
Pristine	P1	(49.4 \pm 0.9)	-	0.02	-
	P2	(23.2 \pm 0.5)	-	0.04	-
	P3	(14.7 \pm 0.2)	-	0.07	-
GS (800nm)		τ'_1 (ps)	τ'_2 (ps)	k^{GS} (Ts)	k^{CTR} (Ts)
Pristine	P1	(43.9 \pm 1.0)	-	0.02	-
	P2	(26.0 \pm 1.1)	-	0.04	-
	P3	(21.3 \pm 1.4)	-	0.05	-

Table 3.2: Kinetics results (lifetime τ and corresponding rate k) from transient fitting (Figure 3.14) with the developed models (Equations 3.1 and 3.2) for 10 % PCBM blend films of P1, P2, and P3 at 1400 nm (excited state) and 800 nm (ground state bleaching) probe wavelengths.

ES (1400nm)		τ_1 (ps)	τ_2 (ps)	k^{GS} (Ts)	k^{ET} (Ts)
10% PCBM	P1	-	(1.39 \pm 0.09)	-	0.72
	P2	-	(2.11 \pm 0.16)	-	0.47
	P3	(23.6 \pm 0.70)	-	0.04	-
GS (800nm)		τ'_1 (ps)	τ'_2 (ps)	k^{GS} (Ts)	k^{CTR} (Ts)
10% PCBM	P1	-	(0.82 \pm 0.11)	-	1.22
	P2	-	(1.61 \pm 0.23)	-	0.62
	P3	(28.3 \pm 2.2)	-	0.04	-

residual signal. Therefore the P2 film also exhibits predominately electron transfer and polaron generation rather than exciton decay to the GS. An additional power-law component is however required to fit both ES and GS transients of the P2 film, exhibiting an additional transient decay that is not observed in the P1 film, with α of 0.22 and α' of 0.12. This suggests the presence of bimolecular recombination of polarons post electron transfer. Although the exciton decay kinetics of the pristine P1 film are slower than the pristine P2 film, the electron transfer kinetics of the 10 % PCBM blend films are comparable, indicating no significant dependence of electron transfer rate on the donor-acceptor system. The ES and GS transients for the P3 film are comparable in both behaviour and kinetics to that of the pristine film, with τ_1 of 24 ps and τ'_1 of 28 ps. There is no apparent electron transfer displayed by the 10 % PCBM blend film of P3, exhibiting solely exciton decay to the GS.

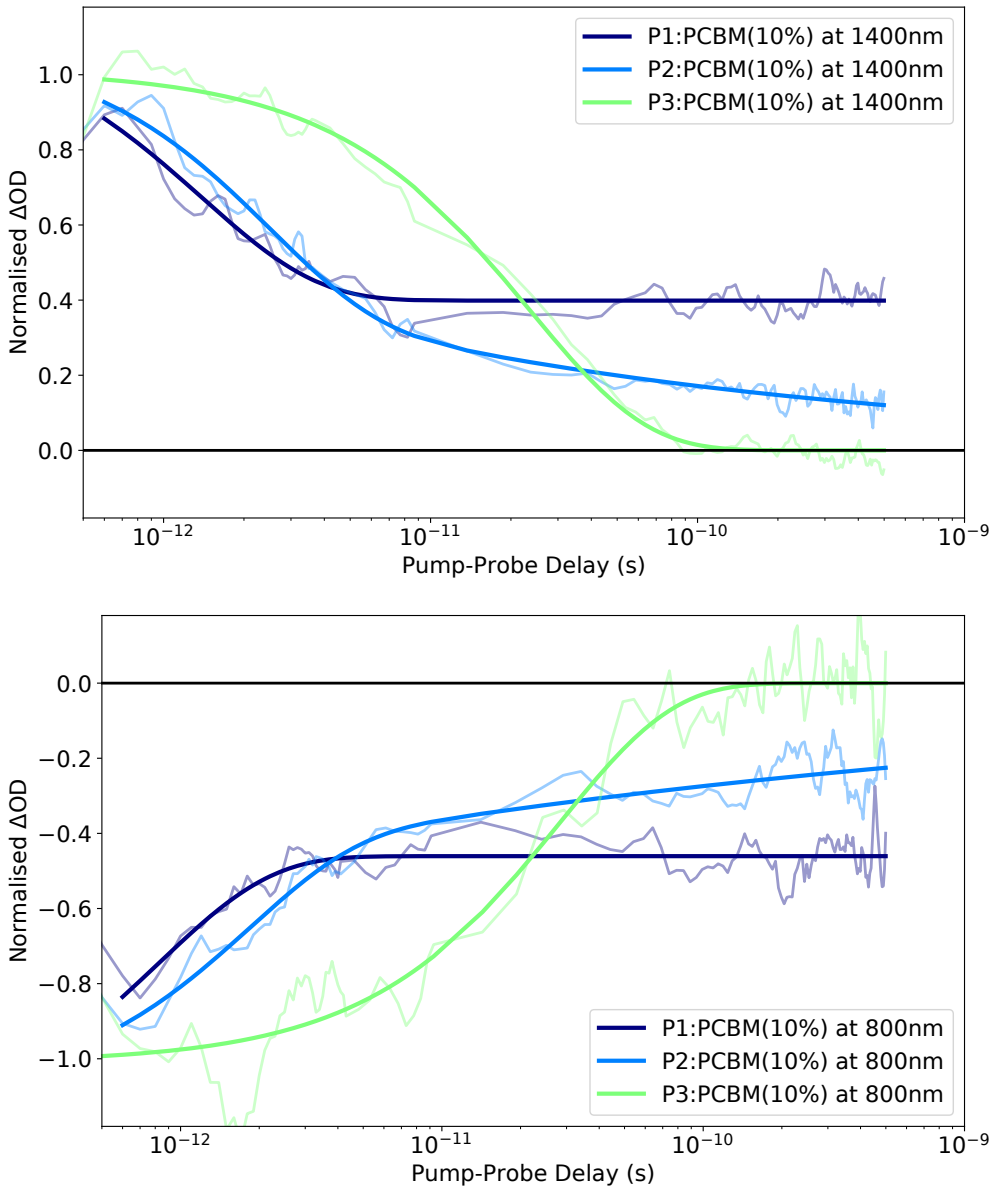


Figure 3.14: Ultrafast transient absorption transients for 10 % PCBM blend films of P1, P2, and P3 donor polymers at 1400 nm (top) and 800 nm (bottom) probe wavelengths, using a 532 nm pump wavelength at an excitation density of $7 \mu\text{J cm}^{-2}$. Fitting of each transient is also displayed (solid line).

Table 3.3: Kinetics results (lifetime τ and corresponding rate k) from transient fitting (Figure 3.15) using the developed models (Equations 3.1 and 3.2) for 70 % PCBM blend films of P1, P2, and P3 at 1400 nm (excited state) and 740 nm (ground state bleaching) probe wavelengths.

ES (1400nm)		τ_1 (ps)	τ_2 (ps)	k^{GS} (Ts)	k^{ET} (Ts)
70% PCBM	P1	-	(0.46 \pm 0.05)	-	2.17
	P2	-	(0.31 \pm 0.04)	-	3.23
	P3	(18.7 \pm 0.4)	-	0.05	-
GS (740nm)		τ'_1 (ps)	τ'_2 (ps)	k^{GS} (Ts)	k^{CTR} (Ts)
70% PCBM	P1	-	(0.66 \pm 0.09)	-	1.52
	P2	-	(0.40 \pm 0.10)	-	2.50
	P3	(19.7 \pm 0.4)	-	0.05	-

Blend Films - 70 % PCBM

Figure 3.15 displays the ES (top) and GS bleaching (bottom) transients for the 70 % PCBM blend films of each donor material. Table 3.3 shows the resultant lifetimes from fitting. The behaviour of both ES and GS transients for the 70 % PCBM blend films of P1 and P2 are comparable to that of the 10 % blend films. Electron transfer is observed for both donors with increased kinetics of the electron transfer process, τ_2 and τ'_2 for the P1 film of 0.5 and 0.7 ps respectively while 0.3 and 0.4 ps respectively for the P2 film. The power-law decay component is again observed in both ES and GS transients of the P2 film only, with α of 0.07 and α' of 0.03. This reduction in slope and magnitude of the power-law decay indicates a reduction in bimolecular recombination in the 70 % PCBM blend film relative to the 10 % blend film. The electron transfer kinetics are again observed to be comparable for the P1 and P2 70 % blend films, indicating no significant dependence of k_{ET} on donor-acceptor system at either PCBM concentration. However an increase in k_{ET} with increasing PCBM concentration is observed, with the 70 % PCBM blend films exhibiting τ_2 on the order of half that of the 10 % blend films. Although an accurate measurement of polaron yield is not possible, a comparison of the 10 % and 70 % PCBM blend film GS bleaching indicates a qualitative increase in the long-lived transient, attributed to a relative increase in polaron yield post electron transfer at the 70 % PCBM concentration. This is particularly apparent in the P2 film, where a large reduction in the relative magnitude of power law decay (bimolecular recombination) is also observed. Finally, the ES and GS transients for the P3 film are again comparable to that of the pristine and 10 % blend films, with τ_1 of 19 ps and τ'_1 of 20 ps. Although there is a slight reduction in decay lifetimes relative to the pristine and 10 % blend films, there is still no resolvable electron transfer at the 1400 nm probe wavelength for the 70 % blend film of P3, exhibiting solely exciton decay to the GS. The GS bleaching response also indicates a complete recovery of GS absorbance at the 740 nm probe wavelength, again suggesting that no significant polaron formation occurs within the P3 blend films.

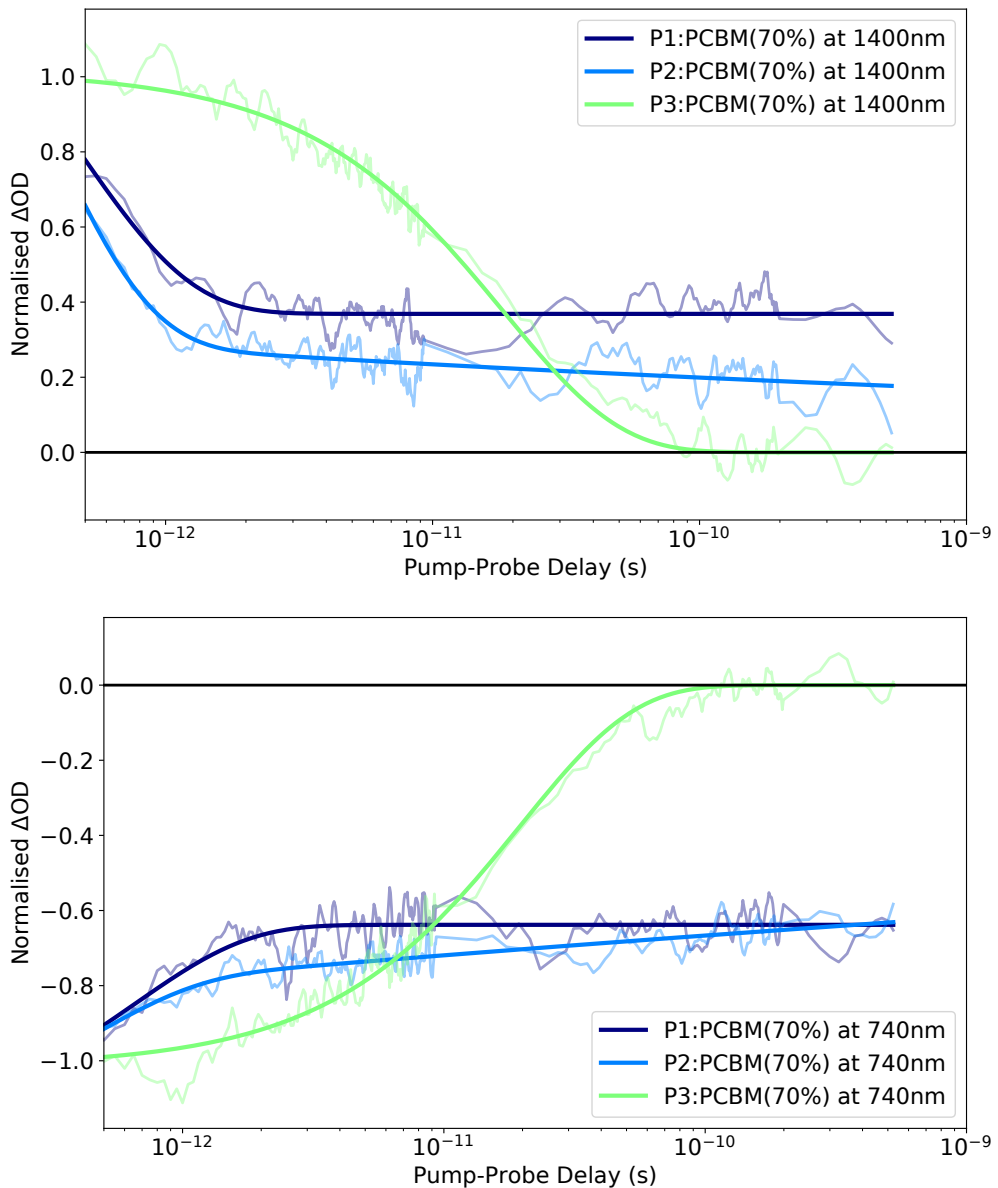


Figure 3.15: Ultrafast transient absorption transients for 70 % PCBM blend films of P1, P2, and P3 donor polymers at 1400 nm (top) and 740 nm (bottom) probe wavelengths, using a 532 nm pump wavelength at an excitation density of $7 \mu\text{J cm}^{-2}$. Fitting of each transient is also displayed (solid line).

Ultrafast Transient Absorption Discussion

The proposed models (Equations 3.1 and 3.2) used for fitting the ES and GS transients yielded a reasonable fit for all pristine donor and PCBM blend films. This fitting enabled the calculation of the kinetics of exciton decay k_{ET} and polaron recombination, as well as provide a quantitative understanding of QY_{ET} and relative polaron generation yield between donor-acceptor systems. A detailed comparison of charge photogeneration processes in these donor-acceptor systems is presented below, with respect to the influence of ΔG_{ET} .

All pristine donor films exhibited solely exciton decay to the GS with lifetimes ranging from 20 to 50 ps, consistent between ES and GS bleaching. Upon the addition of 10 % PCBM to the donor films, both the P1 and P2 blends exhibited a significant acceleration of exciton signal decay, to an average lifetime of 1.8 ps, and exhibited a long-lived transient signal. This is attributed to the quenching of polymer excitons through electron transfer to the PCBM acceptor, resulting in the formation of long-lived polymer polarons. No component of exciton decay directly to the GS was observed under these conditions in either P1 or P2 blend films, indicating an apparent unity QY_{ET} . The GS bleaching transients also exhibited an accelerated decay upon addition of PCBM to the polymer donor films. The kinetics of this process mirror that of the ES transient electron transfer process, with an average lifetime of 1.2 ps.

As this probe wavelength (ground-state bleaching recovery at 800/740 nm) monitors only ES transitions to the GS, and no component of exciton signal decay directly to the GS was observed in the ES transients, this is attributed to the recombination of charge-transfer states formed during electron transfer.

The 70 % PCBM blend films of P1 and P2 exhibit comparable electron transfer behaviour to that of the 10 % blend films, however the electron transfer kinetics (k_{ET}) are further accelerated, with an average lifetime of only 380 fs. The GS bleaching transients also indicate an increased polaron generation yield relative to the 10 % blend films, attributed to a reduction in the relative fraction of charge-transfer states that undergo recombination after the initial electron transfer process. In both blend films of the P2 donor, a power-law decay is observed following electron transfer in both ES and GS bleaching transients, attributed to the bimolecular recombination of generated polarons. This recombination process also appears to be influenced by the PCBM concentration, with a reduction in α' from 0.12 to 0.03 at the higher 70 % PCBM concentration.

The observed increase in k_{ET} with increasing PCBM concentration is attributed to an increase in donor-acceptor interfacial area, yielding a reduced exciton diffusion length in the 70 % relative to the 10 % blend films. An increase in crystallinity of the PCBM phase in the 70 % blends, leading to a larger driving force for electron transfer through a downward shift of the PCBM LUMO levels (on the order of 0.1 eV) may also play a role.^{19,76} The increase in domain interfacial area would also result in a greater fraction of the photogenerated exciton population being initially delocalized across the donor-acceptor interface, leading to more efficient charge separation prior

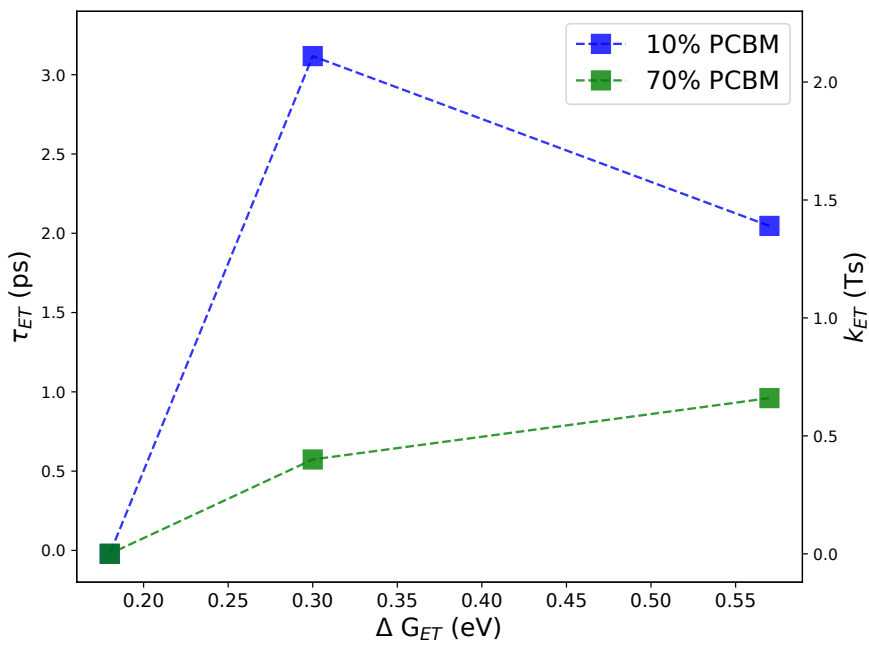


Figure 3.16: Measured electron transfer lifetime (τ_{ET}) and kinetics (k_{ET}) as a function of driving force for electron transfer (ΔG_{ET}), at PCBM blend film concentrations of 10 and 70 % for each P1, P2, and P3 donor polymers. The kinetics values were obtained through fitting of ultrafast transient absorption decay transients at a 1400 nm probe wavelength, using a 532 nm pump wavelength and an excitation density of $7 \mu\text{J cm}^{-2}$ (reference Figures 3.14 and 3.15, and Tables 3.2 and 3.3).

to charge-transfer state formation and relaxation (thereby reducing losses through charge-transfer state decay).^{72,97} The electron transfer kinetics for both P1 and P2 blend films do not show any significant correlation to the ΔG_{ET} of the donor-acceptor system (P1 = 0.57 eV, P2 = 0.30 eV) at either PCBM concentration, indicating an increase in ΔG_{ET} does not produce an increase in k_{ET} .

Finally, the P3 blend films exhibits solely exciton decay to the GS in both ES and GS bleaching transients, with no resolvable electron transfer at either PCBM concentration, and a decay lifetime that is consistent throughout. This suggests that a ΔG_{ET} greater than that of the P3 system (0.18 eV) is required to produce a high QY_{ET} in these donor-acceptor systems. The above observations are consistent with that of the photoluminescence quenching results with respect to the relative difference in exciton quenching between donor-acceptor systems, as well as the observed relative polaron generation yield and recombination kinetics obtained from picosecond transient absorption measurements.

To summarise, unity QY_{ET} was observed in donor-acceptor systems with a ΔG_{ET} greater than 0.18 eV, while no resolvable electron transfer was observed otherwise. This suggests that a ΔG_{ET} greater than that 0.18 eV is required to produce a high QY_{ET} in these donor-acceptor systems. Both k_{ET} and charge-transfer state recombination kinetics also appear independent of ΔG_{ET} in the systems that exhibit unity QY_{ET} . The initial polaron generation yield appears limited by charge-transfer state recombination, rather than the initial electron transfer kinetics. A qualitative measure of relative polaron generation yield indicates no significant dependence of N_{CS} on ΔG_{ET} , however ΔG_{ET} may influence picosecond bimolecular recombination kinetics which were observed in the P2 donor blend films.

3.4 Conclusions

The combination of photoluminescence, and both sub-nanosecond and femtosecond transient absorption spectroscopy was used to investigate polymer exciton decay and electron transfer processes in PCBM blend films, as well as polaron generation and recombination processes. A unique set of polymer donor materials enabled the direct comparison of k_{ET} , QY_{ET} , and approximate N_{CS} in these donor-acceptor systems, thereby facilitating the investigation of the influence of ΔG_{ET} on these charge carrier photogeneration processes. The results suggest that a ΔG_{ET} greater than that 0.18 eV is required to produce ultrafast electron transfer with a high QY_{ET} in these donor-acceptor systems, however k_{ET} appears independent of ΔG_{ET} above this value. The initial N_{CS} appears limited by charge-transfer state recombination, rather than the initial electron transfer kinetics, and indicates no significant dependence on ΔG_{ET} . The primary findings of this chapter have been published in the Journal of Physical Chemistry C.⁵⁰

There are however issues inherent with using solely optical measurement techniques performed on films to infer the performance of these donor-acceptor systems in operational organic photovoltaic devices. This includes the ambiguity in accurate assignment of the transient species observed in transient absorption measurements, due to coexisting polymer exciton, polaron, and possible charge-transfer state absorption at the 1400 nm probe wavelength. Determination of how these results relate to an extractable charge density in devices is problematic, leading to the necessity for verification of the outcomes of this optical study through the use of electronic measurement techniques performed on operational photovoltaic devices. In particular, the difficulty in accurately measuring polaron generation yield from these measurements alone leaves significant uncertainty as to extractable current in an operational device. Charge extraction losses (transport and trapping) can also severely limit device open-circuit potential and short-circuit current, and cannot be accurately estimated with these optical techniques.

Therefore the investigation of suitable electronic (charge extraction) measurement techniques, and detailed device characterisation is required to complete this study of charge carrier generation kinetics and yield, which can be correlated with the findings of this optical study. The time resolved charge extraction method is well suited to measurement of charge carrier generation and recombination processes in photovoltaic devices. Therefore, the investigations presented in Chapters 4 and 5 seek to determine the suitability of this measurements technique, investigate and quantify measurement limitations, and improve the technique through the first time incorporation of an applied bias during extraction measurement. Finally, the fabrication of photovoltaic devices incorporating the P1, P2, and P3 polymer donors blend films will be performed, and the developed charge extraction technique employed to understand the influence of material energetics on charge carrier generation and recombination processes (Chapter 6).

Chapter 4

Suitability of a Novel Charge Extraction Technique to Determine Charge Generation Yield, Recombination Kinetics, and Trap State Density Distribution

4.1 Introduction

4.1.1 Motivation and Objectives

The overall objective of this thesis is to understand the influence of the driving force for electron transfer in organic photovoltaic systems and operational devices, with the motivation of reducing this driving force as a method for increasing device photovoltage (reduce energy losses), while maintaining high device current (high charge generation/separation efficiency and yield). The previous chapter investigated the influence of driving force on the ultrafast charge generation/separation processes in organic photovoltaic systems. Optical techniques are not able to determine directly whether photogenerated charge carriers are freely mobile (desired for high photovoltaic efficiency) or bound electron-hole pairs. There is therefore a need to examine these processes using an electrical characterisation technique, capable of directly measuring free charge carrier generation yield and recombination kinetics. Chapters 4 and 5 will investigate and further develop charge extraction techniques for the investigation of charge carrier generation yield and recombination dynamics in

operational devices. Chapter 6 will then investigate the influence of donor-acceptor material system driving forces on charge generation yield, recombination kinetics, and operational performance of photovoltaic devices (extracted current, photovoltage, and efficiency).

The optical studies of the previous chapters indicated that a driving force within the range of 0.18 to 0.30 eV is not sufficient to yield ultrafast charge generation/separation, while driving forces above this value are. However further complications were observed, including the influence of driving force on charge generation yield and recombination processes, which is expected to impact photovoltaic device current. Donor-acceptor material system energy levels (driving force) will also directly impact device photovoltage. Device current (extraction of charge density) and photovoltage (trap state density distribution) are also strongly correlated, through the influence of trap state occupancy on recombination kinetics and charge extraction processes. The relaxation of charge carriers into a distribution of trap states reduces the average electrochemical potential of these charge carriers (proportional to open circuit voltage), as well as reducing the total extractable charge density (proportional to device current). Therefore a comprehensive study is performed to investigate the impact of driving force on charge generation/recombination processes, and trap state density distribution in operational photovoltaic devices (Chapter 6). In order to accomplish this, a measurement technique is required to measure charge density and recombination kinetics, while also capable of measuring the dependence of photovoltage on charge density (trap state density distribution and occupancy) independent of charge generation and recombination processes.

The following chapters will examine the suitability of a relatively novel charge extraction technique incorporating a nanosecond switch to address the above issues. In Chapters 4 and 5, a detailed investigation of measurement limitations is performed, with an assessment of their impact on the measurement of charge density, recombination kinetics, and trap state density distribution. Further development of this charge extraction technique is performed, through incorporation of an applied bias, in order to improve the measurement technique and overcome the identified limitations (Chapter 5). Finally, the developed technique is used to study photovoltaic devices incorporating the novel material systems investigated previously (Chapter 3), featuring an engineered variation in driving force. The novel charge extraction technique enables the measurement of charge generation yield, facilitates further investigation of charge recombination processes on the micro to millisecond time scale (not accessible by ultrafast transient absorption), and provides concurrent measurements of trap state density distribution (Chapter 6).

4.1.2 Background of Time Resolved Charge Extraction Techniques

The study of recombination kinetics and material energy levels in bulk heterojunction organic photovoltaic devices has been performed extensively using charge extraction based techniques. Additionally, charge extraction techniques using an externally applied reverse bias have also been used to determine charge carrier transport and recombination kinetics. Many of these techniques

however suffer from a loss of charge density during the measurement extraction process, leading to errors in the results obtained. Photoinduced charge extraction by linearly increasing voltage (Photo-CELIV) and bias amplified charge extraction (BACE) techniques involve the application of a reverse-bias potential (linearly increasing for Photo-CELIV, constant for BACE) to facilitate charge extraction.^{104, 117, 118} The amount of extracted charge in BACE measurements is greater than that extracted at short circuit (without an applied bias), as accelerated charge transport during extraction competes with recombination, and is therefore better at obtaining the device internal charge density by reducing charge extraction losses.

Typically for Photo-CELIV and BACE measurements, a forward bias is applied to the device prior to illumination to compensate for the device photovoltage, and is maintained during the delay time until the application of the reverse-bias.¹¹⁷ This produces a major limitation for charge carrier lifetime measurements. The open-circuit voltage during the delay time constantly decays due to charge recombination, but the applied forward bias is constant, and therefore results in charge injection. This complicates transient analysis and requires assumptions for the determination of the charge carrier lifetime due solely to photogenerated charge.¹¹⁹ Furthermore, the photogenerated charge distribution in bulk heterojunction solar cells at open-circuit condition may not be homogeneous, and change with charge density.^{120, 121} The application of a constant forward bias during the delay time may change the charge distribution, and therefore alter recombination kinetics compared to that under open-circuit conditions. The open-circuit corrected charge carrier extraction technique was developed by Baumann and Dyakonov et al as a method to overcome the problem of constant forward bias during the delay time in Photo-CELIV and BACE measurements.¹²² The open-circuit voltage decay is measured, and this same voltage signal is applied as the forward bias during delay time, maintaining open-circuit conditions without injection. The widespread adoption of this technical measurement procedure is however hindered by its practical complexity.

Alternatively, charge recombination lifetime can be obtained through transient photovoltage decay measurements.^{24, 104} The photovoltage decay is analysed based on the assumption that the voltage scales with charge density, and that the charge density decreases only due to recombination. However if charge density is not homogeneous, changes in charge density are caused by both recombination and transport through the active layer, requiring a more complicated analysis. Charge extraction or transient photocurrent measurements (TPC) are however still required to obtain lifetime as a function of charge density.²⁴ As TPC measures the transient photocurrent induced by a pulsed light at short-circuit conditions, the integrated charges may be underestimated due to charge recombination. The BACE technique could be employed to avoid recombination during extraction, however the issues with maintaining open-circuit condition during delay time remain.

A charge extraction technique is required that avoids the complicated analysis and assumptions needed to overcome the experimental difficulty in maintaining open-circuit condition during delay time, while minimising charge recombination losses during extraction. The switched time resolved charge extraction technique provides the potential for such an opportunity. The study of recombination kinetics and material energy levels has been previously performed using a switched charge extraction technique for dye-sensitized solar cells (DSSCs),¹¹⁵ and was subsequently applied for bulk heterojunction organic photovoltaic devices.¹¹⁶ Measurement at various steady-state illumination intensities provides a measure of charge density as a function of the open-circuit voltage, and can be used to infer donor/acceptor material energy levels and density/energetics of charge traps (trap state density distribution). In applying a delay time between stopping illumination and charge extraction measurement, the extracted charge represents charge carriers that survived recombination during the delay time, and can therefore be used to obtain charge recombination lifetime and recombination coefficients.^{104, 115} The determination of photogenerated charge density, recombination kinetics, and trap density distribution in operational organic photovoltaic devices provides insight into the origins of device performance. Charge extraction measurements have been used for the measurement of charge density in devices under a range of operational conditions, while time resolved charge extraction can be used to measure the recombination of charge density over time, and thereby study the recombination kinetics. Further measurements of transient photovoltage decay can be correlated with these charge density measurements to characterise charge carrier trap state occupancy within the device.

Time Resolved Charge Extraction

The time resolved charge extraction (TRCE) measurement utilises a nanosecond FET switch to switch rapidly between open circuit and short circuit conditions. A circuit diagram (top) and timing diagram (bottom) are presented in Figure 4.1 to illustrate the set-up and operation of TRCE measurements. The switch is capable to switching from an internal impedance R_{SW} of 2.2 MΩ to less than 1 Ω in under 100 ns. A photovoltaic device (OPV) is connected in series with the switch, and charge carriers are generated using a laser pulse for photoexcitation. A variable delay time T_{del} is imposed between stopping laser illumination T_0 and switching T_{SW} , during which time the device is held at open circuit and charge carriers are left to recombine. Upon switching, the device is short circuited and an extraction transient is measured across the variable measurement impedance R_M .

The total extracted charge is obtained through integrating the current transient response over time at a range of delay times to yield the decay of extracted charge as a function of delay time. The measured extracted charge can be used to calculate the device's internal photogenerated charge density given a known device volume. As the excitation-extraction delay time is the time that the photovoltaic device is held at open circuit after laser illumination is stopped, the decay of charge density over time is governed by bimolecular recombination occurring within the device, and

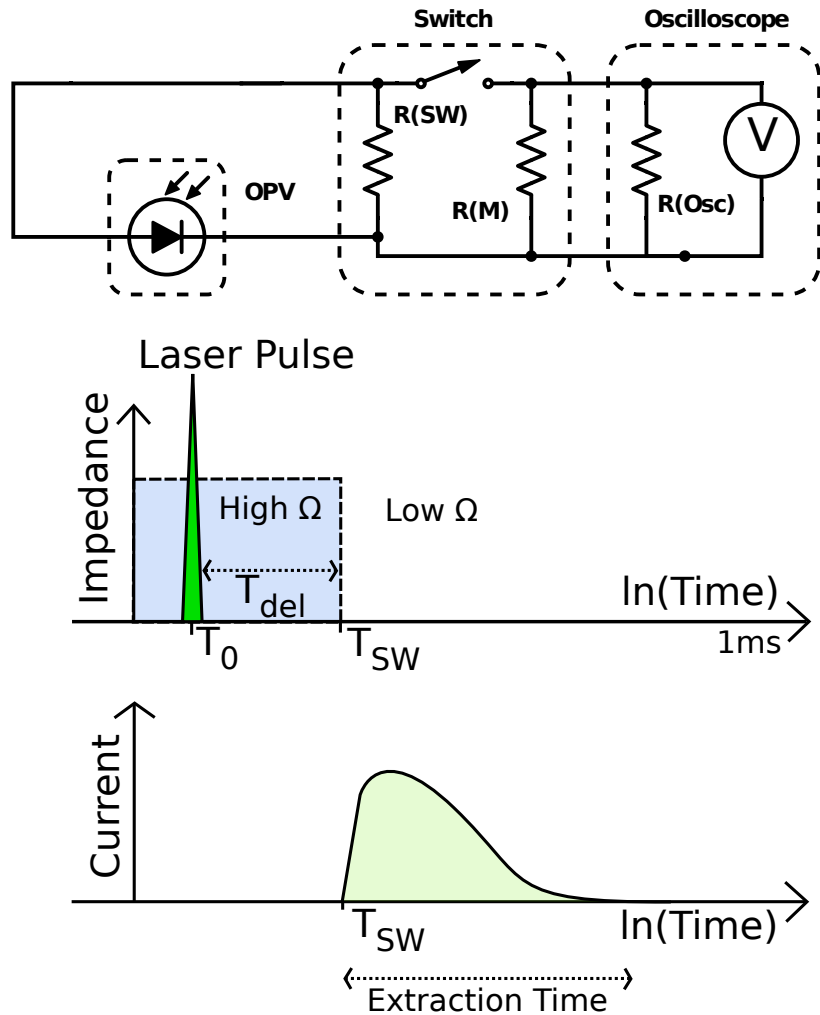


Figure 4.1: **Top:** Time resolved charge extraction circuit diagram, illustrating the organic photovoltaic device (OPV), FET switch with internal high impedance resistor R_{SW} and measurement resistance R_M , and oscilloscope with internal resistance R_{Osc} . **Bottom:** Timing diagram for operation of extraction measurements, illustrating the laser excitation pulse at T_0 , high initial circuit impedance ($M\Omega$) switching to low ($< 1 \Omega$) at T_{SW} , variable delay time T_{del} , and an illustration of an extraction current transient as a function of extraction time.

therefore the charge carrier lifetime and bimolecular recombination coefficient can be calculated as a function of charge density. The empirical reaction order of the recombination reaction can also be calculated from the measured charge density decay, and describes how the charge carrier recombination rate scale with charge carrier density. This parameter incorporates all measured charge carriers, including both free carriers and those within the distribution of trap states, and is therefore dependent on trap state occupancy and charge density.

Photovoltage decay and charge density decay results can be combined to yield the dependence of photovoltage on charge density. Photovoltage decay transients can also be combined with the charge carrier lifetime calculated from the charge density decay results to yield the dependence of photovoltage on lifetime. The dependence of photovoltage and lifetime on charge density can be used to calculate values for the diode ideality factor and empirical reaction order, and can further be compared to values calculated using steady-state measurements. Additionally, as the photovoltage is proportional to the Fermi level splitting across the device contacts, the rate of increase in photovoltage with charge density provides information on the trap state density distribution, and can be used to calculate the characteristic exponential slope of the trap state density distribution E_{ch} . This provides a measure of the density and distribution of trap states within the device active layer. A large E_{ch} indicates that a broad exponential tail of intra-bandgap trap states exists, with corresponding large density of trap states, while a small E_{ch} indicates a narrow exponential tail and small density of trap states.

Further details of the above analysis methodology and parameter calculations are provided in Chapter 2, Section 2.3.5, including additional details of time resolved charge extraction measurement operation.

4.2 Outstanding Issues in Time Resolved Charge Extraction Measurements

4.2.1 Influence of Charge Extraction Losses on the Measurement of Charge Density and Recombination Kinetics

Measurement at various steady-state illumination intensities provides a measure of charge density as a function of the open-circuit voltage, and can be used to infer donor/acceptor material energy levels and density/energetics of charge traps (trap state density distribution). In applying a delay time between stopping illumination and charge extraction measurement, the extracted charge represents charge carriers that survived recombination during the delay time, and can therefore be used to obtain charge recombination lifetime and recombination coefficients.^{104,115} These charge extraction measurements do however rely on the assumption that the measured extracted charge is representative of the charge density within the device, assuming no charge recombination occurs

during extraction. Recombination during extraction is not typically observed for high efficiency DSSCs, where the loss fraction for P3HT:PCBM based photovoltaic devices has been estimated to be less than 10 percent.¹¹⁶ However, for organic photovoltaic systems that exhibit fast recombination, slow transport, or use thick active layers, recombination during extraction could result in a much more significant underestimation of charge density. This underestimation of charge density introduces an error in measurement of charge carrier lifetime, energy levels, and trap state density distribution. As an unresolved issue of charge extraction measurements, the limitations (particularly charge recombination losses) have not been systematically quantified to date. Therefore a detailed quantitative assessment of measurement limitations, recombination losses during extraction, and their influence on the calculation of recombination kinetics and trap state density distribution in time resolved charge extraction measurements will be performed in this and the following chapter.

After photoexcitation and charge generation, the separated charge carriers diffuse within the active layer until they reach a device contact and are extracted, or recombine and result in the loss of charge density. Charge extraction is in direct competition with recombination, with efficient extraction of charge carriers requiring diffusion lengths longer than the active layer thickness.^{24,25} The diffusion length is proportional to the mobility-lifetime product, which is in turn dependent on the material system used and the morphology of the active layer. The degree of recombination during extraction is therefore strongly dependent on charge carrier mobility and lifetime, and the active layer thickness. Increasing either charge carrier lifetime or effective mobility, or reducing device thickness should therefore reduce these charge extraction losses.

Influence of charge density on charge extraction losses

As lifetime is dependent on charge density, recombination losses during extraction should also be dependent on charge density for a constant mobility and device thickness. Therefore variation of charge density in time resolved charge extraction measurements, through changing excitation density and excitation-extraction delay time, is performed in this chapter to study the influence of charge density and lifetime on recombination losses during charge extraction (Section 4.4.1). It is expected that variation of the laser pulse excitation density used to photogenerate charge carriers will vary the initial charge density, while an increasing excitation-extraction delay time will reduce charge density due to bimolecular recombination. Organic photovoltaic devices are fabricated using the PCDTBT donor blended with the PCBM acceptor as the active layer (bulk heterojunction), an extensively studied donor-acceptor material system (material structures provided in Chapter 1, Figure 1.6). The PCDTBT:PCBM system is known to exhibit charge generation yields approaching unity, with the predominant loss mechanism attributed to bimolecular recombination processes.¹⁰⁶ This material system also exhibits high charge carrier mobility and short lifetime. The recombination characteristics exhibit the signature of Langevin type recombination behaviour, and therefore thin active layers are optimal to achieve efficient current extraction.^{40,135}

It is therefore anticipated to incur significant recombination on a timescale comparable to that of the charge extraction measurement process, enabling the effective investigation of recombination losses during extraction under a range of measurement conditions. Time resolved charge extraction measurements are performed at a range of excitation densities and delay times, with an analysis of transient response both with and without photoexcitation. The extracted charge under varied measurement conditions is used to obtain charge density decay plots, and an analysis of distinct regions of behaviour is presented to specifically evaluate at which time-scales and charge density ranges charge recombination during extraction may become a dominant factor.

Influence of extraction losses on the measurement of charge density, recombination kinetics

Following the study of charge extraction losses and the measurement of charge density presented in this chapter (Section 4.4.1), a further study is performed to investigate the influence of these extraction losses on the subsequent determination of charge density and recombination kinetics (Section 4.4.2). The charge density decay results obtained through time resolved charge extraction measurements (Section 4.4.1) are used to calculate reaction order, charge carrier lifetime, and bimolecular recombination coefficient, each as a function of charge density and at a range of excitation densities. A detailed analysis of the distinct regions of behaviour identified in Section 4.4.1 is performed, in order to understand the influence of identified charge extraction losses on these recombination kinetics measurements.

Further investigations of the influence of recombination losses during extraction on the subsequent determination of charge density and recombination kinetics is performed in Chapter 5, in concert with investigations of the influence of an applied bias in time resolved charge extraction measurements.

Influence of applied reverse bias on charge extraction losses

The charge carrier transit time may be increased through the application of an electric field, leading to faster extraction and thereby reduce recombination during extraction. This effect will be explored in Chapter 5 through the introduction of an applied reverse bias to time resolved charge extraction measurements, with a study of it's influence on recombination losses, and subsequent determination of charge density, recombination kinetics, and trap state density distribution.

Influence of device thickness on charge extraction losses

Increasing the active layer thickness for a constant diffusion length (mobility-lifetime product) should lead to increased charge extraction losses. This effect will be investigated in Chapter 5, through charge extraction measurement performed on a range of devices with relative differences in active layer thickness.

4.2.2 Measurement of Trap State Density Distribution using Time Resolved Charge Extraction

Localisation of charge carriers into trap states can occur during diffusion/transport, with the spatial and energetic distribution of these trap states (trap state density distribution) dependent on the material system and morphology. These trap states arise from energetic disorder within the active layer, leading to a broadening of electronic state distribution. Trapping results in a reduced average mobility and increased average lifetime for a given charge density, thereby reducing charge extraction efficiency. Trapping can also reduce the extractable and therefore measurable charge density, leading to underestimation of charge density.

Trapping can further influence the bimolecular recombination process, where localised trap states in the band gap (exponential band tail) participate in the recombination of free charge carriers. This degree of influence, and how recombination scales with charge density is typically characterised through determination of the diode ideality factor and reaction order. The P3HT:PCBM material system (material structures provided in Chapter 1, Figure 1.6) is known to exhibit a broad trap state density distribution, and typically displays an ideality factor on the order of 1.25 or above, while numerous other organic photovoltaic systems including PCDTBT:PCBM typically exhibit an ideality factor closer to 1.0.^{125, 126, 126, 136} Studies have shown that the deliberate introduction of trap states into an organic photovoltaic devices can increase the value of ideality factor, with PCDTBT:PCBM devices showing an increase in ideality factor from 1.01 to 1.43.¹³⁶ A reaction order of approximately 2 is typical of devices with balanced carrier mobilities and only modest bimolecular recombination losses at short circuit, while reaction orders higher than 5 have been reported, attributed to the interaction of trap states in the bimolecular recombination process.^{34–36}

As charge density and photovoltage are strongly correlated, through the influence of trap state occupancy on recombination kinetics and charge extraction processes, the determination of trap state density distribution is important in investigating the impact of driving force on charge carrier recombination processes. However gaps in understanding exist regarding the determination of trap state density distribution through a correlation of charge density and photovoltage decay results, and how this is influenced by charge extraction losses. Additionally, investigation is required to understand the influence of changing trap state occupancy on the measurement of charge density, recombination kinetics, and trap state density distribution in time resolved charge extraction, and will be explored in Chapters 4 and 5.

The influence of charge extraction losses on trap state density distribution measurement

Steady-state current-voltage measurements are performed to characterise the fabricated PCDTBT:PCBM devices performance, and to calculate steady-state ideality factor and reaction order for comparison to values calculated through transient measurements (Section 4.4.1). A study is then performed

to investigate the correlation of charge density and photovoltage decay results for the determination of trap state density distribution, as well as the influence of charge extraction losses (Section 4.4.2). The charge density decay results (Section 4.4.1), and the calculated charge carrier lifetime as a function of charge density (Section 4.4.2) are combined with photovoltage decay measurements performed at a range of excitation densities, to provide the dependence of photovoltage and lifetime on charge density. An analysis of these results is performed to investigate the influence of identified charge extraction losses on the calculation of trap state density distribution, ideality factor, and reaction order. Additional measurements are performed in this chapter on a device incorporating the P3HT:PCBM material system (Section 4.4.3), which is less influenced by charge extraction losses than the PCDTBT:PCBM device (Sections 4.4.1 and 4.4.2). This enables further assessment of the measurement of trap state density distribution, through correlation of charge density and photovoltage decay results, and the influence of charge extraction losses.

Further investigations of the influence of charge extraction losses on the measurement of trap state density distribution are performed in Chapter 5, in concert with investigations of the influence of an applied reverse bias, and thickness dependence in time resolved charge extraction measurements.

The influence of photoexcitation pulse length on trap state occupancy

In transient charge extraction measurements, the initial charge density is dependent on excitation density. Increasing excitation density increases the generated charge density, however the charge density dependence of lifetime results in an increase in recombination. If the excitation pulse length is sufficiently shorter than the lifetime of the generated charge carriers for a given charge density, no significant recombination will occur during excitation. However when the excitation pulse length becomes comparable to lifetime, recombination during excitation will become significant. The limit of this is reached at steady-state (constant) illumination, where a balance of generation and recombination is reached at open-circuit (no current extraction), resulting in a constant charge density for a given excitation density. The relaxation of charge density over time may result in an increasing trap state occupancy for increasingly long excitation pulse length. Differences in charge density (dependent on excitation density over time) and recombination kinetics (trap state occupancy) can be expected when transient charge extraction measurements are performed using different photoexcitation pulse lengths. Therefore, a study of charge extraction measurements is performed using different excitation pulse lengths, in order to study the influence of this parameter on the initial state of photogenerated charge density (trap state occupancy), and any subsequent influence on the measured extracted charge, recombination kinetics, and trap state density distribution (Section 4.4.3).

Time resolved charge extraction and photovoltage decay measurements are performed using either a nanosecond or millisecond pulse length for laser excitation, under comparable measurement

conditions (charge density). Organic photovoltaic devices are fabricated using the poly-3-hexylthiophene (P3HT) donor blended with the methanofullerene (PC_{60}BM) acceptor (P3HT:PCBM) as the active layer (bulk heterojunction), another extensively studied donor-acceptor material system. The recombination kinetics observed in P3HT:PCBM blend films are typically significantly reduced compared to Langevin behaviour, with lifetimes on the order of $40\ \mu\text{s}$ at charge density of $4\times 10^{16}\ \text{cm}^{-3}$ (compared to a lifetime of $2\ \mu\text{s}$ for PCDTBT:PCBM).¹²⁵ Efficient charge extraction is also possible in devices with active layer thicknesses over twice those required for PCDTBT:PCBM devices.³⁹ The efficiency of PCDTBT:PCBM devices still typically far exceeds that of P3HT:PCBM devices. The P3HT:PCBM material system is known to exhibit a broad trap state density distribution and significant charge trapping, compared to the relatively trap-free PCDTBT:PCBM system. Devices utilising P3HT:PCBM are therefore ideal to study the influence of excitation pulse length, and thereby trap state occupancy in time resolved charge extraction measurements.

Time resolved charge extraction measurements are performed at a range of excitation densities, using both a short (6 ns) and long (10 ms) excitation laser pulse length (Section 4.4.3). An analysis of transient response and extracted charge is performed to compare differences in charge extraction behaviour between excitation pulse lengths. Further comparison and analysis of charge density decay and corresponding charge carrier lifetime is performed to identify the influence of excitation pulse length on recombination kinetics. Photovoltage decay measurements are then performed, and used to calculate the dependence of photovoltage and lifetime on charge density. An analysis of these results is performed to identify the influence of excitation pulse length on the transient measurement of trap state density distribution, ideality factor, and reaction order.

4.2.3 Summary of Outstanding Issues and Chapter Objectives

To summarise the above, the overall objective of this chapter is to examine the suitability of the time resolved charge extraction technique for the measurement of charge generation yield, charge recombination processes, and trap state density distribution in operational photovoltaic devices. A number of outstanding issues were identified in the above discussions, representing gaps in understanding that are to be addressed through the studies presented in this chapter. These are covered under the following chapter objectives:

1. Quantify charge extraction losses in time resolved charge extraction, and their influence on the measurement of charge density, recombination kinetics, and trap state density distribution, through measurements of charge density under a range of excitation densities and delay times, and subsequent analysis of charge density decay.
2. Assess the correlation of transient charge extraction and photovoltage decay measurements for determining trap state density distribution, through a comparison of transient derived ideality factor and reaction order to those obtained using steady-state measurements.

3. Determine the influence of trap state occupancy on the measurement of charge density, recombination kinetics, and trap state density distribution in time resolved charge extraction, through measurement of charge density using different excitation pulse lengths, and subsequent analysis of charge density decay.

4.3 Experimental

4.3.1 Photovoltaic Device Fabrication

Multiple sets of photovoltaic devices were fabricated for use in the charge extraction measurement studies detailed in this chapter (2 devices for each active layer thickness, 4 pixels per device). The poly[N-9"-hepta-decanyl-2,7-carbazole-alt-5,5-(4',7'-di-2-thienyl-2',1',3'-benzothiadiazole)] (PCDTBT) (Solaris, SOL4280, 68-85Dka, electronic grade) and [6,6]-phenyl-C₆₀-butyric acid methyl ester (PCBM) (Solaris, SOL5061A, 99.5 % purity) (1:4) blend solution was prepared by dissolution in o-dichlorobenzene at 20 mg mL⁻¹ and stirring at 120 C° for 20 hours under an Ar atmosphere. The poly(3-hexylthiophene-2,5-diyl) (P3HT) (LumTec., LT-S909, 45Dka, electronic grade, 93 % regioregular) and PCBM (5:4) blend solution was prepared by dissolution in chlorobenzene at 50 mg mL⁻¹ and stirring at 80 C° for 20 hours under an Ar atmosphere.

Pre-patterned Indium Tin Oxide (ITO) coated glass slides (LumTec., 90 nm thick ITO, variable active pixel area, typical conductivity of 15 Ω cm⁻², above 85 % transmission at 550 nm) are used for the transparent device anode, as well as providing a rigid substrate. The substrates are cleaned by 15 min under sonication in surfactant/H₂O, followed by two subsequent 5 min sonication rinses in H₂O, and 15 min under sonication each in acetone and isopropanol, prior to a 20 min UV-ozone treatment. This ensures a clean, particulate free substrate and improves wettability for solution/active layer deposition.

The cleaned substrates are coated with the poly(3,4-ethylenedioxythiophene):poly(styrenesulfonate) (PEDOT:PSS) hole selective layer, using 0.5 wt % PEDOT:PSS solution (Heraeus Clevios Al 4083) diluted 1:1 in isopropanol. The PEDOT:PSS solution is filtered through a 0.45 μm PVDF filter to remove any particulates prior to dilution, and maintained under stirring. The layer is then deposited using spin coating (Laurell WS-560HZ-15NPP) at 5000 rpm for 30 s, followed by annealing in air at 140 C° for 20 min.

Directly prior to deposition of the active layer, the active layer polymer(blend) solutions are cooled to room temperature. For both P3HT and PCDTBT based devices, the polymer(blend) solutions were spin-coated in air onto the prepared substrate at between 1500 and 5000 rpm, for times ranging from 90 to 240 s, depending on the active layer thickness required.

To produce the amorphous titanium oxide (TiO_x) electron selective interfacial layer, a titanium oxide sol-gel precursor solution is diluted (1:10) into isopropanol prior to deposition onto the

device active layer. TiO_x layer deposition is performed directly after active layer deposition (and any required active layer solvent drying time) using spin coating at 5000 rpm for 30 s, and is left to hydrolyze in air for 20 min (or under heating where the active layer requires annealing).

Aluminium (Al) is then evaporated under vacuum through a mask of defined device active area (0.095 cm^{-2} unless otherwise stated), to produce a cathode thickness on the order of 100 nm. A ramp in evaporation rate is used to ensure good contact with the active layer (initial 5 nm at 0.5 \AA s^{-1} , following 50 nm at 1.5 \AA s^{-1} , final $\sim 50 \text{ nm}$ at $2.5+ \text{ \AA s}^{-1}$). The deposition chamber is left to cool down for 30 minutes before returning to atmospheric pressure. These devices were then sealed under an inert Ar atmosphere using a cover glass slide and UV-curable epoxy (Ossila, E131), manually cured using a handheld UV gun. Effort is made to ensure that no epoxy is in contact with the device active layer, and that no significant UV illumination is incident on the device active area. Finally, a metal contact is soldered (ultrasonic) onto the exposed anode/cathode contact regions for increased durability during measurement.

4.3.2 Steady-State Device Performance

Current-voltage (*JV*) measurements are performed to assess steady-state device performance, and characterise a number of important device parameters including open circuit voltage V_{OC} , short-circuit current J_{SC} , fill factor FF , solar conversion efficiency η , series resistance R_S , and shunt resistance R_{Sh} , using known parameters for device area A and device thickness d . The solar simulator and measurement system used (TriSol Solar Simulator, IV16-L, PV Measurements Inc.) comprises components for variable electronic load and data acquisition (Keithley 2400, PVM QEX10), and a white light source (constant illumination, 1.5 air mass global solar spectrum) calibrated using a standard silicon diode to 1 sun equivalent (100 mW cm^{-2}). The photovoltaic device is held under illumination at a range of constant applied potentials (V), from forward to reverse bias, and the extracted current density (J) is measured, to produce a *JV* response plot. A dark measurement (without illumination) is also performed across the range of measured applied potentials. Further, the illumination intensity can be varied below 1 sun through the use of reflective neutral density filters, thereby obtaining *JV* response at a range of steady-state current densities.

J_{SC} and V_{OC} are obtained directly as the *JV* response intersection with the voltage and current density axis respectively. The FF is calculated as the quotient of P_{max} and the product of J_{SC} and V_{OC} , illustrated as the ratio of the two square regions in Figure 2.1. The power conversion efficiency η of a device can then be obtained. The series and shunt resistance are then calculated for each device, using the slope of the dark *JV* plot about 1 V and 0 V respectively. Further analysis of these measurement results can be performed to obtain the empirical reaction order δ' and diode ideality factor n'_{id} , and can be compared to those obtained through transient measurement and analysis. The δ' can be calculated from the dependence of short circuit current J_{SC} on illumination

intensity ϕ , while the n'_{id} can be calculated from the dependence of open circuit voltage V_{OC} on ϕ . Further details are provided in Chapter 2, Section 2.1.2.

4.3.3 Transient Charge Extraction and Photovoltage Decay

The time resolved charge extraction (TRCE) measurement utilises a nanosecond FET switch (SR-05, Asama Lab) to switch rapidly between open circuit and short circuit conditions. The switch is capable of switching from an internal impedance R_{SW} of $2.2\text{ M}\Omega$ to less than $1\text{ }\Omega$ in under 100 ns. A high switch impedance is used to maintain open circuit rather than a true open circuit (infinitely large impedance) to protect the switch. A photovoltaic device (OPV) is connected in series with the switch, and charge carriers are generated using a laser pulse for photoexcitation (532 nm, 6 ns pulse width, Spectra Physics Quanta Ray Lab 170; or during long pulse measurements a 641 nm, variable pulse width, Nation Instruments Coherent CUBE continuous wave). A variable delay time T_{del} is imposed between stopping laser illumination T_0 and switching T_{SW} using a delay generator, during which time the device is held at open circuit, and charge carriers are left to recombine. Upon switching, the device is short circuited and an extraction transient is measured across the variable measurement impedance R_M ($50\text{ }\Omega$ unless otherwise stated) using an oscilloscope (DPO4000 Series, Tektronix).

Each extraction transient is recorded as an average of 50 individual measurements, per set of conditions, to minimise noise and account for any variability in laser excitation. All transients presented herein are displayed with an 80 ns shift for illustration purposes, such that switching occurs at 80 ns as presented in figures. Unless otherwise specified, the characteristic switch response has been subtracted from all transients, recorded individually for each set of measurements, as well as the dark (no laser illumination) transient response. The transient voltage response is measured as a function of extraction time, and converted to extracted current using the known measurement resistance. The total extracted charge is obtained through integrating the current transient response over time. The extracted charge is obtained at a range of delay times to yield the decay of extracted charge as a function of delay time, with laser illumination also varied.

Photovoltage decay measurements are performed to obtain the open circuit potential at the device contacts as a function of time that the photovoltaic device is held at open circuit after laser illumination is stopped. Variation of excitation density is also used to alter the initial charge density. These measurements are performed using a laser excitation source (532 nm, 6 ns pulse width, Spectra Physics Quanta Ray Lab 170; OR for long pulse measurements a 641 nm, variable pulse width, Nation Instruments Coherent CUBE continuous wave), with the photovoltaic device connected in series with the oscilloscope high impedance of $1.0\text{ M}\Omega$ to maintain open circuit. The photovoltage decay transients are then recorded using the oscilloscope (DPO4000 Series, Tektronix), from the time of stopping laser excitation until complete decay of photovoltage.

Table 4.1: Summary of device parameters and steady state performance (current-voltage results displayed in Figure 4.2), open circuit voltage V_{OC} , short-circuit current J_{SC} , fill factor FF , solar conversion efficiency η , device area A , device thickness d , series resistance R_S , and shunt resistance R_{Sh} . Average and standard deviation for solar performance parameters are also displayed, incorporating results from 8 individual devices.

	V_{OC} (mV)	J_{SC} (mA cm $^{-2}$)	FF -	η (%)	A (cm $^{-2}$)	d (nm)	R_S (Ω cm $^{-2}$)	R_{Sh} (Ω cm $^{-2}$)
PCDTBT:PCBM	900	8.89	0.57	4.58	0.06	90	30	3.7×10^5
Mean (8 devices)	894	8.44	0.55	4.16				
Standard Deviation	7	0.53	0.02	0.39				

Further details of time resolved charge extraction and photovoltage decay measurements and analysis methodology are presented in Chapter 2, Sections 2.3.1 and 2.3.2.

4.4 Results and Discussion

4.4.1 Influence of Laser Excitation Density and Delay Time on Extracted Charge Density

Steady-State Performance

Photovoltaic devices were fabricated incorporating the PCDTBT:PCBM (1:4) donor-acceptor system with an active layer thickness of 90 nm. Current-voltage measurements were performed to assess steady-state performance of this device under a range of illumination intensities. Average device performance parameters for the eight devices, including standard deviation, are presented in Table 4.1. Each transient and steady-state measurement was performed on multiple devices to ensure reproducibility of findings, however for simplicity, all results presented within this chapter are for a single representative high performance device.

Figure 4.2 displays the current-voltage response of the PCDTBT:PCBM device using a 100 mW cm $^{-2}$ illumination intensity (top), with log-scaled plots (bottom) at illumination intensities ranging from 100 to 0.1 mW cm $^{-2}$ (solid lines) as labelled. The dark response (no illumination) is also included (broken line) for each plot. The key device performance parameters calculated from these results (100 mW cm $^{-2}$, AM1.5 solar spectrum) are summarised in Table 4.1. At the 100 mW cm $^{-2}$ illumination intensity, this device exhibits an open-circuit voltage of 900 mV, a short-circuit current density of 8.9 mA cm $^{-2}$, a fill factor of 0.57, and solar conversion efficiency of 4.58 %. The measured current density is observed to increase only slightly under a reverse bias potential of 1 V, to 9.4 mA cm $^{-2}$, relative to the 8.9 mA cm $^{-2}$ measured at short-circuit, indicating efficient current extraction at short circuit. A high shunt resistance of 3.7×10^5 Ω cm $^{-2}$ is calculated, with a low injection

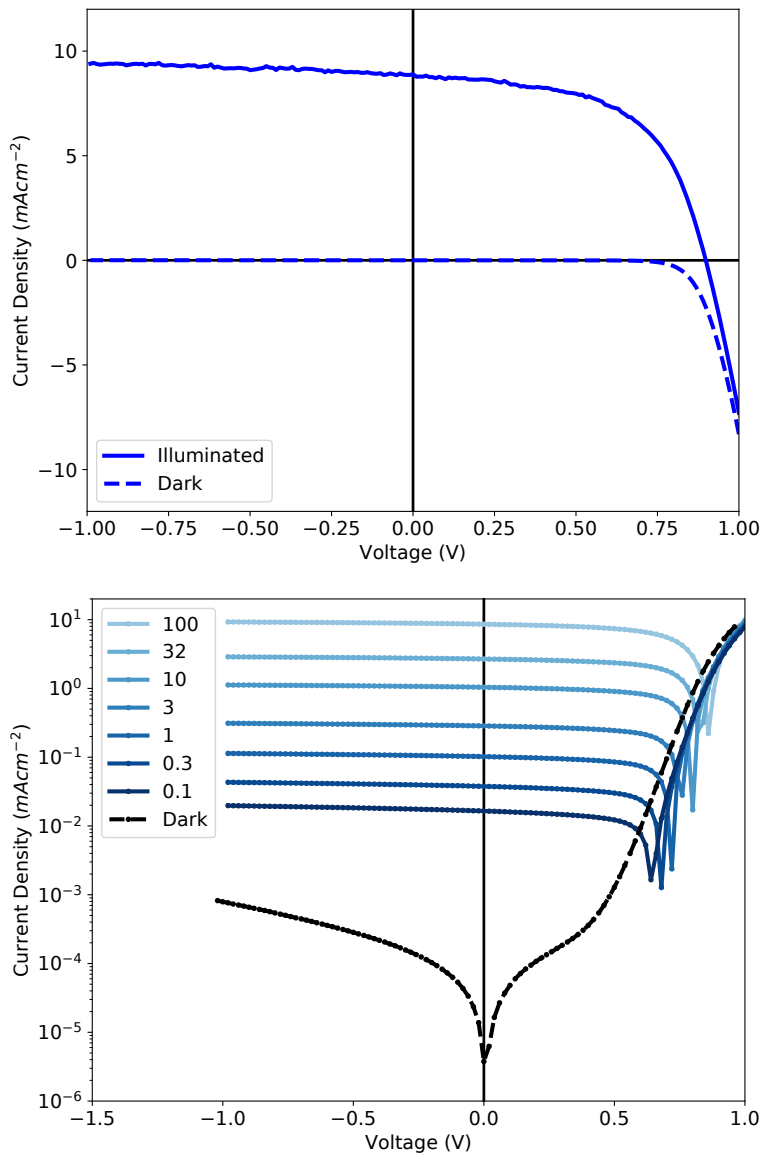


Figure 4.2: Current density versus voltage measurement response for a PCDTBT:PCBM device using a 100 mW cm^{-2} illumination intensity (top), with log-scaled plots (bottom) at illumination intensities ranging from 100 to 0.1 mW cm^{-2} (solid lines) as labelled. The dark response (no illumination) is also included (broken line) for each plot.

current under high reverse bias indicating good diode behaviour and blocking contacts. Steady-state current-voltage measurements were repeated after performing transient charge extraction measurements (up to 2 month post initial measurement) for the displayed PCDTBT:PCBM device, and exhibited less than a 5 % reduction in open circuit voltage, short circuit current, and fill factor, indicating that the device was not significantly degraded during the various measurements.

Literature reports of photovoltaic devices incorporating the PCDTBT donor polymer show solar conversion efficiencies ranging from 4 to 6 % depending on the fullerene adduct used (C_{60}/C_{70}) and interfacial layers employed.^{40, 100, 101, 106, 135} The average device performance reported herein of 4.2 % compares well to literature reports of comparable device architecture and active layer.

The current-voltage measurements were performed covering three orders of magnitude in illumination intensities from 100 to 0.1 mW cm^{-2} , and are used to obtain the dependence of short-circuit current and open-circuit voltage on illumination intensity, as displayed in Figure 4.3. The displayed plots of short-circuit current and open-circuit voltage exhibit a power law and exponential dependence respectively on illumination intensity, with regressions to each plot displayed (broken line). The values of diode ideality factor and reaction order are calculated from these plots as a means to link steady-state measurements with the transient measurements presented later in the chapter. The ideality factor (n_{id}) calculated using the dependence of open-circuit voltage on illumination intensity and Equation 2.5 is 1.22. The reaction order (δ) calculated using the dependence of short-circuit current on illumination intensity and Equations 2.3 and 2.4 is 2.09. The measured ideality factor of 1.22 indicates the influence of trap states in the recombination process, which is consistent with a reaction order of 2.09, slightly above that expected for trap free bimolecular recombination at 2. Low device shunt resistance has been shown to increase the measured ideality factor in steady-state measurements, however this device exhibits a sufficiently high shunt resistance such that this is unlikely the origin of the deviation from an ideality factor of 1.0.³⁵ PCDTBT:PCBM devices have been reported to exhibit ideality factors ranging from a relatively trap free 1.01 to a heavily trap state influenced 1.43, consistent with the results presented herein for this device.¹³⁶

Charge Extraction Transients

Time resolved charge extraction measurements performed using devices incorporating the PCDTBT:PCBM system are presented, including a range of excitation densities (by changing the intensity of the laser pulse using neutral density filters) and excitation-extraction delay times. Charge extraction transients for the PCDTBT:PCBM device are displayed in Figure 4.4 (top), and transient integral as a function of extraction time (cumulative extracted charge) is also displayed (bottom), obtained using an excitation density of 10 $\mu\text{J cm}^{-2}$ and 100 ns delay time ('light', blue solid line). The response transient without excitation is also displayed ('dark', black solid line). The subtracted transient ('sub', blue broken line) is produced by subtracting the dark response from the light re-

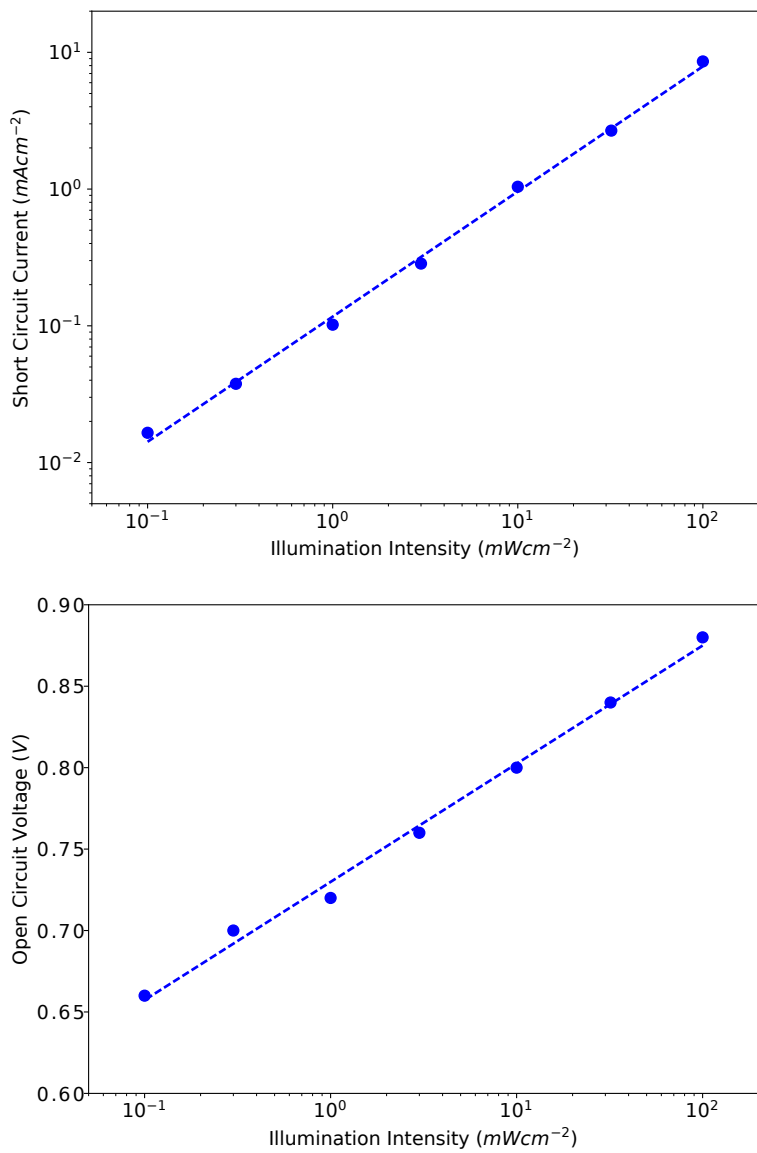


Figure 4.3: Short-circuit current density (top) and open-circuit voltage (bottom) as a function of illumination intensity for a PCDTBT:PCBM device, with regression to plots included (broken line).

spose. The dark response exhibits an initial negative response, followed by a small positive peak, before reaching zero extraction current beyond $1 \mu\text{s}$. This response is due to the displacement current of the switch circuit and is independent of device characteristics and excitation conditions (not shown). The light transient exhibits an identical initial switch response, superimposed with a significant additional current, corresponding to the extraction of photogenerated charge carriers. Subtraction of the dark current response from the light current response yields the extracted current due solely to the photogenerated charge density. Integration of this light extraction transient yields a total extracted charge of 6.2 nC , corresponding to a charge density of $7.6 \times 10^{16} \text{ cm}^{-3}$ calculated using the geometric volume of the active layer film.

The small continued extraction tail (increasing integral of extracted charge) towards the end of the measured transient (beyond $10 \mu\text{s}$) indicates the requirement for a longer measurement extraction time. The extraction current of the illuminated/subtracted transient should eventually reach zero (depletion of photogenerated charge density), with any extra extracted charge beyond $10 \mu\text{s}$ typically only amounting to a small percentage of total charge density. For this device, the charge extraction process requires an extraction time greater than $5 \mu\text{s}$ to extract over 95 % of the total extracted charge, during which time both recombination or trapping of charge carriers may occur, leading to extraction losses and therefore an underestimation of charge density.

The initial rise time of the light transients is limited by the time response of the measurement circuit, which is a product of circuit resistance R_M and device capacitance C_{OPV} (see Figure 4.1). For a measurement resistance of 50Ω , device capacitance of 2.34 nF , and device series resistance of 20Ω (obtained from the dark JV response), one obtains a response time of 165 ns . This compares well with the subtracted transient response in Figure 4.4 (rise-time of 80 ns), although the switch opening response somewhat obscures the shape of this rise. This measurement circuit response dictates the upper limit in time resolution for all charge extraction measurements in this section (using the same device and resistance). Therefore if recombination and transport losses during charge extraction are not significant (highly efficient extraction), the measurement of charge carrier lifetimes on the order of 200 ns should be possible with this charge extraction measurement.

Changing the Excitation-Extraction Delay Time

By varying the excitation-extraction delay time, the change in the extraction transients as a function of delay time at open-circuit condition can be monitored. Figure 4.5 displays the transients for a PCDTBT:PCBM device at a range of delay times from nanoseconds to milliseconds, using a fixed $10 \mu\text{J cm}^{-2}$ excitation density. A reduction in magnitude of extraction transient and corresponding reduction in extracted charge is observed with increasing delay time. A charge density of $7.6 \times 10^{16} \text{ cm}^{-3}$ is obtained at 100 ns delay time, reducing to $1.9 \times 10^{16} \text{ cm}^{-3}$ at 1 ms . The response at sufficiently long delay times tends towards the transient response without photoexcitation ('dark'). The transients exhibit a peak in extracted current within 100 ns , decreasing

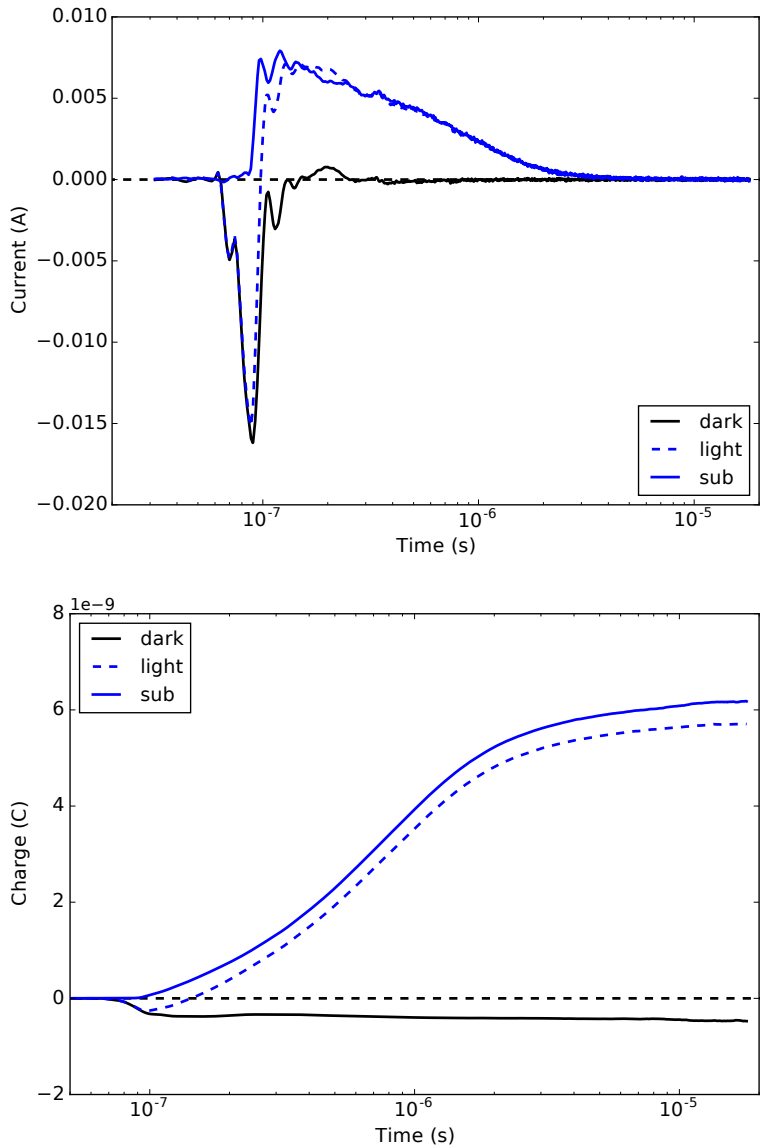


Figure 4.4: Charge extraction transients (extracted current as a function of extraction time) for a PCDTBT:PCBM device using $10 \mu\text{J cm}^{-2}$ excitation density and 100 ns excitation-extraction delay. Displayed are the response transients, both with illumination ('light', broken line) and without ('dark', solid black), and the subtracted transient ('dark' subtracted from 'light', solid blue). Transient integral (cumulative extracted charge) as a function of extraction time is also shown (bottom). All transients are been shifted by 80 ns from T_0 for ease of illustration on a logarithmic time scale.

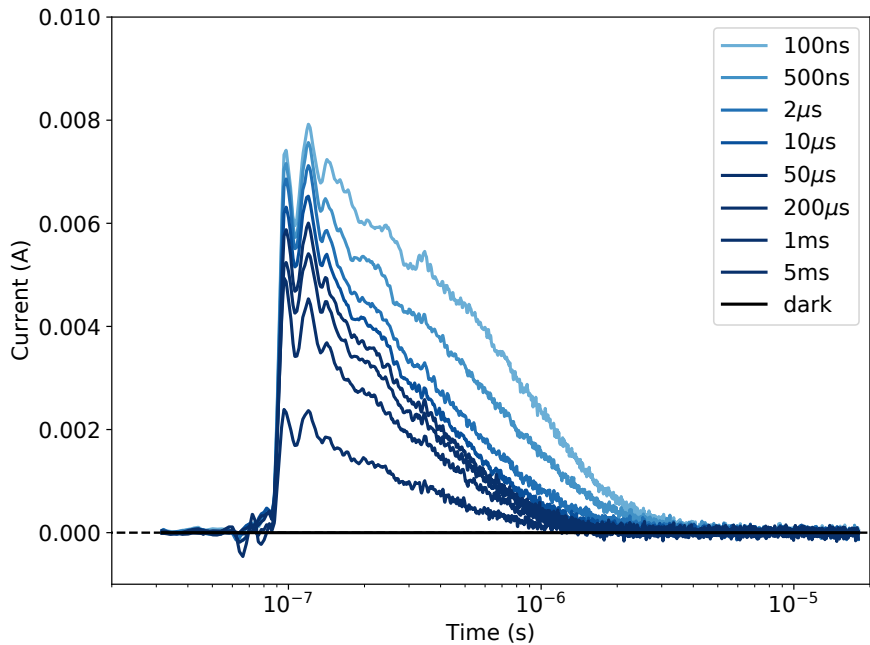


Figure 4.5: Time resolved charge extraction transients (subtracted transients as in Figure 4.4) for a PCDTBT:PCBM device, using $10 \mu\text{J cm}^{-2}$ excitation density at a range of excitation-extraction delays (as labelled).

as a function of extraction time with no significant extracted current beyond $5 \mu\text{s}$ at any delay time.

The reduction in extracted charge with increasing delay time demonstrated above provides a measure of the recombination of photogenerated charge density as a function of time. However, since the extraction process also takes time (around $5 \mu\text{s}$ in this case), the charge density at any given delay time could be underestimated due to recombination during extraction (after the switch is closed) or trapping (charges are not extracted due to low mobility). Therefore the obtained value of charge density may be an underestimation of the internal charge density. Changing the light intensity of excitation pulse is another way of influencing charge recombination during charge extraction. At higher illumination intensity (higher charge density), bimolecular recombination should be faster, causing an increasing fraction of charge loss (not extracted). This will be investigated next by changing the light intensity by two orders of magnitude in addition to changing the delay time.

Changing the Laser Light Intensity

Figure 4.6 shows the same PCDTBT:PCBM extraction transients at excitation densities ranging from 10 to $0.1 \mu\text{J cm}^{-2}$, and at delay times of 100 ns (top) and $100 \mu\text{s}$ (bottom). An increase in current extraction at the 100 ns delay time is observed with increasing excitation density, yielding a corresponding increase in the calculated charge density. A ten-fold increase in excitation density

from 0.1 to 1 $\mu\text{J cm}^{-2}$ results in an increase in charge density from 2.6×10^{16} to $6.4 \times 10^{16} \text{ cm}^{-3}$ (146 %), while from 1 to 10 $\mu\text{J cm}^{-2}$ only results in an increase from 6.4×10^{16} to $7.6 \times 10^{16} \text{ cm}^{-3}$ (19 %), suggesting a saturation of charge density with increasingly high excitation density. Assuming that photogeneration efficiency does not change with excitation density, a 10-fold increase in excitation density would yield an approximate 10-fold increase in the extracted charge density, as was observed in the steady-state dependence of short circuit current on illumination intensity. While slightly over a 10-fold increase in charge density is observed between the 0.1 and 1 $\mu\text{J cm}^{-2}$ measurements at 100 ns delay time, the increase is only 19 % from 1 to 10 $\mu\text{J cm}^{-2}$. This behaviour is very different from what is observed in steady state measurements, possibly due to the different nature of the light sources used (steady state versus short pulse). The greater than expected increase between 0.1 to 1 $\mu\text{J cm}^{-2}$ measurements may indicate charge extraction losses that are not linearly dependent on charge density. At longer delay times, the extracted charge increases even less with increasing excitation density. For example, at 100 μs delay time, no increase in charge density or any significant change to the shape of the transient response is observed with increasing excitation density. This light intensity independent extracted charge suggests very strong recombination of charge carriers during the delay time, and may also indicate the same concentration of trapped charge being extracted at these long delay times independent of the excitation density.

The saturation of initial charge density can be explained by the dependence of higher order recombination kinetics on charge density, causing increasing recombination losses during extraction. As the initial charge density is increased, the charge recombination is faster, leading to a greater loss of charge density during extraction. The extracted charge densities obtained for this PCDTBT:PCBM device at a 100 ns delay time, of 7.5×10^{16} , 6.4×10^{16} , and $2.7 \times 10^{16} \text{ cm}^{-3}$ at 10, 1, and 0.1 $\mu\text{J cm}^{-2}$ respectively, provide charge extraction yields (incident photons to extracted charges) of 1.3, 11.0, and 46.0 %. This clearly illustrates the impact of increasing recombination losses at high excitation densities. As a result, at sufficiently high excitation densities, and therefore high charge densities, the recombination kinetics are too fast to be accurately measured using charge extraction. This is due to the time resolution of the setup (~ 160 ns) and the time required to extract charges without any additional driving force ($\sim 5 \mu\text{s}$). Therefore at high excitation densities, in this case those above 10 $\mu\text{J cm}^{-2}$, charge density is underestimated in charge extraction measurements.

Charge Density Decay

Figure 4.7 displays the measured charge density as a function of delay time for each excitation density, divided into three regions based on the characteristic behaviour observed.

Region 1: In the delay time region beyond 100 μs , corresponding to charge densities below $2.3 \times 10^{16} \text{ cm}^{-3}$, the charge density decay is fast (relative to longer delay time regions) and consistent between all excitation density plots. The charge densities at three different excitation densities

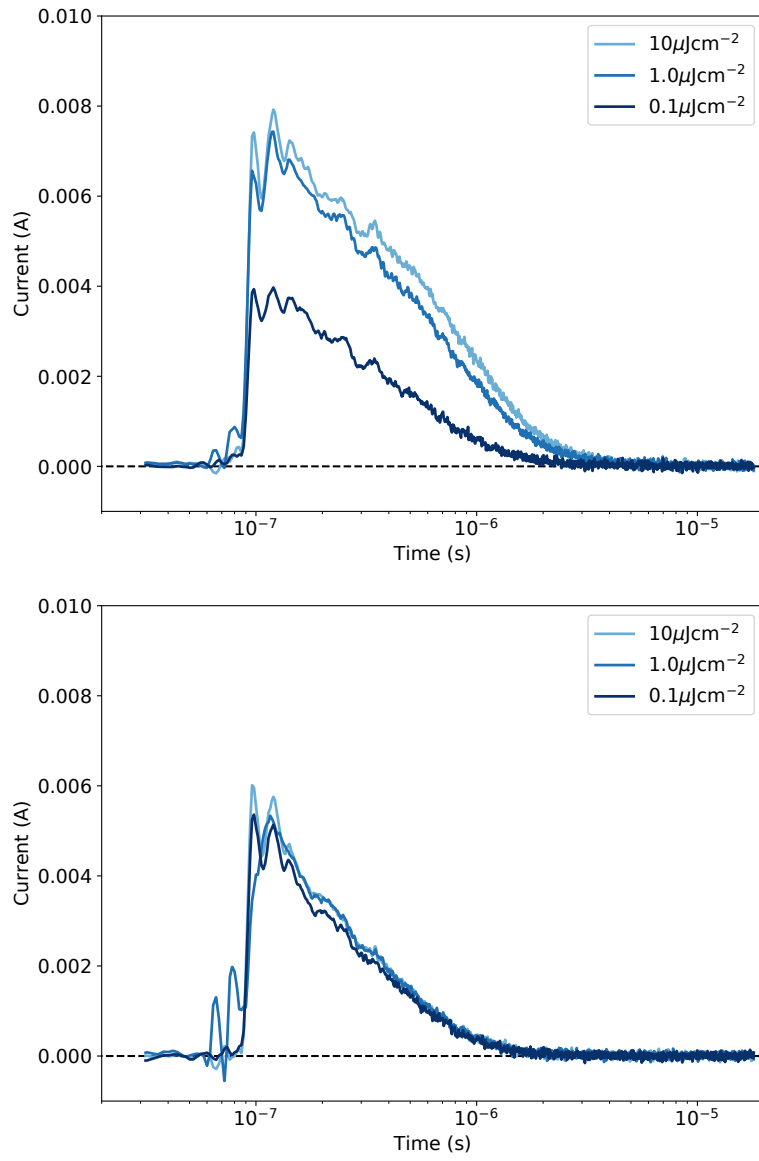


Figure 4.6: Charge extraction transients for a PCDTBT:PCBM device at 100 ns (top) and 100 μ s (bottom) excitation-extraction delay times, for a range of excitation densities (as labelled).

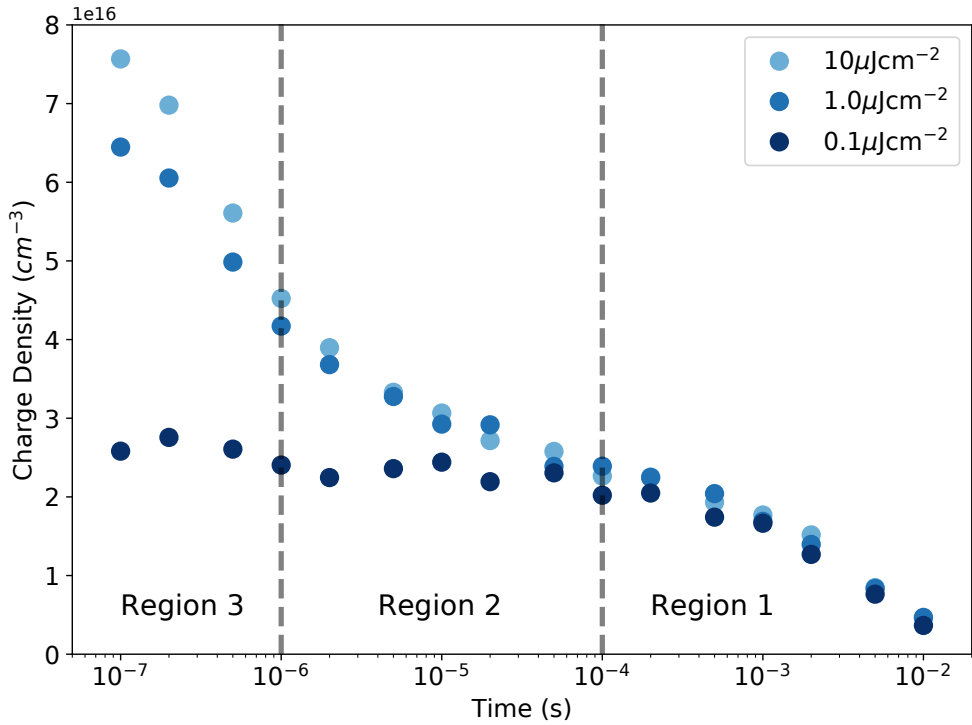


Figure 4.7: Extracted charge density as a function of delay time at multiple excitation densities (as labelled) for a PCDTBT:PCBM device. Three distinct regions of behaviour are illustrated (broken line, labelled) to aid understanding.

are similar, and exhibit similar charge density decay. The excitation density independent charge density could indicate a fixed concentration of trapped charge surviving recombination, localised into long-lived trap states. These similar decays are attributed to leakage of charge through the external resistor as will be explained in more detail later in this chapter.

Region 2: In the delay time region between 1 and 100 μ s, corresponding to charge densities between 4.2×10^{16} and 2.3×10^{16} cm^{-3} , a relatively stable charge density decay is observed within each excitation density plot. Both the absolute charge density and the decay in time is comparable between both 1 and 10 $\mu\text{J cm}^{-2}$ plots, while the 0.1 $\mu\text{J cm}^{-2}$ plot exhibits a lower relative charge density at shorter delay times, and does not exhibit any significant decay. The comparable results observed for both high excitation density plots within this region may be explained by charge carrier lifetimes long enough at these intermediate delay times (due to a reduced charge density), such that recombination losses during charge extraction may not be so significant. Further investigation to verify this explanation will be performed in the following chapter, through the application of an applied bias to aid in charge extraction measurement over the entire measured time domain (Chapter 5).

Region 3: In the delay time region shorter than 1 μ s, corresponding to charge densities above 4.2×10^{16} cm^{-3} , even the 1 and 10 $\mu\text{J cm}^{-2}$ excitation density plots exhibit different relative charge

density and decay, with a strong dependence on excitation density observed. The initial sharp charge density decays are explained by a recombination lifetime shorter than the charge extraction time, indicating extraction losses during charge extraction measurement, especially at the higher excitation densities. This observation will be further investigated in the following chapter, through the application of a reverse bias during extraction in this high charge density region (Chapter 5).

The above three regions observed in charge extraction measurements will be consistently used to explain the observed recombination characteristics of the studied samples, with Region 2 most closely representing the recombination behaviour obtained from steady state measurements and thus assumed to be the most accurate representation of recombination behaviour.

4.4.2 Recombination Kinetics and Trap State Density Distribution

Empirical Reaction Order

Using the data presented in Figure 4.7, the empirical reaction order δ as a function of charge density is plotted in Figure 4.8 by calculating the power law slope α of the charge density versus time (Equations 2.7 and 2.8). The plots in Figure 4.8 for empirical reaction order as a function of charge density exhibit three distinct regions of behaviour:

Region 1: In the charge density region below $2.3 \times 10^{16} \text{ cm}^{-3}$, a sharp reduction in calculated reaction order with decreasing charge density is observed, from 10.8 at $2.3 \times 10^{16} \text{ cm}^{-3}$ to as low as 2.8 at $1.3 \times 10^{16} \text{ cm}^{-3}$, and is consistent between all excitation density plots. This sharp apparent fall in reaction order is not indicative of sudden shift to trap free recombination, but rather is due to an artefact of the time resolved charge extraction measurement circuit. The reduction in charge density on the millisecond timescale is predominately due to leakage of charge through the switch's high internal impedance (R_{SW}), and only significantly influences measurements on a timescale comparable to the RC response time of the closed switch circuit (open circuit condition, during delay time), in this case 5.1 ms. This effect has previously been observed in similar measurement circuits, where the measured lifetime was observed to plateau at low charge densities, consistent with an upper lifetime limit imposed by the RC discharge time of the device through the smaller of either its own shunt resistance ($3.7 \times 10^5 \Omega$) or the resistance used to hold the device at open-circuit ($2.2 \text{ M}\Omega$).³⁶ Therefore the recombination kinetics measured in this region are not reliable. As the influence of this leakage current is dependent on both device capacitance and switch high impedance, increasing either parameter should improve charge extraction measurements. It is noted that there is a practical upper limit on the resistance value used in the switch. The main purpose of the resistance is to protect the switch from high internal voltages, where values above a few $\text{M}\Omega$ would quite likely destroy the switch under the typical mA currents measured through the circuit.

Region 2: In the charge density region between 4.2×10^{16} and $2.3 \times 10^{16} \text{ cm}^{-3}$, a steady increase in calculated reaction order is observed, from 6.0 at $4.2 \times 10^{16} \text{ cm}^{-3}$ to 10.8 at $2.3 \times 10^{16} \text{ cm}^{-3}$, and is comparable between both 1 and $10 \mu\text{J cm}^{-2}$ excitation density plots. This behaviour is relatively consistent between the 1 and $10 \mu\text{J cm}^{-2}$ excitation density plots, both showing comparable charge density and decay, and an apparent reduction in reaction order with increasing charge density. This region should not be influenced by switch leakage as in Region 1. Also, the recombination lifetime has decayed sufficiently such that it is longer than the charge extraction time. Therefore charge extraction limitations should not be so severe as in Region 3.

The observed strong charge density dependence of reaction order is attributed to factors other than solely the concentration dependence of the reaction rate. As the charge density decay measured using time resolved charge extraction is derived from recombination during a delay time, increasing delay times will also result in an increase in trap state occupancy over time (relaxation of charge carriers into the trap state density distribution), with a corresponding reduction in the fraction of total charge density corresponding to free charge carriers, relative to those residing in trap states. This is expected to be significant for systems with short free carrier lifetimes (PCDTBT:PCBM), where only those charge carriers within trap states remain to be extracted at increasingly long delay times (due to a relative extension of lifetime for trap states). The observed high reaction orders, significantly greater than a value of 2 which would indicate pure free carrier recombination, suggests a population of charge carriers residing predominately in trap states of varying energetic depth, while free carriers represent only a small fraction of the total charge density. The above explanation is also consistent with the observed strong charge density dependence of reaction order.

Region 3: In the charge density region above $4.2 \times 10^{16} \text{ cm}^{-3}$, the calculated reaction order peaks at 6.0 and 5.2 for the 1 and $10 \mu\text{J cm}^{-2}$ excitation density plots respectively. As discussed in the previous section, when recombination kinetics are fast enough (short delay times, high excitation densities) such that charge recombination is in competition with charge extraction, the measured charge density represents an underestimation of actual charge density, due to significant recombination losses during extraction. These extraction limitations can be observed in Region 3, where rather than the dependence of reaction order on charge density continuing the trajectory apparent in Region 2 (towards a higher initial free charge carrier fraction of total charge density), a plateau in reaction order is observed. In the absence of significant trap state occupancy or recombination losses during extraction, empirical reaction orders approaching 2 would be expected within this shorter delay time, increasingly high charge density region.

Differences Between Transient and Steady-State Derived Reaction Orders

The calculated empirical reaction orders derived from transient measurements presented above, ranging from 5.2 to 10.8 (Regions 2 and 3), are significantly higher than the value of 2.09 calcu-

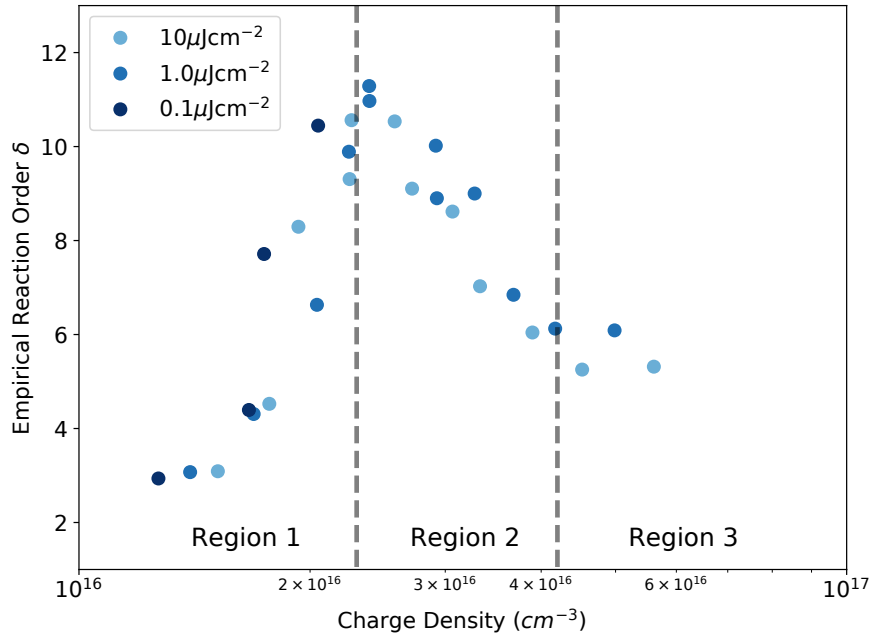


Figure 4.8: Empirical reaction order as a function charge density, at multiple excitation densities (labelled) for a PCDTBT:PCBM device. Three distinct regions of behaviour are also illustrated (broken line, labelled) to aid understanding.

lated from the steady-state measurements presented in the previous section. Empirical reaction orders higher than 5 have been reported in transient charge extraction measurements, attributed to significant trap state occupancy influencing recombination processes.³⁴ The magnitude of difference between steady-state and transient charge extraction derived reaction orders may indicate a fundamental difference between measurements, particularly evident for this material system.

As explained in the above section, using charge density decay results derived through a delay time introduces a major difference between transient and steady-state measurements for the calculation of reaction order. The charge density under observation may have a significantly different trap state occupancy, and as such a different fraction of total charge density corresponding to free charge carriers. Transient measurements may consistently probe charge carrier populations which exhibit a greater influence of trap states on recombination kinetics, and therefore consistently exhibit higher calculated reaction orders than steady-state measurements. The degree of this influence is also expected to be dependent on the specific trap state density distribution and inherent recombination kinetics of the device (material system and morphology) under investigation. Further measurements of devices incorporating the P3HT:PCBM material system are performed in Section 4.4.3, which features inherently different trap state density distribution and recombination kinetics, enabling verification of the above explanation for the observed difference between transient and steady-state derived reaction orders.

Charge Carrier Recombination Kinetics

Charge carrier lifetime τ and bimolecular recombination coefficient β are calculated from the charge density decay (Figure 4.8) as a function of charge density, using Equations 2.9 and 2.10. These plots displayed in Figure 4.9 for charge carrier lifetime and bimolecular recombination coefficient as a function of charge density exhibit three distinct regions of behaviour:

Region 1: In the charge density region below $2.3 \times 10^{16} \text{ cm}^{-3}$, a sharp shift in the dependence of lifetime on charge density is observed, tending to a single lifetime of 6.5 ms, and is consistent between all excitation density plots. This lifetime is in close agreement with the RC response time of 5.1 ms calculated from the switch high impedance of $2.2 \text{ M}\Omega$ and device capacitance. This strongly supports the previous attribution of altered kinetics in Region 1 to that of charge carrier loss due to switch leakage current.

Region 2: In the charge density region between 4.2×10^{16} and $2.3 \times 10^{16} \text{ cm}^{-3}$, a constant dependence of either lifetime or bimolecular recombination coefficient on charge density is observed, with strong agreement between both 1 and $10 \mu\text{J cm}^{-2}$ excitation density plots. Although higher excitation densities were observed to yield a greater initial charge density (Figure 4.7), no difference is observed in either charge carrier lifetime or bimolecular recombination coefficient between excitation densities plots over the measured charge density range. This indicates that the recombination kinetics measured using time resolved charge extraction are independent of excitation density. The excitation density does however determine the maximum observable charge density, and therefore shortest measurable lifetime.

Region 3: In the charge density region above $4.2 \times 10^{16} \text{ cm}^{-3}$, both 1 and $10 \mu\text{J cm}^{-2}$ plots exhibit a significant shift in the dependence of lifetime/recombination coefficient on charge density. The lifetimes within this region are shorter than $5 \mu\text{s}$, which are increasingly comparable to the time required to extract charge carriers (Figure 4.4). These observations support the conclusion that Region 3 is significantly influenced by extraction limitations, with recombination losses during extraction measurement leading to an underestimation of both charge carrier lifetime and bimolecular recombination coefficient. Modelling based on a simple power law regression to the $10 \mu\text{J cm}^{-2}$ excitation density plot over Region 2, yields values for the expected lifetime and recombination coefficients at a charge density of $7.0 \times 10^{16} \text{ cm}^3$ of 210 ns and $6.8 \times 10^{-11} \text{ cm}^3 \text{ s}^{-1}$ respectively. This provides an approximation of the underestimation of charge density as measured using charge extraction, under conditions where extraction limitations are significant (lifetime comparable to extraction time). In this case, the fastest measured lifetime is underestimated by over 5 times that of the estimated value, with an equivalent underestimation of charge density close to the measurement response limit.

The calculated lifetimes for each excitation density show a strong dependence on charge density, with charge carrier lifetimes spanning four orders of magnitude within the charge density range of

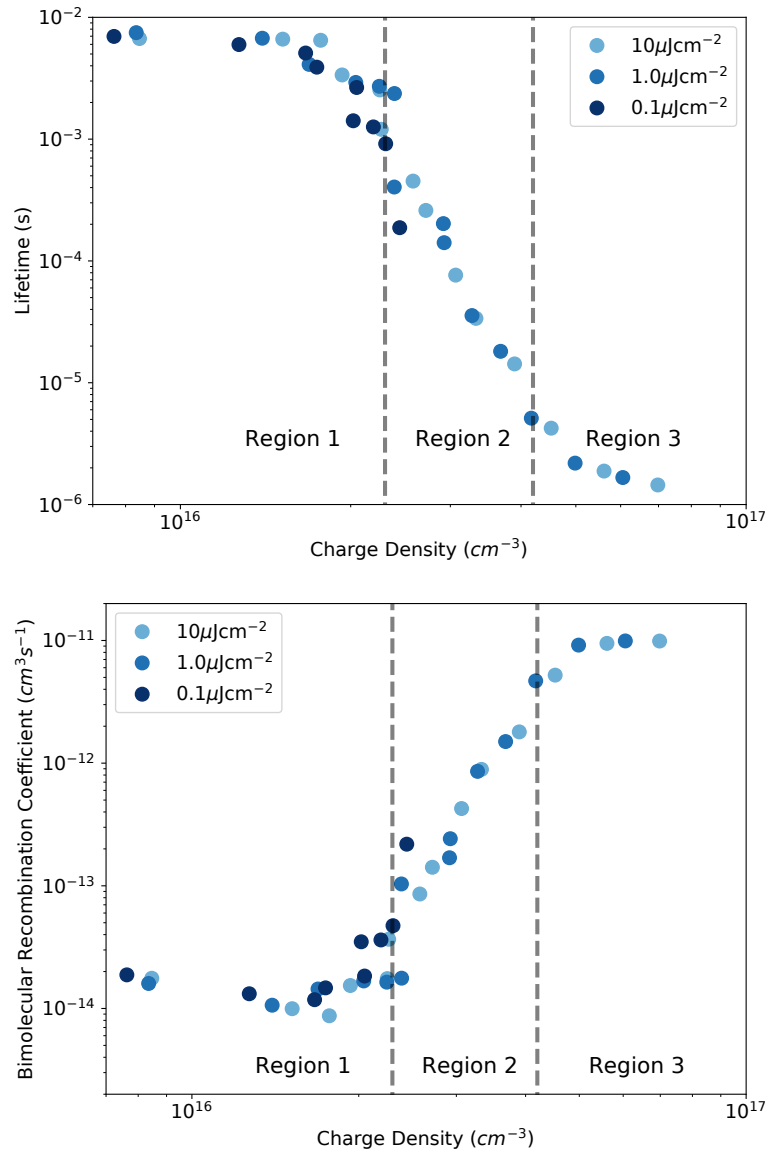


Figure 4.9: Charge carrier lifetime (top) and bimolecular recombination coefficient (bottom) as a function of charge density for a PCDTBT:PCBM device at a range of excitation densities (as labelled). Three distinct regions of behaviour are illustrated (broken line, labelled) to aid understanding.

1.4×10^{16} to $7.0 \times 10^{16} \text{ cm}^{-3}$, and a shortest lifetime of $1.4 \mu\text{s}$. Similarly, the calculated bimolecular recombination coefficient β spans from 10^{-14} to $10^{-11} \text{ cm}^3 \text{ s}^{-1}$. These values for β compare well with previously reported charge extraction based measurements of the PCDTBT:PCBM system, on the order of $10^{11} \text{ cm}^3 \text{ s}^{-1}$ at a comparably high charge density.¹³⁵ Further, β obtained through transient absorption measurements of a similar PCDTBT:PCBM system showed a value of $1.7 \times 10^{-12} \text{ cm}^3 \text{ s}^{-1}$ at a charge density of $5.0 \times 10^{15} \text{ cm}^{-3}$.¹⁰¹ The presented charge extraction results indicate that a comparable β is obtained at a charge density of $3.2 \times 10^{16} \text{ cm}^{-3}$, with the discrepancy in charge density possibly due to differences in calculation between transient absorption and charge extraction measurements. Additionally, those devices used in the transient absorption study exhibited a significantly lower V_{OC} and FF , which may further contribute to the observed difference in β . Overall however, the consistent power law of Region 2 observed at all excitation densities, is indicative of a constant reaction order and implies that the recombination kinetics of this device are reliably measured over a wide range of charge densities, with calculated values for τ and β consistent with those found in literature for comparable systems.

Photovoltage Decay

In order to assess the correlation of transient charge extraction and photovoltage decay measurements for determining trap state density distribution, a comparison of transient derived ideality factor and reaction order to those obtained using steady-state measurements is performed. Firstly, photovoltage decay measurements are performed on the PCDTBT:PCBM device using the same range of excitation densities as in the charge extraction measurements, and are displayed in Figure 4.10. This provides device photovoltage decay over the same time domain as charge extraction decay results, enabling correlation in time to yield the dependence of photovoltage on charge density. The photovoltage decay transients in Figure 4.10 exhibit three distinct regions of behaviour, aligning closely in time to that exhibited in charge density decay plots (Figure 4.7):

Region 1: In the region beyond $200 \mu\text{s}$, the photovoltage decays rapidly (relative to shorter delay times) for all three transients. This is due to leakage of charge density, through the circuit high impedance used to maintain open-circuit condition (in this case $1.0 \text{ M}\Omega$ with a response time of 2.3 ms). At a photovoltage of 600 mV , the leakage current over the high impedance is $0.6 \mu\text{A}$, which corresponds to $6 \times 10^{-10} \text{ C}$ integrated over a millisecond, or a charge density of $7.3 \times 10^{15} \text{ cm}^{-3}$ lost per millisecond, however decaying as the photovoltage decreases. As the measured extracted charge density on this timescale was on the order of $2.5 \times 10^{16} \text{ cm}^{-3}$, this leakage current represents a significant portion of the remaining internal charge density. This is similar to the switch leakage current observed at long delay times in time resolved charge extraction measurements, although exhibits a faster decay time due to the smaller impedance ($1.0 \text{ vs } 2.2 \text{ M}\Omega$). This region is therefore indicative of photocurrent decay over a $1.0 \text{ M}\Omega$ resistor and not charge recombination kinetics, which is expected to be slower than the observed photovoltage decay (the internal recombination resistance is higher than external one). This is the first time that the influence of the external

resistance during the delay time in charge extraction measurements has been specifically clarified to date, with the observable influence indicating that consideration should be made regarding the practical interpretation of these measurement results.

Region 2: Within the region from 2 to 200 μ s, both 10 and 1 μ J cm $^{-2}$ excitation density transients exhibit comparable photovoltage, and an exponential decay in photovoltage due to a reduction in charge density (through non-geminate recombination), thereby reducing the density of states occupancy and consequently the measured photovoltage. The 0.1 μ J cm $^{-2}$ transient does not exhibit a comparable photovoltage or decay transient to that of the high excitation densities, and will be addressed in the next section.

Region 3: In the region prior to 2 μ s, both 10 and 1 μ J cm $^{-2}$ transients display no decay in photovoltage, and exhibit an initial photovoltage of 890 mV which compares well with the open circuit voltage of 900 mV measured at steady-state. The 0.1 μ J cm $^{-2}$ transient however exhibits a lower initial photovoltage of 440 mV, which rises to 610 mV by 2 μ s, with a peak observed at 10 μ s (Region 2) of 640 mV. The initial photovoltage exhibits a dependence on excitation density, with a 98 % increase in initial photovoltage from 0.1 to 1 μ J cm $^{-2}$, however only a minor 2 % further increase at 10 μ J cm $^{-2}$. This dependence of photovoltage on excitation density is related to the occupancy of the density of states distribution, as well as recombination of charge density within the measurement response at sufficiently high excitation densities (high initial charge density, short lifetime). The increasing charge density produced at higher excitation densities increases the splitting of respective charge carrier Fermi levels, resulting in an increased potential difference across the device contacts. Eventually the photovoltage will saturate, with a logarithmic increase in charge density required to linearly increase photovoltage (the number of available states greatly exceeds the charge density, dependent on the shape of the density of states distribution), and eventually recombination of free carriers begins to dominate charge photogeneration within the rise time of the transient measurement, and thereby limit charge density (dependent on recombination kinetics). As the internal charge density only saturates due to the domination of free carrier recombination, the photovoltage and charge density measurements saturate at different rates with increasing excitation density. This can be observed where the charge extraction measurements exhibits a lesser saturation of initial charge density relative to photovoltage saturation at identical excitation densities (compare Figures 4.7 and 4.10).

Spatial Redistribution of Charge Carriers

The time-resolution of these transient photovoltage measurements is determined by the measurement circuit response time of 165 ns (calculated in the previous section). Since any charge extraction to the external circuit is insignificant in these measurements (unlike charge extraction), the measured photovoltage as a function of time represents the difference in potential between the two device contacts, which is in turn determined by electron and hole density and energy levels

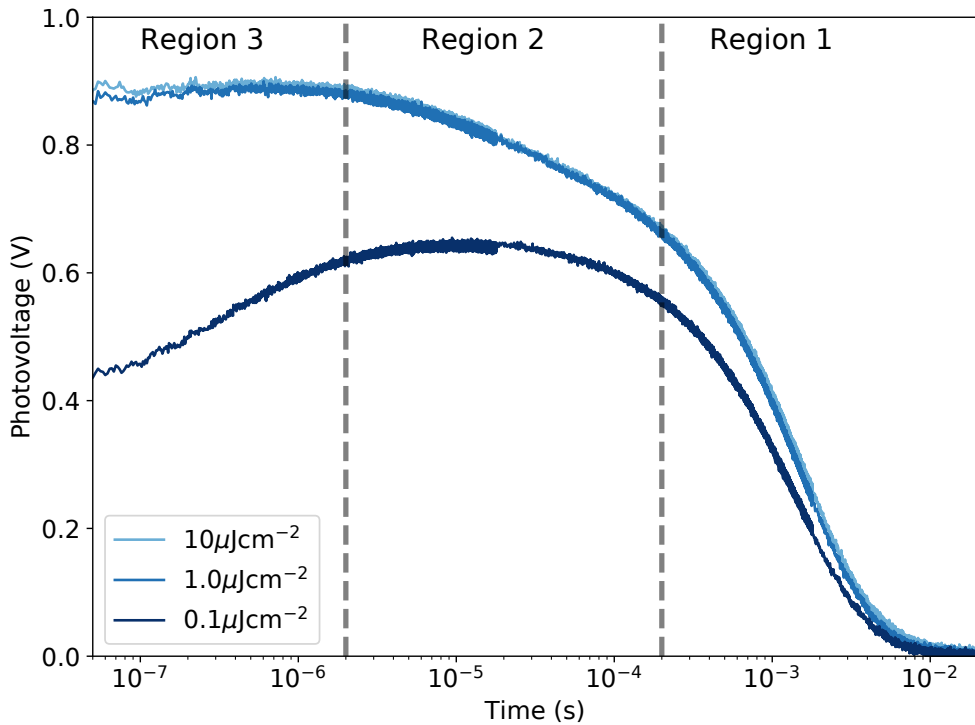


Figure 4.10: Photovoltage decay transients (decay in open-circuit voltage after stopping photoexcitation) at multiple excitation densities for a PCDTBT:PCBM device. Three distinct regions of behaviour are illustrated (broken line, labelled) to aid understanding.

at the contacts. The observed photovoltage rise in the $0.1 \mu\text{J cm}^{-2}$ excitation density transient of Figure 4.10 is therefore related to the rise of charge density at either or both contacts. Surface photogeneration caused by a low excitation density, non-uniformly absorbed laser pulse can result in a charge carrier population with an initially higher electron and hole density at the illumination side of the device. In such surface generation conditions, the spatial redistribution of charge may also occur during transient measurements, which will influence the measured photovoltage. The observed rise in photovoltage is therefore attributed to changes in charge density at the contacts, caused by a microsecond timescale redistribution of charge carriers within the device. Spatial redistribution of charge carriers across the device active layer (e.g. charge diffusion driven by a concentration gradient) will result in a more spatially uniform charge density throughout the active layer and at the contacts. Therefore an increase in Fermi level splitting will occur between the illuminated and back contact, yielding an increase in measured photovoltage as a function of time. The photovoltage at $10 \mu\text{s}$ for the $0.1 \mu\text{J cm}^{-2}$ transient (peak) of 460 mV does not reach that measured for the higher excitation densities of 830 mV due to a lower initial charge density, and the possible influence of spatially variable recombination kinetics (charge density dependent). Sufficiently high excitation densities should ensure spatially more uniform charge density distribution within the measurement response (prior to 100 ns delay time), and therefore photovoltage decay transients should exhibit less or no rise, as is observed of both 1 and $10 \mu\text{J cm}^{-2}$ transients. This

will however depend on the device and material system used, influencing the charge generation profile (degree of initial spatial uniformity), charge transport (rate of transient rise, dependent on mobility), and the shape of the density of trap states distribution (which governs the dependence of photovoltage on charge density).

Photovoltage decay is a relatively fast measurement of surface potentials, while charge extraction is a slower integrated measurement of bulk charge density. As spatial redistribution of charge carriers during transient measurements can influence the measured photovoltage, as well as recombination kinetics across the device active layer, this will impact subsequent correlation of charge density and photovoltage decay results, and therefore the determination of the trap state density distribution.

Transient Measurement of Trap State Density Distribution

The dependence of photovoltage on charge density is obtained for a range of excitation densities using the photovoltage decay and charge density decay results presented above (Figures 4.8 and 4.10). The slope m (Equation 2.11) as a function of charge density is used to calculate the characteristic exponential of the trap state density distribution tail E_{ch} (Equation 2.12). The resulting plots are displayed in Figure 4.11.

All excitation density plots at charge densities below $2.4 \times 10^{16} \text{ cm}^{-3}$ exhibit an initial strong dependence of photovoltage on charge density (with m of 28), which reduces with decreased charge density (to m as low as 10). Due to the mismatch of high impedance used to maintain open circuit between time resolved charge extraction ($2.2 \text{ M}\Omega$) and photovoltage decay ($1.0 \text{ M}\Omega$) measurements, the current leakage response times are different. This deviation between measurements yields a region of increasingly inaccurate results, and is therefore not representative of the trap state density distribution. Additionally, the $0.1 \mu\text{J cm}^{-2}$ plot is not comparable to either higher excitation density plots beyond charge densities of $2.4 \times 10^{16} \text{ cm}^{-3}$. This is due to a combination of insufficient initial photogenerated charge density, and the influence of charge carrier spatial redistribution as discussed in the previous section. A high excitation density (high initial charge density) is therefore required to measure trap state density distribution using this transient measurement approach.

In the high charge density region above $4.2 \times 10^{16} \text{ cm}^{-3}$, a plateau in photovoltage is observed for increasing charge density, with a peak photovoltage of 890 mV and is consistent between both 1 and $10 \mu\text{J cm}^{-2}$ excitation density plots. This plateau may indicate a large density of available states at sufficiently high charge density, such that increasing charge density does not raise the charge carrier Fermi level and therefore does not further increase the photovoltage. The slope of this region approaches zero as photovoltage is independent of trap state occupancy, and therefore does not provide a meaningful measure of E_{ch} . Fast recombination (within the measurement response) at sufficiently high charge densities will also begin to dominate measurements, leading to a limit in both charge density and photovoltage. Also, as the two transient measurements techniques have

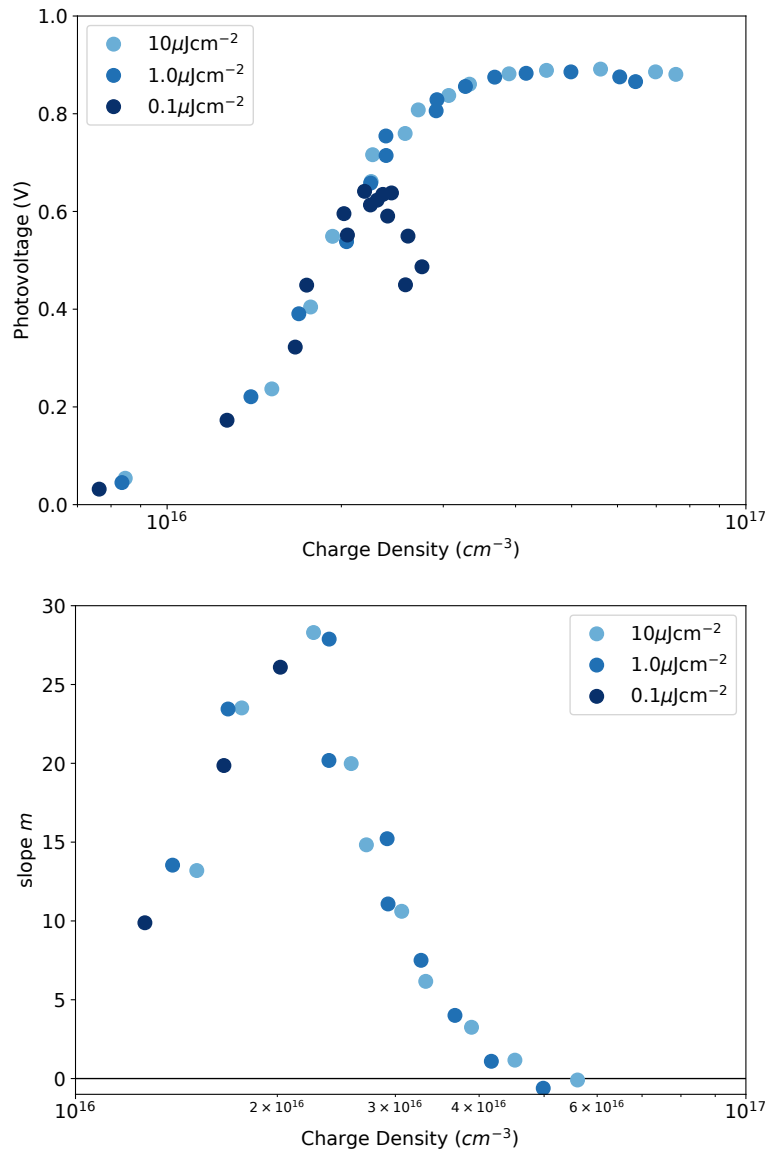


Figure 4.11: The dependence of photovoltage on charge density (top), and corresponding slope m (bottom) at multiple excitation densities for a PCDTBT:PCBM device.

different effective measurement response times (the fast response of a surface potential compared to the slower charge extraction process), the basic assumption of correlating these results in time will no longer be valid at increasingly high charge densities (shorter lifetimes), and increasing recombination losses during charge extraction result in an underestimation of charge density.

At charge densities between 4.2×10^{16} and $2.4 \times 10^{16} \text{ cm}^{-3}$, the photovoltage decreases as a function of charge density (from 890 to 700 mV) with calculated values of m ranging from 1.7 to 28 and is consistent between both 1 and $10 \mu\text{J cm}^{-2}$ excitation density plots. This region corresponds to measurement within a broad distribution of energetic trap states, such that progressively increasing the charge density results in the increasing occupancy of progressively higher energetic states, thereby increasing the charge carrier Fermi level. This in turn produces an increase in the measured photovoltage, with m proportional to the characteristic exponential of trap state density distribution E_{ch} . Using Equation 2.12 and the calculated m yields values for E_{ch} ranging from 24 meV to over 350 meV. The wide range of calculated E_{ch} is likely due to a narrow trap state density distribution (low degree of trapping) within this device, that is not exponential in shape and therefore will not provide a consistent m as a function of charge density. Typical values for E_{ch} on the order of 40 to 100 meV in similar material systems are significantly lower than the values calculated above (average of 200 meV, with significant variation over the charge density range). This measurement approach therefore may not be appropriate for obtaining E_{ch} in this device or material system. This conclusion will be further investigated in following section, using a material system with greater degree of trap state occupancy.

Ideality Factor and Comparison Between Transient and Steady-State

In order to further test the above methodology for determining trap state density distribution, ideality factor and reaction order are calculated using the presented transient correlation of charge density and photovoltage (Figure 4.11), with a comparison to those values obtained using steady-state measurement presented at the start of this chapter (Section 4.4.1). The dependence of photovoltage on charge carrier lifetime is also obtained for a range of excitation densities, using the photovoltage decay and lifetime as a function of charge density results presented above (Figures 4.9 and 4.10), with corresponding slope v (Equation 2.13) as a function of lifetime also calculated. The resulting plots are displayed in Figure 4.12, including the three observed regions of behaviour from Figure 4.9.

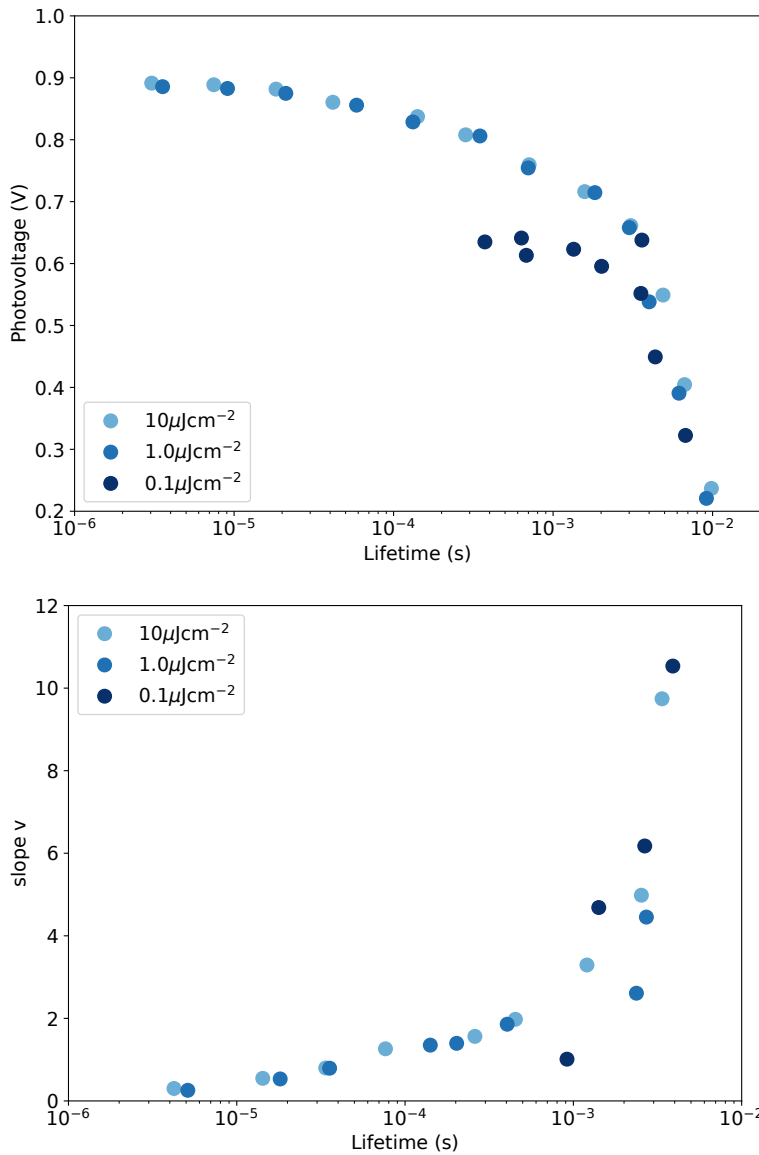


Figure 4.12: Photovoltage as a function of charge carrier lifetime (left) and corresponding slope v (right) for a PCDTBT:PCBM device at multiple excitation densities.

Both 1 and $10 \mu\text{J cm}^{-2}$ excitation density plots exhibit comparable dependence of photovoltage on lifetime, with calculated v ranging from 0.3 at $5 \mu\text{s}$ up to 2.0 at $450 \mu\text{s}$. The $0.1 \mu\text{J cm}^{-2}$ plot exhibits a deviation from the higher excitation density plots due to the lower initial charge density, as well as the influence of spatial redistribution as explained previously. All excitation density plots exhibit a sharp decline in photovoltage at charge carrier lifetimes on the millisecond timescale, due to leakage current influencing the measurement of both lifetime (charge density) and photovoltage, as explained previously.

Using the calculated dependence of photovoltage on both charge density and lifetime, values of v and m at a given photovoltage can be used to calculate the ideality factor n_{id} and empirical reaction order δ , using Equations 2.15 and 2.14. Due to the large variation in calculated m and v

as a function of photovoltage or charge density, a corresponding large range of reaction order and ideality factor are obtained. As discussed at the start of Section 4.4.2, using charge density decay results derived through a delay time can introduce an additional time dependence of trap state occupancy that is coupled with the measurement of charge density. The increased fraction of charge density corresponding to trap states at low charge densities (long delay times) may account for the observed dependence of either m or v on charge density. Again, the degree of this influence is also expected to be dependent on the specific trap state density distribution and inherent recombination kinetics of the device (material system and morphology) under investigation.

Based on the above explanation for the charge density dependence of measured trap state density distribution, the most accurate measure of trap state density distribution is likely in the higher charge density region, corresponding to shorter delay times (less influence on trap state occupancy), while also in a region where lifetime is greater than charge extraction time (recombination losses during extraction less significant). Therefore at a charge density of $3.5 \times 10^{16} \text{ cm}^{-3}$ with corresponding values for m of 4.0 (E_{ch} of 51 meV) and v of 0.7, calculation yields an ideality factor of 0.60 and reaction order of 6.6. This calculated ideality factor is half that measured at steady-state of 1.22, while the calculated reaction order is three times that measured at steady-state of 2.09. The magnitude of difference between steady-state and transient charge derived reaction order or ideality factor may again indicate a fundamental difference between measurements, particularly evident for this material system. Further measurements will be performed in the following section to support/challenge the above conclusions on a device incorporating the P3HT:PCBM material system, which exhibits greater trapping than the presented PCDTBT:PCBM device and should therefore yield transient derived ideality factor and reaction order more comparable to those obtained at steady-state.

4.4.3 Excitation Pulse Length

The primary objective of this section is to determine the influence of variation in trap state occupancy on the measurement of charge density, recombination kinetics, and trap state density distribution in time resolved charge extraction. This is performed through the variation of excitation laser pulse length, used to influence the initial trap state occupancy prior to charge extraction measurement. Additionally, these measurements are used to further assess the observed difference between steady-state and transient derived reaction order, using a device with different inherent recombination kinetics and trap state density distribution (the P3HT:PCBM material system) to that of the PCDTBT:PCBM device presented in the previous sections.

Steady-State Device Performance

Photovoltaic devices were fabricated incorporating the P3HT:PCBM (5:4) donor-acceptor system, with an active layer thickness of 170 nm. Current-voltage measurements were performed to assess steady-state device performance under a range of illumination intensities, including a

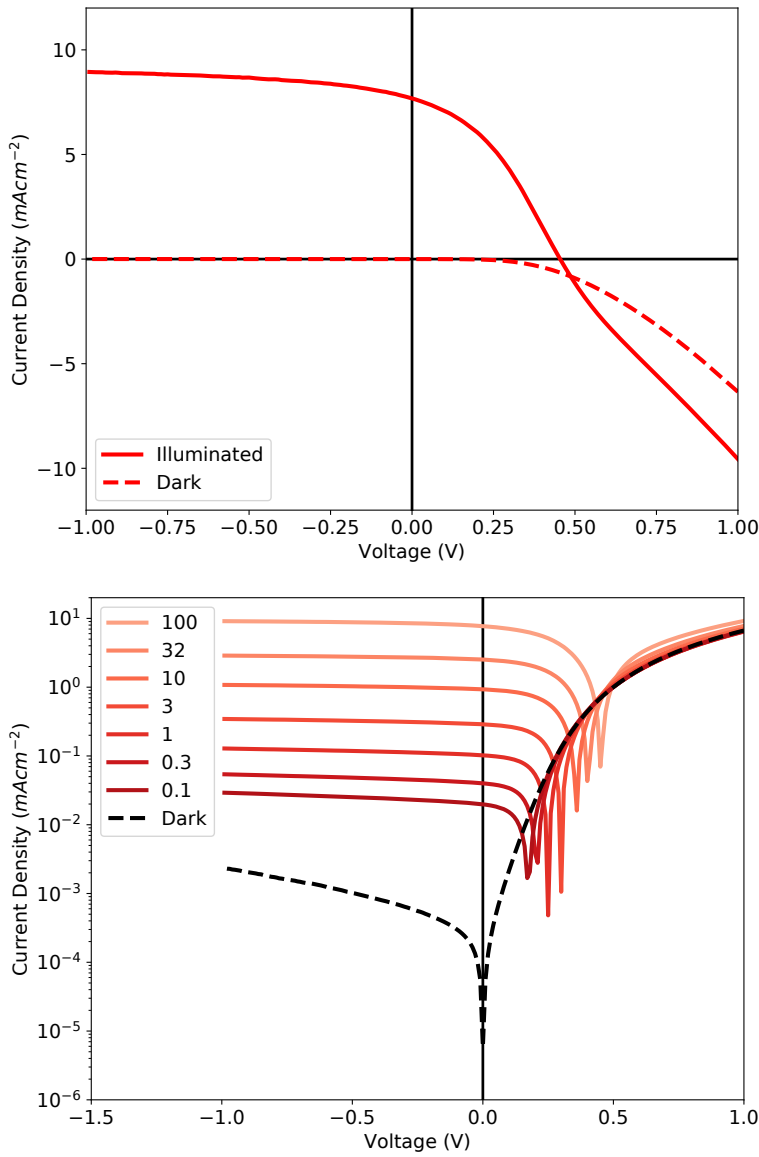


Figure 4.13: Current density versus voltage measurement response for a P3HT:PCBM device using a 100 mW cm^{-2} illumination intensity (top), with log-scaled plots (bottom) at illumination intensities ranging from 100 to 0.1 mW cm^{-2} (solid lines) as labelled. The dark response (no illumination) is also included (broken line) for each plot.

Table 4.2: Summary of device parameters and steady state performance (current-voltage results displayed in Figure 4.13), open-circuit voltage V_{OC} , short-circuit current J_{SC} , fill factor FF , solar conversion efficiency η , device area A , device thickness d , series resistance R_S , and shunt resistance R_{Sh} .

	V_{OC} (mV)	J_{SC} (mA cm $^{-2}$)	FF	η (%)	A (cm $^{-2}$)	d (nm)	R_S (Ωcm^{-2})	R_{Sh} (Ωcm^{-2})
P3HT:PCBM	460	7.68	0.37	1.32	0.06	150	60	5.6×10^5

discussion of device trap state density and occupancy. Figure 4.13 displays the current-voltage response of a single P3HT:PCBM device using a 100 mW cm^{-2} illumination intensity (top), with log-scaled plots (bottom) at illumination intensities ranging from 100 to 0.1 mW cm^{-2} (solid lines) as labelled. The dark response (no illumination) is also included (broken line) for each plot. The key device performance parameters calculated from these results (100 mW cm^{-2}) are summarised in Table 4.2. At 100 mW cm^{-2} illumination intensity, this device exhibits an open-circuit potential of 460 mV, a short-circuit current density of 7.7 mA cm^{-2} , a fill factor of 0.37, and solar conversion efficiency of 1.32 %. A high shunt resistance of $5.6 \times 10^5 \Omega \text{ cm}^{-2}$ is calculated, with a low injection current under high reverse bias, indicating good diode behaviour and blocking contacts. Steady-state current-voltage measurements were repeated after performing transient charge extraction measurements (5 days post initial measurement) for the displayed P3HT:PCBM device, and exhibited less than a 3 % reduction in open-circuit voltage, short-circuit current, and fill factor, indicating that the device was not significantly degraded during the various measurements.

The current-voltage measurements performed at illumination intensities from 100 to 0.1 mW cm^{-2} were used to obtain the dependence of short-circuit current and open-circuit voltage on illumination intensity, as displayed in Figure 4.3. The displayed plots of short-circuit current and open-circuit voltage exhibit a power law and exponential dependence respectively on illumination intensity, with regressions to each plot displayed (broken line). The diode ideality factor can be calculated using the dependence of open-circuit voltage on illumination intensity and Equation 2.5, yielding a value of 1.61. The reaction order can be calculated using the dependence of short-circuit current on illumination intensity and Equations 2.3 and 2.4, yielding a value of 2.14.

A comprehensive survey of literature reports for P3HT:PCBM based solar cells indicate an average power conversion efficiency of 3.0 %, with short-circuit current, open-circuit voltage, and fill factor on the order of 8 mA cm^{-2} , 600 mV, and 0.50 respectively, incorporating predominately device architectures and fabrication parameters comparable to those used in this study.³⁹ While the P3HT:PCBM device reported herein has a comparable short circuit current (charge generation/separation efficiency), the relatively high device series resistance and S-shape current-voltage response observed at high forward bias limit current extraction (Figure 4.13), primarily responsible for the devices low fill factor, limited open-circuit voltage, and corresponding low efficiency, attributed to sub-optimal device contacts. The measured ideality factor of 1.61 indicates a significant influence of trap states in the recombination process which is consistent with the calculated reaction order of 2.14, above that expected for trap free bimolecular recombination of 2.0. This device exhibits a sufficiently high shunt resistance such that this is unlikely the origin of the deviation from an ideality factor of 1.0.³⁵ The P3HT:PCBM material system is known to exhibit a broad trap state density distribution, and typically displays an ideality factor on the order of 1.25 or above.^{125,126} For the purpose of studying the influence of trap state occupancy on time resolved charge extraction measurements presented in the following sections, the high trap state occupancy of this device will not negatively influence the outcomes of these investigations. The steady-state

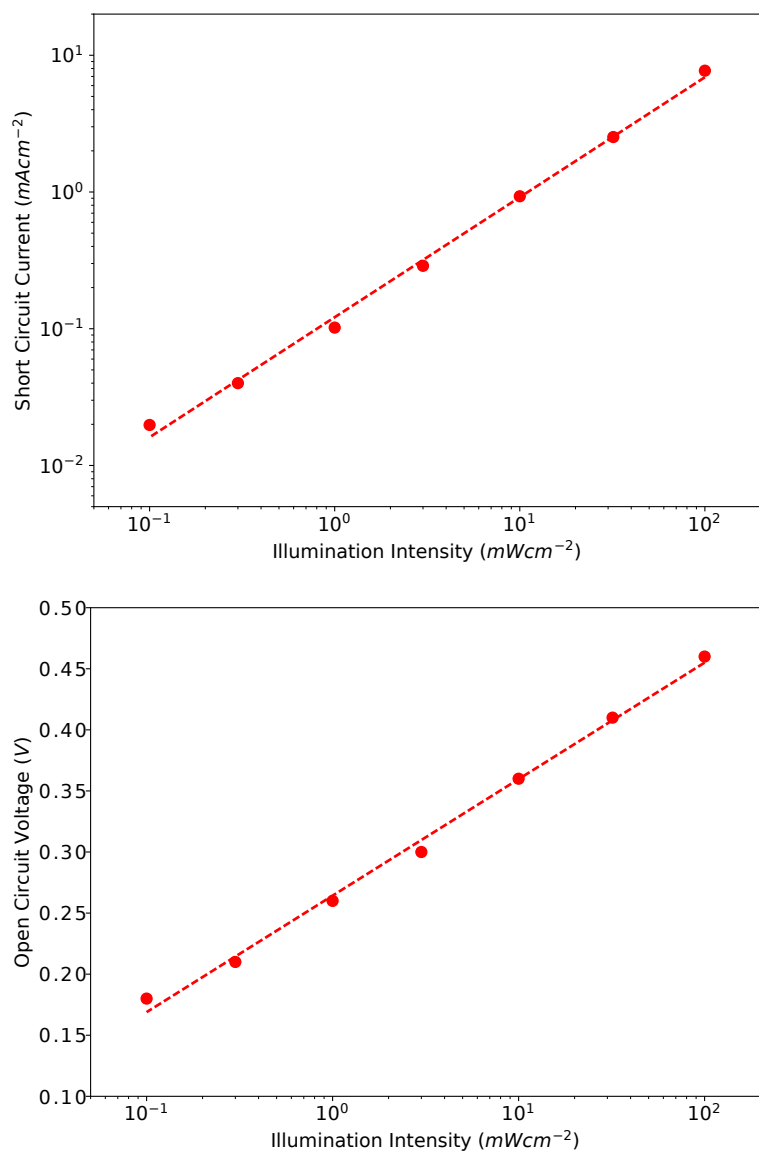


Figure 4.14: Short-circuit current density (top) and open-circuit voltage (bottom) as a function of illumination intensity for a P3HT:PCBM device, with regression to plots included (broken line).

values of ideality factor and reaction order will be used later in this section for comparison with values obtained through transient measurements as in the previous section, in order to further investigate the deviation observed between calculated transient and steady-state values for the PCDTBT:PCBM device.

The measured current density is also observed to increase under a reverse bias potential of 1 V, to 8.9 mA cm^{-2} relative to the 7.7 mA cm^{-2} measured at short-circuit, representing a 16 % increase. This indicates that not all current is efficiently extracted at short-circuit and would likely benefit from an applied bias in charge extraction measurements. This will be further investigated in Chapter 5.

Influence of Excitation Pulse Length on Charge Extraction Measurements

Time resolved charge extraction measurements were performed on the P3HT:PCBM device detailed above, using either a 'short' 6 ns or 'long' 10 ms excitation pulse length. While the short laser pulse exhibits an intensity rise/fall time of less than 3 ns, the long pulse exhibits a rise/fall time of just under 1 μs . This slower laser turn-off time limits the time resolution of the long pulse excitation method kinetics measurements to the microsecond timescale. A range of excitation densities are used, with a 641 nm excitation wavelength (imposed by the long pulse laser excitation source). It should be noted that the reported values of excitation density for both pulse length excitation methods represent the integrated laser pulse over time, however as the pulse lengths vary by orders of magnitude these values are not directly comparable (total photons vs rate of photon incidence). Rather effort has been made to illustrate and compare measurement results at comparable initial charge densities, either through variation of excitation density or delay time, enabling the analysis of relative changes in decay kinetics between the two excitation pulse lengths.

Extracted Charge Density and Lifetime

Charge density decay (top) and charge carrier lifetime as a function of charge density (bottom) plots for the P3HT:PCBM device, using either short (6 ns) or long (10 ms) excitation laser pulse length at multiple excitation densities, are displayed in Figure 4.15. The extracted charge densities obtained for this P3HT:PCBM device at a 100 ns delay time using the short excitation pulse length, of 1.3×10^{17} , 1.1×10^{17} , and $0.3 \times 10^{17} \text{ cm}^{-3}$ at 100, 10, and $1 \mu\text{J cm}^{-2}$ respectively, provide charge extraction yields (incident photons to extracted charges) of 0.2, 1.7, and 4.6 %. The charge decay plots (Figure 4.15, top) obtained using the short excitation pulse length exhibit much greater peak charge densities at short delay times than the charge decay plots obtained using the long excitation pulse length. Although the initial charge density of the $100 \mu\text{J cm}^{-2}$ short pulse plot is twice that of the $60 \mu\text{J cm}^{-2}$ long excitation pulse length plot, the charge density is comparable beyond 20 μs , with the long excitation pulse length plot even exceeding that of the short excitation pulse length plot by up to 25 % at 1 ms delay time. The observation of the long excitation pulse length plots exhibiting greater comparable charge density in the long delay time region is consistent across

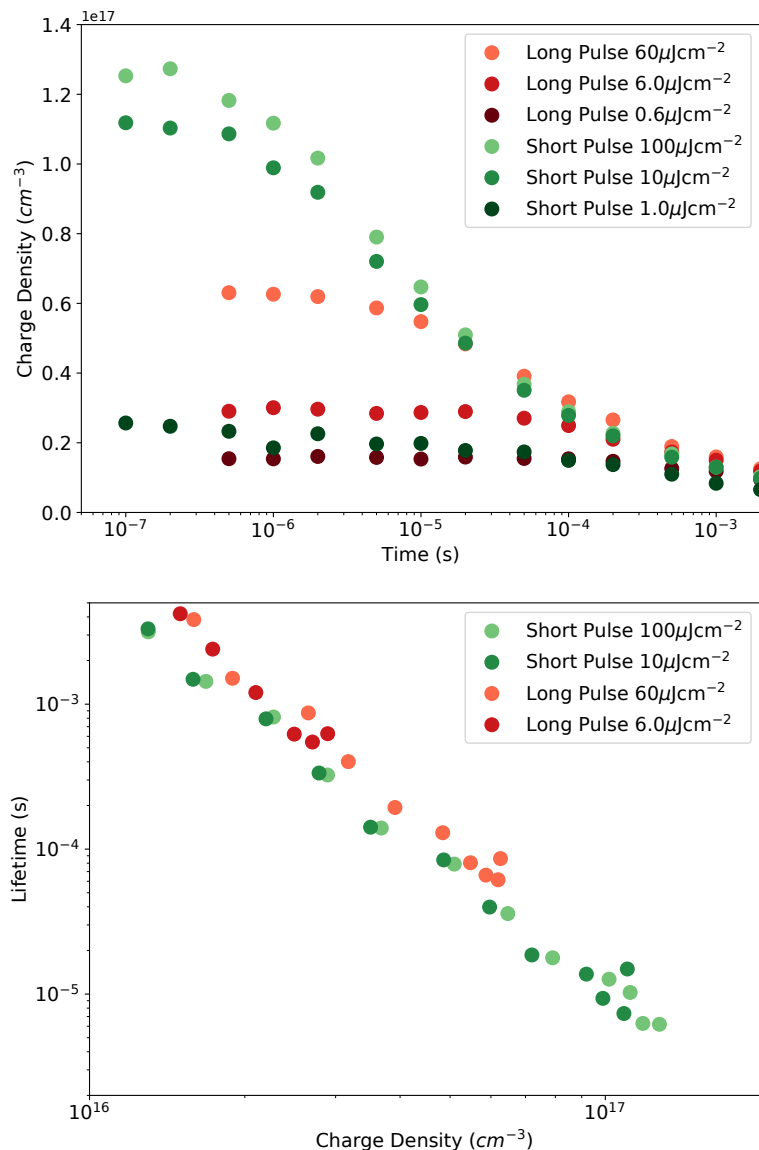


Figure 4.15: Charge density decay (top) and charge carrier lifetime as a function of charge density (bottom) for a P3HT:PCBM device using a short (6 ns) and long (10 ms) excitation laser pulse at multiple excitation densities (as labelled).

the presented excitation densities. Further to the above observation, the plot of charge carrier lifetime as a function of charge density (Figure 4.15, bottom) clearly illustrate a consistently longer lifetime for the plots obtained using a long excitation pulse length, relative to the short excitation pulse length plots for any given charge density within the measured charge density range (for example, a shift from 40 to 66 μs at $6 \times 10^{16} \text{ cm}^{-3}$). Equivalently, this can be interpreted as the measurement of a greater relative charge density for a given lifetime in the long excitation pulse length measurements, indicating a greater extraction of charges from deep within the trap state density distribution (longer relative lifetime).

Photovoltage Decay Transients

Photovoltage decay measurements were performed on the P3HT:PCBM device using short and long excitation laser pulse lengths at a range of excitation densities, displayed in Figure 4.16. The top plot displays the full decay transient, while the bottom plot is a close-up of the transient tail beyond 500 μs . The long pulse excitation method does not generate charge densities as high as the short pulse excitation method under the excitation densities presented, and consequently exhibit lower peak photovoltage. A distinct difference is however observed in transient shape between excitation pulse methods (Figure 4.16, top). The long pulse transients do not exhibit any initial decay in photovoltage prior to 5 μs , with a plateau in photovoltage for all excitation densities. The short pulse transients exhibit a transient rise at excitation densities below 100 $\mu\text{J cm}^{-2}$, attributed to charge carrier redistribution post excitation as discussed in the previous section. However, even at the lowest excitation density of 0.6 $\mu\text{J cm}^{-2}$, no initial transient rise is observed for the long pulse excitation transients, indicating that long pulse excitation produces a stable, steady-state spatial distribution of charge carriers with no redistribution during transient measurement. The 10 ms illumination time allows sufficient time for the photogenerated charge density to undergo any redistribution prior to stopping illumination.

If not for the limited response time of the long pulse excitation method used herein, it would be advantageous to use a long excitation pulse at low excitation densities, as there are no complications due to spatial redistribution of charge. However as long as a high excitation density is used with a short pulse excitation, the delay time of time resolved charge extraction can be used to obtain low charge densities, with a wider overall range of charge densities. Further investigation is presented in the following section to assess the influence of the observed differences in trap state occupancy on the determination of trap state density distribution.

Another distinct difference in observed photovoltage decay transients between short and long pulse methods is illustrated in Figure 4.16 (bottom), focusing on the transient tail beyond 500 μs . Although this region of decay is significantly influenced by leakage current across the measurement high impedance, the measurement setup is identical for these two excitation methods, and therefore this influence should be identical. The long pulse transients are observed to decay slower than the

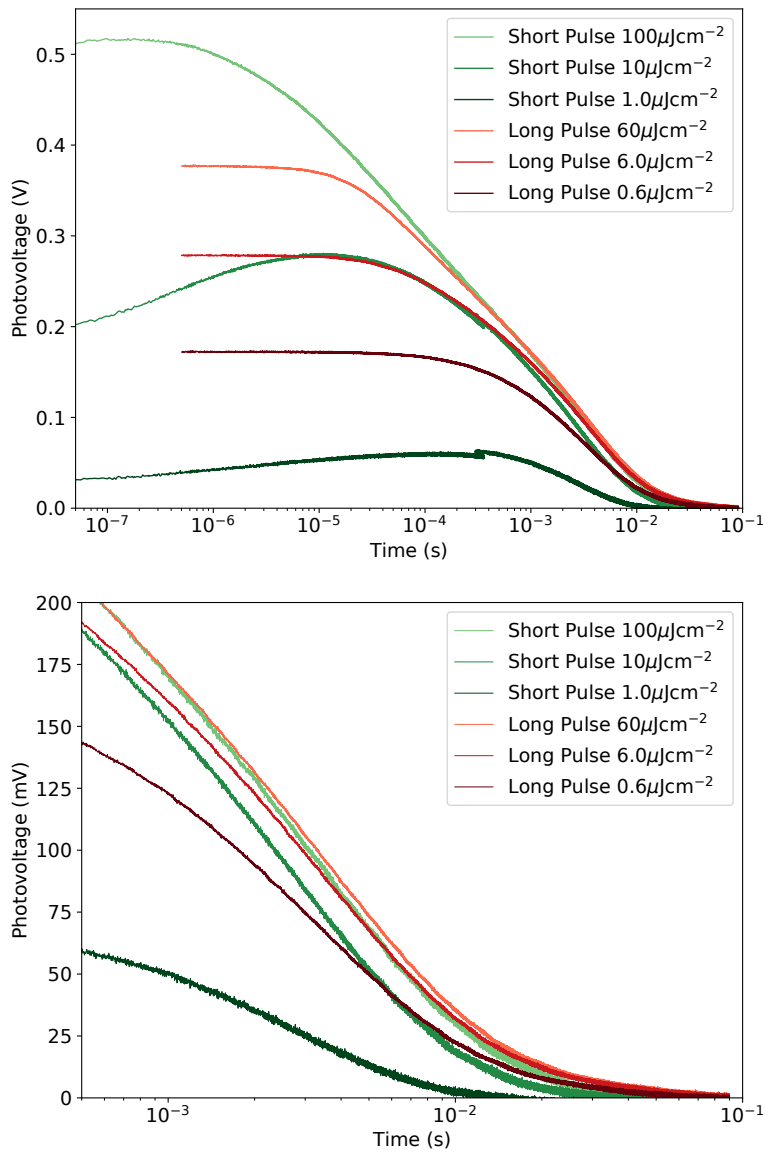


Figure 4.16: Photovoltage decay transients for a P3HT:PCBM device using a short (6 ns) and long (10 ms) excitation laser pulse at multiple excitation densities (as labelled). The top plot displays the full decay transients while the bottom plot is a close-up of the transient tail beyond 500 μs .

short pulse transients under all excitation densities, independent of initial photovoltage. This behaviour is best illustrated through a direct comparison of $10 \mu\text{J cm}^{-2}$ short pulse and $0.6 \mu\text{J cm}^{-2}$ long pulse transients. The short pulse transient exhibits a higher initial photovoltage than the long pulse transient, however at 6 ms both transients exhibit equal photovoltage of 400 mV, while beyond this point the long pulse transient exhibits a greater photovoltage until both transients completely decay within 100 ms. The slower relative transient decay observed in the long pulse excitation transients is consistent with the previous assertion of greater relative trap state occupancy in measurements using long pulse excitation. This influences the average recombination lifetime for a given charge density, with a longer lifetime in the long versus short pulse excitation method, as observed in the charge extraction measurements presented previously (Figure 4.15).

Trap State Density Distribution

To confirm the above observation of different trap state occupancy between short and long pulse excitation methods, and to determine any subsequent influence on the measurement of trap state density distribution, the time resolved charge extraction and photovoltage decay measurements presented above (Figures 4.15 and 4.16) are used to calculate the dependence of photovoltage on charge density at a range of excitation densities. The slope m (Equation 2.11) as a function of charge density is used to calculate the characteristic exponential of the trap state density distribution tail E_{ch} (Equation 2.12), with the resulting plots displayed in Figure 4.17. The low excitation density, short excitation pulse length plots exhibit an artefact at higher charge densities, with a peak and decay of photovoltage with increasing charge density. This has been previously observed and attributed to charge carrier spatial redistribution after stopping illumination at open circuit, and is therefore not representative of the trap state density distribution. As the long pulse method does not exhibit a initial rise in photovoltage decay transient, no such artefact is observed for the long pulse excitation method plots. For both pulse length excitation methods, the highest excitation density plots exhibit the largest range of charge densities, are the least influenced by any spatial redistribution, and therefore best to use for calculating trap state density distribution.

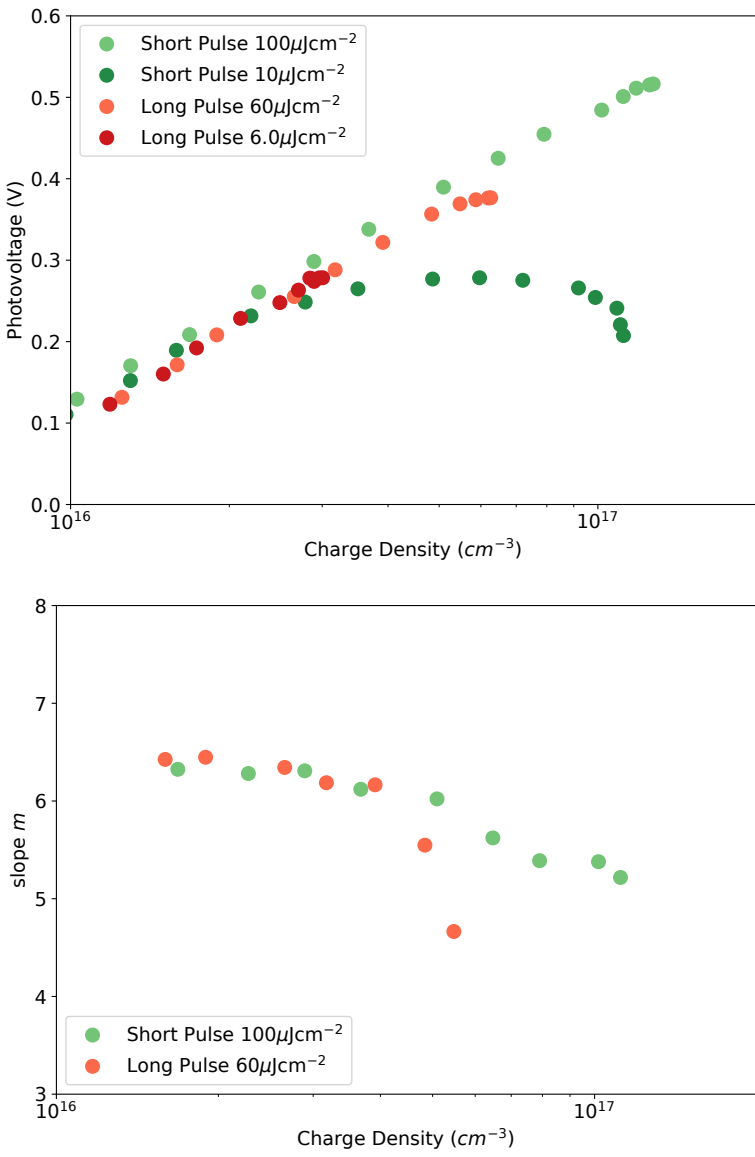


Figure 4.17: The dependence of photovoltage on charge density (top) and corresponding slope m (bottom) for a P3HT:PCBM device using a short (6 ns) and long (10 ms) excitation laser pulse, at multiple excitation densities (as labelled).

A direct comparison between the highest excitation density plots, 100 and $60 \mu J cm^{-2}$ for the short and long pulse lengths respectively, illustrates the key differences in measurement results between the two excitation pulse length. The long pulse plot is shifted to a higher charge density for any given photovoltage, relative to the short pulse plot (Figure 4.17, top). This observation is consistent with the previously presented charge extraction and photovoltage decay results and discussion. The long pulse excitation yields an internal charge density that has had greater time to relax into the density of states distribution (during the 10 ms excitation pulse) thereby occupying a large degree of trap states. The short pulse excitation however yields an internal charge density that has not undergone a comparable relaxation within the density of states distribution, and therefore has a lower relative proportion of trap state occupancy than the long pulse excitation for

any given charge density.

The calculated m for both excitation pulse lengths is comparable at low charge densities (Figure 4.17, bottom), indicating that both excitation pulse lengths provide a comparable measure of trap state density distribution (E_{ch}). The calculated long pulse m deviates from that of the short pulse excitation method at charge densities above $5 \times 10^{16} \text{ cm}^{-3}$, corresponding to the plateau observed in both charge density and photovoltage decay measurements. This is again due to a lower peak photogenerated charge density and slower measurement response time in the long pulse excitation measurements, rather than any shift in trap state density distribution, thereby limiting the range of charge densities over which long pulse excitation can measure E_{ch} . Using the calculated value for m of 5.4, obtained for the short pulse excitation method at high charge density, provides a value for E_{ch} of 70 meV for this P3HT:PCBM device, which is in agreement with literature reports for comparable devices ranging from 35 to 70 meV.^{137,138}

Ideality Factor, Reaction Order, and Comparison Between Transient and Steady-State

The device characterised in the previous sections is further used to investigate the observed difference between steady-state and transient derived reaction order and ideality factor, comparing devices with different inherent recombination kinetics and trap state density distribution (P3HT:PCBM and PCDTBT:PCBM material systems). The dependence of photovoltage on charge carrier lifetime is obtained for a range of excitation densities, using the photovoltage decay and lifetime as a function of charge density results presented above (Figures 4.16 and 4.15), with corresponding slope v (Equation 2.13) also calculated. Both short and long pulse excitation exhibit a comparable dependence of photovoltage on charge carrier lifetime, with the calculated value of v observed to be independent of pulse length excitation method, yielding a range of v from 1.8 to 2.2 across the measured charge density range.

The ideality factor and reaction order can be calculated for this P3HT:PCBM device using the calculated m and v . As both m and v were found to be independent of excitation pulse length, the values used to calculate both ideality factor and reaction order are obtained from the $100 \mu\text{J cm}^{-2}$ excitation density short pulse length excitation measurement results in the high charge density region. This ensures coverage of the widest range of charge densities, and yields the most consistent results over this range. The values for m of 5.4 and v of 2.0 are used to calculate an ideality factor of 1.46 and reaction order of 3.7 (using Equations 2.14 and 2.15). P3HT:PCBM devices have been reported to exhibit a reaction order in the range of 2.5 to 3.5 and above, measured using both transient absorption and charge extraction measurement techniques,^{36,139} which is comparable to the value of 3.7 calculated herein.

The calculated steady-state values for ideality factor of 1.61 and reaction order of 2.14 were obtained using results presented at the beginning of this section. The transient derived ideality

factor is lower than that measured at steady-state, while the transient derived reaction order is higher than that measured at steady-state. This trend is consistent with that observed in the previous section for the PCDTBT:PCBM device, and support the conclusion that fundamental differences exist between steady-state and transient measurements, attributed to a delay time induced variation in trap state occupancy that is coupled with charge density decay. Both the dependence of m on charge density, and the dependence of v on lifetime is far lower for the P3HT:PCBM device, than was observed for the PCDTBT:PCBM device, with variation in m and v of 15 and 18 % for P3HT:PCBM, while 89 and 85 % for PCDTBT:PCBM over an order of magnitude in charge density. This indicates that the delay time induced variation in trap state occupancy is also strongly influenced by the material system (inherent recombination kinetics and trap state density distribution).

4.5 Summary of Results and Discussion

The overall objective of this chapter was to examine the suitability of the time resolved charge extraction technique for the measurement of charge generation yield, recombination processes, and trap state density distribution, in operational photovoltaic devices. The primary results are summarised below, with respect to the specific chapter objectives:

- 1. Quantify charge extraction losses in time resolved charge extraction, and their influence on the measurement of charge density, recombination kinetics, and trap state density distribution, through measurements of charge density under a range of excitation densities and delay times, and subsequent analysis of charge density decay.**

Excitation density determines the initial charge density, while a reduction in charge density through an excitation-extraction delay time provides a direct measure of recombination kinetics (charge carrier lifetime) and reaction order, both found to be independent of excitation density for a given charge density. However, higher transient pulse excitation densities are advantageous, as they provide coverage of the widest range of charge densities (and lifetimes), while minimising any influence of charge carrier spatial redistribution which introduces error into the correlation of transient charge extraction and photovoltage decay measurements. Charge carrier losses during the extraction measurement process (recombination or trapping) were observed at charge densities where lifetime is comparable to the extraction time (on the order of 5 microseconds, transition between regions 2 and 3). This is well beyond the measurement circuit response (on the order of 200 ns), and results in an underestimation of charge density and limits the fastest observable recombination kinetics, estimated to be up to a factor of five.

- 2. Assess the correlation of transient charge extraction and photovoltage measurements for determining trap state density distribution, through a comparison of transient derived results for ideality factor and reaction order to those obtained using**

steady-state measurements.

The correlation of transient time resolved charge extraction and photovoltage decay measurements was successfully employed to determine trap state density distribution, in tandem with recombination kinetics measurements, with a 15 % variation over the measured charge density range for P3HT:PCBM. A far larger variation was observed for PCDTBT:PCBM, indicating a dependence of this measurement/analysis approach on inherent device recombination kinetics and trap state density distribution. Consistent differences were observed between transient derived diode ideality factor and empirical reaction order to that measured at steady-state, indicating fundamental differences between transient and steady-state measurements, attributed to time dependent variation in trap state occupancy in transient measurements (due to excitation-extraction delay time) that is coupled with charge density decay.

3. Determine the influence on trap state occupancy on the measurement of charge density, recombination kinetics, and trap state density distribution in time resolved charge extraction, through measurement of charge density using different excitation pulse lengths, and subsequent analysis of charge density decay.

Trap state occupancy was successfully varied through changing excitation pulse length, with the long (10 ms) excitation pulse length measurements exhibiting a greater relative trap state occupancy than short (10 ns) excitation pulse length measurements. This resulted in slower recombination kinetics and higher photovoltage measured for a given charge density. The calculation of trap state density distribution (dependence of photovoltage on charge density) was however found to be independent of excitation pulse length and therefore trap state occupancy.

4.6 Conclusions

The overall objective of this chapter was to examine the suitability of the time resolved charge extraction technique for the measurement of charge generation yield, charge recombination processes, and trap state density distribution in operational devices, with the eventual aim of investigating the impact of driving force on these factors and validating the outcomes of the previous optical driving force studies of Chapter 3.

A series of detailed time resolved charge extraction measurements were performed on devices incorporating two frequently studied photovoltaic systems, with results confirming the utility of this technique in the measurement of charge density and recombination kinetics, in tandem with the determination of trap state density distribution, and capable of covering a large range of charge densities. A number of measurement limitations were identified, including charge carrier losses due to recombination during the extraction process, which have a significant impact on the extraction

measurements including an estimated five fold underestimation of charge density and five fold overestimation charge carrier lifetime at charge densities on the order of 10^{16} cm^{-3} .

This measurement technique shows promise for the measurement of charge generation yield, charge recombination processes, and trap state density distribution, in further investigations of the driving force dependence of these parameters in operational devices. However further investigations are required to quantify the identified extraction losses, and to develop methods to reduce their influence on the measurement of charge density and recombination kinetics. This will be performed in the following chapter through the novel application of a bias during time resolved charge extraction measurement, with further detailed investigations of the influence of extraction limitations on the measurement of charge density and recombination kinetics, including their dependence on device parameters and measurement conditions (applied reverse bias, active layer thickness and surface area, measurement impedance, material system).

Chapter 5

Applied Bias in Time Resolved Charge Extraction Measurements

5.1 Introduction

5.1.1 Motivation and Objectives

The current uncertainty regarding the exact mechanisms of non-geminate recombination in state-of-the-art donor-acceptor photovoltaic devices limits the continued improvement of these systems. As such, clarification of these processes through the development of new models, improved experimental techniques for the study of charge carrier generation/recombination, and quantification of transport/extraction and recombination losses in photovoltaic devices are areas of high importance. Consequently, these uncertainties represent primary motivations for this thesis, with the objectives of quantifying and identifying the origins of extraction losses, developing improved investigative techniques, and improving the understanding of charge carrier transport/trapping and recombination processes in donor-acceptor photovoltaic systems.

Inherent to electronic measurement techniques are temporal limitations imposed either by the measurement circuit response, or by the time required for extraction of device internal charge density. This limits the time resolution of these measurement techniques to the observation of processes on the nanosecond timescale or slower. Additionally these charge extraction based measurements rely on the assumption that the extracted charge is representative of the device internal charge density, such that no recombination occurs during the extraction measurement. However for photovoltaic devices exhibiting fast recombination kinetics, slow charge transport, or utilising thick active layers, charge extraction times can be comparable to, or longer than the charge carrier recombination lifetime, leading to a significant underestimation of charge density. Furthermore, space-charging effects (build up of charge carriers causing screening of internal electric field) occurring during extraction can limit the rate of charge carrier sweep out, leading to further re-

combination during extraction. These recombination losses during charge extraction also introduce error into the measured charge density dependence of photovoltage and charge carrier lifetime, and it is non-trivial to quantify extraction losses in typical charge extraction measurements.

To date, transient charge extraction measurement limitations and recombination losses during extraction have not been systematically quantified for donor-acceptor photovoltaic systems, with the influence of these effects on the calculation of charge density, bimolecular recombination kinetics, and trap state density distribution remaining an unresolved issue. Addressing this uncertainty is therefore a primary objective of this chapter.

The previous chapter identified a number of limitations of the novel switched transient charge extraction measurement technique, as well as the influence of these limitations on the measurement of charge density, recombination kinetics, and trap state density distribution/occupancy, using well-studied material systems and covering a range of measurement conditions. Charge extraction techniques using an externally applied reverse bias have been extensively used to determine charge carrier transport and recombination kinetics in organic photovoltaic devices (see Chapter 1, Section 1.4 for a detailed discussion). However, a charge extraction technique is required that avoids the complicated analysis and assumptions needed to overcome the experimental difficulty in maintaining open-circuit condition during delay time, while achieving accelerated charge extraction (through an applied bias). In order to overcome the observed charge extraction losses, particularly that of recombination losses during the extraction process, the development of an improved time resolved charge extraction measurement technique is presented within this chapter, through the first time inclusion of an applied bias during charge extraction. The capabilities and limitations of the developed technique are thoroughly characterised for a range of measurement conditions (excitation density, magnitude of applied reverse bias, measurement circuit impedance) and device parameters (donor-acceptor material system, active layer thickness and surface area). These investigations are further used to accurately determine the origin of, and systematically quantify the observed extraction losses, enabling the attribution of the operational device performance limitations to the underlying loss mechanisms, and determine the influence of each on subsequent measurement of charge density, recombination kinetics, and trap state density distribution.

5.1.2 Time Resolved Charge Extraction with an Applied Bias

The time resolved charge extraction (TRCE) measurement utilising a nanosecond high impedance FET switch, as presented in the Chapter 4, is modified through the addition of the ability to apply a bias during charge extraction measurement. In concert with switching at T_{SW} , a reverse bias square pulse potential is applied across the device contacts using a function generator to aid in charge extraction. The pulse length of the applied bias was maintained well beyond typical extraction times. A circuit diagram (top) and timing diagram (bottom) are presented in Figure 5.1 to illustrate the set-up and operation of novel applied bias TRCE measurement. In the course of

measurements, the magnitude of the applied reverse bias can be varied in addition to both delay time and excitation density. Further details of measurement operation are presented in Chapter 2, Section 2.3.3.

5.2 Outstanding Issues in Time Resolved Charge Extraction Measurements and the Benefits of Incorporating an Applied Bias

5.2.1 Charge Carrier Extraction Processes under an Applied Bias

Significant extraction losses (recombination or trapping) were identified in time resolved charge extraction measurements in the previous chapter, leading to an underestimation of charge density, and influencing subsequent calculation of recombination kinetics and trap state density distribution. The rate of extraction can be increased through the application of an electric field, and thereby reduce recombination during extraction. However, in addition to faster charge extraction, an applied reverse bias is expected to yield a number of significant influences on charge extraction measurements, including changes to trap state extraction and space charge limited extraction. The influence of these behaviours on the rate of extraction under various charge densities, and a comprehensive understanding of measurement/device parameters on each of these behaviours is currently lacking. Each of these effects will be explored through the introduction of an applied bias to time resolved charge extraction measurements, and through a study of its influence on extraction processes and recombination losses, as well as subsequent determination of charge density, recombination kinetics, and trap state density distribution in the well studied (PCDTBT/P3HT):PCBM material systems.

Measurement Response Limitations

A large limitation of charge extraction measurements arises from the measurement circuit response time τ_{RC} , dependent on the measurement resistance R and device capacitance C . This response time represents the temporal limit of current extraction for the measurement circuit. Therefore charge extraction measurements will require a minimum of τ_{RC} (typically on the order of 100 ns) to measure the charge density, even where charge carriers have a mobility sufficient to be extracted faster than this limit. Typical charge extraction measurements however require significantly longer than this to completely extract the device charge density (on the order of 50 μ s for P3HT:PCBM based devices, see Figure 5.2). This measurement response time can influence the measurement of charge density under conditions when the lifetime is comparable to τ_{RC} , and recombination of charge density occurs during the extraction measurement resulting in an underestimation of charge density. These recombination losses are typically observed at high charge densities, and are more significant in thicker active layers (greater transport and extraction time)

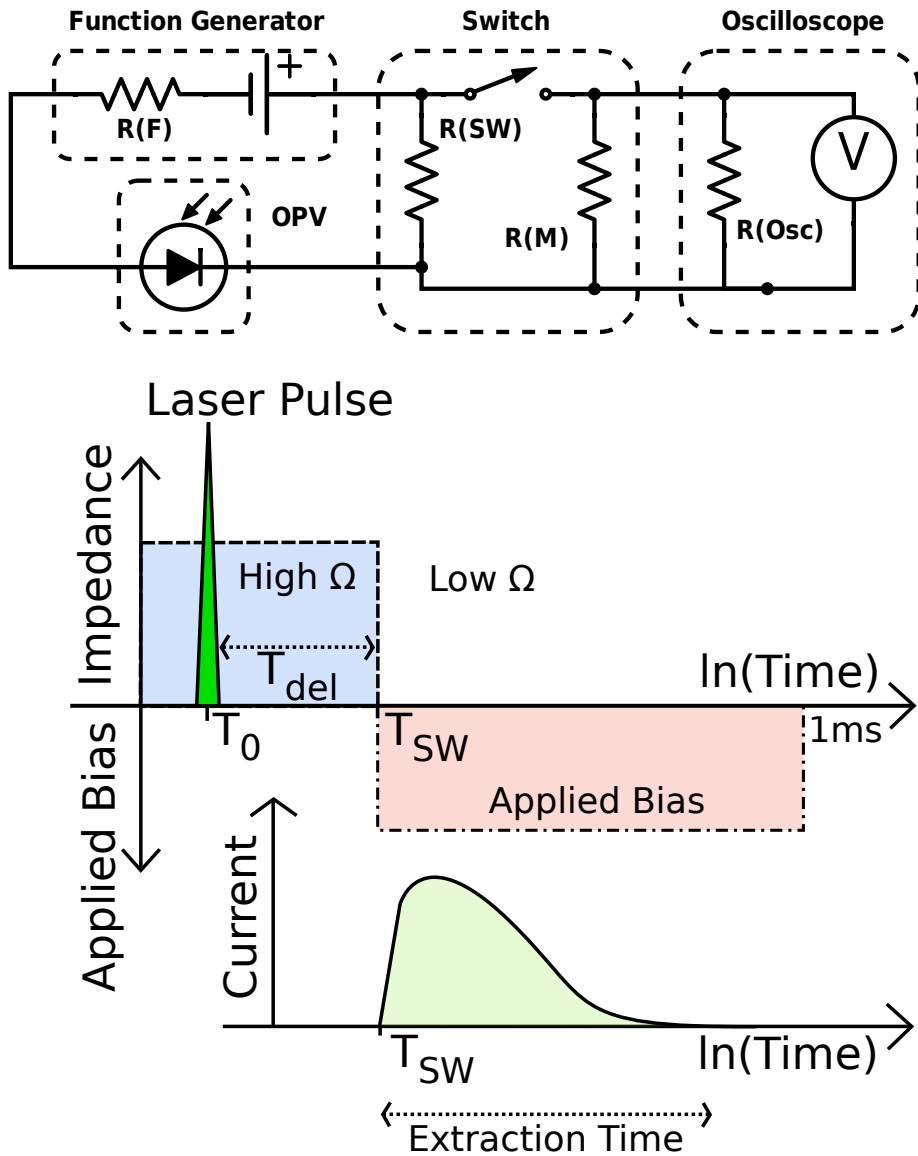


Figure 5.1: **Top:** Time resolved charge extraction circuit diagram featuring an applied bias, illustrating the organic photovoltaic device (OPV), FET switch with internal high impedance resistor R_{SW} and measurement resistance R_M , oscilloscope with internal resistance R_{Osc} and potentiometer V , and function generator with internal impedance R_F and variable potential. **Bottom:** Timing diagram for operation of extraction measurements, illustrating the laser excitation pulse at T_0 , high initial circuit impedance ($M\Omega$) switching to low ($< 1 \Omega$) at T_{SW} , variable delay time T_{del} , variable bias applied at T_{WS} , and an illustration of an extraction current transient as a function of extraction time.

and in material systems (or morphologies) with inherently faster recombination kinetics. Reducing either measurement resistance or device capacitance (through active layer thickness or surface area) will yield a faster measurement response, however practical limitations of device fabrication and measurement noise limit this approach. Therefore recombination during extraction will always limit the fastest measurable recombination kinetics of charge carriers in charge extraction measurements.

Space Charge Limited Extraction

In the case of space charge limited extraction, only a fraction of charge (CU) is extracted at a given time, due to accumulation of charge carriers at their respective device electrodes causing screening of the electric field. The remaining charges exist within a field-free region of the device. This effect is illustrated in Figure 5.8. If the charge carrier lifetime is longer than the extraction time, a charge density greater than CU can be extracted, otherwise the charge carriers within this reservoir recombine and do not contribute to extracted charge and therefore the measured charge density.⁹⁹ Space charge limited extraction could also limit the rate of carrier sweep out, leading to further recombination losses during extraction. This underestimation of charge density introduces an error in measurement of charge carrier lifetime and trap state density distribution. It is however not trivial to quantify these charge recombination losses in typical charge extraction measurements, and has therefore never previously been systematically quantified.

The response of a photovoltaic device without illumination to a reverse bias square pulse potential is expected to be comparable to that of a dielectric parallel plate capacitor. As such, the extracted charge due to the capacitive charging current will be CU for a device with capacitance C and applied potential U . This charging current will be greatest initially, limited by RC , beyond which decaying exponentially until extracted charge reaches CU , with a decay time constant of τ_{RC} . Additional extraction current may also be exhibited in cases of significant active layer doping density, or through DC injection/extraction.

The influence of an applied bias during charge extraction is expected to increase the extracted charge through an increase in the rate of extraction, thereby reducing recombination losses during extraction at high charge densities. However the effect of space charge limited extraction, as well as the influence of capacitive charging current on the charge extraction process is uncertain. In order to quantify the influence of an applied reverse bias on extraction losses and measured charge density, applied bias time resolved charge extraction measurements are presented in Section 5.4.1, with a detailed analysis of charge extraction under a range of applied bias and charge densities. Further analysis of measured charge density decay, recombination kinetics, and trap state density distribution is also presented within this chapter.

Device Active Layer Thickness Variation

Changing the device active layer thickness for a constant diffusion length (mobility-lifetime product) will influence extraction losses. The influence of a given applied reverse bias is also dependent on active layer thickness, determining the electric field and therefore rate of extraction. The degree of influence that this effect has on the measurement of charge density, recombination kinetics, and trap state density distribution has not been clarified for applied bias time resolved charge extraction measurements, as many of the previously outlined charge extraction processes will be strongly influenced by variations in device thickness, either through altered device capacitance or relative differences in the magnitude of internal electric field for a given applied reverse bias.

Even under conditions of spatially uniform charge photogeneration, the spatial distribution of charge density has been known to tend towards a non-uniform state in devices with sufficiently thin active layers at low charge densities.³⁴ Charge carriers concentrate at their respective device contacts at open-circuit, leading to a reduced average overlap of charge carrier populations. The influence of an applied bias under conditions of inherent spatial separation requires investigation.

5.2.2 Summary of Issues and Chapter Objectives

The overall objective of this chapter is to improve the time resolved charge extraction technique, through the novel incorporation of an applied bias, and investigate the influence of this applied bias on measurement limitations, as well the measurement of charge generation yield, charge recombination processes, and trap state occupancy in operational devices. These are covered under the following chapter objectives:

1. Assess to what extent incorporating an applied bias in time resolved charge extraction can improve the measurement of charge density, recombination kinetics, and trap state density distribution, through quantifying charge extraction losses under a range of measurement conditions.
2. Investigate the influence of measurement and device parameters (applied reverse bias, measurement impedance, device capacitance, active layer thickness) in applied bias time resolved charge extraction through controlled variation of individual parameters under a range of charge densities, and further their impact on the measurement of charge density, recombination kinetics, and trap state density distribution.

5.3 Experimental

5.3.1 Photovoltaic Device Fabrication

Multiple sets of photovoltaic devices were fabricated for use in the charge extraction measurement studies presented in this chapter. Minor variations to the standard fabrication procedure were

introduced, as necessitated by the fabrication of devices with various active layer thickness and surface area, achieved by adjusting the active layer deposition parameters (spin coater rate) and cathode evaporation process (reduced area mask) respectively. Details of photovoltaic device active layer thickness determination is also detailed in Chapter 2, Section 2.1.3.

The poly[N-9"-hepta-decanyl-2,7-carbazole-alt-5,5-(4',7'-di-2-thienyl-2',1',3'-benzothiadiazole) (PCDTBT) (Solaris, SOL4280, 68-85Dka, electronic grade) and [6,6]-phenyl-C₆₀-butyric acid methyl ester (PCBM) (Solaris, SOL5061A, 99.5 % purity) (1:4) blend solution was prepared by dissolution in o-dichlorobenzene at 20 mg mL⁻¹ and stirring at 120 C° for 20 hours under an Ar atmosphere. The poly(3-hexylthiophene-2,5-diyl) (P3HT) (LumTec., LT-S909, 45Dka, electronic grade, 93 % regioregular) and PCBM (5:4) blend solution was prepared by dissolution in chlorobenzene at 50 mg mL⁻¹ and stirring at 80 C° for 20 hours under an Ar atmosphere.

Pre-patterned Indium Tin Oxide (ITO) coated glass slides (LumTec., 90 nm thick ITO, variable active pixel area, typical conductivity of 15 Ω cm⁻², above 85 % transmission at 550 nm) are used for the transparent device anode, as well as providing a rigid substrate. The substrates are cleaned by 15 min under sonication in surfactant/H₂O, followed by two subsequent 5 min sonication rinses in H₂O, and 15 min under sonication each in acetone and isopropanol, prior to a 20 min UV-ozone treatment. This ensures a clean, particulate free substrate and improves wettability for solution/active layer deposition.

The cleaned substrates are coated with the poly(3,4-ethylenedioxythiophene):poly(styrenesulfonate) (PEDOT:PSS) hole selective layer, using 0.5 wt % PEDOT:PSS solution (Heraeus Clevios Al 4083) diluted 1:1 in isopropanol. The PEDOT:PSS solution is filtered through a 0.45 μm PVDF filter to remove any particulates prior to dilution, and maintained under stirring. The layer is then deposited using spin coating (Laurell WS-560HZ-15NPP) at 5000 rpm for 30 s, followed by annealing in air at 140 C° for 20 min.

Directly prior to deposition of the active layer, the active layer polymer(blend) solutions are cooled to room temperature. For both P3HT and PCDTBT based devices, the polymer(blend) solutions were spin-coated in air onto the prepared substrate at between 1500 and 5000 rpm, for times ranging from 90 to 240 s, depending on the active layer thickness required.

To produce the amorphous titanium oxide (TiOx) electron selective interfacial layer, a titanium oxide sol-gel precursor solution is diluted (1:10) into isopropanol prior to deposition onto the device active layer. TiOx layer deposition is performed directly after active layer deposition (and any required active layer solvent drying time) using spin coating at 5000 rpm for 30 s, and is left to hydrolyze in air for 20 min (or under heating where the active layer requires annealing).

Aluminium (Al) is then evaporated under vacuum through a mask of defined device active area (0.095 cm⁻² unless otherwise stated), to produce a cathode thickness on the order of 100 nm. A

ramp in evaporation rate is used to ensure good contact with the active layer (initial 5 nm at 0.5 \AA s^{-1} , following 50 nm at 1.5 \AA s^{-1} , final $\sim 50 \text{ nm at } 2.5+ \text{ \AA s}^{-1}$). The deposition chamber is left to cool down for 30 minutes before returning to atmospheric pressure. These devices were then sealed under an inert Ar atmosphere using a cover glass slide and UV-curable epoxy (Ossila, E131), manually cured using a handheld UV gun. Effort is made to ensure that no epoxy is in contact with the device active layer, and that no significant UV illumination is incident on the device active area. Finally, a metal contact is soldered (ultrasonic) onto the exposed anode/cathode contact regions for increased durability during measurement.

5.3.2 Transient Applied Bias Charge Extraction and Photovoltage Decay

The time resolved charge extraction (TRCE) measurement utilises a nanosecond FET switch (SR-05, Asama Lab) to switch rapidly between open circuit and short circuit conditions. The switch is capable of switching from an internal impedance R_{SW} of $2.2 \text{ M}\Omega$ to less than 1Ω in under 100 ns. A high switch impedance is used to maintain open circuit rather than a true open circuit (infinitely large impedance) to protect the switch. A photovoltaic device (OPV) is connected in series with the switch, and charge carriers are generated using a laser pulse for photoexcitation (532 nm, 6 ns pulse width, Spectra Physics Quanta Ray Lab 170; or during long pulse measurements a 641 nm, variable pulse width, Nation Instruments Coherent CUBE continuous wave). A variable delay time T_{del} is imposed between stopping laser illumination T_0 and switching T_{SW} using a delay generator, during which time the device is held at open circuit, and charge carriers are left to recombine. Upon switching, the device is short circuited and an extraction transient is measured across the variable measurement impedance R_M (50Ω unless otherwise stated) using an oscilloscope (DPO4000 Series, Tektronix).

The TRCE measurement is modified through the addition of the ability to apply a bias during charge extraction measurement. This facilitates improved charge extraction under the applied bias, relative to standard operation which relies solely on the device's built in potential to drive charge extraction. In concert with switching at T_{SW} , a reverse bias square pulse potential is applied across the device contacts (through the FET switch) using a function generator (WF1974 Wave Factory Multifunction Generator, NF Corp.). The pulse length of the applied bias was maintained for 1 ms, well beyond typical extraction times on the order of $50 \mu\text{s}$. In the course of measurements, the magnitude of the applied reverse bias can be varied in addition to both delay time and excitation density.

Each extraction transient is recorded as an average of 50 individual measurements, per set of conditions, to minimise noise and account for any variability in laser excitation. All transients presented herein are displayed with an 80 ns shift for illustration purposes, such that switching occurs at 80 ns as presented in figures. Unless otherwise specified, the characteristic switch response

has been subtracted from all transients, recorded individually for each set of measurements, as well as the dark (no laser illumination) transient response. The transient voltage response is measured as a function of extraction time, and converted to extracted current using the known measurement resistance. The total extracted charge is obtained through integrating the current transient response over time. The extracted charge is obtained at a range of delay times to yield the decay of extracted charge as a function of delay time, with laser illumination also varied.

Photovoltage decay measurements are performed to obtain the open circuit potential at the device contacts as a function of time that the photovoltaic device is held at open circuit after laser illumination is stopped. Variation of excitation density is also used to alter the initial charge density. These measurements are performed using a laser excitation source (532 nm, 6 ns pulse width, Spectra Physics Quanta Ray Lab 170; OR for long pulse measurements a 641 nm, variable pulse width, Nation Instruments Coherent CUBE continuous wave), with the photovoltaic device connected in series with the oscilloscope high impedance of $1.0\text{ M}\Omega$ to maintain open circuit. The photovoltage decay transients are then recorded using the oscilloscope (DPO4000 Series, Tektronix), from the time of stopping laser excitation until complete decay of photovoltage.

Further details of time resolved charge extraction and photovoltage decay measurements and analysis methodology are presented in Chapter 2, Sections 2.3.1 and 2.3.2.

5.4 Results and Discussion

The measurement results presented in this chapter for both P3HT:PCBM and PCDTBT:PCBM material systems utilise the devices characterised and presented in the prior chapter for consistency (excluding those requiring variation in active layer thickness or surface area). However all applied bias charge extraction measurements have been performed on a range of devices, incorporating either P3HT:PCBM or PCDTBT:PCBM, and using various active layer thicknesses. The primary outcomes of the results and discussion presented herein are consistent across all surveyed sets of devices.

5.4.1 Applied Bias in Time Resolved Charge Extraction for Charge Density Measurement

A photovoltaic device incorporating the P3HT:PCBM (5:4) donor-acceptor system, as presented previously (see Chapter 4, Section 4.4.3 for device details), was used in applied bias time resolved charge extraction measurements at a range of applied reverse bias, excitation-extraction delay times, and excitation densities. These measurements are performed to study the influence of an applied bias in time resolved charge extraction for the measurement of charge density, and to quantify charge extraction losses due to recombination or transport at a range of charge densities.

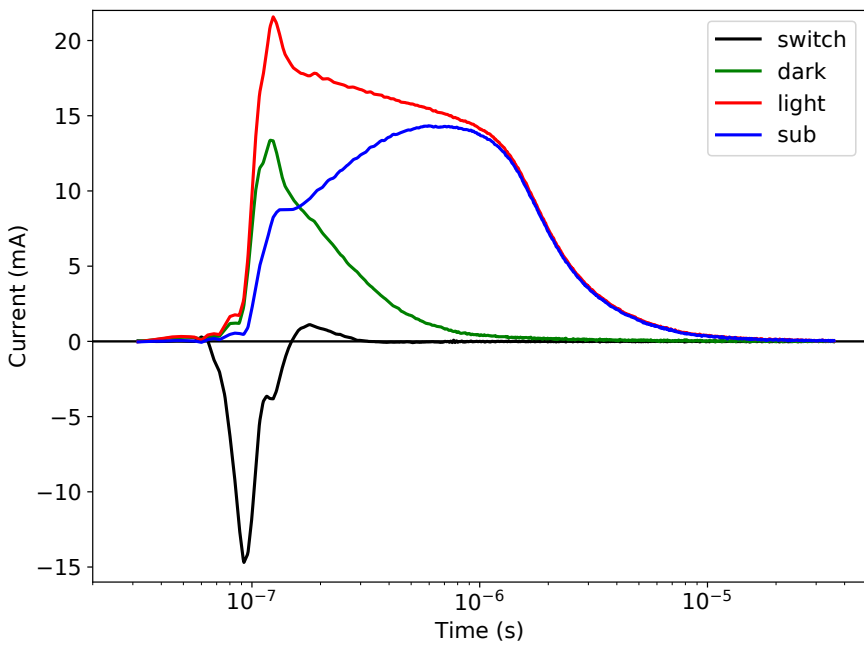


Figure 5.2: Charge extraction transients (extracted current as a function of extraction time) for a P3HT:PCBM device, using an applied reverse bias of 2 V, a $100 \mu\text{J cm}^{-2}$ excitation density, and 100 ns excitation-extraction delay. The transients displayed include: the response without illumination or an applied bias ('switch', solid black, characteristic switch response); the response when using an applied bias (with switch response subtracted), both with illumination ('light', solid red), and without ('dark', solid green); and the subtracted transient ('dark' subtracted from 'light', solid blue).

Shape of Charge Extraction Transients with an Applied Bias

Figure 5.2 displays example charge extraction transients for the P3HT:PCBM device using an applied reverse bias potential of 2 V, a $100 \mu\text{J cm}^{-2}$ excitation density, and 100 ns excitation-extraction delay time. The transients displayed include: the response without an applied bias or illumination ('switch', black, characteristic switch response); the response when using an applied bias (with switch response subtracted), both with illumination ('light', red), and without ('dark', green); and the subtracted transient ('dark' subtracted from 'light', blue). The characteristic switch response is subtracted from both applied bias response transients. The applied bias response without illumination ('dark', green) exhibits an extracted current in addition to the switch response. As no photogeneration of charge density has occurred, this response current is due to the capacitive charging current of the photovoltaic device in response to an applied electric field. This capacitive charging current response will be further investigated later in this chapter.

The applied bias response with illumination ('light', red) exhibits an extracted current in addition to both switch response and dark capacitive charging current, due to the extraction of photogenerated charge density. This transient exhibits a fairly stable initial extraction current directly after the RC limited rise, with only a slight reduction up until a shoulder at 1 μs , beyond which a fast decay in extracted current is observed. The subtracted transient ('sub', blue), comprising extracted current solely due to photogenerated charge density exhibits an initial rise in extracted current to a peak around 1 μs , correlating with the observed shoulder of the illuminated transient and the decay of capacitive charging current. Additionally, this transient response exhibits characteristics of space charge limited extraction which will be further discussed later in this chapter.

The illuminated response transients for the P3HT:PCBM device are presented in Figure 5.3 for a range of delay times using a applied reverse bias of 2 V and $100 \mu\text{J cm}^{-2}$ excitation density. The response transient without illumination ('dark') has also been included and all transients have had the switch response subtracted. The illuminated transients at long delay times (reduced charge density through recombination at open circuit) tend towards that of the transient response without illumination. The 1 ms illuminated transient exhibits a total extracted charge of only 10 % greater than that of the transient response without illumination, while at 100 ns delay time an additional 100 % extracted charge is observed. This confirms that at sufficiently low charge density (long delay time), the illuminated transient is merely that of the transient response without illumination. It is therefore correct to subtract the dark response from the illuminated response in order to obtain solely the photogenerated charge density, as in charge extraction measurements without an applied bias.

Figure 5.4 displays the illuminated extraction transients (with dark response subtracted) for the P3HT:PCBM device at 100 (top) and 1 (bottom) $\mu\text{J cm}^{-2}$ excitation density, using a 100 ns

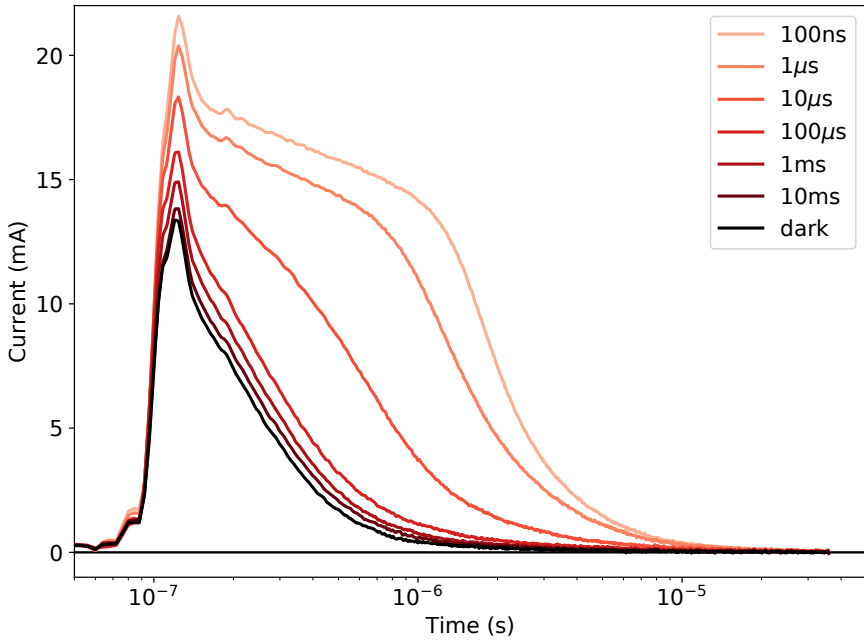


Figure 5.3: Illuminated charge extraction transients for a P3HT:PCBM device at a range of delay times (as labelled), using a 2 V applied reverse bias and $100 \mu\text{J cm}^{-2}$ excitation density, as well as the response transient without illumination ('dark'). All transients have had the switch response subtracted.

delay time at a range of applied reverse bias up to 2 V, including no applied bias. The short 100 ns delay time represents the conditions of highest measured charge density for a given excitation density, with corresponding shortest charge carrier lifetime, and therefore should experience a high degree of charge carrier recombination during the extraction measurement (see Chapter 4, Section 4.4.2 for discussion). During these investigations, the application of a reverse bias above 2 V was frequently observed to damage photovoltaic devices, and therefore has been the limit of potential applied in the measurements presented herein. An increase in applied reverse bias results in an increase in current response, and the corresponding total extracted charge (transient integral). An increase in extracted current is observed directly after the initial RC rise at high applied reverse bias, consistently rising to a peak (broken line, blue). This peak is observed to be independent of applied bias for the $100 \mu\text{J cm}^{-2}$ excitation density, with an average peak position of $0.67 \mu\text{s}$. The $1 \mu\text{J cm}^{-2}$ excitation density transients however exhibits a shift in peak position to faster extraction times with increasing reverse bias, from $0.67 \mu\text{s}$ at 0.5 V down to $0.49 \mu\text{s}$ at 2 V. The tail of the transients beyond $2 \mu\text{s}$ appears independent of applied bias for the $100 \mu\text{J cm}^{-2}$ excitation density transients, while the $1 \mu\text{J cm}^{-2}$ transients exhibit a shift to faster extraction with increasing applied reverse bias.

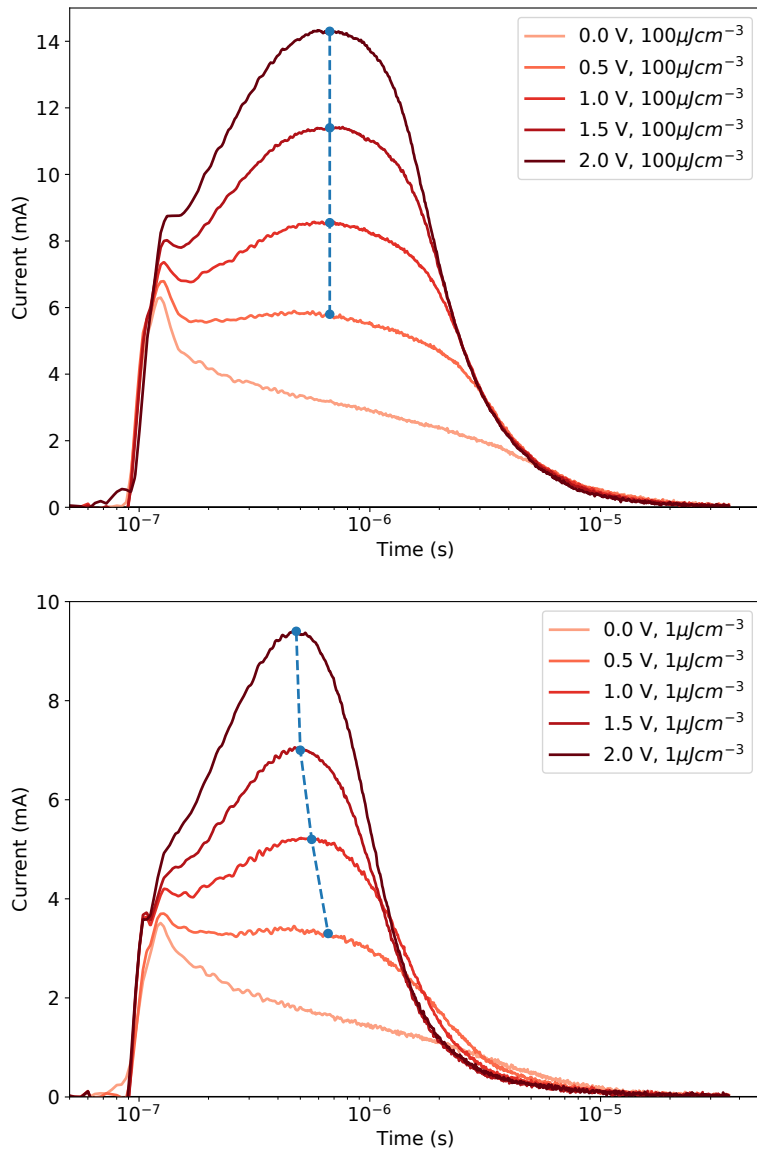


Figure 5.4: Illuminated extraction transients for a P3HT:PCBM device at 100 (top) and 1 (bottom) $\mu\text{J cm}^{-2}$ excitation density, using a 100 ns delay time for a range of applied reverse bias. Peak point and line to guide the eye (broken, blue) is included to illustrate the transient peak position as a function of applied bias.

Quantifying Charge Extraction Losses, Assisted by an Applied Bias

For the illuminated transients presented in Figure 5.4 corresponding solely to the extraction of photogenerated charge density, the total extracted charge with no applied bias is 20 nC while for an applied reverse bias of 2.0 V is 39 nC. This equates to an increase in extracted charge of 98 % with the application of a 2 V reverse bias for an identical excitation density and delay time. This indicates that at least 50 % of charge density is lost during the charge extraction process without the application of an applied bias, and represents a significant underestimation of charge density under these conditions. The influence of an applied reverse bias on the total extracted charge is presented in Figure 5.5, both as a function of delay time (top) and excitation density (bottom). Increasing excitation density corresponds to an increase in initial charge density, while increasing delay times correspond to a reduction from this initial charge density through recombination.

The increase in extracted charge with an increasing applied reverse bias from zero up to 2 V is observed to be greatest at the highest excitation density and shortest delay time, corresponding to the conditions of highest charge density (and a lifetime comparable/shorter than extraction time). Relative to no applied bias, the 2 V applied reverse bias results in an increase in extracted charge of 98 % using $100 \mu\text{J cm}^{-2}$ excitation density and 100 ns delay time, while reducing the excitation density to $1 \mu\text{J cm}^{-2}$ results in an increase of only 63 %, or increasing the delay time to 10 μs results in an increase of only 31 %. However, for the $100 \mu\text{J cm}^{-2}$ excitation density, even at a delay time of 200 μs (with a relatively low charge density), an increase in extracted charge of 93 % is still observed indicating that an applied bias results in a greater extraction of charge density under all measured charge density conditions. For high charge densities (short delay time, high excitation density), the increase in extracted charge is greatest at the lower applied reverse bias. For the 100 ns delay time, $100 \mu\text{J cm}^{-2}$ excitation density plot, an increase from no applied bias to a 0.5 V reverse bias results in an increase in extracted charge of 38 %, while from 1.5 to 2 V reverse bias results in a lesser 9 % increase. For low charge densities however (low excitation density, long delay time), a linear dependence of extracted charge on applied bias is observed at excitation densities below $10 \mu\text{J cm}^{-2}$ or at delay times of 50 μs or longer for the $100 \mu\text{J cm}^{-2}$ excitation density.

The observed saturation of extracted charge with increasing applied reverse bias at high charge densities may indicate the near complete extraction of charge density under a sufficiently high reverse bias, or could be the result of measurement limitations. The observation of a linear dependence at low charge densities however does not indicate a comparable complete extraction of charge density. Even without the observation of saturation in extracted charge, up to half of the photogenerated charge density is lost during the extraction process without an applied bias in time resolved charge extraction measurements. This is due to the extraction of additional charge carriers that would otherwise not be extracted (lost through recombination or trap state occupancy), representing a large underestimation of charge density and therefore significant measurement error

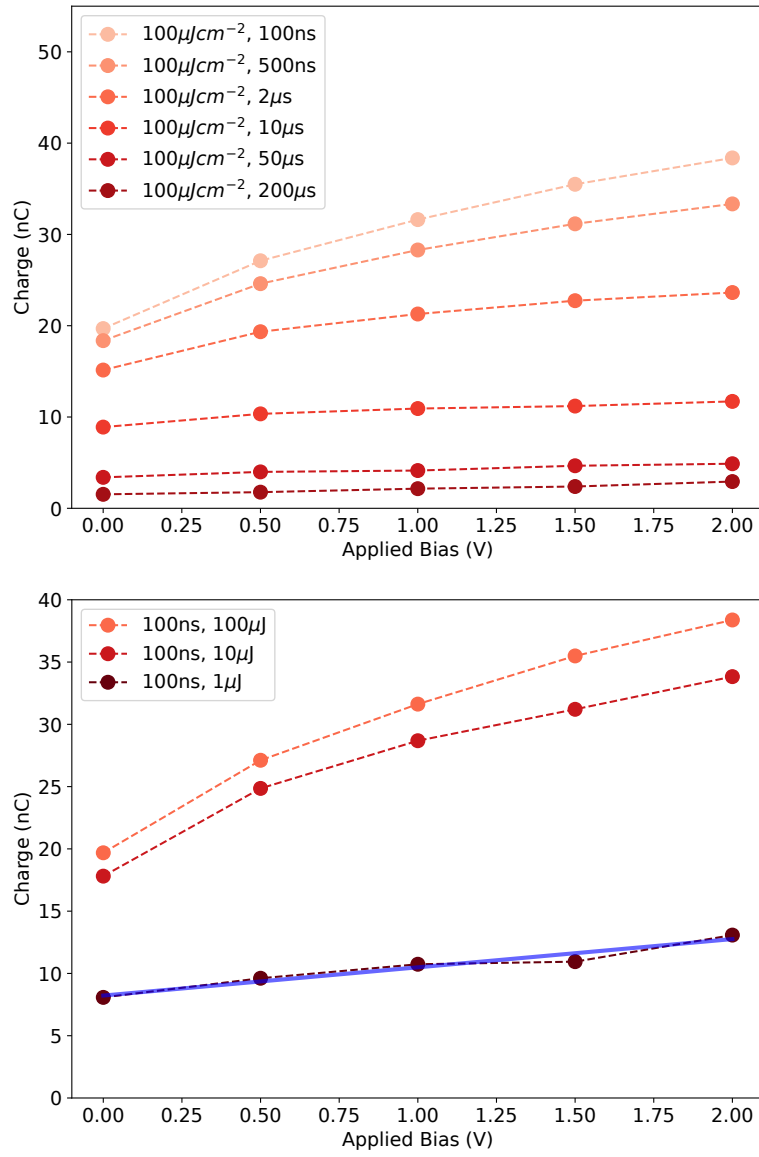


Figure 5.5: Extracted charge as a function of applied reverse bias for a P3HT:PCBM device: at a range of delay times using a $100 \mu J/cm^2$ excitation density (top); and at a range of excitation densities for a 100 ns delay time (bottom).

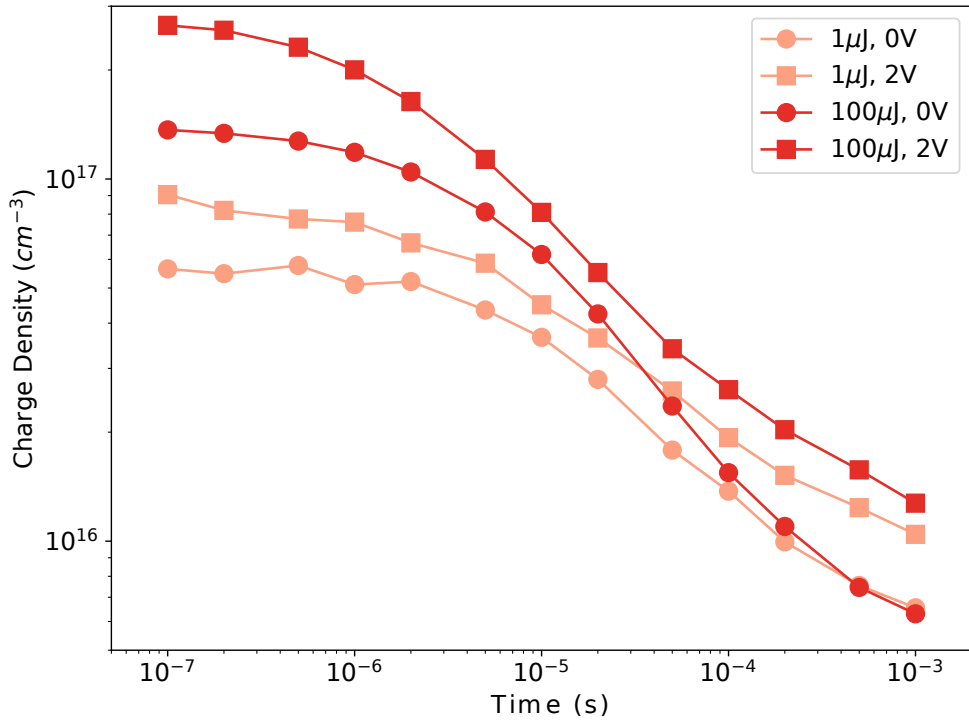


Figure 5.6: Charge density decay as a function of delay time for a P3HT:PCBM device with both zero and 2 V applied reverse bias, for a high and low excitation density (as labelled).

without an applied reverse bias for these P3HT:PCBM devices.

The Influence of Charge Density and Delay Time on Extraction Losses

In order to determine the origins of the observed charge density dependent increase in extracted charge with the application of a reverse bias, further investigation is performed through analysis of charge density decay for the P3HT:PCBM device, with comparison of with/without a 2 V applied reverse bias at two excitation densities (high and low initial charge density). Figure 5.6 displays the measured charge density decay plots for the P3HT:PCBM device using an applied bias of zero (circles) or 2 V (squares), and at excitation densities of 100 and $1 \mu\text{J cm}^{-2}$ to provide high and low initial charge densities respectively. For the charge density decay plots without an applied bias, the $100 \mu\text{J cm}^{-2}$ excitation density plot exhibits a greater initial charge density than the $1 \mu\text{J cm}^{-2}$ plot, both decaying over the microsecond timescale before exhibiting comparable charge density beyond 500 μs delay time. The application of a 2 V reverse bias is observed to increase the measured charge density for both excitation densities over the entire measured charge density range, and is greatest at either high or low charge density regions. This increase in charge density with an applied bias is reduced to less than half that observed at high/low charge density within the region from 2 to 50 μs for both excitation densities. The higher $100 \mu\text{J cm}^{-2}$ plot exhibits a consistently greater relative increase (on the order of 20 %) over the entire charge density range.

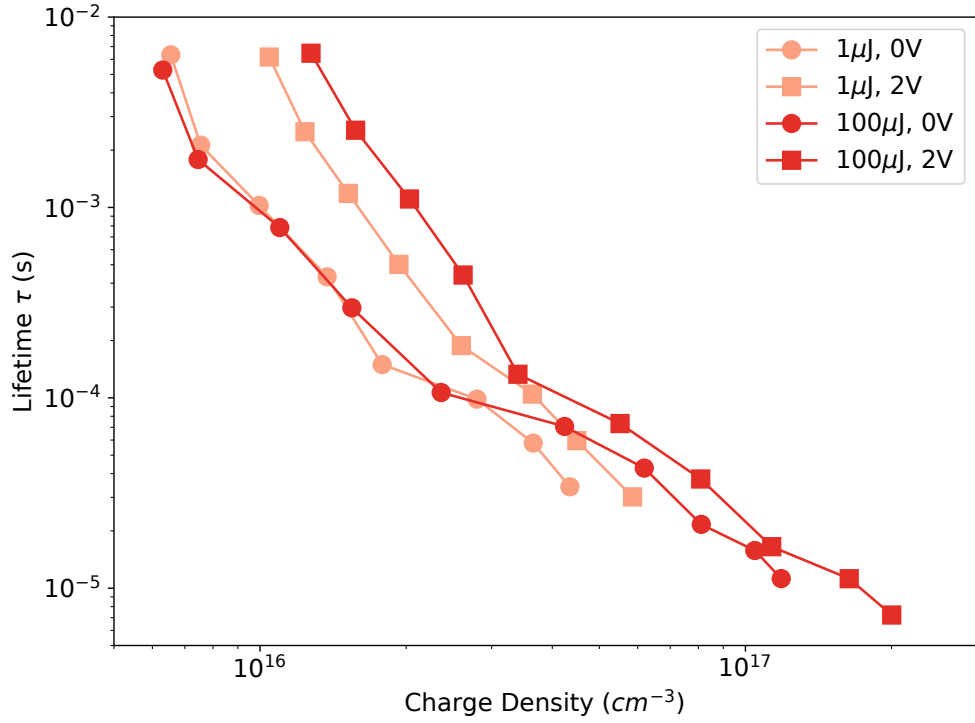


Figure 5.7: Charge carrier lifetime as a function of charge density for a P3HT:PCBM device with both zero and 2 V applied reverse bias, for two excitation densities (as labelled).

Two distinct regions of behaviour are observed, regarding the dependence of extracted charge density on applied bias, one for the high charge density region (delay times shorter than 2 μs) and one for low charge density region (delay times longer than 50 μs), with a reduced dependence observed between these regions. This may indicate that the origin of the increase in extracted charge density with an applied bias has multiple distinct components that are charge density dependent. A detailed outline and discussion of possible origins for the observed extraction losses is presented in Section 5.4.2.

Influence of Extraction Losses on the Measurement of Charge Carrier Lifetime

Following the observed charge density dependent increase in extracted charge with an applied reverse bias during charge extraction, a corresponding influence is expected on subsequent analysis of charge density decay for the study of recombination kinetics. Therefore, measurement results for the P3HT:PCBM device presented in the previous section are used to further investigate the influence of extraction losses in applied bias time resolved charge extraction measurements through the calculation of charge carrier lifetime.

Using the charge density decay results presented in the previous section (Figure 5.6), charge carrier lifetime is calculated as a function of charge density (Equation 2.9) for an applied reverse bias of zero and 2 V, each at both 100 and 1 $\mu J\ cm^{-2}$ excitation densities, displayed in Figure 5.7. Both excitation density plots without an applied bias are comparable for charge densities

below $4.0 \times 10^{16} \text{ cm}^{-3}$, while the $100 \mu\text{J cm}^{-2}$ plot exhibits an extension to higher charge densities (and corresponding shorter lifetimes) due to the higher initial charge density relative to the $1 \mu\text{J cm}^{-2}$ plot. The application of a 2 V reverse bias is observed to result in a shift to longer charge carrier lifetimes for any given charge density. This shift is greatest at low charge densities, and more significant in the higher $100 \mu\text{J cm}^{-2}$ plot, where an order of magnitude longer lifetime is observed with the application of a 2 V reverse bias (relative to no bias) below $4.0 \times 10^{16} \text{ cm}^{-3}$, corresponding to lifetimes on the order of 50 μs or longer. At charge densities above $4.0 \times 10^{16} \text{ cm}^{-3}$, the extension of lifetime is significantly reduced to the order of 50 %, and further reducing to below 20 % at $1.0 \times 10^{17} \text{ cm}^{-3}$. The application of a 2 V reverse bias also yields an extension in the shortest measured lifetime, on the order of 40 % shorter for the $100 \mu\text{J cm}^{-2}$ excitation density.

The above results indicate that extraction losses present in charge extraction measurements without an applied reverse bias result in significant underestimation of charge carrier lifetimes at high charge densities, while a large variation in measured lifetimes is observed at low charge densities. A detailed outline and discussion of possible origins for these observations is presented in Section 5.4.2.

5.4.2 The Origins of Increased Charge Extraction with an Applied Bias

An increase in extracted charge density is obtained through the application of a bias in time resolved charge extraction measurements, with the degree of influence dependent on both charge density and delay time. A detailed discussion is presented below, outlining the possible origins of this increase in extracted charge density based on the results presented in the previous section for a range of measurement conditions.

1. Increased Rate of Extraction

The reverse bias square pulse potential used in these measurements is applied simultaneously with closing the switch, and therefore does not influence the internal charge density during delay time (held at open circuit condition). Therefore the origins of the increased extracted charge with an applied bias must arise solely from the charge extraction process, i.e. after closing the switch.

The measurement circuit RC limits the rise of the charge extraction transient (τ_{RC}), in this case on the order of 200 ns. When the charge carrier lifetime is comparable to, or faster than τ_{RC} , the transients are RC influenced and recombination during the RC limited extraction process is in competition with the extraction of charge. These conditions are observed at high charge densities, produced through high excitation density and short delay time. This effect results in the loss of charge carriers and an underestimation of device internal charge density. As this limit is determined solely by the measurement circuit response (RC), in principle, a reverse bias applied in concert

with switching cannot make the extraction of charge carriers faster than τ_{RC} . It follows that in case of RC limited extraction, recombination losses should be minimised by lowering C and/or R .

For charge carriers with lifetimes longer than τ_{RC} , but still comparable to the extraction time (on the order of 20 to 50 μs), the charge extraction process will be limited by a competition between the rates of charge extraction and recombination. Charge extraction is therefore dependent on the charge carrier mobility and lifetime. Under these conditions, a possible explanation for the observed increase in extracted charge with an applied reverse bias could be that faster charge transport, facilitated by an increasing applied reverse bias, results in a reduction in recombination during extraction and thereby accounts for the observed increase in extracted charge. This influence is expected to be strongly coupled with the mobility-lifetime product of the device active layer under investigation.

The $1 \mu\text{J cm}^{-3}$ excitation density extraction transients presented in Figure 5.3 (bottom) exhibit a shift in peak position to faster extraction times, as well as faster transient extraction tails with an increasing applied bias. These observations are in agreement with the above explanation, where an increased extraction rate is produced at higher applied reverse bias and could account for the increase in extracted charge with increasing applied reverse bias. However, the $100 \mu\text{J cm}^{-3}$ excitation density transients (Figure 5.3, top) were not observed to be noticeably faster at increasing applied reverse bias, with the extraction tail beyond 5 μs independent of applied bias and no shift in transient peak position observed. A shift to faster extraction times would be expected if the increase in extracted charge was due to an increased rate of extraction. Therefore the above explanation of faster charge transport under an applied reverse bias competing with recombination during extraction cannot be the sole origin of the observed increase in extracted charge, and likely not the dominant component at high charge densities within these photovoltaic devices. The influence of changing RC (through device capacitance and measurement circuit impedance) and the magnitude of applied reverse bias on the extraction rate will be investigated in Section 5.4.3.

2. Space Charge Limited Extraction

As was previously mentioned, the illuminated transients with an applied reverse bias as presented in Figure 5.3 exhibit characteristics consistent with space charge disturbed extraction transients at short delay times (high charge densities), where an initial extraction current plateau is observed (or initial current rise in subtracted transients). In the case of space charge limited extraction, only a fraction of charge (equal to the product of device capacitance and applied reverse bias CU) can be extracted from the device at any given time, causing the accumulation of charge carriers at their respective electrodes and screening of the applied electric field, while the remaining bulk of the charge density exists in a field-free charge reservoir.⁹⁹ The extracted charge measured at high excitation densities ($100 \mu\text{J cm}^{-2}$) and short delay times (below 5 μs) exceeds CU (2.1 nC for a 2 V applied reverse bias and device capacitance of 1.05 nF), suggesting the screening of applied

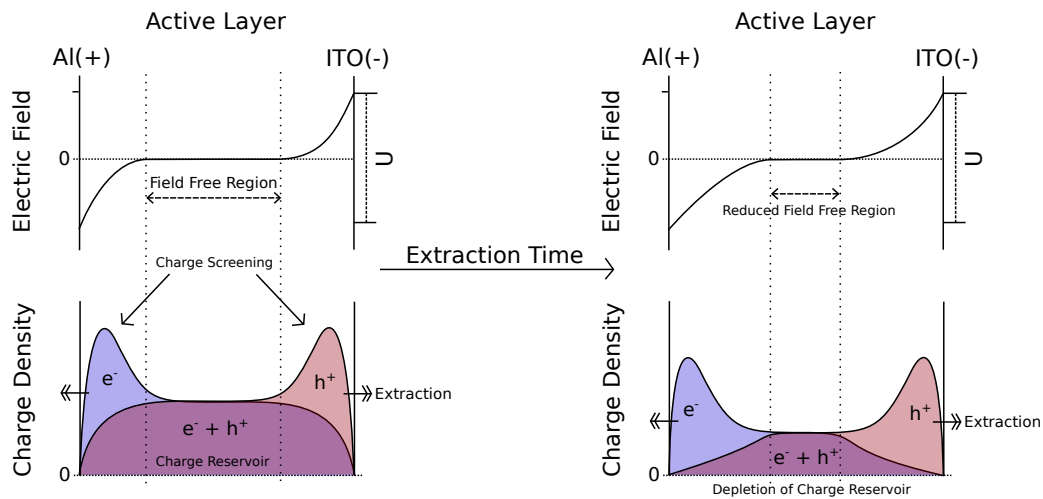


Figure 5.8: Illustrative figure of space charge perturbed extraction under an applied reverse bias at high charge density, with electric field (top) and charge density (bottom) as a function of the spatial distribution across the device active layer. Initially (left) during the charge extraction process (short circuit), charge carriers redistribute/drift to respective contacts for extraction under the influence of an applied reverse bias U . The maximum extraction rate of charge is limited, resulting in charge carrier accumulation at the device contacts. This accumulation charge density screens the applied field, and results in the formation of a field free region within the device (charge reservoir). Charge carrier overlap is greatest within this field free region. After an increased extraction time (right), the field free region is reduced as the charge reservoir is depleted through extraction of charge carriers.

electric field by the photogenerated charge stored within the device during charge extraction.

Charge extraction can be contact limited (RC as discussed above) or space charge limited. In the former case there is a barrier and that controls the current flow, determined by the device contacts and measurement circuit. In the latter, the contacts are ohmic, or at least not limiting and thus space charge limits extraction. Figure 5.8 illustrates space charge perturbed extraction under an applied reverse bias at high charge density, with electric field (top) and charge density (bottom) as a function of the spatial distribution across the device active layer. Initially (left) during the charge extraction process (short circuit), charge carriers redistribute/drift to respective contacts for extraction under the influence of an applied reverse bias U . The maximum extraction rate of charge is limited (CU), resulting in charge carrier accumulation at the device contacts. This accumulation of charge density screens the applied potential and results in the formation of a field free region within the device (charge reservoir). Charge carrier overlap is greatest within this field free region and consequently recombination is greatest within this reservoir. After an increased extraction time (right), the field free region is reduced as the charge reservoir is depleted

through the extraction of charge carriers.

Under space charge limited extraction, the maximum rate of current extraction is limited to CU which in turn determines the time required to extract all charge carriers. If the charge carrier lifetime is longer than the extraction time (no significant recombination during extraction), charge densities greater than CU can be extracted. Otherwise the charge carriers within the reservoir recombine during extraction and therefore do not contribute to the extracted charge.⁹⁹ As CU is directly proportional to applied bias, increasing the applied reverse bias will result in a corresponding increase in the rate of charge extraction. This faster extraction of charge will lead to a rapid decrease in the carrier density within the reservoir during extraction, producing a longer carrier lifetime during extraction at increasing applied reverse bias. This relative extension of lifetime during extraction will in turn reduce recombination losses within the reservoir, yielding a higher measured charge density. This effect explains the observed bias dependence of extracted charge when charge density exceeds CU , without the observation of faster extraction transients (Figure 5.4, extracted charge for the $100 \mu\text{J cm}^{-2}$ transients (top) is an order of magnitude greater than CU , while $1 \mu\text{J cm}^{-2}$ transients (bottom) are comparable to CU). This does not however account for the observed increase in extracted charge with applied reverse bias when the charge density is lower than CU , or lifetime is longer than the extraction time. The influence of changing CU (through device capacitance and the magnitude of applied reverse bias) on charge extraction behaviour under space charge limited conditions will be investigated in Section 5.4.3.

3. Spacial Separation of Electrons and Holes through Electrode Polarisation

Under conditions where charge density is less than CU , charge extraction is not strongly space charge disturbed, however an increase in extracted charge with increasing applied reverse bias is consistently observed. The extraction of a charge carrier population that would otherwise not be extracted without the application of a bias, either due to too short a lifetime (recombination during extraction) or due to the energetic depth within the density of states distribution (trap state occupancy), can account for the observed increase in extracted charge.

Where charge carrier lifetime is shorter than, or comparable to the extraction time, the reduction of recombination during extraction under an applied reverse bias may account for some of the observed increase in extracted charge. One origin of this behaviour may be through an increased rate of extraction under an applied reverse bias, as discussed above. Another possible origin is through the spatial separation of charge carriers to their respective device contact during extraction, caused by the polarisation of device contacts under an applied potential. This leads to a reduced average overlap of respective charge carrier populations, thereby effectively reducing the recombination probability during extraction. This behaviour is illustrated in Figure 5.9, comparing the extraction of a given charge density (below CU , with lifetime comparable to extraction time), both with and without an applied bias. The influence of this spatial separation of charge

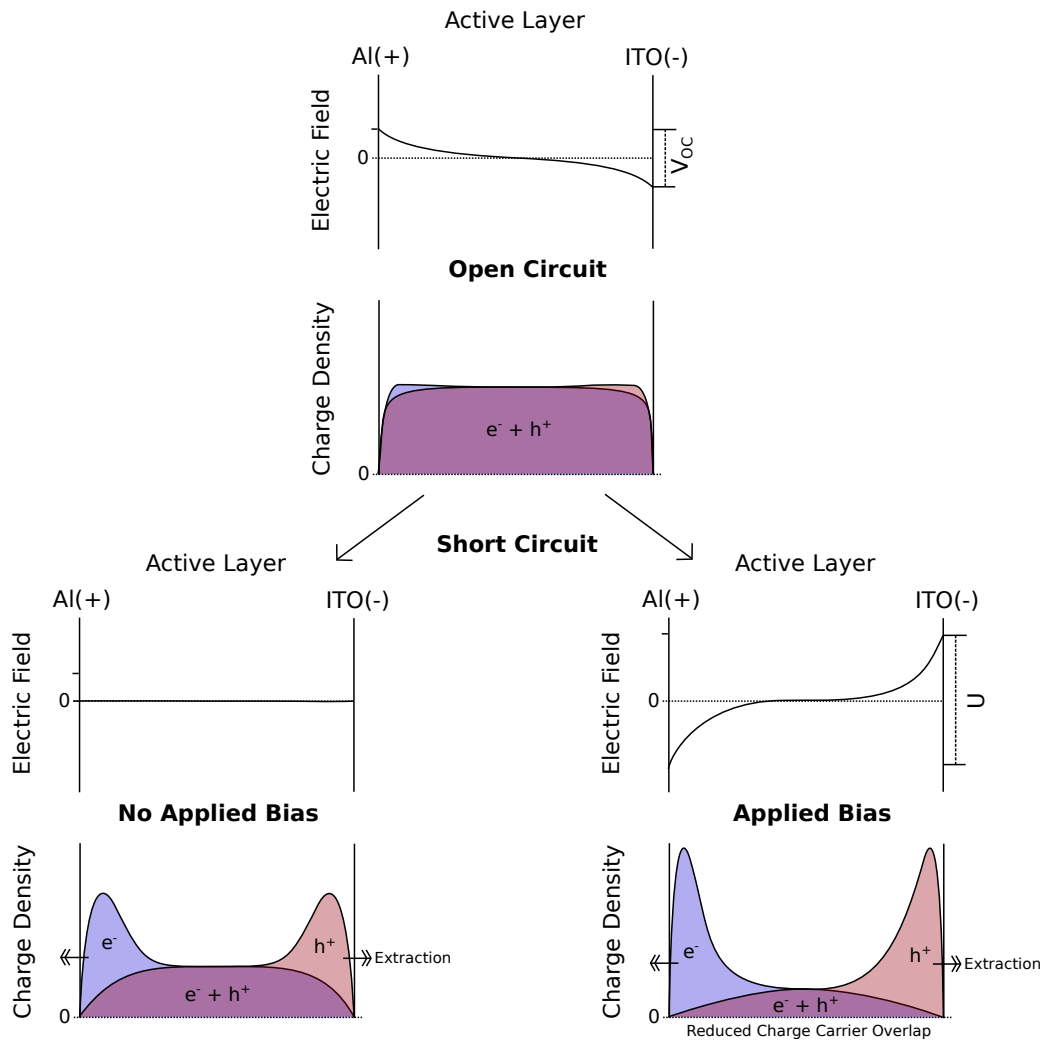


Figure 5.9: Illustrative figure of spatial separation of charge carriers under an applied reverse bias at low charge density, with electric field and charge density across the device active layer. At open-circuit (top) prior to charge extraction, the charge carrier spatial distribution is uniform. Upon short-circuit conditions (bottom) charges are extracted. The spatial overlap of respective charge carriers is reduced with an applied reverse bias U (bottom right) relative to no applied bias (bottom left).

carriers during extraction is expected to be strongly influenced by active layer thickness, and will be further investigated in Section 5.4.3.

4. Charge Carrier Losses due to Trapping

Where charge density is below CU and charge carrier lifetime is significantly longer than the extraction time (for example, at delay times on the order of $100 \mu\text{s}$), recombination during extraction does not account for a significant loss of charge density, and therefore a reduction in recombination during extraction (either through an increased rate of extraction or spatial separation) is insufficient to explain the observed increase in extracted charge with an applied reverse bias under these conditions. This increase in extracted charge is still however due to the extraction of a charge carrier population that would otherwise not be extracted. Therefore, a possible explanation for the observed increase in extracted charge with an applied bias under these conditions is due to the increased extraction of charge carriers at energetic depths within the density of states distribution (trap state occupancy), such that they would not be extracted without the additional potential of an applied reverse bias. An increasing applied reverse bias would allow extraction of these charge carriers at increasing energetic depths within the trap state density distribution, thereby accounting for the observed increase in measured charge density. This behaviour is therefore expected to be strongly influenced by the trap state density distribution, and will be further investigated in Section 5.4.4. The increased extraction of trap states is also expected to influence the measured average lifetime for a given charge density, as an increasing portion of extracted charge density will correspond to trapped charges with longer relative lifetimes. This can be observed in the low charge density region of Figure 5.7. Further investigations of the influence of an applied bias on the measurement of recombination kinetics will also be presented in Section 5.4.4.

5.4.3 Distinguishing the Dominant Charge Extraction Loss Mechanism

The application of a reverse bias in time resolved charge extraction measurements results in an increase in extracted charge density, up to twice that without an applied bias, indicating that at least half of all charge density is lost during charge extraction measurements without an applied bias. Based on the discussions presented in the previous Section 5.4.2, this increase in extracted charge density is attributed to multiple factors that influence the charge extraction process, with the contribution of each expected to depend on: the charge density n relative to device capacitive response CU , and the charge carrier lifetime τ relative to the charge extraction time τ_{Q_e} .

With respect to the expected origin of the increase in extracted charge density with an applied bias in time resolved charge extraction measurements:

1. ($n \geq CU, \tau \leq \tau_{Q_e}$) due to a reduction in recombination losses during extraction facilitated by an increased rate of extraction under space charge limited conditions.
2. ($n < CU, \tau \leq \tau_{Q_e}$) due to a reduction in recombination losses during extraction facilitated

by a combination of: an increased rate of transport/extraction under an applied reverse bias limited by the measurement circuit response (RC); and the spatial separation of charge carriers during extraction under an applied reverse bias.

3. ($n < CU$, $\tau > \tau_{Q_e}$) due to extraction of deep trap states that would otherwise not be extracted, facilitated by an applied potential reverse bias.

Further investigations are presented in this section with the aim of verifying the above assignments for origins of the observed increases in extracted charge density with an applied reverse bias, as well as determining the relative contribution of each case under a range of charge densities (variation of excitation density and delay time). This will be accomplished through variation of: photovoltaic device geometry (device capacitance C and thickness), measurement circuit resistance (R), and measurement conditions (applied reverse bias U and charge density). This will enable a systematic investigation of extraction loss mechanisms through variation of n/τ , RC , CU , and device geometry. Additional investigations are then performed in Section 5.4.4 to determine the influence of the reduced extraction losses (facilitated by an applied reverse bias) on the measurement of recombination kinetics and trap state density distribution in time resolved charge extraction measurements.

Variation of Applied Bias, Device Capacitance, and Measurement Resistance

Space charge limited extraction conditions were previously identified when using an applied reverse bias during charge extraction, influencing the charge extraction process, where capacitive charging initially dominates current extraction. This behaviour is expected to depend on the device capacitance C and the magnitude of applied reverse bias U . The measurement circuit response RC will also influence the charge extraction process, determining the limit of extraction rate τ_{RC} . Therefore an analysis of charge extraction behaviour with variation of U , C , and R is presented in the following sections. Variation of C is achieved through fabrication of devices with different active surface area. Variation of C can also be achieved through variation of device active layer thickness, however this would influence extraction behaviour through a number of additional mechanisms (for example, charge transport) and will be explored in detail later in this chapter.

Modelling Transient Response Without Illumination and Varied of Applied Bias

The response of a photovoltaic device to a reverse bias square pulse potential without illumination is expected to be comparable to that of a dielectric parallel plate capacitor. As such, the extracted charge due to the capacitive charging current will be CU for a device with capacitance C and applied potential U . This charging current will be greatest initially, limited by the measurement circuit response τ_{RC} , beyond which decaying exponentially until the extracted charge approaches CU with a decay time constant equal to τ_{RC} . In order to fit the photovoltaic device responses without illumination, the following model was used

$$A(t) = A_1 \exp(-t/\tau_1) + g(t) \quad (5.1)$$

where the extracted current as a function of extraction time $A(t)$ is equal to the sum of an exponential decay term A_1 with decay lifetime τ_1 used to model the capacitive charging current, and some function $g(t)$ representing any additional current extraction due to free carriers within the active layer (doping facilitating additional charge carrier injection/extraction). The fitted decay lifetime τ_1 is a direct measurement of the circuit response τ_{RC} arising from the total circuit impedance and device capacitance. The total circuit impedance comprises the measurement impedance R_M ($50\ \Omega$ unless otherwise stated), the device series resistance R_S , and the impedance of the function generator and switch ($\approx 80\ \Omega$).

Applied bias charge extraction measurements were performed on both P3HT:PCBM and PCDTBT:PCBM devices presented and characterised in the previous chapter for consistency. A range of applied reverse bias (U) were used without illumination, with the above model used to fit the transient response. This is performed to assess the validity of the presented model, and used as a baseline for further analysis of transient response with variation of R and C presented later in this section. The calculated series resistance for the presented PCDTBT:PCBM and P3HT:PCBM devices was 30 and $60\ \Omega$ respectively (obtained through steady-state current-voltage measurements presented in the previous chapter), yielding an estimated total circuit impedance of 160 and $190\ \Omega$. The device active layers are 90 and 150 nm for PCDTBT:PCBM and P3HT:PCBM respectively.

Figure 5.10 displays the charge extraction response transients (top) and integral (bottom) without illumination for the PCDTBT:PCBM device under a range of applied reverse bias. Fits to the model (Equation 5.1) are also displayed (broken lines) for each transient and integral, representing the capacitive charging current. The exponential decay component A_1 is sufficient to fit the transients well, indicating solely capacitive charging current CU . A minor charge injection component is however observable beyond $2\ \mu\text{s}$ extraction time in the transient integral plots. The calculated extracted charge increases linearly with applied reverse bias and exhibits a constant decay lifetime τ_1 . An average device capacitance C of $2.20\ \text{nF}$ and τ_{RC} of $350\ \text{ns}$ are obtained, yielding a total circuit resistance of $160\ \Omega$ which compares well with the previously estimated value of $160\ \Omega$. This measured value of C also compares well with a device active layer thickness of $90\ \text{nm}$, using the device surface area of $0.06\ \text{cm}^{-2}$ and assuming a dielectric constant of 3.8 for the PCDTBT:PCBM (1:4) blend.^{135, 140}

Figure 5.11 display the charge extraction response transients (top) and integral (bottom) without illumination for the P3HT:PCBM device under a range of applied reverse bias. Fits to the model (Equation 5.1) are also displayed for each transient and integral (broken line), representing the capacitive charging current. Although the transient response appears to approach zero beyond $10\ \mu\text{s}$ extraction time, the transient integral clearly indicates a component of continued current extraction. The initial transient response is dominated by the exponential decay component A_1

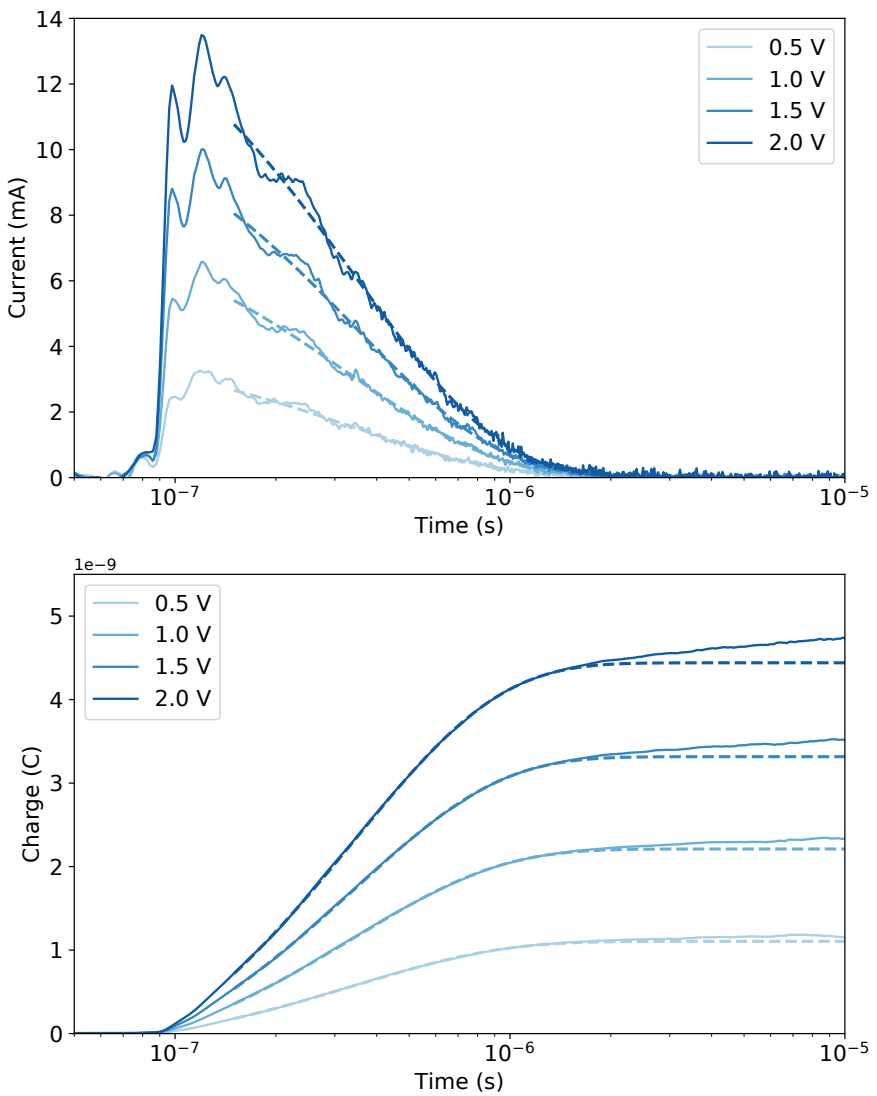


Figure 5.10: Charge extraction response transients (top) and integral (bottom) without illumination for a PCDTBT:PCBM device under a range of applied reverse bias. Fits to the model (Equation 5.1) are also displayed (broken lines) for each transient and integral, representing the capacitive charging current.

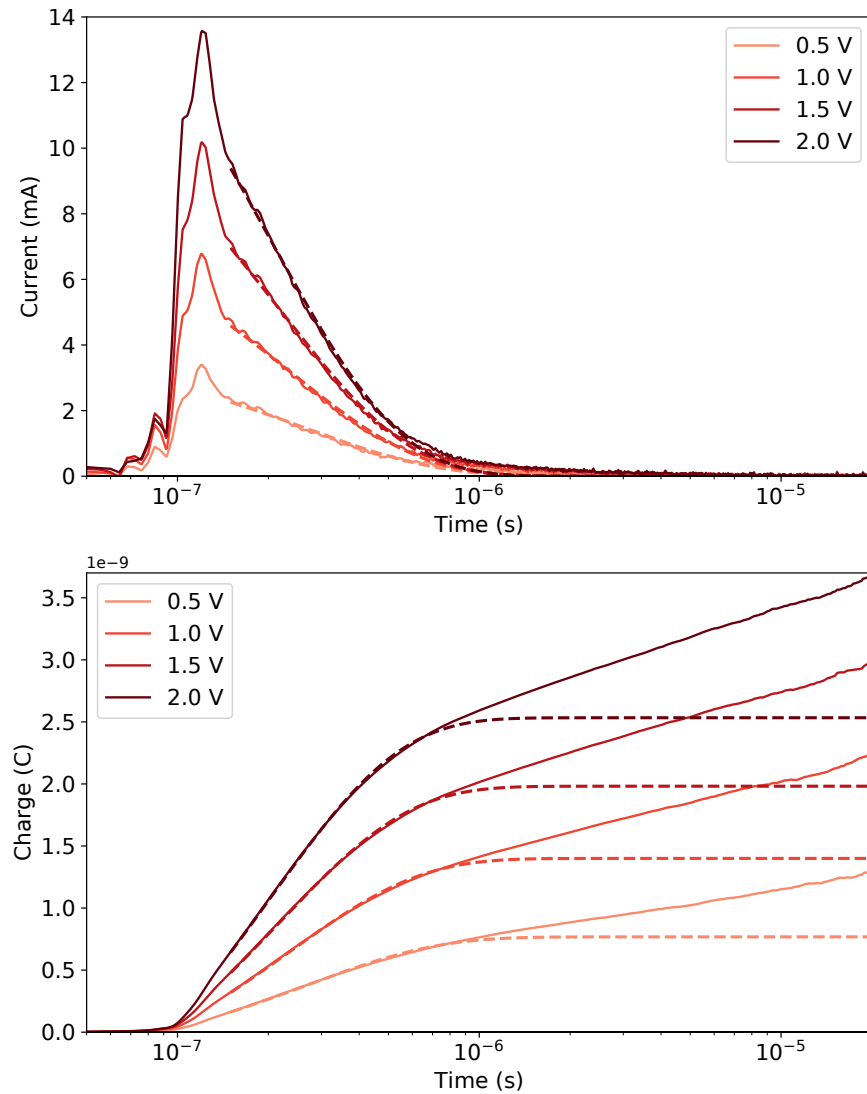


Figure 5.11: Charge extraction response transients (top) and integral (bottom) without illumination for a P3HT:PCBM device under a range of applied reverse bias. Fits to the model (Equation 5.1) are also displayed for each transient and integral (broken line), representing capacitive charging current.

prior to $1 \mu\text{s}$ extraction time, while an additional non-zero component $g(t)$ is apparent for the remainder of the transient. This indicates the existence of current injection/extraction in this P3HT:PCBM device in addition to the capacitive charging current. This behaviour has been observed for P3HT:PCBM systems in similar charge extraction measurements, and is due to positive doping of the blend film.¹⁴¹ The calculated extracted charge increases linearly with applied reverse bias and exhibits a constant τ_1 . An average C of 1.30 nF and τ_{RC} of 220 ns are obtained, yielding an R_T of 170Ω which compares well with the previously estimated value of 190Ω . This measured value of C also compares well with a device active layer thickness of 150 nm , using the device surface area of 0.06 cm^{-2} and assuming a dielectric constant of 3.5 for the P3HT:PCBM (5:4) blend.¹⁴⁰

For both PCDTBT:PCBM and P3HT:PCBM devices, the transient response without illumination exhibits a capacitive charging current CU that linearly depends on applied reverse bias with a constant exponential decay time τ_{RC} , where fitting of transients yield values for device capacitance and total circuit impedance that compare well with independent measurements of device volume and estimates of total measurement circuit impedance. The P3HT:PCBM device exhibits an additional transient response component due to positive doping of the blend film, however the model employed is sufficient to separate this component from the capacitive charging current component, as the CU response is significantly faster than charge extraction and initially dominates the transient response. Fitting and analysis of transient response without illumination and with an applied reverse bias can be employed to directly determine CU and τ_{RC} , and are independent of the magnitude of applied reverse bias. This will be utilised in the following studies incorporating variation of measurement impedance and device capacitance.

Variation of Measurement Impedance

In order to assess the influence of measurement circuit response τ_{RC} on the applied reverse bias charge extraction process at charge carrier lifetimes τ comparable to, or faster than τ_{RC} , applied bias time resolved charge extraction measurements are performed on a P3HT:PCBM device at a range of measurement circuit impedances R_M , from the typical 50Ω down to 10Ω . A reduction in R_M will reduce τ_{RC} and therefore alter the relative difference between τ and τ_{RC} for a given charge density, impacting the degree of recombination losses during extraction under these high charge density (short τ) conditions. A high excitation density of $100 \mu\text{J cm}^{-2}$ is used to ensure high initial charge density and corresponding short initial τ , in order to best illustrate the influence of variation in R_M on the charge extraction process (see Case 1 as discussed at the beginning of this Section 5.4.3). A device was fabricated with an active layer thickness of 70 nm rather than the previously presented 150 nm , in order to increase the magnitude of CU response and to extend τ_{RC} as to provide greater clarity (signal-to-noise at low impedance) for a reduction in R_M below the typical 50Ω .

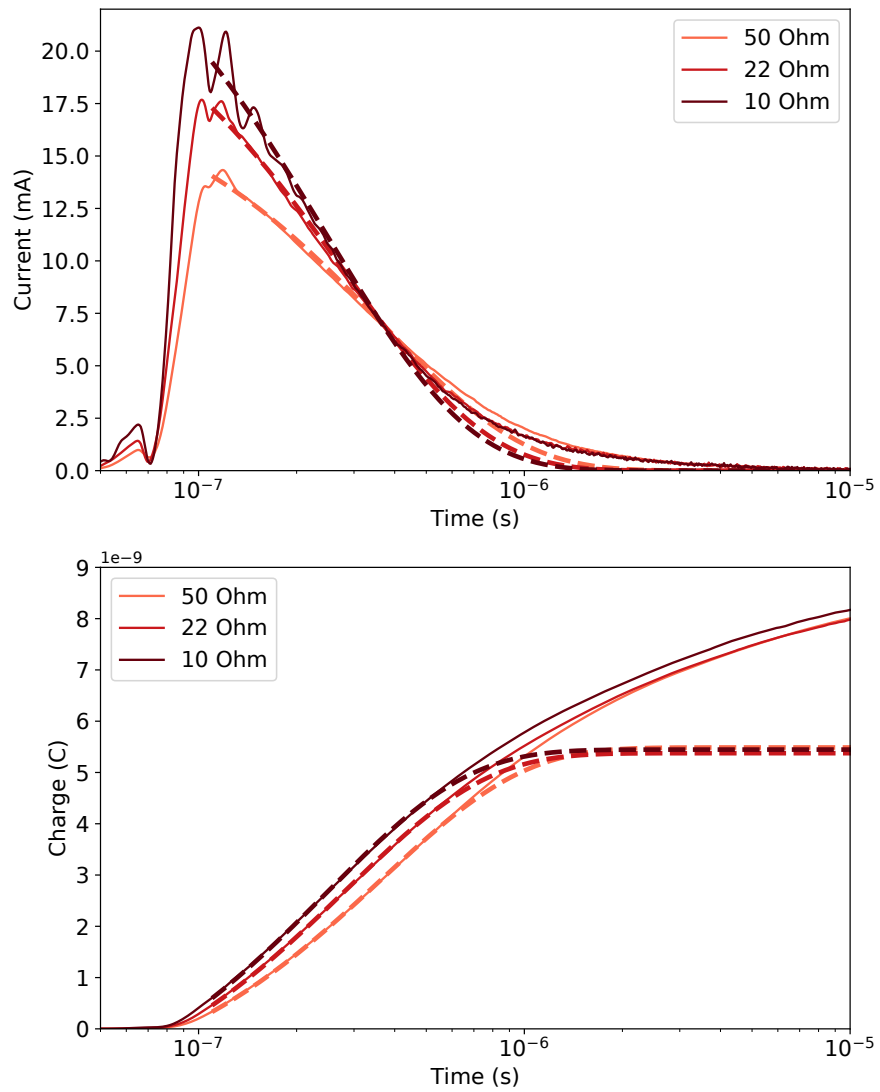


Figure 5.12: Charge extraction transients (top) and integral (bottom) without illumination for a P3HT:PCBM device at a range of measurement impedances (as labelled) using a 2 V applied reverse bias. Fits to the model (Equation 5.1) are also displayed for each transient and integral (broken line), representing the capacitive charging component.

Figure 5.12 displays the charge extraction transients (top) and integral (bottom) without illumination for the P3HT:PCBM device at multiple measurement impedances from 50 to 10 Ω using a 2 V applied reverse bias. Fits to the model (Equation 5.1) are also displayed for each transient and integral (broken line), representing the capacitive charging component. The initial transient response is dominated by the CU response prior to 1 μs extraction time, while the remainder of the transient exhibits an additional current extraction component indicating significant doping injection/extraction current. A clear trend is observed in both transient response and integral, where a reduction in R_M yields a reduction in τ_{RC} from 370 ns at 50 Ω to 250 ns at 10 Ω , and results in faster extraction transients at lower R_M . The total extracted charge (including additional doping current component) and measured CU are however independent of a variation in R_M , with an average calculated C of 1.70 nF that compares well with the device active layer thickness of 70 nm. For a constant applied reverse bias and device capacitance the CU response should be independent of R_M and therefore τ_{RC} , consistent with the above observations.

Figure 5.13 displays the illuminated charge extraction transients (top) and integral (bottom) for a range of delay times (as labelled), each at multiple R_M using an applied reverse bias of 2 V and 100 $\mu\text{J cm}^{-2}$ excitation density. The observed rise in extraction current indicates space charge limited extraction under the applied bias as discussed previously. For the presented delay times:

- **100 ns** represents a high charge density where τ should be faster than, or comparable to τ_{RC} , and significant recombination losses will occur during extraction (RC and space charge limited extraction);
- **1 μs** represents a charge density where τ is longer than τ_{RC} , however still shorter than the extraction time, and recombination losses during extraction should still be significant (space charge limited extraction);
- **5 μs** represents a charge density where τ is much longer than τ_{RC} , however still comparable to the extraction time, and recombination losses during extraction should be less significant (space charge limited extraction);
- **50 μs** represents a charge density where τ is significantly longer than both τ_{RC} and extraction time, and therefore should not incur significant recombination losses during extraction (neither RC or space charge limited extraction).

All delay times exhibit faster extraction transients with a reduction in R_M , displaying a shift in extraction current peak and shift in transient tail towards faster extraction times. The total extracted charge however is only altered through a variation in R_M for the 100 ns and 1 μs delay times, exhibiting a 10 % and 5 % increase in extracted charge respectively with reduction in R_M from 50 to 10 Ω . Both longer delay times exhibit a total extracted charge independent of R_M , even with the observed slower extraction transients. The charge density decay as a function of delay time (from 10 ns to 50 μs) is presented in Figure 5.14.

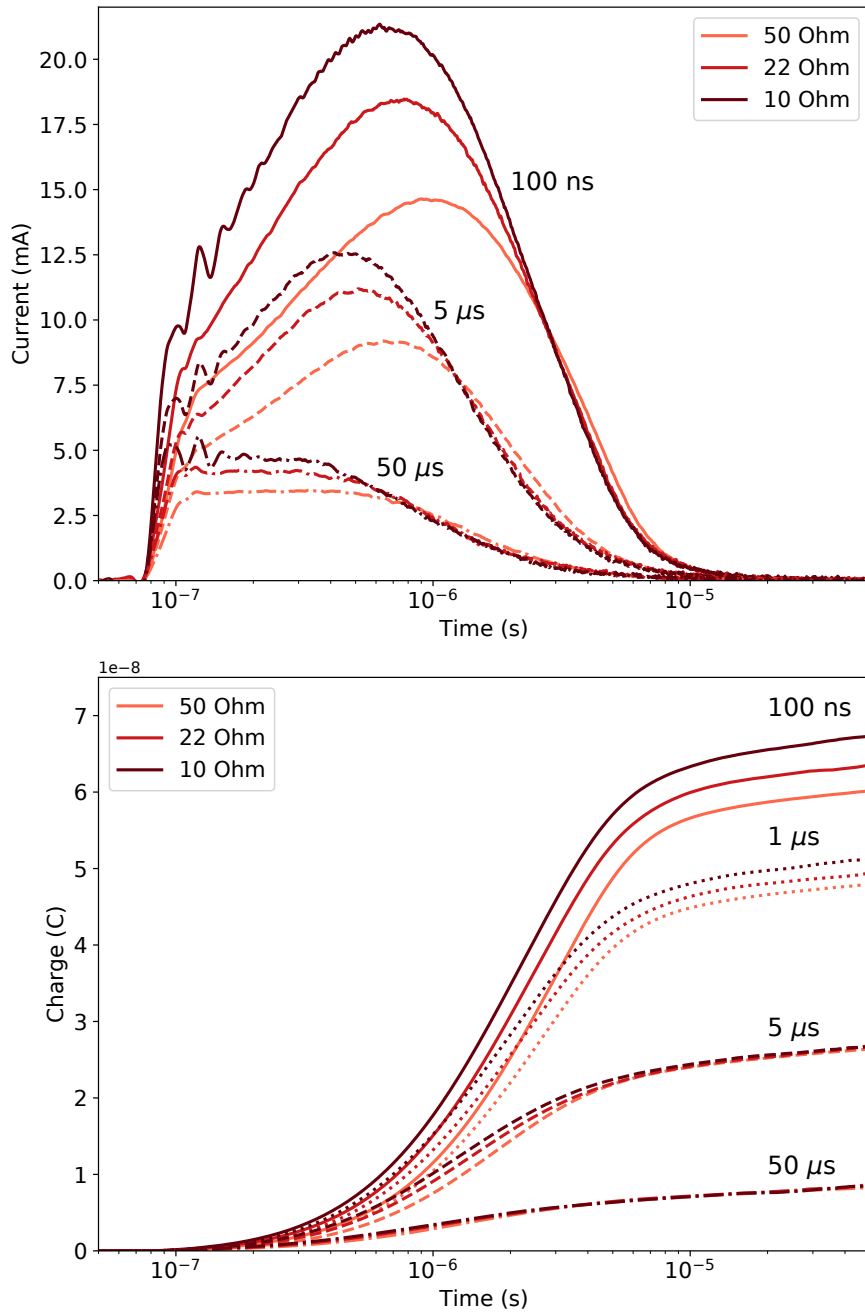


Figure 5.13: Charge extraction transients (top) and corresponding integral (bottom) for a P3HT:PCBM device at multiple delay times (as labelled), each at a range of measurement impedances (as labelled). An applied reverse bias of 2 V and $100 \mu\text{J cm}^{-2}$ excitation density was used. Please note that the $1 \mu\text{s}$ extraction transients have been excluded (top) for clarity.

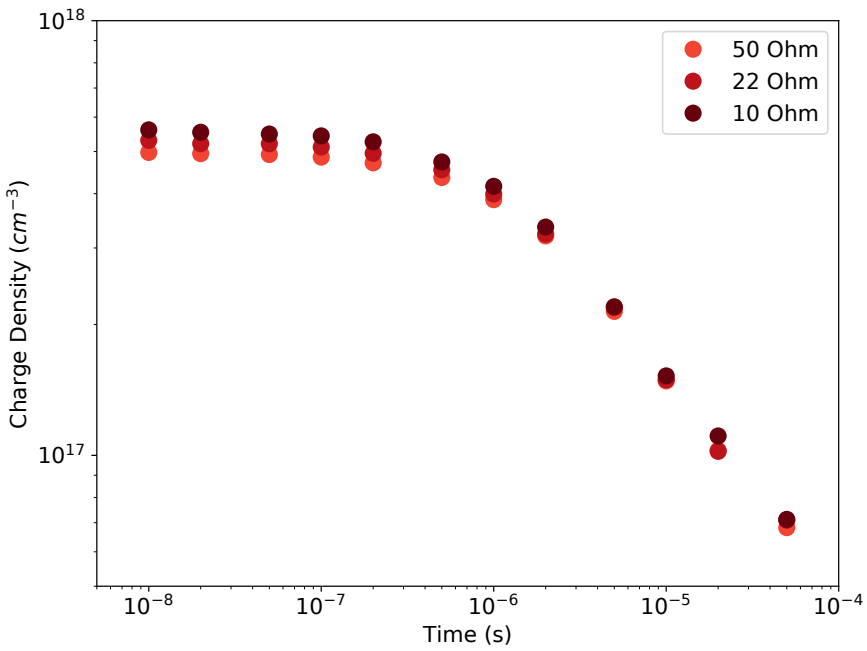


Figure 5.14: Charge density decay for a P3HT:PCBM device at a range of measurement impedances (as labelled). An applied reverse bias of 2 V and $100 \mu\text{J cm}^{-2}$ excitation density was used.

At the 100 ns delay time where τ is faster than, or comparable to τ_{RC} , an increased rate of extraction facilitated by a reduction in R_M and therefore τ_{RC} is expected to reduce recombination losses during extraction, and can therefore account for the observed increase in extracted charge. However at a delay time of 1 μs , the measured τ of 5 μs is over an order of magnitude greater than the slowest measured τ_{RC} of 350 ns at 50 Ω . The observation of an increase in extracted charge with a reduction in measurement impedance at charge densities with a charge carrier lifetime significantly longer than τ_{RC} indicates that R_M can influence the charge extraction process beyond τ_{RC} . An explanation for this observation is that, under space charge limited extraction conditions as observed herein, the total extraction current is limited by CU , with this capacitive charging current initially dominating the contact polarisation, and therefore controlling the extracted current (as the dielectric charging response is significantly faster than τ_{RC} while charge extraction is limited by internal charge carrier redistribution and relatively slow charge transport). As the current flow due to the CU charging response decays, more of the photogenerated charge density can be extracted. Although CU is independent of R_M , the CU response decays with a lifetime proportional to τ_{RC} . Therefore a reduction in R_M will cause the CU response to decay faster, thereby allowing a greater relative extraction rate of the photogenerated charge density with a corresponding reduction in recombination during extraction. As the CU response is not significant beyond 1 μs for this device, this effect does not influence the total extracted charge density when the charge carrier lifetime longer than 1 μs (longer delay times, reduced charge density). This is indicated by the independence of extracted charge on R_M at the 5 μs delay time, even though recombination losses during extraction should still be significant at this delay time.

To summarise the influence of measurement impedance variation with regards to the dominant loss mechanisms in applied bias time resolved charge extraction measurements, an order of magnitude reduction in R_M at high charge densities only results in an increase in extracted charge of less than 10 %. This increase represents a reduction in recombination losses during τ_{RC} facilitated by a reduced τ_{RC} and consequently increased rate of charge extraction (visible as a shift in transient peak Figure 5.13). The small magnitude of increase in extracted charge (and limited time domain of influence) observed indicates that an increased rate of extraction facilitated by reducing RC limitations is significantly less effective at reducing overall extraction losses than the application of a reverse bias, and cannot provide improvements where the charge carrier lifetime exceeds τ_{RC} by greater than 4-fold.

Variation of Device Capacitance (Surface Area)

Variation of device capacitance C will result in a variation of RC , as well as the capacitive charging current CU which as discussed in Section 5.4.2, are both expected to influence the charge extraction process under space charge limited conditions. That is, through changes in extraction rate or space charge limited extraction, and thereby influencing the degree of recombination during extraction. In a similar approach to the above variation of measurement impedance, variation of device capacitance was performed through the fabrication of otherwise identical P3HT:PCBM devices with active surface areas of 0.06 and 0.04 cm² and an active layer thickness of 160 nm. Applied bias time resolved charge extraction measurements were then performed on these devices at a range of applied reverse bias and excitation densities.

Figure 5.15 displays the charge extraction transients (top) and integral (bottom) without illumination for the two P3HT:PCBM devices with 0.06 and 0.04 cm⁻² device active surface areas, using a 2 V applied reverse bias and 10 $\mu\text{J cm}^{-2}$ excitation density. Fits to the model (equation 5.1) are also displayed for each transient and integral (broken line), representing the capacitive charging component. Both devices exhibit predominately capacitive charging current CU , with a calculated C of 1.15 and 0.75 nF for the 0.06 and 0.04 cm⁻² surface area devices respectively, in agreement with a device active layer thickness of 160 nm. A 30 % reduction in surface area is observed to yield a 30 % reduction in CU response, while the measured τ_{RC} decreased from 150 to 95 ns, again in agreement with a direct 30 % reduction in device capacitance C .

Figure 5.16 displays the illuminated charge extraction transients (top) and integral (bottom) for the two P3HT:PCBM devices, using a 2 V applied reverse bias and 10 $\mu\text{J cm}^{-2}$ excitation density, and a range of delay times (as labelled). As the larger volume device will produce a greater photogenerated charge population, both transient response and integral have been normalised to device active surface area to enable a direct comparison of extracted charge proportional to charge density. All transients exhibit an initial rise in extracted current indicating space charge limited extraction at these high initial charge densities. The smaller surface area exhibits faster relative

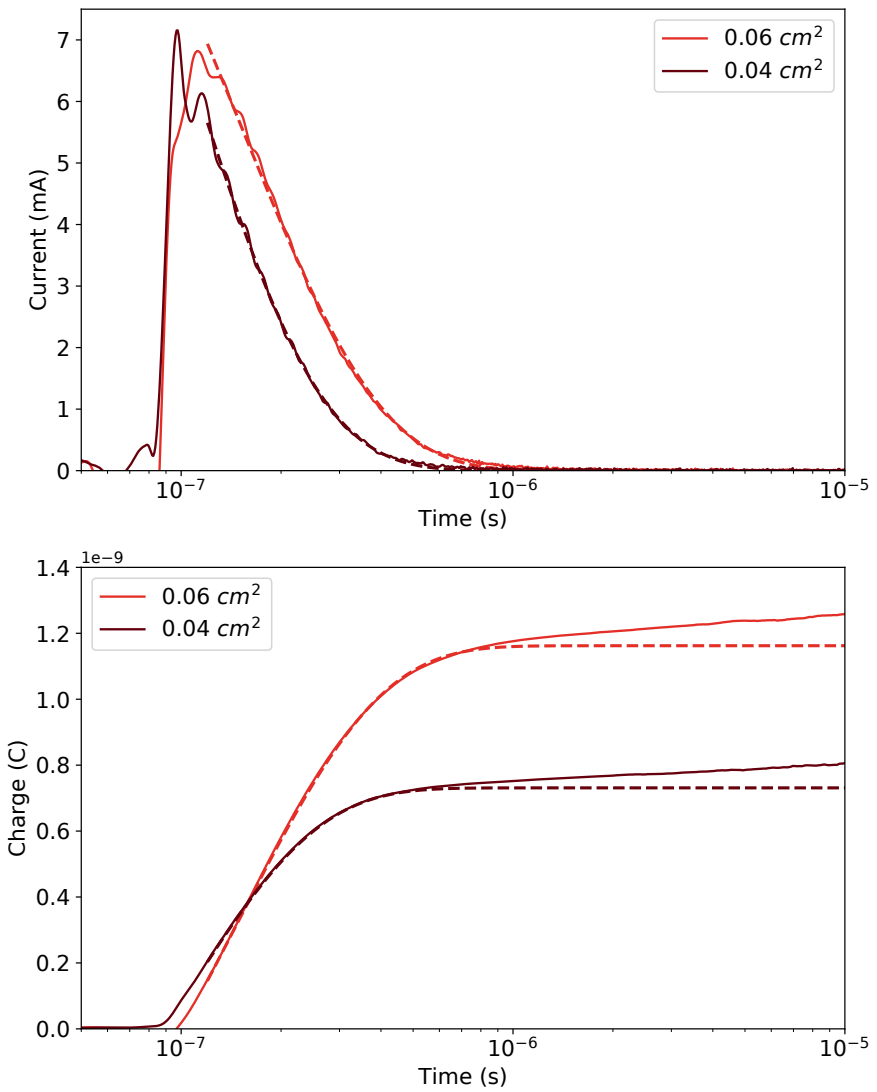


Figure 5.15: Charge extraction transients (top) and integral (bottom) without illumination for two P3HT:PCBM devices with 0.06 and 0.04 cm^{-2} device active surface areas, using a 2 V applied reverse bias and $10 \mu\text{J cm}^{-2}$ excitation density. Fits to the model (Equation 5.1) are displayed for each transient and integral (broken line), representing the capacitive charging component.

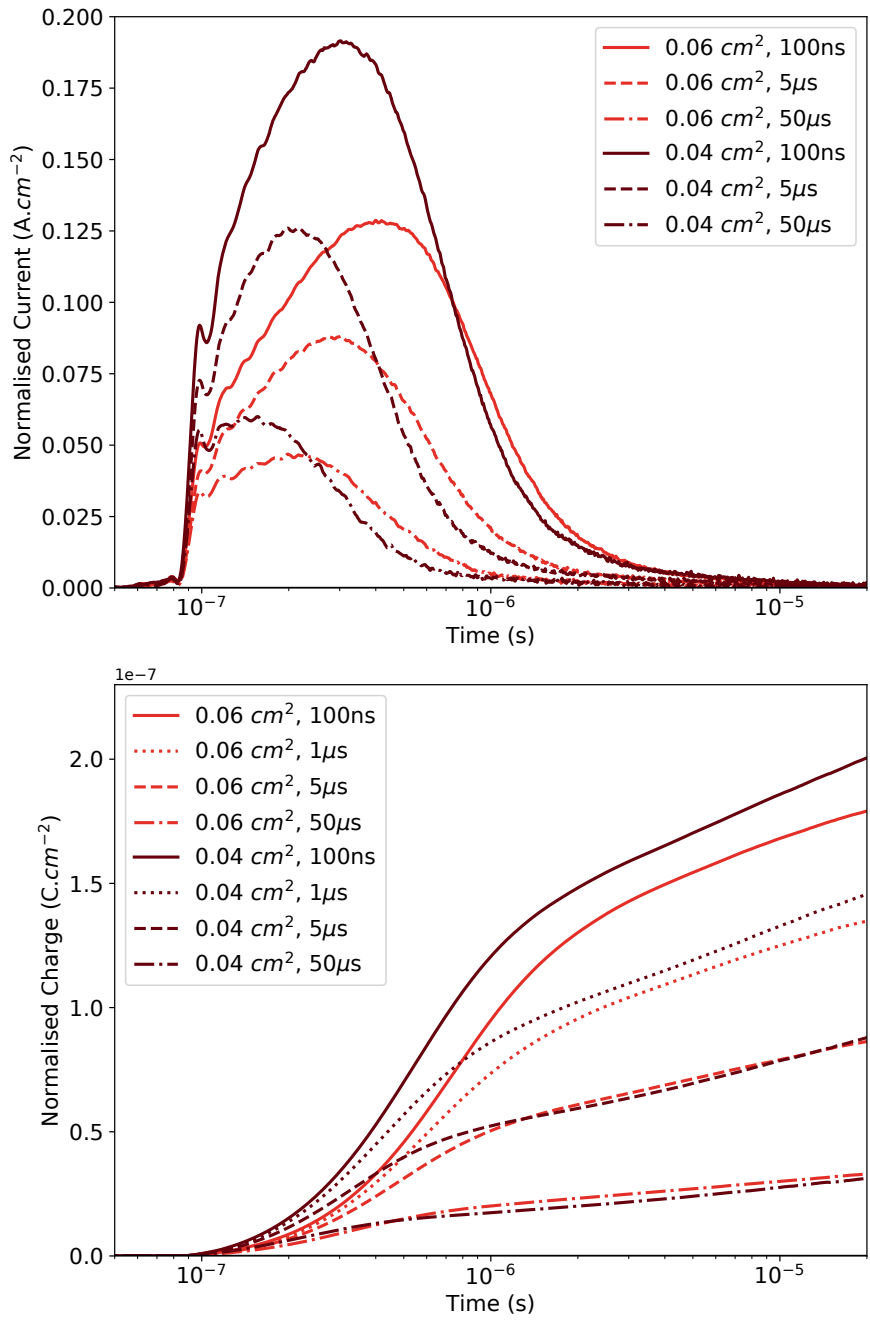


Figure 5.16: Illuminated charge extraction transients (top) and integral (bottom) for two P3HT:PCBM devices with 0.06 and 0.04 cm^{-2} device active surface areas, using a 2 V applied reverse bias, $10 \mu\text{J cm}^{-2}$ excitation density, and a range of delay times (as labelled). Both transient response and integral have been normalised to device active surface area for a direct comparison. Please note that the $1 \mu\text{s}$ extraction transients have been excluded (top) for clarity.

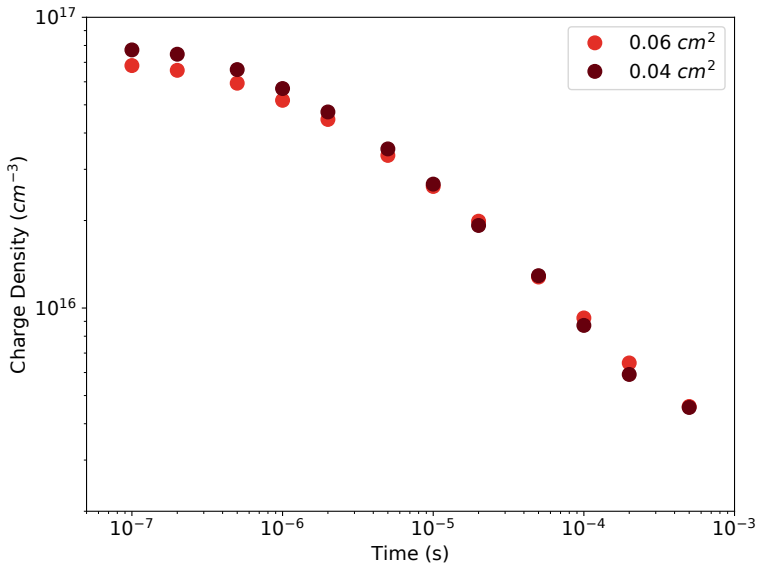


Figure 5.17: Charge density decay for P3HT:PCBM devices with difference active surface area (as labelled). An applied reverse bias of 2 V and $10 \mu\text{J cm}^{-2}$ excitation density was used.

extraction transients at all delay times, and exhibits a greater relative extracted charge at both 100 ns and 1 μs delay times of 15 and 7 % respectively. At delay times beyond 1 μs however, extracted charge is independent of device capacitance (active surface area). The charge density decay as a function of delay time (from 100 ns to 500 μs) is presented in Figure 5.17.

The above results are similar to those observed in Figure 5.13 for a variation in measurement impedance, where an increase in extracted charge is still obtained at charge carrier lifetimes longer than τ_{RC} . This is again attributed to the shift in *CU* charging current response decay with a variation of τ_{RC} , leading to reduced recombination during extraction under space charge limited conditions when the charge carrier lifetime is comparable to, or faster than the *CU* decay. In addition to the variation of τ_{RC} , a reduction of *C* also reduces the magnitude of the *CU* response which can further increase the influence of this outlined behaviour. However a reduction in *CU* also reduces the charge density at which space charge begins to limit extraction, and therefore may not significantly change the extraction process regarding the degree of recombination losses.

To summarise the influence of device active surface area variation with regards to the dominant loss mechanisms in applied bias time resolved charge extraction measurements, a 30 % reduction in area at high charge densities only results in an increase in extracted charge density of less than 15 %, with a time domain of influence limited to the nanosecond timescale. Although a reduction in measurement *RC*, through a reduction of either measurement impedance or device surface area can result in a reduction of recombination losses during extraction under space charge limited conditions, practical limits to the utility of this approach are imposed by the signal-to-noise ratio generated at increasingly low measurement impedances, and the inherent complexity of fabricating

device with increasingly small active surface area.

Variation of Device Active Layer Thickness

A variation in device capacitance has an influence on the degree of recombination losses during extraction under space charge limited conditions. Variation of device active layer thickness will vary device capacitance and is therefore expected to yield a similar effect on the extraction process, altering both CU response and τ_{RC} . However variation in device active layer thickness is expected to introduce additional complexity to the interpretation of charge extraction transients. Active layer thickness also influences the internal electric field under an externally applied potential, as well as charge carrier transport and trap state extraction behaviour, and will influence the relative portion of charge density within the field-free charge reservoir under space charge limited extraction conditions. Each of these effects will impact the measurement of charge density and are expected to be charge density/charge carrier lifetime dependent. Beyond the influence of active layer thickness on the charge extraction process, inherent spatial separation of charge carriers in thin active layers has been reported to influence recombination kinetics at open circuit,³⁴ and is therefore also expected to influence the measurement of charge density decay through time resolved charge extraction, as well as subsequent analysis and calculation of charge carrier lifetime and trap state density distribution. These behaviours will be further investigated in Section 5.4.4.

This section seeks to investigation the influence of device active layer thickness on the charge extraction process, and further the influence of an applied reverse bias at various active layer thickness on the measurement of charge density. Multiple sets of P3HT:PCBM devices were fabricated, identical other than a variation in active layer thickness, with charge extraction measurements performed under a range of charge densities and applied reverse bias. All measurements presented below have additionally been performed on devices incorporating the PCDTBT:PCBM material system, with analysis yielding outcomes consistent with those presented herein, and have therefore been excluded for simplicity of illustration.

Applied bias time resolved charge extraction measurements were performed on three P3HT:PCBM devices with active layer thickness of 80, 100, and 190 nm, using a range of applied reverse bias and excitation densities. Figure 5.18 displays the charge extraction transients for each device without illumination, including fits to the model (Equation 5.1, broken line) for each transient and integral, representing the capacitive charging current response CU . The 2 V applied reverse bias extraction transients exhibit predominately CU response prior to 1 μ s, with device capacitance of 2.4, 1.8, and 1.0 nF for the 80, 100, and 190 nm thick active layer thickness devices respectively, with corresponding measured τ_{RC} of 350, 280, and 150 ns. This shift in both both CU and τ_{RC} is clearly exhibited as both smaller and faster transient response for the thicker active layer devices. All active layer thickness device also exhibit an additional extraction current component beyond the initial CU response, attributed to positive doping of the active layer as previously discussed.

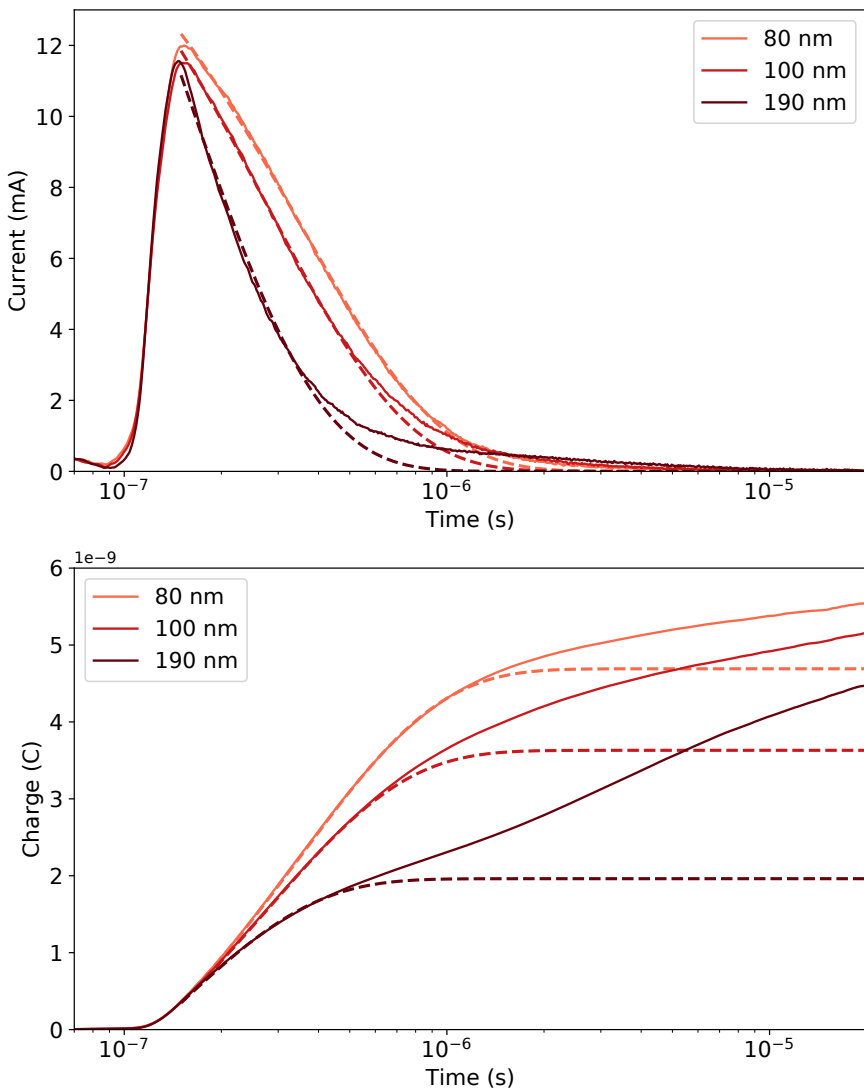


Figure 5.18: Charge extraction transients (top) with integral (bottom) without illumination for three P3HT:PCBM devices with different active layer thickness (as labelled), using an applied reverse bias of 2 V. Fits to model (Equation 5.1, broken line) for each transient and integral are also displayed, representing the capacitive charging current response.

This component is observed to increase relative to CU in the thicker devices, consistent with a greater device volume and corresponding greater total charge doping.

Figure 5.19 displays the illuminated charge extraction transients (top) and integral (bottom) for each device, using an excitation density of $10 \mu\text{J cm}^{-2}$ and 2 V applied reverse bias, and at a range of delay times (as labelled). The identical excitation density used should provide comparable photogenerated charge densities between devices, independent of active layer thickness (assuming optical cavity effects and optical density at the excitation wavelength to not produce a significant difference at the high excitation density used herein). The illuminated transients for all devices exhibit an initial transient rise to a peak, most prominent at the $1 \mu\text{s}$ delay time, indicative of space charge limited extraction with peak position shifted to earlier time for the thicker devices, as well as greater initial extracted current prior to the peak in the thicker devices. This behaviour is consistent with the above discussion, where thicker device active layers yield a reduced CU response and faster τ_{RC} , resulting in faster transients and therefore an increased rate of extraction under space charge limited conditions. This behaviour is consistent between each of the increasing delay times displayed. An inversion of the above trend is observed beyond the transient peak (on the order of $1 \mu\text{s}$), with the extraction current of the thinnest 80 nm device quickly decaying within $5 \mu\text{s}$, while the thicker device display extended current extraction, the thickest 190 nm device still exhibiting current extraction up to $20 \mu\text{s}$ extraction time. This trend is consistent between all delay times with thicker devices requiring longer total extraction times.

The thin devices are depleted of charge density during extraction significantly faster than thick devices due to a number of underlying factors that influence the charge extraction process in addition to a reduced transport length. For a given applied potential to each of the devices, a larger internal field will be present in the thinner devices, proportional to the difference in active layer thickness. Therefore a greater relative increase in the rate of extraction under an applied reverse bias in thin devices will result in faster depletion of the field-free reservoir. In addition to this, the thicker devices will have a greater relative portion of charge density within the charge reservoir and therefore require longer extraction times to completely extract all charge carriers. Both of these influences on the charge extraction process are expected to additionally result in greater recombination losses during extraction in the thicker active layer devices, as recombination during extraction is strongly coupled to the total extraction time. This may however be somewhat offset by the initially higher rate of extraction in the thick active layer devices.

If recombination losses during extraction were independent of device active layer thickness (assuming comparable charge photogeneration at the high excitation density used), the total extracted charge (Figure 5.19, bottom) at each delay time should be greater in the thickest devices, directly proportional to the relative device volume. Although the thicker devices do exhibit a greater total extracted current, with a 24 % increase between the 80 and 190 nm devices, this is significantly less than the 140 % increase expected based on the difference in device volume and therefore to-

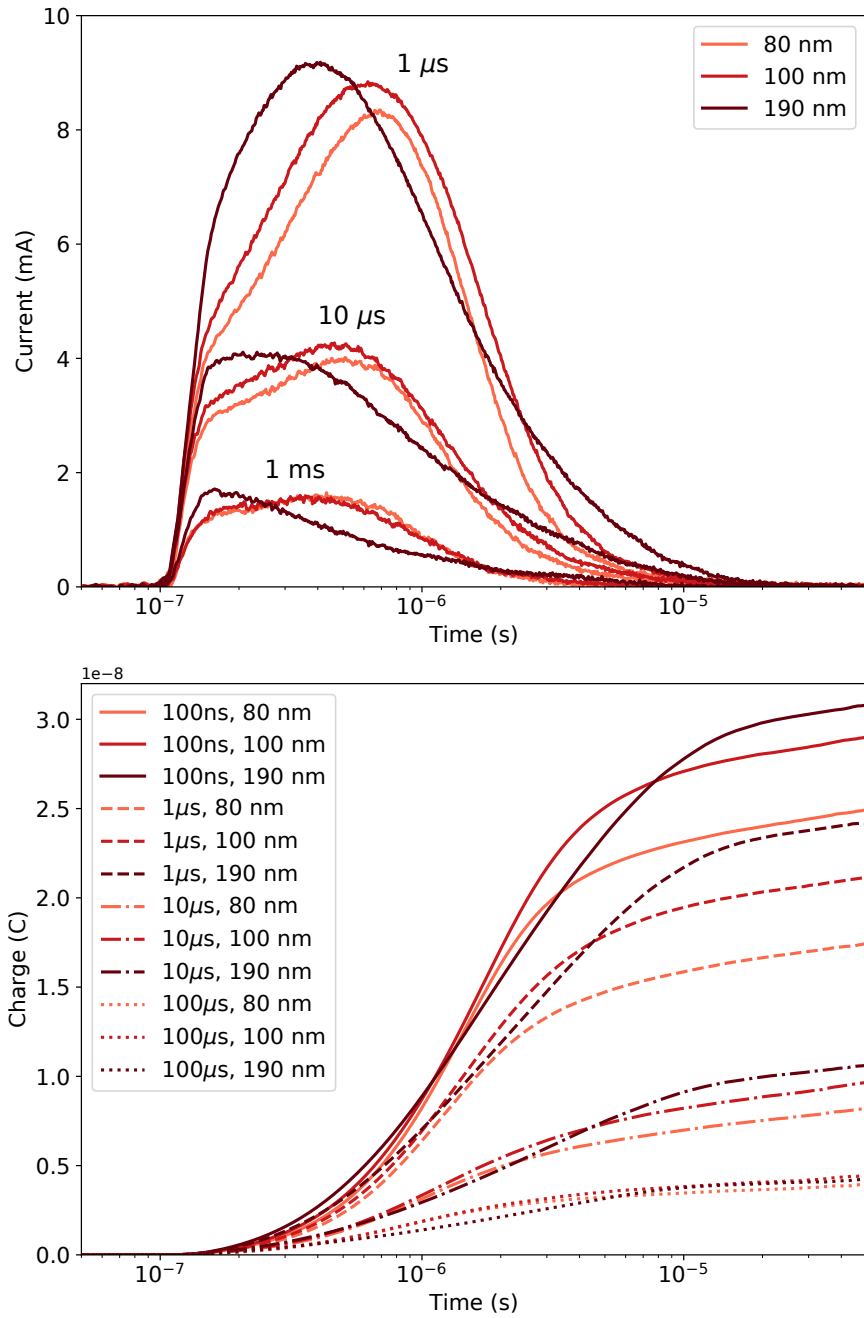


Figure 5.19: Charge extraction transients (top) with integral (bottom) for three P3HT:PCBM devices with different active layer thickness (as labelled), using an applied reverse bias of 2 V at 100 ns delay time, showing both 10 (solid line) and 1 (broken line) μJcm^{-2} excitation densities. Please note that the 100 ns extraction transients have been excluded (top) for clarity.

tal charge carrier population. This indicates that significant extraction losses are present in the thicker device measurements, and that device active layer thickness has a significant impact on the measurement of charge density using applied bias time resolved charge extraction. A consistent behaviour is observed at all delay times, where: the extracted charge is initially greatest for thicker devices due to a reduced relative CU and τ_{RC} ; followed by the thinner devices exhibiting greater extracted current through a greater rate of extraction under a higher relative internal field; and finally the thickest device overtakes and exhibits the greatest total extracted charge due to the extended tail of current extraction. The interaction of these multiple underlying extraction processes, and their dependence on device active layer thickness shifts as a function of delay time (charge density).

The extracted current as a function of time (transient response) is a complex product of changing extraction conditions, initially dominated by RC and CU limited extraction, then the rate of extraction under space charge limited conditions, and finally depletion of the charge reservoir. All of these factors are further influenced by variations in device active layer thickness and in turn lead to a disparity in recombination losses and total extracted charge density. Additionally, as greater extraction time and charge carrier transport distance are involved for thicker devices, a greater degree of trap state occupancy may further impact the total extracted charge.

Figure 5.20 displays the total extracted charge as a function of applied reverse bias for each of the P3HT:PCBM devices at multiple excitation densities (top) or multiple delay times (bottom). Note that while a reduction in excitation density will reduce the initial charge density, an increase in delay time for a given excitation density will additionally result in a change in trap state occupancy, as charge carriers relax into the trap state density distribution over time. Under all charge densities presented (excitation density or delay time), the thicker active layer devices exhibit a greater increase in extracted charge with the application of a reverse bias, relative to the thin devices. This is most prominently illustrated in the $1 \mu\text{J cm}^{-2}$ excitation density, 100 ns delay time plots where the 80 nm device exhibits an 84 % increase in extracted charge with a 2 V applied reverse bias relative to no bias, while the 190 nm device exhibits a 400 % increase. Therefore the application of an applied bias results in a more significant increase in extracted charge for thicker device active layers. This is likely due to the greater relative degree of extraction losses exhibited by thick devices.

Even with the greater increase in extracted charge under an applied reverse bias for thicker devices, the measured charge density is still much lower than in thinner active layer devices under identical measurement conditions. This is illustrated in Figure 5.21 with a clear dependence of extracted charge density on device active layer thickness from zero up to 2 V applied reverse bias. At a 100 ns delay time, a 2 V applied bias does however result in a 200 % increase in measured charge density relative to no applied bias in the 190 nm device, while a 110 % is observed for the thinner 80 nm device, thereby reducing the measured disparity between active layer thickness.

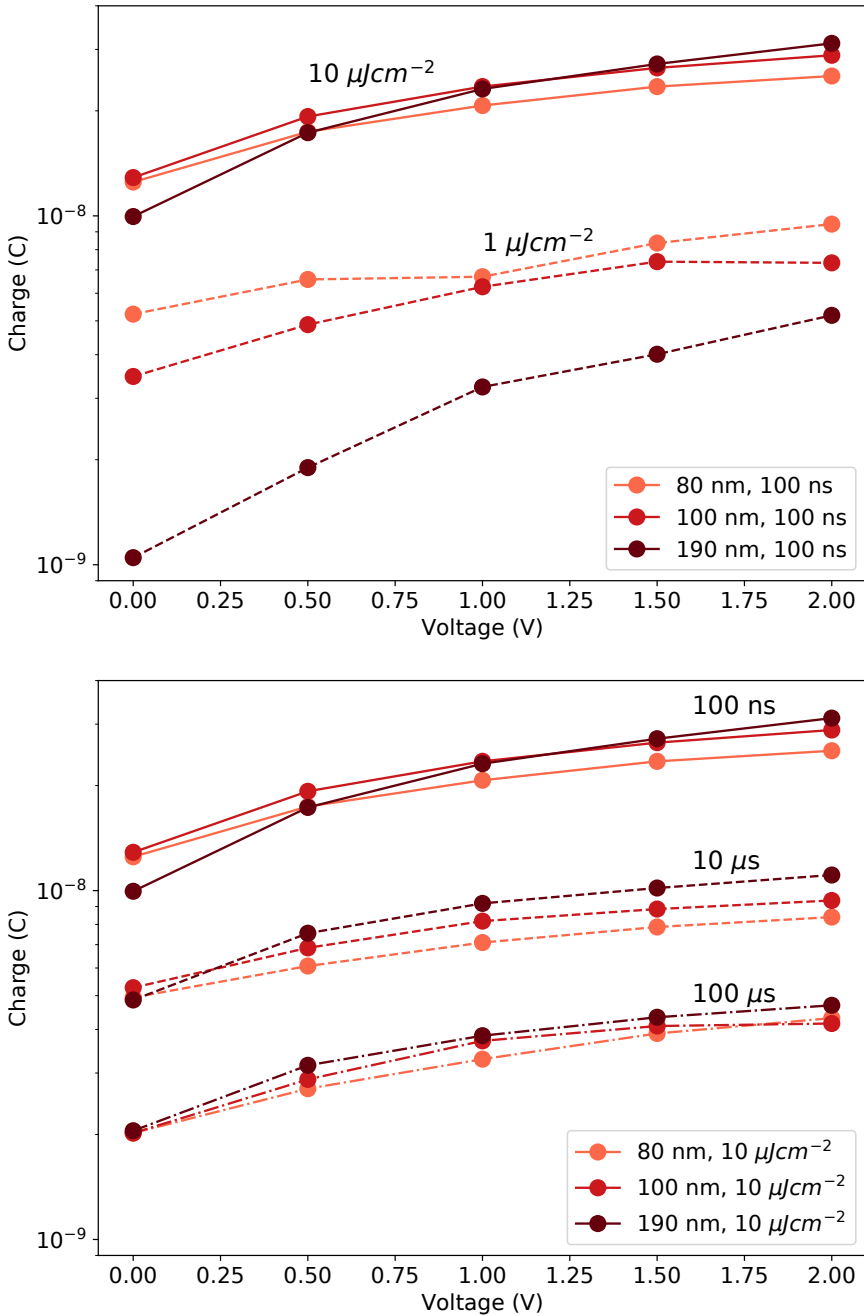


Figure 5.20: Extracted charge as a function of applied reverse bias for three P3HT:PCBM devices with different active layer thickness (as labelled), covering a range of excitation densities and delay times (Top: fixed 100 ns delay time, variable excitation density; Bottom: fixed $10 \mu\text{J cm}^{-2}$ excitation density, variable delay time).

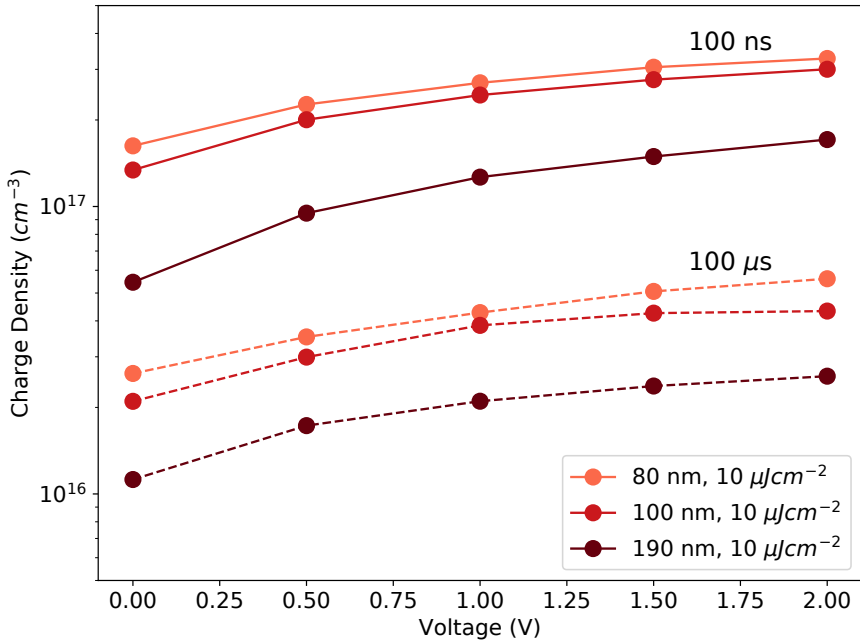


Figure 5.21: Charge density as a function of applied reverse bias for three P3HT:PCBM devices with different active layer thickness, using a $10 \mu\text{J cm}^{-2}$ excitation density, and both 100 ns and 100 μs delay times (as labelled).

Therefore the application of a reverse bias in time resolved charge extraction measurements can aid in comparison of devices with slight variations in active layer thickness, through a reduction in the disparity observed without an applied bias. Note that the maximum applied reverse bias used herein of 2 V may not be sufficient to extract all charge carrier within the thicker active layer devices, and as such further increases can be expected with a greater applied reverse bias.¹²⁴ The ability to measure the internal charge density of a device more accurately with the application of a bias in time resolved charge extraction, in particular for thick device active layers, enables a more reliable comparison of performance and behaviour between devices under investigation. This can therefore facilitate the improved investigation and analysis of non-geminate recombination mechanisms in state-of-the-art donor-acceptor photovoltaic devices, through the study of charge carrier generation/recombination and quantification of transport/extraction and recombination losses.

5.4.4 Influence of Extraction Losses on the Measurement of Recombination Kinetics and Trapping

The following section presents investigations undertaken to determine the influence of the reduced extraction losses (facilitated by an applied bias) on the measurement of recombination kinetics and trap state density distribution in time resolved charge extraction measurements. These investigations are also used to further validate the presented origins for increased extracted charge with an applied reverse bias as discussed in the Section 5.4.2. Measurement results for the P3HT:PCBM

device presented in Section 5.4.1 are used for the calculation of recombination kinetics and reaction order, as well as the measurement of trap state density distribution in combination with photovoltage decay measurements.

Influence of an Applied Bias on Empirical Reaction Order

Using the charge density decay results presented in Section 5.4.1 (Figure 5.6), the empirical reaction order as a function of charge density is calculated (Equation 2.8) and presented in Figure 5.22 for an applied reverse bias of zero and 2 V, each at both 100 and 1 $\mu\text{J cm}^{-2}$ excitation densities. The calculated empirical reaction order is lowest at high charge densities, and comparable between both zero and 2 V applied reverse bias on the order above $4.0 \times 10^{16} \text{ cm}^{-3}$, at an average 3.1 for the 100 $\mu\text{J cm}^{-2}$ excitation density. However at charge densities below $4.0 \times 10^{16} \text{ cm}^{-3}$ the applied bias plots exhibit reaction orders over 30 % greater than that without an applied reverse bias at both excitation densities. The observed increase in reaction order at charge densities approaching CU ($1.8 \times 10^{16} \text{ cm}^{-3}$ at 2 V) and below, with corresponding lifetimes significantly longer than the extraction time, is again consistent with an increased extraction of deep trap states with a greater relative reaction order representing more trap influenced/limited recombination kinetics. The application of a bias therefore enables a greater investigation of the trap state density distribution through extraction of trap states that would otherwise not be observed. At lifetimes comparable to, or shorter than the extraction time, the measured reaction order is less influenced by the application of a reverse bias as a reduction in recombination losses during extraction is the main origin of the increase in extracted charge density.

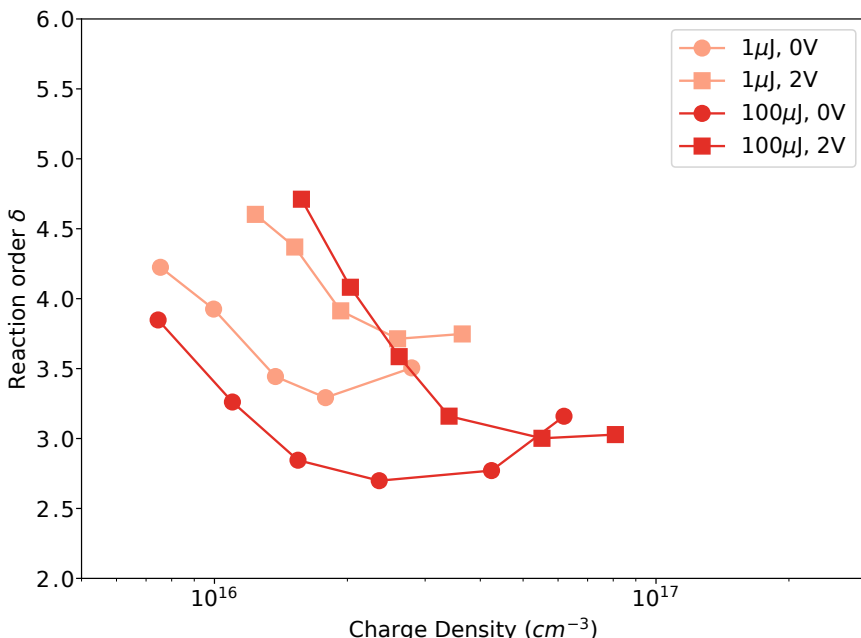


Figure 5.22: Empirical reaction order (bottom) as a function of charge density for a P3HT:PCBM device with both zero and 2 V applied reverse bias, for two excitation densities (as labelled).

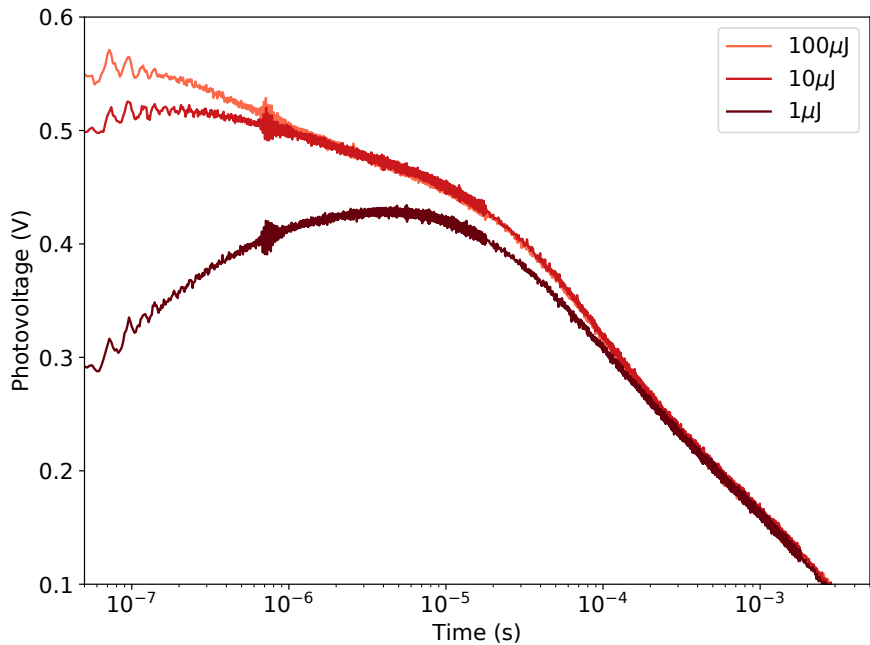


Figure 5.23: Photovoltage decay transients for a P3HT:PCBM device at a range of excitation densities (as labelled).

Influence of an Applied Bias on the Measurement of Trap State Density Distribution

Photovoltage decay measurement were performed with the resulting transients for the P3HT:PCBM device presented in Figure 5.23 for a range of excitation densities, used in the correlation with charge density decay results to yield the dependence of photovoltage on charge density, and further for the calculation of the trap state density distribution E_{ch} (Equations 2.11 and 2.12). Both excitation density plots for the dependence of photovoltage on charge density (Figure 5.24, top) exhibit a shift to higher charge densities for a given photovoltage over the measured charge density range, and is greatest at charge densities below $4.0 \times 10^{16} \text{ cm}^{-3}$. The calculated trap state density distribution (Figure 5.24, bottom) displays a corresponding increase in measured E_{ch} for a given charge density with the application of a 2 V reverse bias at charge densities below $4.0 \times 10^{16} \text{ cm}^{-3}$, up to 60 % for the $100 \mu\text{J cm}^{-2}$ excitation density. This shift in calculated E_{ch} with applied reverse bias is reduced at high charge densities and is comparable for the $100 \mu\text{J cm}^{-2}$ excitation density plot above $8.0 \times 10^{16} \text{ cm}^{-3}$ with an average E_{ch} of 35 meV.

The observed influence of an applied reverse bias on the measured trap state density distribution is again consistent with the recombination kinetics and reaction order measurements presented above, and is attributed to an increase in deep trap state extraction with an applied reverse bias at charge densities below CU and lifetimes longer than the extraction time. An apparent increase in calculated E_{ch} at low charge densities is due to a time dependent trap state occupancy introduced through the use of a delay time in time resolved charge extraction measurements, where the proportion of free to trap state charge carriers extracted dominates the measured E_{ch} . As the

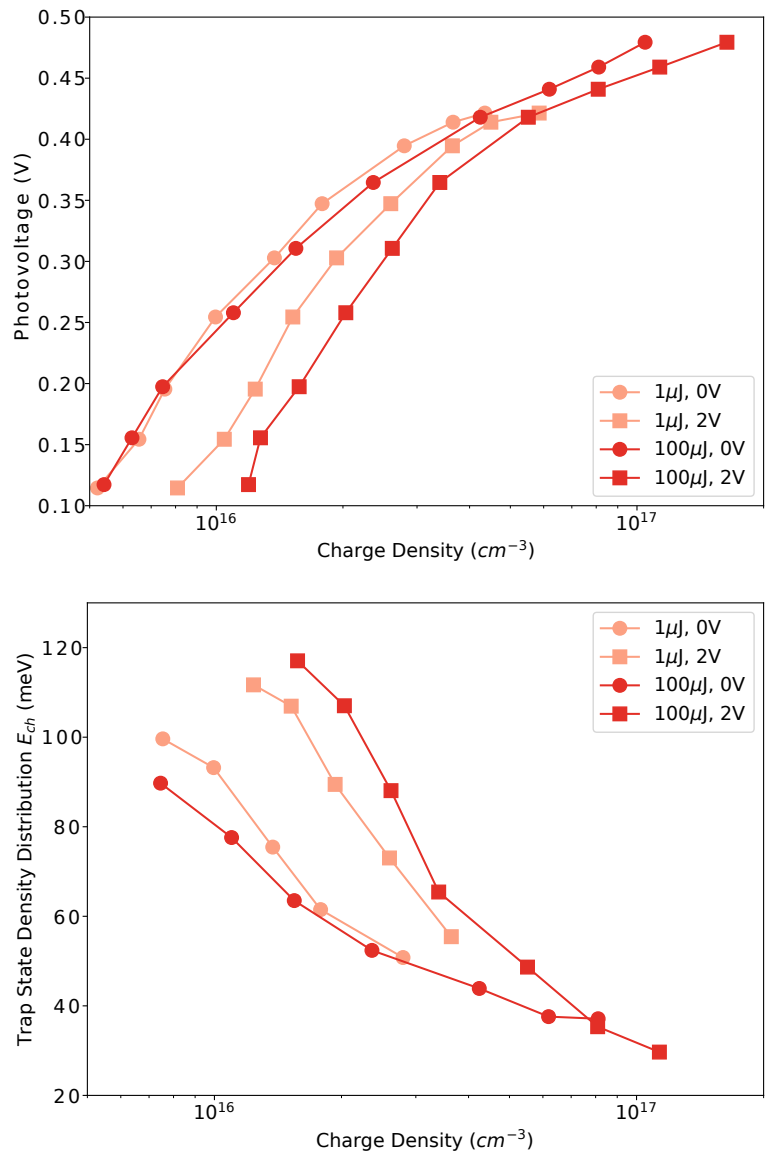


Figure 5.24: The dependence of photovoltage on charge density (top) for a P3HT:PCBM device, using both zero and 2 V applied reverse bias and at 100 and 1 μ J cm^{-2} excitation densities. The calculated trap state density distribution as a function of charge density is also displayed (bottom).

application of an applied reverse bias increases this proportion of free to trap states extracted, an increase in the calculated trap state density distribution is observed. At lifetimes comparable to, or shorter than the extraction time, the measured trap state density distribution is less influenced by the application of a bias as a reduction in recombination losses during extraction is the main origin of the increase in extracted charge density, rather than a shift in the proportion of free to trap state charge carriers extracted.

5.4.5 Inherent Spatial Separation in Devices with Thin Active Layers Device

Variation of device active layer thickness was found to influence the measured charge density in time resolved charge extraction, with thicker active layers found to exhibit significantly greater relative extraction losses at all measured charge densities. The application of a reverse bias was found to reduce this observed disparity between devices with different active layer thickness, however a disparity was still consistently observed for P3HT:PCBM devices with active layer thickness ranging from 80 to 190 nm. Within the low charge density, long charge carrier lifetime region an increase in charge density with applied reverse bias was attributed to the increased extraction of trap states at increasing applied bias. Although the above measurements were performed using an identical applied reverse bias, the internal field will be less in the thicker active layer devices (a fixed potential over an increasing distance). This may in turn reduce the extractable trap states for thick devices and thereby account for the increased relative charge density in thin devices. However the observed deviation in charge density between active layer thickness is also observed without an applied reverse bias (see Figure 5.21), and therefore the above explanation is insufficient to account for this behaviour.

The increase in extracted charge density with decreasing device active layer thickness, at charge densities where the charge carrier lifetime is significantly longer than the extraction time, is therefore attributed to different recombination kinetics at open circuit. As illustrated in Figure 5.25, inherent spatial separation of respective charge carrier populations at open circuit can occur in devices with a sufficiently thin active layer thickness.³⁴ The potential difference between device contacts produced by the photogenerated charge density (photovoltage) results in the formation of space charge regions at the device contacts and an accumulation of respective charge carriers. These regions have a reduced overlap of charge carriers, relative to the bulk, and consequently have a reduced recombination probability. This spatial inhomogeneity is most significant for thin active layers and at low charge densities, where an increasing portion of total charge density experiences reduced recombination. This results in reduced recombination in devices with thin active layers, relative to thick active layers for a given charge density, and can account for the observed thickness dependence in the charge density decay plots (Figure 5.26).

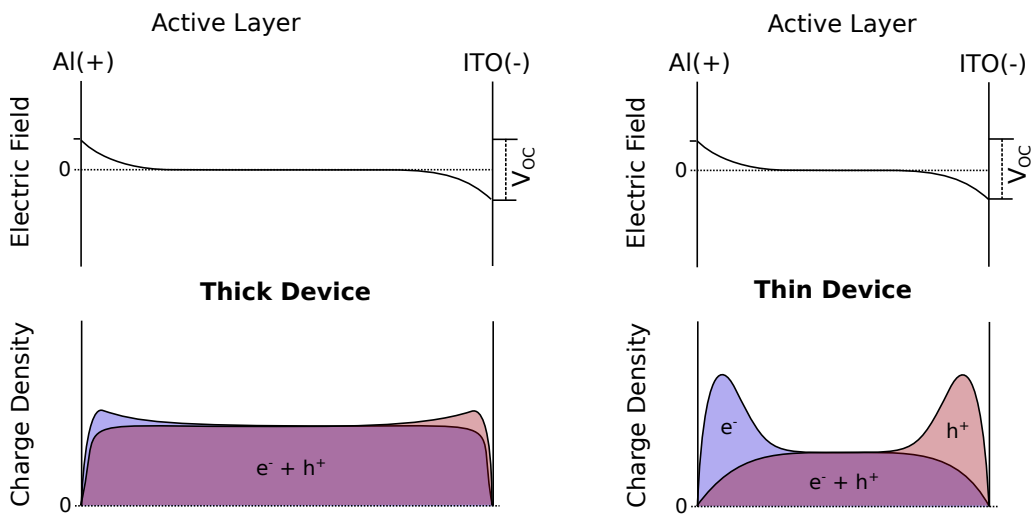


Figure 5.25: Illustrative figure of inherent spatial separation of charge carriers at open-circuit in a thin device (right), relative to a thick device (left) at an identical low charge density. The electric field (top) and charge density (bottom) is displayed across the device active layer. The charge carrier spatial distribution is more uniform in for the thick device, resulting in a greater proportion of charge carrier overlap relative to the thin device.

Influence of Inherent Spatial Separation on Recombination Kinetics

The application of a reverse bias in time resolved charge extraction measurements has shown to reduce the disparity in extracted charge density between devices with different active layer thickness. However the following section seeks to investigate the influence of inherent spatial separation of charge carriers in thin device active layers on the measurement of recombination kinetics. A series of four P3HT:PCBM devices were fabricated with active layer thickness ranging from 110 to 225 nm. Applied bias time resolved charge extraction measurements were performed on these devices, with analysis and discussion of the thickness dependence of charge density decay and subsequent calculation of charge carrier lifetime and trap state density.

Figure 5.26 (top) displays the measured charge density decay of the four P3HT:PCBM devices with different active layer thickness (as labelled) using a 2 V applied reverse bias and $100 \mu\text{J} \text{ cm}^{-2}$ excitation density. A dependence of charge density on active layer thickness is observed over the entire delay time (charge density) range, with thinner devices exhibiting a greater relative charge density. Although significant at short delay times, the observed deviation in measured charge density between devices is greatest at delay times longer than $20 \mu\text{s}$, while lowest within the range of 2 to $10 \mu\text{s}$. The deviation in charge density between active layer thickness at charge densities above 10^{17} cm^{-3} ($\sim CU$ for these devices) can be accounted for through the influence of active layer thickness on extraction processes as discussed in the previous sections, where this

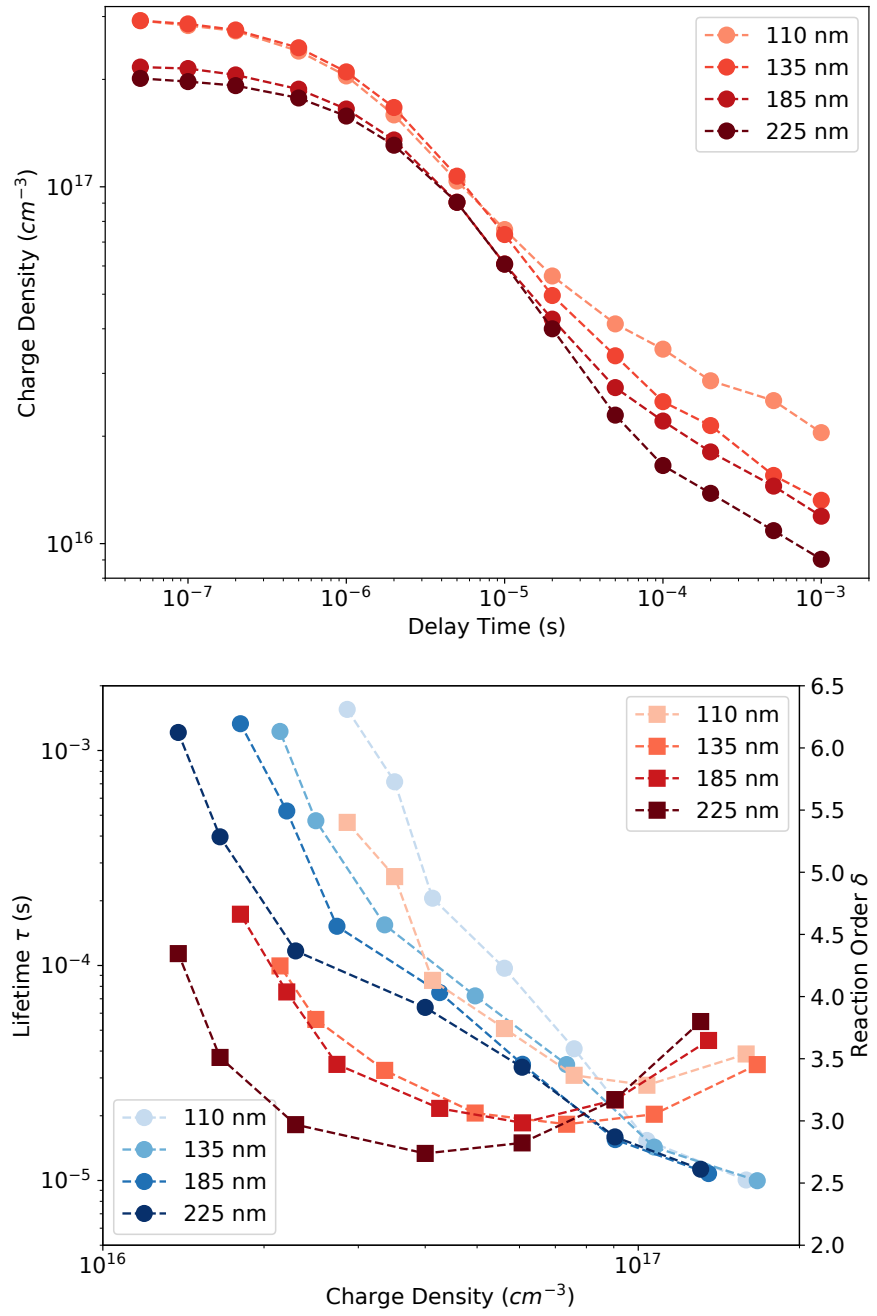


Figure 5.26: Charge density decay (top), and both charge carrier lifetime (bottom, left axis, blue circles) and empirical reaction order (bottom, right axis, red squares) as a function of charge density for P3HT:PCBM devices with a range of active layer thickness (as labelled), using an applied reverse bias of 2 V at $100 \mu\text{Jcm}^{-2}$ excitation density.

charge density region corresponds to space charge limited conditions and charge carrier lifetimes are comparable to the extraction time. However at charge densities significantly below 10^{17} cm^{-3} where extraction is not space charge limited and the charge carrier lifetime is significantly longer than the extraction time, recombination losses during extraction should not be significant. However the measured difference in charge density between active layer thickness is observed to increasingly deviate, with the 110 nm device exhibiting 44 % greater charge density than the 225 nm device at a delay time of $20 \mu\text{s}$, while up to 125 % at 1 ms. Therefore a variation in active layer thickness is influencing the recombination kinetics at open-circuit, attributed to relative differences in the degree of inherent spatial separation of charge carriers.

Inherent spatial separation in thin devices has shown to alter the measured recombination kinetics. The charge carrier lifetime and empirical reaction order are calculated as a function of charge density (Equations 2.9 and 2.8) for each of the devices with varied active layer thickness, displayed in Figure 5.26 (bottom). The charge carrier lifetime and empirical reaction order are observed to be comparable between active layer thickness at charge densities above 10^{17} cm^{-3} , while at increasingly low charge densities the thinner devices exhibit an extended relative lifetime, up to an order of magnitude between the 110 and 225 nm active layer thickness devices by $3.0 \times 10^{17} \text{ cm}^{-3}$. This region of low charge density corresponds to conditions where inherent spatial separation of charge carriers during the delay time leads to an extension of lifetime. A corresponding deviation in calculated reaction order between devices is also observed. This effect is less significant at high charge densities where additional extraction processes begin to dominate the measurement of charge density.

In summary, the observed variation in recombination kinetics between devices with different active layer thickness at low charge densities (long delay times) is in fact due to differences in recombination kinetics at open circuit. These altered kinetics are attributed to the inherent spatial separation of charge density in devices with thin active layers, rather than any difference in extraction losses. These results provide further experimental verification of the influence of inherent spatial separation in thin devices on measured recombination kinetics, and indicate that care should be taken when comparing/interpreting results obtained from multiple devices with variations in active layer thickness.

5.5 Conclusions

The overall objective of this chapter was to improve the time resolved charge extraction technique, through the novel incorporation of an applied bias, and investigate the influence of this applied reverse bias on measurement limitations, as well the measurement of charge generation yield, charge recombination processes, and trap state occupancy in operational devices, with the eventual aim of investigating the impact of driving force on these factors, and validating the outcomes of the optical driving force studies od Chapter 3.

An applied reverse bias was introduced into the time resolved charge extraction technique for the first time, with the aim of reducing the significant extraction losses identified in the previous chapter. The application of a reverse bias yields an increase in extracted charge density, up to twice that without an applied bias, indicating that at least half of all charge density is lost during charge extraction measurements without an applied reverse bias in the studied systems. This increase was observed to be even greater in thicker device active layers (up to 400 %). The investigations within this chapter also identified and quantified the charge density/lifetime dependent limitations of the time resolved charge extraction technique, with respect to the behaviour and interaction of underlying extraction processes (loss mechanisms). In particular, space charge limitations dominate the rate of extraction at high charge densities, fundamentally limiting the range of measurable charge carrier lifetimes and resulting in significant extraction losses under typical measurement conditions. An applied reverse bias does however improve the extraction of charge density under these conditions through reducing recombination losses, while at low charge densities an applied reverse bias enables the more comprehensive measurement of trap state occupancy. In addition, the influence of commonly variable device/measurement parameters on these extraction processes have been characterised, as well as the impact on subsequent determination of charge density, recombination processes, and trap state occupancy. A reduction of measurement impedance or device capacitance in applied bias charge extraction measurements can further reduce recombination losses during extraction, however practical measurement and device fabrication limitations provide a limit on the utility of this approach. Device active layer thickness variation was also found to strongly influence charge extraction processes, as well as yield inherent differences in recombination kinetics. An applied reverse bias can however be employed in time resolved charge extraction to effectively reduce this disparity between devices with different active layer thickness due to extraction losses.

These chapter outcomes show that the application of a reverse bias in time resolved charge extraction is an effective method to improve the investigation of charge generation yield, charge recombination processes, and trap state occupancy over standard time resolved charge extraction in operational photovoltaic devices. Additionally the primary extraction loss mechanisms have been quantified for a range of measurement conditions. The primary findings of this, and the previous Chapter 4 have been published in reference.¹²⁴ The developed measurement technique and understanding of limitations will be further utilised in the following chapter, for the investigation of the driving force dependence of charge generation yield, recombination processes, and trap state occupancy in operational devices incorporating the donor-accepter material systems presented in the optical driving force studies (Chapter 3).

Chapter 6

Donor-Acceptor Material Energy Levels and Charge Carrier Generation/Recombination in Photovoltaic Devices

6.1 Introduction

A key step in the charge photogeneration process is photoinduced electron transfer from a photoexcited donor to an electron acceptor, which is in competition with excited-state decay to the ground state. The driving force for electron transfer ΔG_{ET} (free-energy offset between donor LUMO and acceptor LUMO) has been shown to influence both electron transfer kinetics and charge generation yield in a number of donor-acceptor photovoltaic systems (see Chapter 1, Section 1.2 for a detailed discussion). The ΔG_{ET} should be sufficiently large such that the rate for electron transfer dominates, producing a high quantum yield for photoinduced electron transfer, a high charge carrier generation yield, and therefore high device short-circuit current (J_{SC}). However, the magnitude of ΔG_{ET} must be balanced with the desire for a high device open-circuit voltage (V_{OC}) which is proportional to the splitting energy of electron and hole quasi Fermi levels, and therefore any increase in driving force will result in a reduction (loss) of V_{OC} for systems with a comparable bandgap. Balancing both J_{SC} and V_{OC} is essential for the development of photovoltaic devices with high operational efficiency.

The series of polymer donors investigated in Chapter 3 provide the opportunity to systematically investigate the influence of material system energetics on charge photogeneration and recombination processes. These polymer donors have nearly identical band gaps (~ 1.5 eV) while exhibiting ΔG_{ET} relative to the PCBM acceptor of 0.57, 0.30, and 0.18 eV for P1, P2, and P3 respectively.

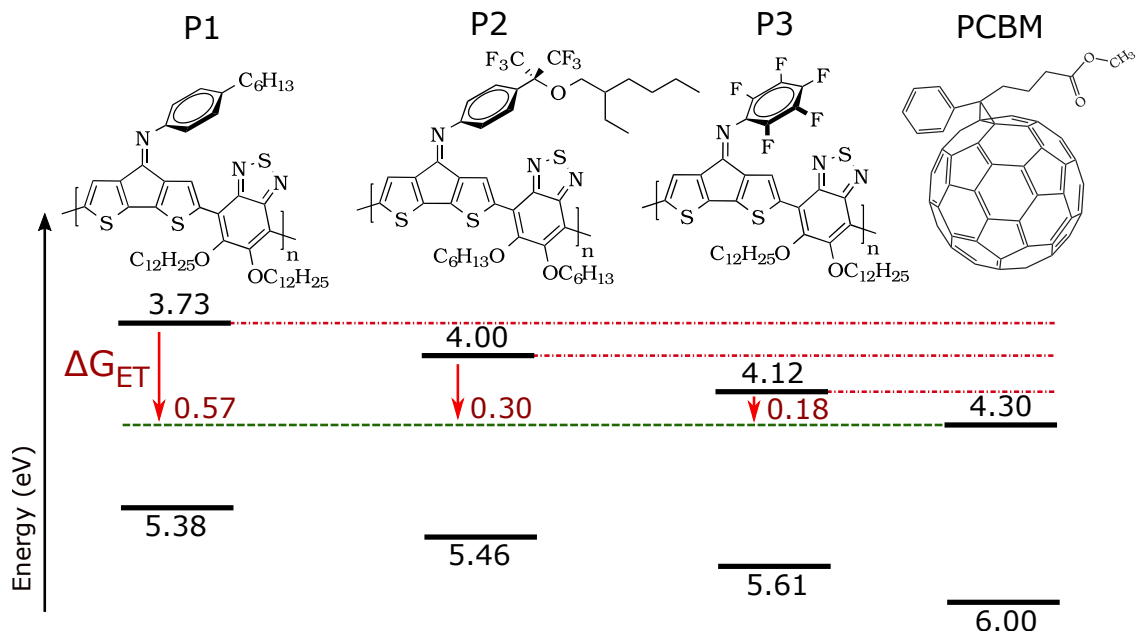


Figure 6.1: Molecular structures of cyclopentadithiophene based polymer donors (P1, P2, and P3) and the fullerene based acceptor (PCBM). Shown are the highest occupied molecular orbital energy level (E_{HOMO}) calculated from the onset of oxidation and the lowest unoccupied molecular orbital energy level (E_{LUMO}) calculated from the onset of reduction, with comparison of the electrochemical band gaps and LUMO offsets of the donors relative to the PCBM acceptor (E vs vacuum). Also displayed are the driving force for electron transfer (ΔG_{ET} , red arrow).

Additionally these donor-acceptor systems exhibit free energy offsets between donor E_{HOMO} and acceptor E_{LUMO} ($\Delta_{HOMO-LUMO}$) of 1.08, 1.16, and 1.31 eV for P1, P2, and P3 respectively, which also represents the driving force for non-geminate recombination ΔG_{rec} . Each of these material systems and energetic driving forces are displayed in Figure 6.1.

The low bandgap polymer donor materials were synthesised by, and obtained from Jason Azoulay and Guillermo Bazan (The Center for Polymers and Organic Solids, University of California, Santa Barbara, USA). All device fabrication and optimisation was however performed by the doctoral candidate locally (Intelligent Polymer Research Institute, University of Wollongong, Australia).

6.1.1 The Influence of Driving Force for Electron Transfer of Charge Generation Yield

Chapter 3 investigated the influence of ΔG_{ET} on electron transfer kinetics and yield in the aforementioned donor-acceptor systems using ultrafast transient absorption measurements on 70 % PCBM blend films. Both P1 and P2 blend films exhibited photoinduced electron transfer without any resolvable exciton decay to the ground state, and as such a qualitative assignment of near unity quantum yield of electron transfer was made. Both the electron transfer kinetics and apparent charge separation yield for P1 and P2 blend films appeared comparable, and therefore

independent of ΔG_{ET} ($P1 = 0.57$ eV, $P2 = 0.30$ eV). A recombination process was however observed for P1 and P2 blend films post electron transfer, attributed to geminate recombination via charge-transfer states, resulting in a charge separation yields below unity. Conversely, the P3 blend films exhibited exciton decay to the ground state with no observable electron transfer, suggesting that a ΔG_{ET} greater than the 0.18 eV of the P3 blend is required to produce a high quantum yield for electron transfer in these donor-acceptor systems.

There is however an inherent ambiguity in using optical techniques for these material systems due to coexisting absorption of polymer excitons, polarons, and possibly charge-transfer states at the 1400 nm probe wavelength used in the transient absorption measurements. Further, some populations of optically detectable charge carriers may not be extracted under device operation due to various transport/trapping/recombination processes. As such, applied bias time resolved charge extraction measurements are performed using operational photovoltaic devices incorporating identical 70 % PCBM blend films of each donor-acceptor material system used in the transient absorption investigations of Chapter 3. A primary objective of this chapter is to use these measurements to determine the influence of ΔG_{ET} on charge extraction yield, and compare these results to the findings of Chapter 3 as outlined above.

Steady-state device characterisation (current-voltage measurements) can provide both the J_{SC} and V_{OC} of devices under a range of steady-state illumination intensities which can then be used for a correlation with device material system ΔG_{ET} . However, the generation and recombination kinetics of the photogenerated charge density in steady-state measurements are in a state of quasi-equilibrium for a given illumination intensity (and corresponding charge density). These measurements are therefore strongly influenced by the inherent device recombination kinetics (charge carrier mobility-lifetime product $\mu\tau$) and trapping behaviour, which will in turn influence the measured J_{SC} and V_{OC} . Transient charge extraction measurements are therefore required to determine the charge generation/extraction yield, device photovoltage, and charge carrier lifetime at identical charge densities, independent of the influence of generation/recombination kinetics and transport/trapping behaviour. This will ensure an accurate comparison of various device/material systems, isolating the influence of $\Delta G_{ET}/\Delta G_{rec}$ on the parameters under investigation.

While active layer morphology can influence the energetics of the donor-acceptor interface through phase crystallinity, reorganisation energy, charge screening, and delocalisation, the use of similar polymer donors blend systems with comparable morphology should minimise the relative influence of these effects (see TEM studies of Chapter 3). The influence of morphology on charge generation and recombination is not the focus of this thesis, but rather the influence of donor-acceptor system energetics on these fundamental processes. The impact of morphology on charge transport, extraction, and trapping presented significant issues when using charge extraction based measurement techniques in determining the photogenerated charge density. As such, the development of an applied bias charge extraction technique and the quantitative investigation

of charge extraction losses (as presented in Chapters 4–5) were critical to the investigation of these polymer donor systems, with improvements in extracted charge and reduced recombination during extraction helping to overcome morphological limitations.

6.1.2 The Influence of Driving Force for Electron Transfer on Device Photovoltage

The device V_{OC} is directly proportional to the splitting of electron and hole quasi Fermi levels at the device contacts. As the magnitude of quasi Fermi level splitting is proportional to $\Delta_{HOMO-LUMO}$, an increase in $\Delta_{HOMO-LUMO}$ for a donor-acceptor blend should produce a corresponding increase in V_{OC} . Further, a reduction in ΔG_{ET} should result in an increase in V_{OC} (proportional to $\Delta_{HOMO-LUMO}$) for a given donor/acceptor material bandgap. The relaxation of charge carriers into a broad density of states distribution, including an exponential tail of trap states is also expected to yield a further reduction in device photovoltage.³⁷ The use of applied bias time resolved charge extraction and photovoltage decay measurements enables the determination of device V_{OC} as a function of internal charge density, independent of the influence of recombination kinetics or charge extraction losses. This also enables the measurement of the dependence of V_{OC} on charge density, and therefore provides a measure of the trap state density distribution. A primary objective of this chapter is therefore to use these measurements to investigate the influence of reducing ΔG_{ET} on device V_{OC} , through a comparison between the aforementioned donor-acceptor material systems at identical charge densities.

As the P1/P2/P3 polymer donors present similar bandgaps (1.49 to 1.67 eV), the corresponding donor-acceptor systems also provide a range of $\Delta_{HOMO-LUMO}$, where polymer donor HOMO is deeper with greater ΔG_{ET} relative to the constant PCBM acceptor LUMO (-4.3 eV). This yields $\Delta_{HOMO-LUMO}$ of 1.08, 1.16, and 1.31 eV for P1, P2, and P3 respectively (see Figure 6.2). Therefore at the same charge density, the device photovoltage should exhibit a positive dependence on decreasing donor HOMO level, with the P3 blend device exhibiting the greatest photovoltage, followed by the P2 and finally P1 blend devices. The device photovoltage at a given charge density is measured and compared between donor-acceptor systems in order to investigate this behaviour, presented in Section 6.3.3.

6.1.3 The Influence of Driving Force for Recombination on Device Recombination Kinetics

The bimolecular recombination of separated charge carriers is another primary loss mechanism in donor-acceptor photovoltaic systems, resulting in a reduced charge carrier extraction yield and consequently reduced device short-circuit current. However there are limited literature studies investigating whether donor-acceptor material system energetics influence the bimolecular recombination process in organic photovoltaic systems. The existence of the Marcus inverted region has

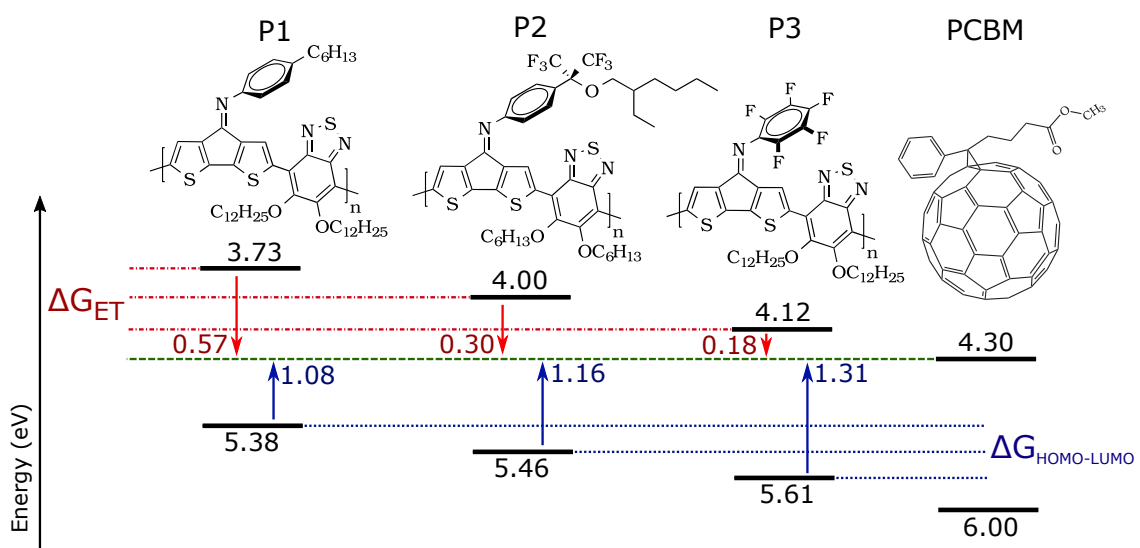


Figure 6.2: Molecular structures of cyclopentadithiophene based polymer donors (P1, P2, and P3) and the fullerene based acceptor (PCBM). Shown are the highest occupied molecular orbital energy level (E_{HOMO}) calculated from the onset of oxidation and the lowest unoccupied molecular orbital energy level (E_{LUMO}) calculated from the onset of reduction, with comparison of the electrochemical band gaps and LUMO offsets of the donors relative to the PCBM acceptor (E vs vacuum). Also displayed are the driving force for electron transfer (ΔG_{ET} , red arrow), and the free energy offset between donor polymer E_{HOMO} and PCBM acceptor E_{HOMO} ($\Delta G_{HOMO-LUMO}$, blue arrow).

been confirmed for charge photogeneration in a number of donor-acceptor systems, and suggests that a ΔG_{ET} significantly greater than the reorganisation energy between reactant and product states (intramolecular component on the order of 0.4 eV)⁷⁴ will significantly reduce the rate of electron transfer between donor and acceptor species.^{55–57,66} As such, it is unlikely that the energetic offsets between donor HOMO and acceptor LUMO typically observed in organic photovoltaic systems (greater than 1.0 eV) would influence the kinetics of charge-transfer state or non-geminate recombination.

However, a recent study by Burke et al suggests that free charge carriers are in fact in equilibrium with charge-transfer states, where the formation and dissociation of these states can better account for the observed recombination probability of charge carriers, as well as the temperature dependence of open-circuit voltage.¹⁰² This may further imply that the charge-transfer state binding energy may play a role in bimolecular recombination kinetics, and therefore may be influenced by the material energy levels of donor and acceptor (driving force for electron transfer). Further, due to the time resolution of the time-resolved microwave conductivity technique employed by Coffey et al, the results obtained regarding the driving force dependence of charge generation yield may include not only geminate recombination, but also possibly non-geminate charge-transfer state mediated recombination.⁷¹ As such, the observed driving force dependence of charge generation may include both electron transfer and recombination driving force contributions, rather than solely being attributed to the electron transfer process.

Therefore, the question remains as to whether this energetic driving force for recombination ΔG_{rec} can influence the non-geminate recombination kinetics of donor-acceptor photovoltaic devices? This concept will be further introduced and discussed in Section 6.3.4, with an outline of new material systems used and investigations performed in order to address this questions.

6.1.4 Summary of Chapter Objectives

The investigations presented within this chapter are undertaken to address outstanding questions regarding to the influence of donor-acceptor material energy levels (driving forces) on charge generation yield and recombination processes. The specific chapter objectives are as follows:

1. Determine the influence of the ΔG_{ET} on charge carrier extraction yield in photovoltaic devices using applied bias time resolved charge extraction measurements, and correlate these with optical measurements of generation yield. (Section 6.3.2)
2. Investigate whether device photovoltage increases for a given charge density with a reduction in ΔG_{ET} (via lowering E_{HOMO} with a constant bandgap), through a combination of applied bias time resolved charge extraction and photovoltage decay measurements on photovoltaic devices. (Section 6.3.3)

3. Investigate whether ΔG_{rec} influences bimolecular recombination kinetics through the use of applied bias time resolved charge extraction measurements on photovoltaic devices, and an analysis of the calculated charge carrier lifetime and reaction order as a function of charge density. (Section 6.3.4)

6.2 Experimental

6.2.1 Photovoltaic Device Fabrication

The active layer blend solutions are prepared with parameters depending on donor-acceptor materials used. Slight variations to solution concentrations and deposition parameters were used where variation of active layer thickness was required. For all cyclopentadithiophene based polymer donor/blend solutions, each donor:PCBM (1:4) blend solution was prepared by dissolution in o-dichlorobenzene at between 15 and 25 mg mL⁻¹ and stirring at 120 C° for 30 hours under an Ar atmosphere. These solutions were then filtered through a 0.45 μm PTFE filter to remove undissolved donor material after cooling to room temperature. For the devices incorporating the diodoctane (DIO) processing additive, 3 vol.% DIO was added to the blend solution prior to filtration and left to stir at 800 rpm for 30 minutes at room temperature, then followed by filtration.

Pre-patterned Indium Tin Oxide (ITO) coated glass slides (LumTec., 90 nm thick ITO, variable active pixel area, typical conductivity of 15 Ω cm⁻², above 85 % transmission at 550 nm) are used for the transparent device anode, as well as providing a rigid substrate. The substrates are cleaned by 15 min under sonication in surfactant/H₂O, followed by two subsequent 5 min sonication rinses in H₂O, and 15 min under sonication each in acetone and isopropanol, prior to a 20 min UV-ozone treatment. This ensures a clean, particulate free substrate and improves wettability for solution/active layer deposition.

The cleaned substrates are coated with the poly(3,4-ethylenedioxythiophene):poly(styrenesulfonate) (PEDOT:PSS) hole selective layer, using 0.5 wt % PEDOT:PSS solution (Heraeus Clevios Al 4083) diluted 1:1 in isopropanol. The PEDOT:PSS solution is filtered through a 0.45 μm PVDF filter to remove any particulates prior to dilution, and maintained under stirring. The layer is then deposited using spin coating (Laurell WS-560HZ-15NPP) at 5000 rpm for 30 s, followed by annealing in air at 140 C° for 20 min.

Directly prior to deposition of the active layer, the active layer polymer(blend) solutions are cooled to room temperature. For all cyclopentadithiophene based polymer donor/blend devices, the polymer(blend) solutions were doctor-bladed (Erichsen Coatmaster 509 MC) in air onto the substrate at between 13 and 15 mm s⁻¹, with a hotplate (Prazitherm PZ35, high stability) temperature of 75 C° and drying times ranging from 5 to 30 s (depending on polymer donor).

To produce the amorphous titanium oxide (TiO_x) electron selective interfacial layer, a titanium oxide sol-gel precursor solution is diluted (1:10) into isopropanol prior to deposition onto the device active layer. TiO_x layer deposition is performed directly after active layer deposition (and any required active layer solvent drying time) using spin coating at 5000 rpm for 30 s, and is left to hydrolyze in air for 20 min (or under heating where the active layer requires annealing).

Aluminium (Al) is then evaporated under vacuum through a mask of defined device active area (0.095 cm^{-2} unless otherwise stated), to produce a cathode thickness on the order of 100 nm. A ramp in evaporation rate is used to ensure good contact with the active layer (initial 5 nm at 0.5 \AA s^{-1} , following 50 nm at 1.5 \AA s^{-1} , final $\sim 50 \text{ nm}$ at $2.5+ \text{ \AA s}^{-1}$). The deposition chamber is left to cool down for 30 minutes before returning to atmospheric pressure. These devices were then sealed under an inert Ar atmosphere using a cover glass slide and UV-curable epoxy (Ossila, E131), manually cured using a handheld UV gun. Effort is made to ensure that no epoxy is in contact with the device active layer, and that no significant UV illumination is incident on the device active area. Finally, a metal contact is soldered (ultrasonic) onto the exposed anode/cathode contact regions for increased durability during measurement.

6.2.2 Steady-State Current-Voltage Characterisation

Current-voltage (JV) measurements are performed to assess steady-state device performance, and characterise a number of important device parameters including open circuit voltage V_{OC} , short-circuit current J_{SC} , fill factor FF , solar conversion efficiency η , series resistance R_S , and shunt resistance R_{Sh} , using known parameters for device area A and device thickness d . The solar simulator and measurement system used (TriSol Solar Simulator, IV16-L, PV Measurements Inc.) comprises components for variable electronic load and data acquisition (Keithley 2400, PVM QEX10), and a white light source (constant illumination, 1.5 air mass global solar spectrum) calibrated using a standard silicon diode to 1 sun equivalent (100 mW cm^{-2}). The photovoltaic device is held under illumination at a range of constant applied potentials (V), from forward to reverse bias, and the extracted current density (J) is measured, to produce a JV response plot. A dark measurement (without illumination) is also performed across the range of measured applied potentials. Further, the illumination intensity can be varied below 1 sun through the use of reflective neutral density filters, thereby obtaining JV response at a range of steady-state current densities.

J_{SC} and V_{OC} are obtained directly as the JV response intersection with the voltage and current density axis respectively. The FF is calculated as the quotient of P_{max} and the product of J_{SC} and V_{OC} , illustrated as the ratio of the two square regions in Figure 2.1. The power conversion efficiency η of a device can then be obtained. The series and shunt resistance are then calculated for each device, using the slope of the dark JV plot about 1 V and 0 V respectively. Further analysis of these measurement results can be performed to obtain the empirical reaction order δ' and diode

ideality factor n'_{id} , and can be compared to those obtained through transient measurement and analysis. The δ' can be calculated from the dependence of short circuit current J_{SC} on illumination intensity ϕ , while the n'_{id} can be calculated from the dependence of open circuit voltage V_{OC} on ϕ . Further details are provided in Chapter 2, Section 2.1.2.

6.2.3 Transient Applied Bias Charge Extraction and Photovoltage Decay

The time resolved charge extraction (TRCE) measurement utilises a nanosecond FET switch (SR-05, Asama Lab) to switch rapidly between open circuit and short circuit conditions. The switch is capable to switching from an internal impedance R_{SW} of $2.2\text{ M}\Omega$ to less than $1\text{ }\Omega$ in under 100 ns. A high switch impedance is used to maintain open circuit rather than a true open circuit (infinitely large impedance) to protect the switch. A photovoltaic device (OPV) is connected in series with the switch, and charge carriers are generated using a laser pulse for photoexcitation (532 nm, 6 ns pulse width, Spectra Physics Quanta Ray Lab 170; or during long pulse measurements a 641 nm, variable pulse width, Nation Instruments Coherent CUBE continuous wave). A variable delay time T_{del} is imposed between stopping laser illumination T_0 and switching T_{SW} using a delay generator, during which time the device is held at open circuit, and charge carriers are left to recombine. Upon switching, the device is short circuited and an extraction transient is measured across the variable measurement impedance R_M ($50\text{ }\Omega$ unless otherwise stated) using an oscilloscope (DPO4000 Series, Tektronix).

The TRCE measurement is modified through the addition of the ability to apply a bias during charge extraction measurement. In concert with switching at T_{SW} , a reverse bias square pulse potential is applied across the device contacts (through the FET switch) using a function generator (WF1974 Wave Factory Multifunction Generator, NF Corp.). The pulse length of the applied bias was maintained for 1 ms, well beyond typical extraction times on the order of $50\text{ }\mu\text{s}$. In the course of measurements, the magnitude of the applied reverse bias can be varied in addition to both delay time and excitation density. Unless otherwise stated, an applied bias of 2 V was used.

Each extraction transient is recorded as an average of 50 individual measurements, per set of conditions, to minimise noise and account for any variability in laser excitation. All transients presented herein are displayed with an 80 ns shift for illustration purposes, such that switching occurs at 80 ns as presented in figures. Unless otherwise specified, the characteristic switch response has been subtracted from all transients, recorded individually for each set of measurements, as well as the dark (no laser illumination) transient response. The transient voltage response is measured as a function of extraction time, and converted to extracted current using the known measurement resistance. The total extracted charge is obtained through integrating the current transient response over time. The extracted charge is obtained at a range of delay times to yield the decay of extracted charge as a function of delay time, with laser illumination also varied.

Photovoltage decay measurements are performed to obtain the open circuit potential at the device contacts as a function of time that the photovoltaic device is held at open circuit after laser illumination is stopped. Variation of excitation density is also used to alter the initial charge density. These measurements are performed using a laser excitation source (532 nm, 6 ns pulse width, Spectra Physics Quanta Ray Lab 170; OR for long pulse measurements a 641 nm, variable pulse width, Nation Instruments Coherent CUBE continuous wave), with the photovoltaic device connected in series with the oscilloscope high impedance of $1.0\text{ M}\Omega$ to maintain open circuit. The photovoltage decay transients are then recorded using the oscilloscope (DPO4000 Series, Tektronix), from the time of stopping laser excitation until complete decay of photovoltage.

Further details of time resolved charge extraction and photovoltage decay measurements and analysis methodology are presented in Chapter 2, Sections 2.3.1 and 2.3.2.

6.2.4 Photo-CELIV

Photoinduced charge extraction in linearly increasing voltage (photo-CELIV) measurements are performed using the FET switch and applied bias TRCE measurement setup, however with minor operational differences. The applied bias is a linearly increasing reverse bias voltage ramp, rather than the square pulse used in applied bias TRCE measurements. Additionally, a $2\text{ }\mu\text{s}$ delay is used between switching and voltage ramp application to separate the CELIV transient and characteristic switch opening response. A reverse bias offset voltage is applied to the device in time with switching, in order to maintain open circuit conditions (oppose the internal potential V_{OC}) and minimise the leakage of charge density during the $2\text{ }\mu\text{s}$ delay prior to application of the voltage ramp. The magnitude of the required offset is determined by the device internal potential (proportional to the V_{OC}), however varies as a function of internal charge density, and consequently changes with delay time and excitation density. The offset is manually adjusted such that the extraction current stabilises at zero within the $2\text{ }\mu\text{s}$ delay time prior to voltage ramp application (and is typically on the order of 600 to 800 mV).

6.3 Results and Discussion

The fabrication of photovoltaic devices incorporating the three polymer donors P1, P2, and P3 in blends with the PCBM acceptor presented a number of challenges that had to be overcome. Small variations in the solubility of these polymer donors in typical organic solvents occasionally resulted in inconsistent active layer deposition and phase mixing, with particulates remaining in the blend film, highly variable surface roughness, and spatial variation in active layer thickness across the device active area. Initial device performance results for these polymer blends were on the order of 0.2 %, however through successive optimisation of fabrication processes, above 2 % solar conversion efficiency has been achieved for both P1 and P2 blend devices. Even P3 blend devices have achieved over 1 % due primarily to a consistently high open-circuit voltage and

fill factor, relative to that obtained for P1 or P2 devices. This behaviour results primarily from better extraction performance (a faster and less dispersive charge carrier mobility), as well more consistent blend film morphology achieved during fabrication. P1 and P2 blend films typically exhibit poor charge transport and extraction behaviour, negatively impacting device fill factor and overall solar conversion efficiency.

6.3.1 Charge Transport and Extraction Behaviour

Photovoltaic devices were fabricated incorporating each of the polymer donor blend films (P1, P2, and P3 donor with 70 % PCBM acceptor), with comparable active layer thickness of 160 nm for use in applied bias time resolved charge extraction measurements. These devices were fabricated with active layers comparable to that of the blend films investigated in Chapter 3. However in this configuration the devices exhibit poor performance, with fill factors (FF) below 0.35 and short-circuit current (J_{SC}) on the order of 2 mA cm^{-2} , resulting in solar conversion efficiencies (η) below 0.5 % and comparable between blend systems (JV plots displayed in Figure 6.3). Although not optimised for η , these devices do provide a direct comparison to the results of Chapter 3 regarding the influence of ΔG_{ET} on charge generation yield.

Charge extraction measurements performed on devices incorporating the P1/P2/P3 donor polymers have presented a number of issues hindering the reliable investigation of charge generation and recombination processes. These issues arise primarily due to the apparent poor charge carrier transport and trapping behaviour, exhibiting a broad distribution of charge carrier mobilities and significant trap state density distribution (details will be presented and discussed in the following sections). The large rise in steady-state current extraction at increasing reverse bias (Figure 6.3) illustrates the poor charge extraction behaviour of these devices, most prominently observed for P1 and P2 blends. The influence of these factors can be observed within the time domain under investigation in charge extraction measurements (nanosecond to millisecond), and more importantly is observed to vary between donor-acceptor system. Applied bias time resolved charge extraction is therefore required to overcome these limitations for the measurement of charge density in operational photovoltaic devices. A characterisation of the transport and extraction behaviour of these systems is presented below.

Photoinduced Charge Extraction in Linearly Increasing Voltage Measurements

Switched photo-CELIV measurements were performed on the blend devices using a reverse bias voltage ramp with a 1 V peak and 10 μs pulse width, with the response transients displayed in Figure 6.4. The illuminated transients (solid line, 'light') for each donor blend device were obtained using a $10 \mu\text{J cm}^{-2}$ excitation density and 5 μs excitation-extraction delay time, while the transient responses without illumination (broken line, 'dark') are also displayed. For the illuminated transients, upon opening the switch (at time zero) a transient response is observed due to the extraction of photogenerated charge density in the time required for the offset bias (580 to

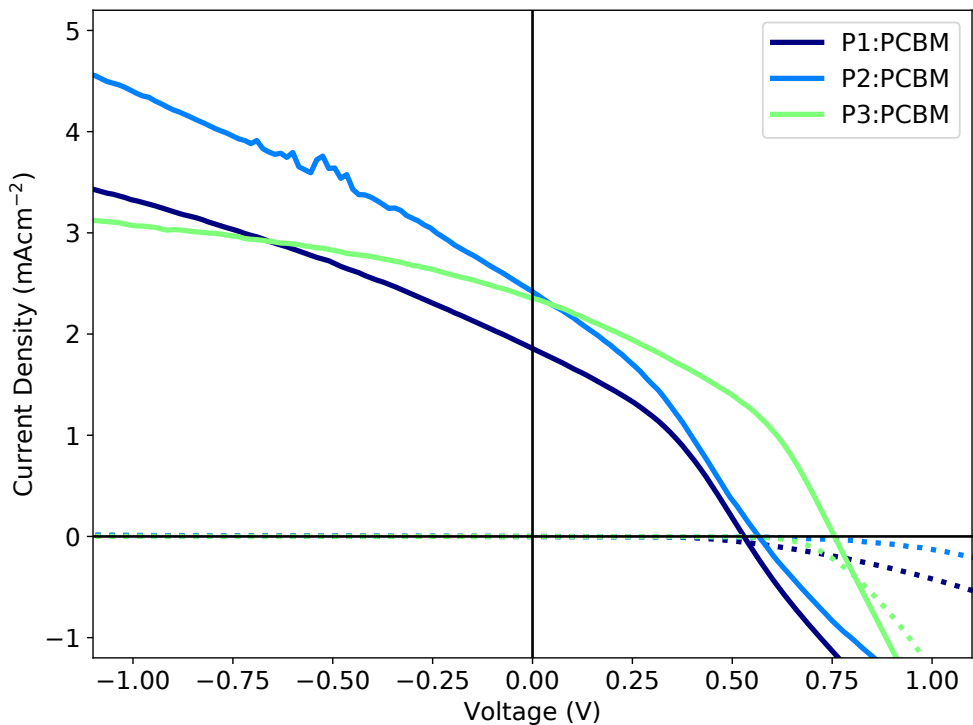


Figure 6.3: Illuminated (solid line) current-voltage response of three blend devices (1:4 donor:acceptor), incorporating different polymer donors (as labelled) at 100 mW cm^{-2} . The response without illumination is also displayed (broken line).

710 mV) to be applied through the switch (identical to that performed in Chapter 5). By $1 \mu\text{s}$ after switching the transient response has stabilised to zero, indicating the restoration of open-circuit condition (no current extraction) prior to the application of the reverse bias ramp. The net loss of charge density prior to the application of the bias ramp is however negligible with the use of switch and offset bias.

The transients without illumination exhibit an initially RC limited rise to a plateau, representing the device capacitive response to a linearly increasing voltage ramp, with no rise during this capacitive response further indicating no mobile charge density or injection within these devices. The minor variation in magnitude of the plateau between devices is attributed to slight differences in active layer thickness on the order of 5 %, however slight differences in the dielectric constant of respective polymer donor materials could equally account for this minor variation (ϵ is assumed to be 3.5 for all donor-acceptor blends, based on electrochemical impedance measurements of device capacitive response). The illuminated transients of all devices exhibit additional current extraction above the capacitive response, indicating the extraction of photogenerated charge density. These results yield calculated charge carrier (electron) mobilities of 2.2×10^{-5} , 2.2×10^{-5} , and $4.2 \times 10^{-5} \text{ cm}^2 \text{ V}^{-1} \text{ s}^{-1}$ for the P1, P2, and P3 devices respectively. Note that the P3 blend device exhibits almost twice the mobility of both P1 and P2 devices. Importantly, complete extraction of internal charge density does not occur for any device within the $10 \mu\text{s}$ pulse, as indicated by a continued

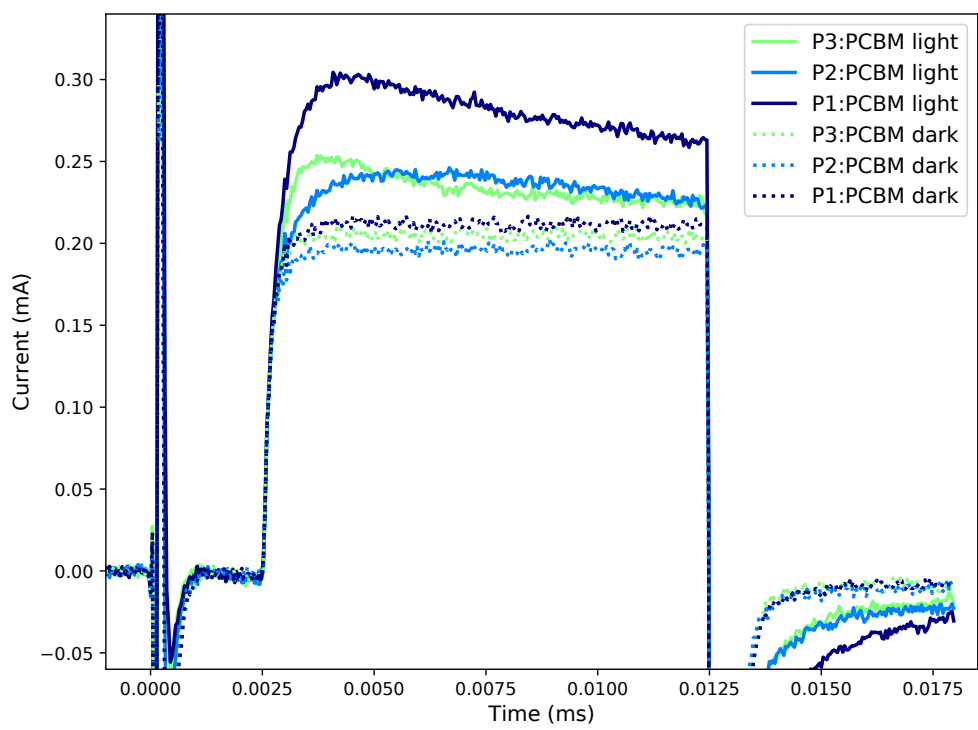


Figure 6.4: Photoinduced charge extraction in linearly increasing voltage (photo-CELIV) response transients for three donor-acceptor blend devices (as labelled), using a $10 \mu\text{J cm}^{-2}$ excitation density, $5 \mu\text{s}$ excitation-extraction delay time, and a $10 \mu\text{s}$ pulse width with 1 V peak reverse bias ramp.

extraction current above that of the capacitive response. This behaviour is observed over a wide range of voltage ramps (from 200,000 down to 2000 V s⁻¹), and performed using both pristine polymer donor (not shown) and blend films. The similarity in transient behaviour and calculated mobility between the blend and pristine films is indicative of a large distribution of charge carrier (hole) mobilities, attributed to a broad density of states distribution with significant trap state occupancy (discussed further in Section 6.3.3). Although the absolute value of the mobilities obtained are comparable to that typically observed for PCDTBT:PCBM based devices on the order of 5×10^{-5} cm² V⁻¹ s⁻¹, the high degree of dispersion is expected to influence both extraction and recombination behaviour of these devices, and will be further discussed in the following section.

Applied Bias Time Resolved Charge Extraction Measurements

Applied bias time resolved charge extraction measurements were performed on each blend device at a range of excitation densities and applied reverse bias. The two sets of charge extraction transients presented in Figure 6.5 are used to illustrate the relative behaviour of each donor-acceptor system at 1 $\mu\text{J cm}^{-2}$ (top) and 100 $\mu\text{J cm}^{-2}$ (bottom) excitation densities, using a short 100 ns excitation-extraction delay time. These conditions enable the analysis of charge transport and extraction behaviour at both low and high initial charge densities respectively. The transients without an applied bias (solid line) for the 1 $\mu\text{J cm}^{-2}$ (Figure 6.5, top) exhibit comparable total extracted charge density (within 15 %), however the transient shapes are distinct for each respective device (current extraction over time). This is particularly noticeable directly after the *RC* rise, with the P3 blend device exhibiting the greatest initial transient amplitude (extraction current), followed by the P2 and P1 blend devices respectively. This can be attributed to the differences in charge carrier mobility and transport behaviour as identified in the photo-CELIV measurements presented previously (Figure 6.4). The faster mobility of the P3 blend device results in a faster extraction rate, and therefore a faster extraction transient with a greater initial amplitude. Further, at the low charge densities produced by the 1 $\mu\text{J cm}^{-2}$ excitation density, spatial redistribution of the initially photogenerated charge density (as observed in photovoltage decay measurements, not shown) will compound the effects of charge transport/mobility disparity between devices on the charge extraction process. Where significant charge redistribution and transport is required during extraction measurement, a faster charge carrier mobility will enable faster redistribution of charge density, and therefore a greater rate of charge extraction.

The application of a 2 V reverse bias during charge extraction (broken lines) at the 1 $\mu\text{J cm}^{-2}$ excitation density shows an increase in total extracted charge density for both P1 and P2 blend devices on the order of 80 %, with the extraction transient exhibiting extended current extraction up to 3 μs extraction time. The P3 blend devices however exhibits no resolvable change in total extracted charge density or transient shape. As discussed at length in Chapter 5, Section 5.4.2, the application of an applied reverse bias can reduce recombination losses during extraction measurement, resulting in an increase in measured charge density. This effect is typically observed

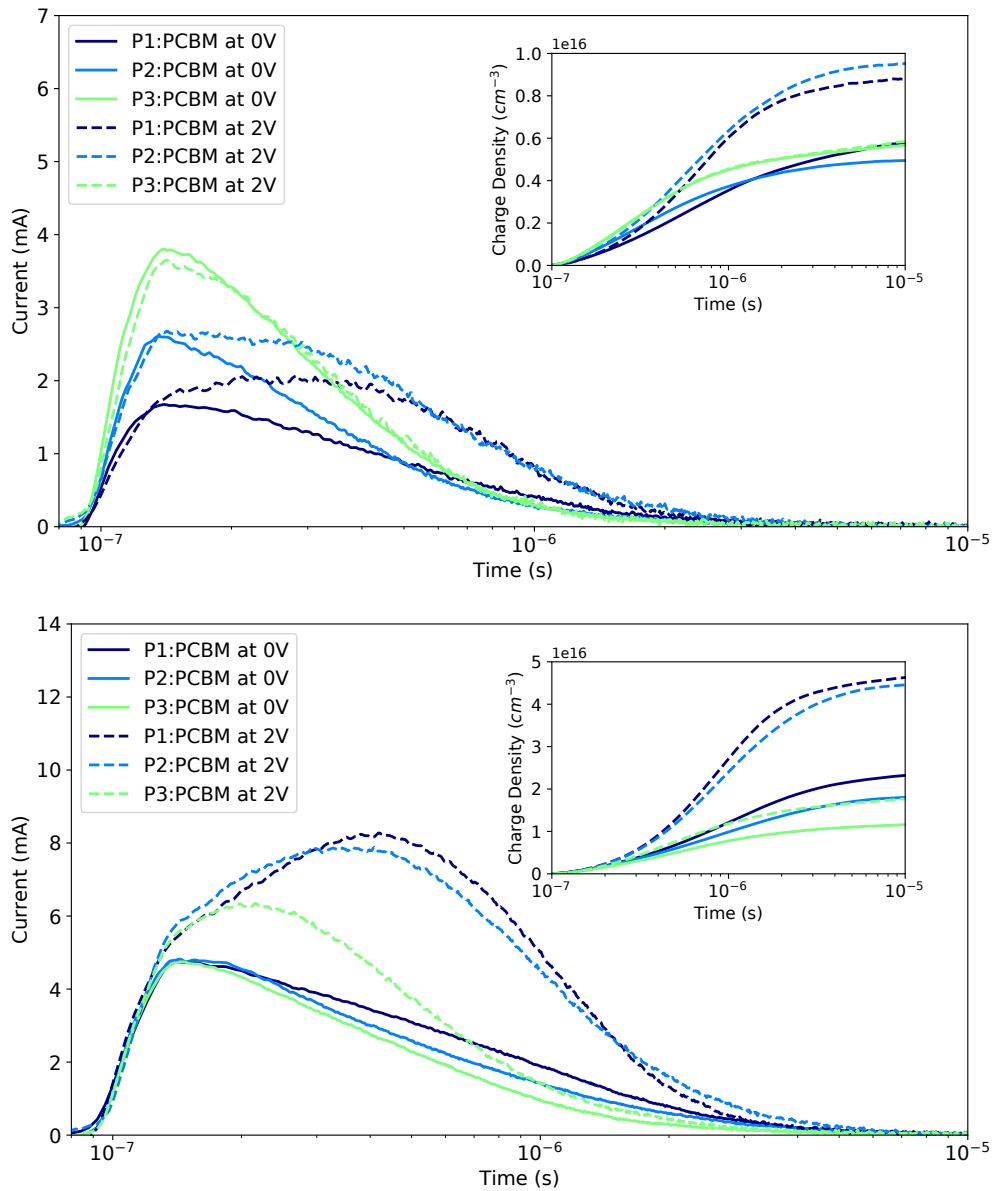


Figure 6.5: Applied bias time resolved charge extraction transients for three donor-acceptor blend devices (as labelled) at either $1 \mu\text{J cm}^{-2}$ (top) or $100 \mu\text{J cm}^{-2}$ (bottom) excitation density, using a 100 ns excitation-extraction delay time, and both 0 V (solid line) and 2 V (broken line) applied reverse bias. The inset of each plot shows the respective transient integral as a function of extraction time.

where significant recombination occurs during the extraction measurement. However the calculated charge carrier lifetime at these low charge densities (not shown) is on the order of $10 \mu\text{s}$ for all devices, longer than the required extraction time. Therefore, extraction of a shallow trap state population that would otherwise not be extracted during measurement is likely the primary source of the observed increase in extracted charge in both P1 and P2 blend devices. Transport and trapping losses are particularly prominent in these devices with a large 160 nm thick active layer, increasing the average transport distance and extraction time. The lack of any resolvable increase in the P3 blend device can be attributed to the already discussed improved charge carrier mobility/transport behaviour and trap state density relative to the P1/P2 blends, where efficient extraction of charge density is achieved without the need for an applied bias.

The increase in extracted charge density with the application of a 2 V reverse bias at the higher $100 \mu\text{J cm}^{-2}$ excitation density (Figure 6.5, bottom) exhibited by the P1, P2, and P3 blend devices of 100, 140, and 50 % respectively is greater than that observed at $1 \mu\text{J cm}^{-2}$. Additionally an increase is observed for the P3 blend device. These transients also exhibit characteristic space charge limited extraction transients (transient rise to a peak). This greater increase in extracted charge density with an applied reverse bias is attributed to the reduction of recombination losses during extraction at these higher charge densities, as the charge carrier lifetime has been reduced to the order of $1 \mu\text{s}$ for all devices, and is therefore comparable to the required extraction time (see Chapter 5 for a detailed discussion extraction losses). As such the effect of applying a reverse bias under these conditions is to improve the extraction of internal charge density that would otherwise recombine during the extraction measurement, and therefore yields a more accurate measure of photogenerated charge density.

To summarise the above results, P3 blend devices exhibit efficient transport and extraction of charge density, while both P1 and P2 blend devices exhibit significantly slower (trap limited) extraction. This variability between donor-acceptor systems may be influenced by a number of factors in addition to the engineered differences in material energy levels, such as through differences in active layer morphology caused by variable solubility and deposition behaviour during device fabrication. Additionally, these results emphasise the utility and necessity of using the developed applied bias time resolved charge extraction technique for the study of these material systems. An applied reverse bias overcomes the limitations of charge transport in these donor-acceptor systems, where as high as 80 % of charge density would have not been extracted otherwise, leading to significant error in results. Further, the disparity in transport behaviour between devices no longer impacts the accurate measurement of charge density, enabling a fair comparison of charge generation yield between donor-acceptor blends systems. This analysis will be presented in the following Section 6.3.2, including a discussion of the observation of photogenerated charge density in P3 blend devices.

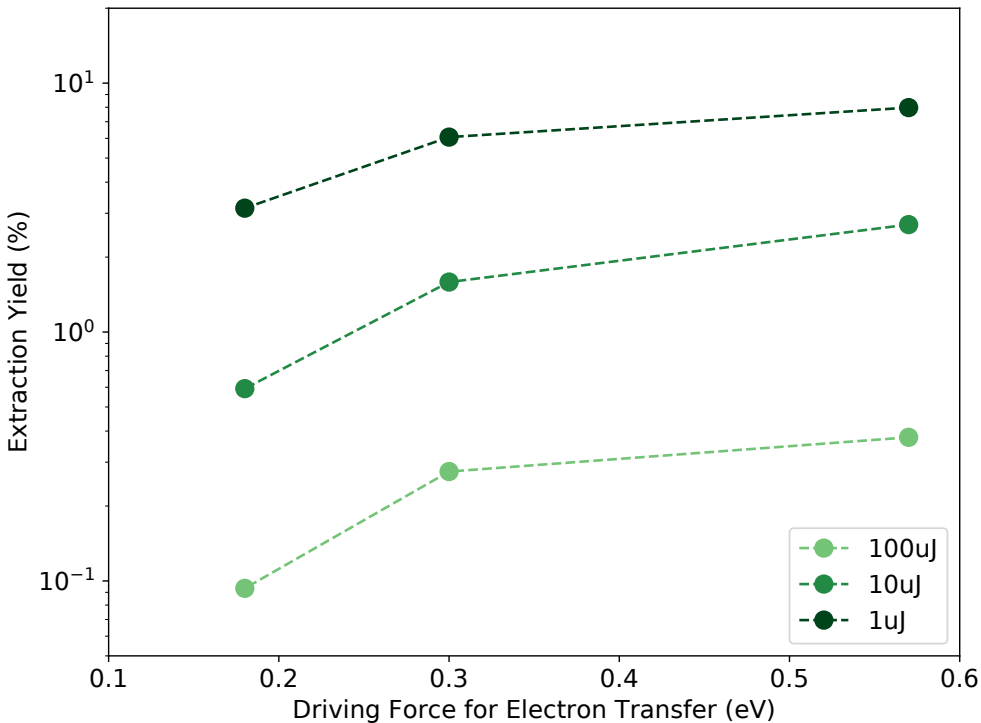


Figure 6.6: Charge extraction yield as a function of the driving force for electron transfer (varied through donor-acceptor blend system) at multiple excitation densities (as labelled). The extraction yield was calculated using extracted charge density, obtained through applied bias time resolved charge extraction measurements on photovoltaic devices, using an applied reverse bias of 2 V and 100 ns excitation-extraction delay time.

6.3.2 Influence of Driving Force for Electron Transfer on Charge Extraction Yield

Using the applied bias time resolved charge extraction measurements discussed in the previous section, the charge carrier extraction yield was calculated for each device at multiple excitation densities (532 nm excitation wavelength) for an applied reverse bias of 2 V and excitation-extraction delay time of 100 ns (conditions of peak extracted charge density). The resulting plot of extraction yield as a function of ΔG_{ET} is presented in Figure 6.6. This charge carrier extraction yield is representative of the charge generation yield of these donor-acceptor material systems, calculated as the fraction of the number of charge carriers collected during charge extraction measurement to the photons incident on the device active layer. The initial charge generation yield of these blend systems is expected to be higher than the measured extraction yield, due to transport losses and non-geminate recombination losses on the picosecond-nanosecond timescale. However calculation of extraction yield using the lower $1 \mu\text{J cm}^{-2}$ excitation density (longer relative charge carrier lifetime), as well as the use of an applied reverse bias during charge extraction measurement should provide a reasonable estimate of charge generation yield such that a relative comparison between donor-acceptor systems can be performed.

The calculated extraction yields at the $1 \mu\text{J cm}^{-2}$ excitation density were 8.1, 6.2, and 3.1 % for P1, P2, and P3 respectively, while at $100 \mu\text{J cm}^{-2}$ the extraction yields are reduced to 0.38, 0.27, and 0.09 % respectively. The P1 blend device consistently exhibits the greatest extraction yield, followed closely by the P2 blend device, while the P3 blend device is consistently much lower than either P1 or P2 blend devices, on the order of 30 % that exhibited by the P1 blend device. Further, a dependence of extraction yield on ΔG_{ET} is observed, with a greater ΔG_{ET} yielding a higher extraction yield under all measured excitation densities.

While the ultrafast transient absorption studies of Chapter 3 indicated a near unity quantum yield of electron transfer, charge-transfer state recombination was estimated to reduce the photo-generation yield of separated charge carriers to an estimated 60 % by 1 ns post excitation in the P1 and P2 blends. Additionally, non-geminate recombination within the measurement response of the charge extraction measurement (on the order of 200 ns) is likely the primary cause of the remaining reduction in charge generation yield. The relative difference in extraction yield between P1 and P2 blend devices may also be explained by differences in nanosecond non-geminate recombination kinetics (mobility-lifetime product), where faster recombination in the P2 blend device would result in a lower extraction yield than the P1 blend device. The recombination kinetics of these donor-acceptor systems will be investigated later in this chapter (Section 6.3.4). The observation of significant charge generation in the P3 blend device, on the order 30 % that of the P1 blend device, is however inconsistent with the complete lack of observable electron transfer or polaron generation in the ultrafast transient absorption studies of Chapter 3. Additional investigations are performed and presented below to further investigate this observation.

Improved Charge Extraction with Incorporation of Processing Additive

New photovoltaic devices were fabricated incorporating each of the P1, P2, and P3 PCBM blends, however with the addition of DIO to the blend solution during active layer deposition, and the use of the more optimum 100 nm active layer thickness. These modifications to device fabrication produce significant improvements in charge carrier transport (blend morphology) and extraction efficiency, resulting in η towards 2 %. A donor:acceptor ratio closer to 1:1 has shown to yield optimal device performance rather than the 1:4 used in the optical studies of Chapter 3 and within the devices fabricated for this chapter investigations.⁴³ However the 1:4 ratio has been used throughout the presented studies to maintain consistency between ultrafast transient absorption and charge extraction measurements.

Using the new devices, applied bias time resolved charge extraction measurements were again performed under identical excitation conditions (532 nm excitation wavelength, 1 to $100 \mu\text{J cm}^{-2}$ excitation densities). Steady-state device performance measurements were also performed, including current-voltage (JV) and incident photon to current conversion efficiency (IPCE) to provide additional insight into the charge photogeneration behaviour of these donor-acceptor systems, and

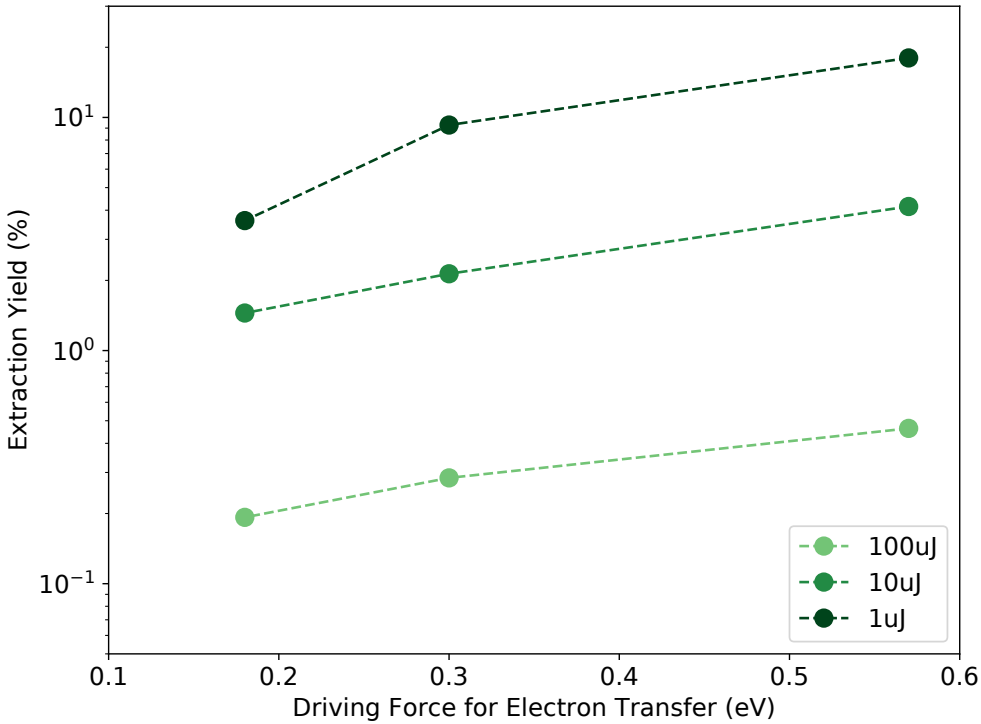


Figure 6.7: Charge extraction yield as a function of the driving force for electron transfer (varied through donor-acceptor blend system) at multiple excitation densities (as labelled). The extraction yield was calculated using peak extracted charge density, obtained through applied bias time resolved charge extraction measurements on improved photovoltaic devices.

thereby investigate the influence ΔG_{ET} on charge photogeneration yield.

The charge extraction yields as a function of ΔG_{ET} for these new devices are presented in Figure 6.7, calculated from charge extraction measurements as outlined in the previous section. The calculated extraction yields at the $1 \mu\text{J cm}^{-2}$ excitation density were 18, 9.4, and 3.6 % for P1, P2, and P3 respectively, while at $100 \mu\text{J cm}^{-2}$ the extraction yields are reduced to 0.47, 0.28, and 0.19 % respectively. The P1 blend device again consistently exhibits the greatest extraction yield, followed by the P2 blend device, while the P3 blend device is consistently lower than either P1 or P2 blend devices. Further, a dependence of extraction yield on ΔG_{ET} is again observed with a greater ΔG_{ET} yielding a higher extraction yield under all measured excitation densities. While the magnitude of extraction yield has increased in all devices relative to those presented in the previous section, identical trends are observed with P3 still exhibiting reproducible charge photogeneration/extraction. The relative difference between P1 and P2 blend devices may again be explained by differences in picosecond-nanosecond non-geminate recombination, and will be further investigated in Section 6.3.4. However the origin of significant charge photogeneration in P3 blend devices remains unclear.

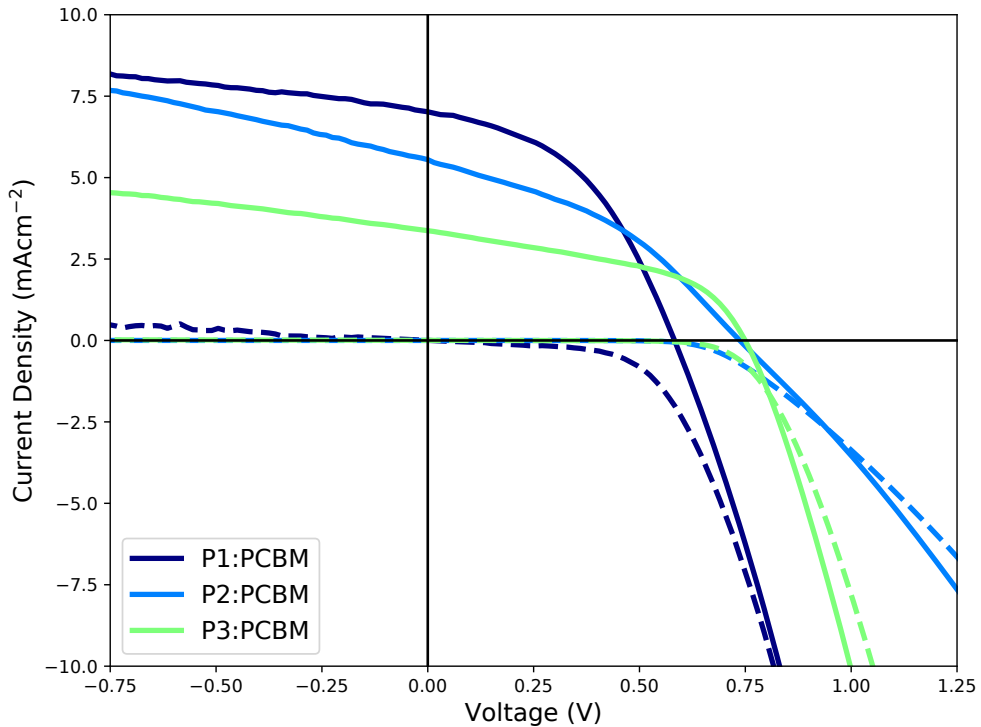


Figure 6.8: Illuminated (solid line) current-voltage response of three blend devices (1:4 donor:acceptor, fabricated using the DIO additive), incorporating different polymer donors (as labelled) at 100 mW cm⁻². The response without illumination is also displayed (broken line).

It is important to note that the relative differences in measured generation yield between donor-acceptor systems, on the order of 10 to 30 % for a given excitation density, is orders of magnitude less than that observed between the presented excitation densities. For example, increasing from 1 to 100 μ J cm⁻² excitation density results in a reduction in extraction yield for the P1 blend device from 18 to 0.47 %. This reduction in extraction yield observed at high excitation densities is attributed to increased bimolecular recombination on the nanosecond timescale. These observations strongly indicate that, while the initial charge photogeneration yield can influence the extraction yield of operational devices, bimolecular recombination has a much greater impact on the overall extraction yield and therefore on photovoltaic device performance. Relative differences in the electron transfer yield of donor-acceptor systems due to differences in ΔG_{ET} may be less important than the relative degree of bimolecular recombination. Further investigations are presented in Section 6.3.4 regarding the influence of energetic driving forces on recombination kinetics.

Steady-state JV and IPCE measurements were performed to investigate the origin of charge photogeneration in P3 blend devices, presented in Figures 6.8 and 6.9, including UV-Visible absorbance spectrum, and a summary of device performance parameters presented in Table 6.1. To summarise the primary device current-voltage behaviours characteristic of devices incorporating each donor blend: P1 exhibits the highest J_{SC} , followed by P2 and finally P3; P3 exhibits the highest V_{OC} , followed closely by P2, while P1 typically displays a much lower relative V_{OC} ; P3

Table 6.1: Summary of device parameters and steady state performance (current-voltage results displayed in Figure 6.8), open circuit voltage V_{OC} , short-circuit current J_{SC} , fill factor FF , and solar conversion efficiency η . For each donor material are displayed the best performing device, and both average and standard deviation from 4 individual devices (1:4 donor:acceptor).

	V_{OC} (mV)	J_{SC} (mA cm $^{-2}$)	FF -	η (%)
P1:PCBM (1:4)				
Best	585	7.0	0.45	1.8
Mean (4 devices)	578	6.4	0.43	1.6
Std. Dev.	8	0.8	0.02	0.3
P2:PCBM (1:4)				
Best	750	5.6	0.37	1.6
Mean (4 devices)	745	4.1	0.39	1.2
Std. Dev.	4	1.4	0.01	0.4
P3:PCBM (1:4)				
Best	750	3.4	0.46	1.2
Mean (4 devices)	750	3.2	0.45	1.1
Std. Dev.	0	0.2	0.01	0.1

consistently displays the highest FF , while P1 also exhibits a high FF , however significantly more variable between devices, and P2 typically displays a low and highly variable FF . This typically results in comparable overall performance (η) between material systems at steady-state operation, where the high J_{SC} of P1 blend devices compensates for a low V_{OC} , while the inverse is true for P3 blend devices, and the performance of P2 blend devices is an average between these two systems with moderate J_{SC} and V_{OC} . For the presented devices, both J_{SC} and η display a positive correlation with the ΔG_{ET} of each respective donor-acceptor system, consistent with the charge extraction yield results obtained through transient charge extraction measurements presented in the previous section.

An inverse correlation is observed for V_{OC} relative to ΔG_{ET} , however the charge densities under steady-state illumination at V_{OC} may not be comparable between blend devices. The steady-state charge density is dependent on a quasi-equilibrium between charge photogeneration and bimolecular recombination rates which may differ between donor-acceptor systems. As such, a direct comparison of the influence of material system energetics on V_{OC} is not accurate using solely steady-state JV measurements. This will be further investigated in the following Section 6.3.3, using applied bias time resolved charge extraction to directly measure V_{OC} as a function of charge density for each blend device.

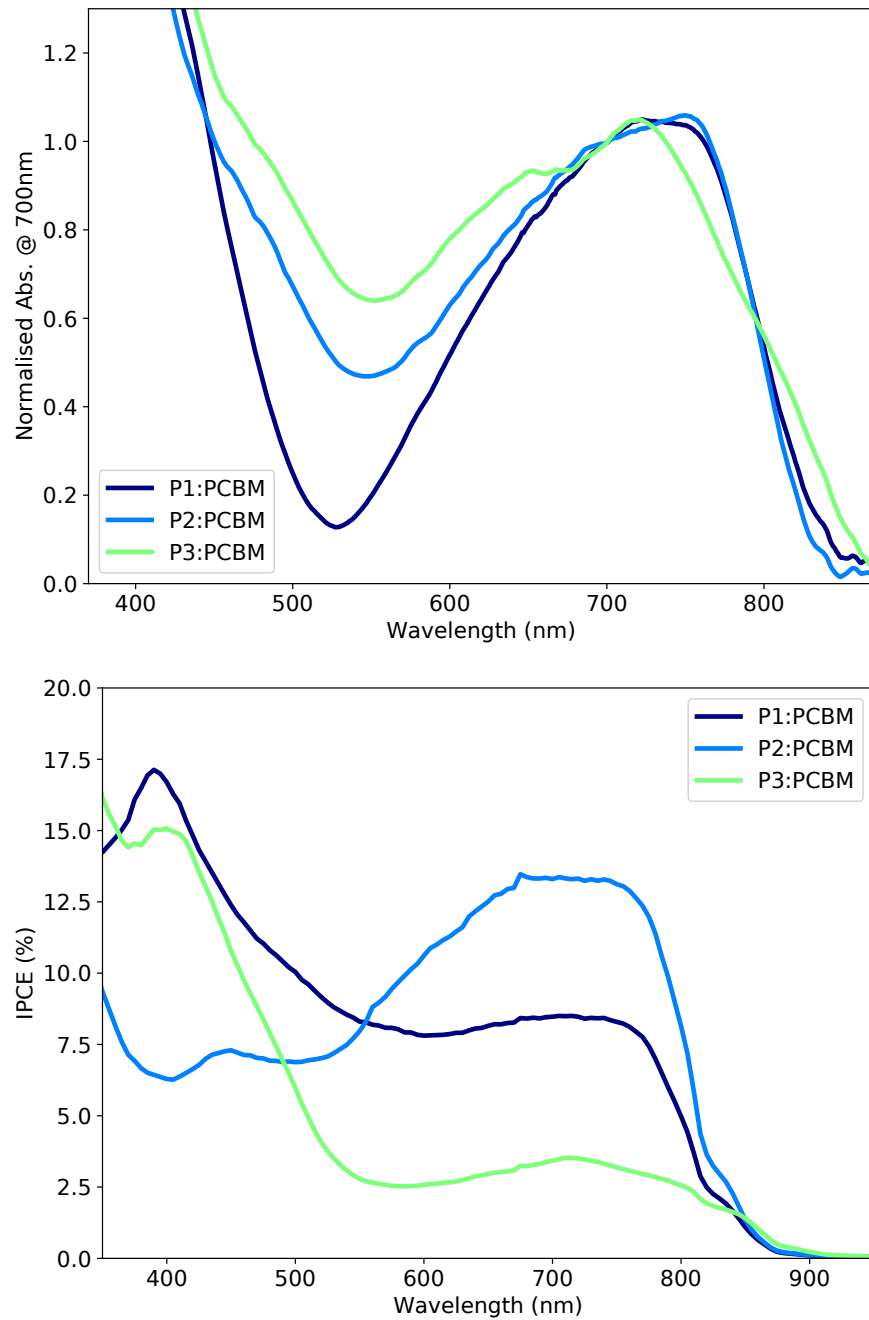


Figure 6.9: UV-Visible absorbance (top) and incident photon to electron conversion efficiency (bottom) as a function of wavelength for three blend devices, incorporating different polymer donors (as labelled), and measured through an optically transparent region of device active layers.

The UV-Visible spectra displayed in Figure 6.9 (top) show the primary donor material absorption peak centred about 700 nm, with typical PCBM absorption dominating below 450 nm. The IPCE spectra displayed in Figure 6.9 (bottom) present a measure of steady-state extraction yield as a function of excitation wavelength. These plots provide a methodology to assign the relative portion of photogenerated charge density to a range of excitation wavelengths, thereby providing information on the primary mechanisms of charge photogeneration in each donor-acceptor blend device. The integrated IPCE from 350 to 900 nm yield values of 8.4, 8.2, and 5.1 % for P1, P2, and P3 respectively. The relative magnitude of these integrated IPCEs is consistent with both the steady-state J_{SC} and transient charge extraction yield trends.

A significant portion of extraction efficiency is derived from the 550 to 850 nm range for both P1 and P2 blend devices, representing 45 and 68 % of the total integrated IPCE respectively. The P3 blend device however only exhibits 29 % within this region. This region of charge photogeneration is attributed primarily to polymer donor material excitation and electron transfer, while the region below 550 nm is attributed primarily to PCBM material excitation and hole transfer. These results indicate that, while both P1 and P2 blend devices exhibit efficient electron and hole transfer, the P3 blend device exhibits primarily hole transfer as the source of charge photogeneration. The energetic driving force for hole transfer ΔG_{HT} in the P3 blend system (0.39 eV) appears large enough to yield efficient hole transfer, however the ΔG_{ET} (0.18 eV) appears insufficient to produce efficient electron transfer. This observation may account for the lack of observed electron transfer in the ultrafast transient absorption studies of Chapter 3, while still exhibiting a charge extraction yield on the order of 30 % that exhibited by P1/P2 (ΔG_{ET} of 0.57 and 0.30 respectively) for an excitation wavelength of 532 nm. Further, the improved relative transport/extraction behaviour of the P3 blend system may enable more efficient extraction of any photogenerated charge, relative to that of P1 or P2 blend systems, thereby somewhat accounting for the observed comparable extraction yields. However, transient charge extraction measurements have been repeated using an excitation wavelength of 700 nm (significantly longer than the primary absorption of PCBM), and result in comparable charge extraction yields to those observed using the 532 nm excitation. While the above results provide some insight, a conclusive understanding of the origin of relatively efficient charge generation in P3 blend devices remains in contrast to the findings of Chapter 3 and therefore remains an outstanding question.

A comparison of the charge extraction yields obtained through charge extraction measurements to the estimated charge generation yields obtained through ultrafast transient absorption measurements of Chapter 3 presents a number of disparities. While the transient absorption results indicate a comparable, high charge generation yield for both P1 and P2 blend films on the order of 60 %, the peak extraction yields obtained through transient charge extraction measurements of the corresponding blend devices were on the order of 10 to 20 %, with the P1 blend device exhibiting twice the extraction yield of the P2 blend device. This disparity, both between techniques and between blends can be accounted for by bimolecular recombination within the time

resolved charge extraction measurement response. Significant recombination on the picosecond to nanosecond timescale will reduce the observed extraction yield from that of the initial generation yield as estimated through ultrafast transient absorption. Additionally, any relative difference in the recombination kinetics of these blends will lead to a disparity, in this case the P2 appears to experience an increased degree of recombination. Accounting for these likely factors, the presented extraction yields are consistent with the results of Chapter 3, with a ΔG_{ET} of 0.30 eV or above yielding a high charge photogeneration yield, while device current extraction appears strongly limited by bimolecular recombination.

The second disparity between optical and charge extraction results is the relatively significant charge generation and extraction yield of the P3 blend devices, as high as 30 % that of the P1 blend device. This is in stark contrast to the lack of observed electron transfer and charge photogeneration in the ultrafast transient absorption results. The origin of charge photogeneration in the P3 blend device appears to arise predominately from hole transfer, leading to significant charge generation even with the low ΔG_{ET} of 0.18 eV. Additionally the P3 blend device exhibits improved charge transport/extraction behaviour and less dispersive mobility, relative to that of the P1 and P2 blend devices, implying that photogenerated charge carries within the P3 blend device are more effectively extracted. The measured extraction yields are still greatly reduced, relative to the P1 and P2 blend devices under identical excitation conditions, indicating that a ΔG_{ET} greater than 0.18 eV is required to produce highly efficient charge generation. However the origin of such a large disparity between results obtained through transient absorption and charge extraction measurements for the P3 blend system remains unclear.

It should also be noted that the reliable measurement of charge extraction yields as low as those presented herein using time resolved charge extraction (as low as 0.2 %) over the nanosecond timescale cannot be achieved using transient absorption techniques due to insufficient measurement sensitivity. The use of charge extraction for this purpose is therefore highly advantageous in accurately investigating the charge photogeneration behaviour of operational photovoltaic devices, and should be performed in concert with transient absorption where possible.

6.3.3 Influence of Material System Energy Levels on Device Photovoltage

Applied bias time resolved charge extraction and photovoltage decay measurements are used to investigate the scaling of device photovoltage with donor-acceptor material system energy levels (ΔG_{ET} and corresponding $E_{HOMO-LUMO}$). Charge density decay and photovoltage decay measurement results are presented in Figure 6.10, obtained from time resolved charge extraction and photovoltage decay measurements respectively on the devices presented in the previous section (see Figure 6.8).

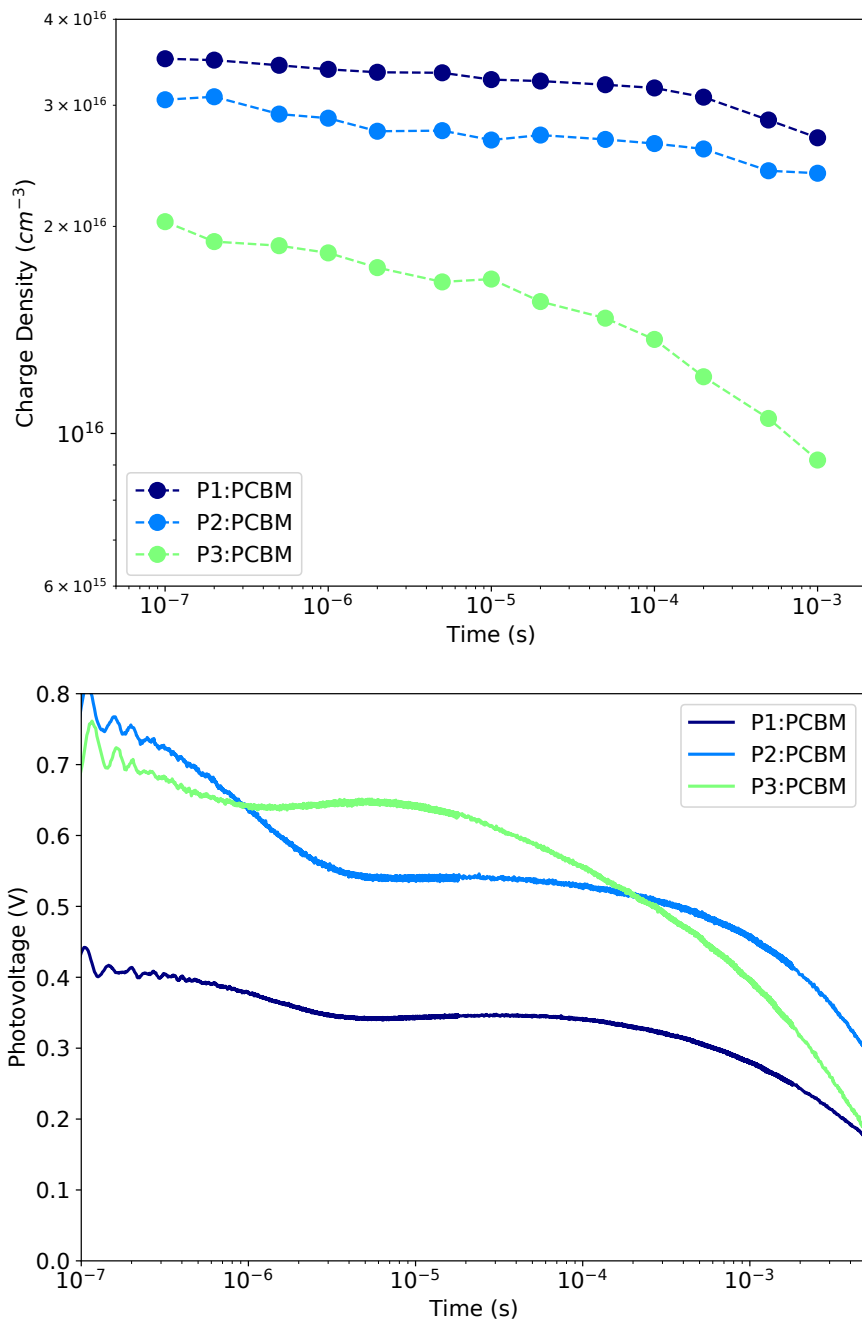


Figure 6.10: Charge density decay (top) and photovoltage decay (bottom) as a function of delay time post excitation for three donor:PCBM blend devices, obtained using an excitation density of $10 \mu\text{J cm}^{-2}$.

As discussed in Chapters 4 and 5, the temporal resolution of time resolved charge extraction measurements is limited by the extraction process on the order of microseconds. The photovoltage decay measurement however is only limited by the measurement circuit response, typically on the order of 200 ns. As such, additional complexity can be observed at the high charge density, short delay time region of the photovoltage decay transients that is not resolvable in the charge density decay plots. Two distinct decay regions are observed in all blend device photovoltage decay transients. The first decay occurs primarily within 1 to 5 μ s, while the second over the microsecond to millisecond timescale. A rise is also observed between these two regions, characteristic of the internal redistribution of charge carriers to the device contacts. These two discrete charge carrier populations with distinct lifetimes likely indicates a large disparity between electron and hole mobility within these donor-acceptor blends. As recombination is proportional to the mobility-lifetime product $\mu\tau$, this leads to initially high recombination of photogenerated charge carriers at the contacts, strongly influenced by the higher relative electron mobility. The remaining recombination is then dominated by the slow transport of holes through the device, leading to an extended lifetime and the observation of a rise in photovoltage decay transient. It is also observed that the peak of the second decay region is shifted to earlier delay times for the P3 blend device, relative to either P1 or P2 blends which exhibit comparable decay kinetics. This further indicates a less dispersive, faster average mobility for the P3 blend system and is in agreement with the photo-CELIV measurements presented earlier in this chapter (Figure 6.4).

A correlation of charge density and photovoltage decay is performed using the results displayed in Figure 6.10. The resulting dependence of charge density on photovoltage is presented in Figure 6.11 (Top), including an exponential fit for each device plot (directly proportional to the characteristic of the trap state density distribution, E_{ch}), and incorporates results from the each 1, 10, and 100 μ J cm⁻² excitation density plots. The dependence of photovoltage V_{OC} on charge density n can be expressed through

$$n = n_0 \exp\left(\frac{qV_{OC}}{mk_B T}\right) \quad (6.1)$$

where $k_B T/q$ is the available thermal energy in meV and m is the slope of the plots presented in Figure 6.11 (Top). E_{ch} can then be calculated where $E_{ch} = mk_B T/2q$. A reasonable fit is obtained for each device, with an exponential increase in charge density yielding a linear increase in device photovoltage. The E_{ch} is calculated from the slope of the charge density versus photovoltage plot (see Equation 2.12), with values of 58, 44, and 38 meV for P1, P2, and P3 blend devices respectively. These values indicate that the P1 blend device exhibits the broadest trap state distribution, while the P3 blend device exhibits a relatively narrower distribution. The P1 blend device exhibits a reasonably high absolute E_{ch} , where the P3HT:PCBM devices presented in the previous chapters exhibited E_{ch} of 70 meV. This is consistent with the dispersive charge carrier mobility and poor extraction behaviour typically exhibited by these blend systems (see Section 6.3.1). It should be noted however that the calculation of E_{ch} within these systems is complicated by the high degree

of spatial redistribution occurring over the microsecond timescale, due to the highly dispersive charge carrier mobilities as previously discussed (see Section 6.3.1), which further varies between donor-acceptor system. The calculated E_{ch} as obtained through a correlation of transient charge extraction and photovoltage measurements for these devices therefore includes a dependence on the donor-acceptor systems beyond solely the trap state density distribution, leading to unreliable determination of E_{ch} .

The dependence of photovoltage on $E_{HOMO-LUMO}$ is presented in Figure 6.11 (Bottom), obtained for each blend device at charge densities of 1.0×10^{16} and $5.0 \times 10^{16} \text{ cm}^{-3}$. An almost linear trend is observed at both charge densities with the P3 blend device exhibiting the greatest photovoltage, followed by the P2 and finally the P1 blend device. The peak charge densities measured for these devices were on the order of $5.0 \times 10^{16} \text{ cm}^{-3}$, limited by recombination and the temporal resolution of the measurement circuit. The V_{OC} obtained through extrapolation of the exponential fit in Figure 6.11 (Top) at the peak $5.0 \times 10^{16} \text{ cm}^{-3}$ charge density are 430, 620, and 900 mV for P1, P2 and P3 respectively.

At sufficiently high charge densities, the device photovoltage should approach an upper limit which can be approximated by $E_{HOMO-LUMO}$ (the donor material bandgap less ΔG_{ET} , at 1.08, 1.16, and 1.31 eV for P1, P2, and P3 blends respectively). However charge carrier relaxation within the broad density of states distribution, including an exponential tail of trap states, and the increasing recombination losses at high charge densities limit the quasi Fermi level splitting across the device contacts, and therefore the measured device photovoltage. These factors are illustrated in Figure 6.12, including the influence of trap state occupancy on Fermi level and how this reduces V_{OC} , while E_{Loss} represents the combined losses due to both trap state occupancy and recombination losses. The loss in V_{OC} should therefore depend on material system recombination kinetics and density of states distribution, in addition to the magnitude of ΔG_{ET} . Where recombination kinetics, density of states distribution, and donor material bandgap are comparable between material systems, the measured V_{OC} loss should be primarily dependant on ΔG_{ET} for a given charge density. Calculating the V_{OC} loss for the blend devices at a charge density of $5.0 \times 10^{16} \text{ cm}^{-3}$ yields values of 1240, 840, and 590 mV for P1, P2 and P3 respectively. From these results it is clear that a greater loss of V_{OC} is observed for the donor-acceptor systems with a larger ΔG_{ET} . Therefore, increasing ΔG_{ET} beyond that necessary for producing efficient charge photogeneration results in a direct loss in V_{OC} and consequently device efficiency. Optimisation of ΔG_{ET} is required to balance and maximise both V_{OC} and J_{SC} , thereby providing the greatest η .

Further subtracting ΔG_{ET} from the calculated V_{OC} loss for each donor-acceptor system (P1 = 0.57, P2 = 0.30, P3 = 0.18 eV) provides an estimate of the component of V_{OC} loss due to density of states occupancy and recombination limitations. At a charge density of $5.0 \times 10^{16} \text{ cm}^{-3}$, this yields values of 670, 540, and 410 mV for P1, P2 and P3 respectively. The difference in these values between blend devices may further indicate differences in recombination kinetics and/or trap state

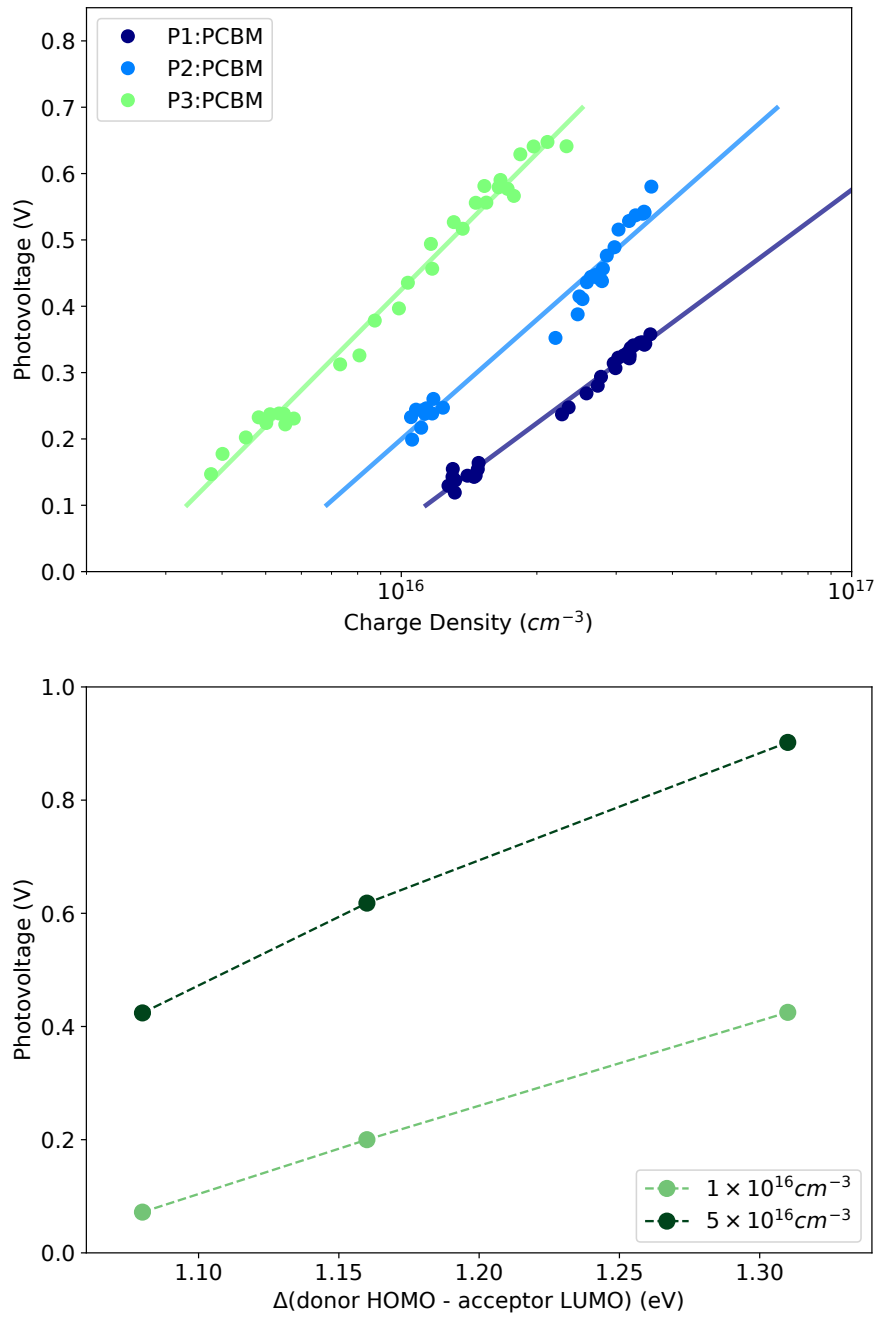


Figure 6.11: **Top:** The dependence of photovoltage on charge density for three donor:PCBM blend devices, obtained through correlation of charge density and photovoltage decay measurements at multiple excitation densities. Exponential fit (solid line) to each plot is also displayed. **Bottom:** The dependence of photovoltage on the energetic difference (donor HOMO - acceptor LUMO) of each donor-acceptor material system for the presented devices (Top), obtained using the fit to each plot at a given charge density.

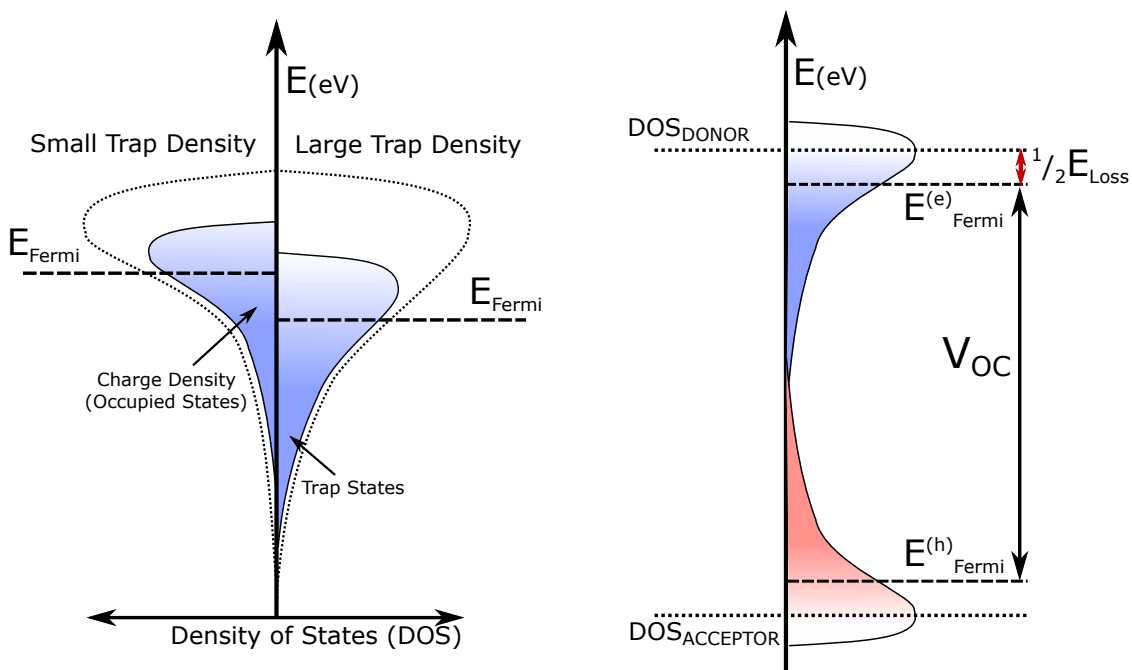


Figure 6.12: Illustrative figure of the relationship between the density of states, trap state occupancy, and device photovoltage. **Left:** Two density of states distributions with either small or large degree of trap states, at an identical charge density (shaded region represents occupied states). The Fermi level of each case is also illustrated. **Right:** An illustration of a photovoltaic device at open-circuit with a charge density, showing both electron (blue) and hole (red) density of states occupancy, and their respective Fermi levels. Also labelled are the maximum of donor and acceptor density of states, and the open circuit potential V_{OC} . The energetic loss E_{Loss} represents the difference between the peak donor/acceptor density of states and the V_{OC} .

occupancy. A difference in trap state occupancy is consistent with the calculated differences in E_{ch} as presented above. These results may further indicate a dependence of recombination kinetics on $E_{HOMO-LUMO}$ (equivalent to the driving force for recombination ΔG_{rec}), and will be investigated further in the following section.

6.3.4 Influence of Material System Energy Levels on Recombination Processes

Can the energetic driving force for recombination ΔG_{rec} influence the non-geminate recombination kinetics of donor-acceptor photovoltaic devices? Diffusion mediated bimolecular recombination at low charge densities is expected to dominate recombination kinetics. However at sufficiently high charge densities, where a significant portion of charge carriers are spatially confined to the donor-acceptor interface, it may be possible that a dependence of bimolecular recombination kinetics on ΔG_{rec} can be observed. Are these high charge densities typically achieved in operational photovoltaic devices? A primary objective of this chapter is to investigate the influence of ΔG_{rec} on the recombination kinetics of donor-acceptor blend devices at identical charge densities. The importance of this was further emphasised in the previous sections, where charge density dependent bimolecular recombination was observed to influence device extraction yield to a much greater degree than any variation in ΔG_{ET} . Additionally as identified in the previous section, ΔG_{rec} (proportional to $E_{HOMO-LUMO}$) has a strong influence on device V_{OC} , and is therefore an important parameter in these donor-acceptor systems.

In order to systematically investigate the influence of ΔG_{rec} on charge carrier recombination processes, two new polymer donors (P4 and P5) are utilised in addition to P1. These donors have increased band gaps relative to the P1/P2/P3 donors, however these donor-acceptor (PCBM) blend systems provide ΔG_{ET} of 0.64 and 0.61, comparable to the 0.57 eV exhibited by the P1 blend system (and therefore should provide comparable charge generation yields and independence from the influence of ΔG_{ET}). These additional donor-acceptor systems provide a range of ΔG_{rec} from 1.08 eV of the P1 blend up to 1.39 eV of the P5 blend system, through variation of donor bandgap rather than ΔG_{ET} . Each of the material systems and respective energetic driving forces are displayed in Figure 6.13.

These additional low bandgap polymer donor materials were again synthesised by, and obtained from Jason Azoulay and Guillermo Bazan (The Center for Polymers and Organic Solids, University of California, Santa Barbara, USA). All device fabrication and optimisation was however performed by the doctoral candidate locally (Intelligent Polymer Research Institute, University of Wollongong, Australia).

The outstanding question to be investigated within this section is whether an increase in ΔG_{rec} results in a corresponding increase in bimolecular recombination kinetics at high charge densities

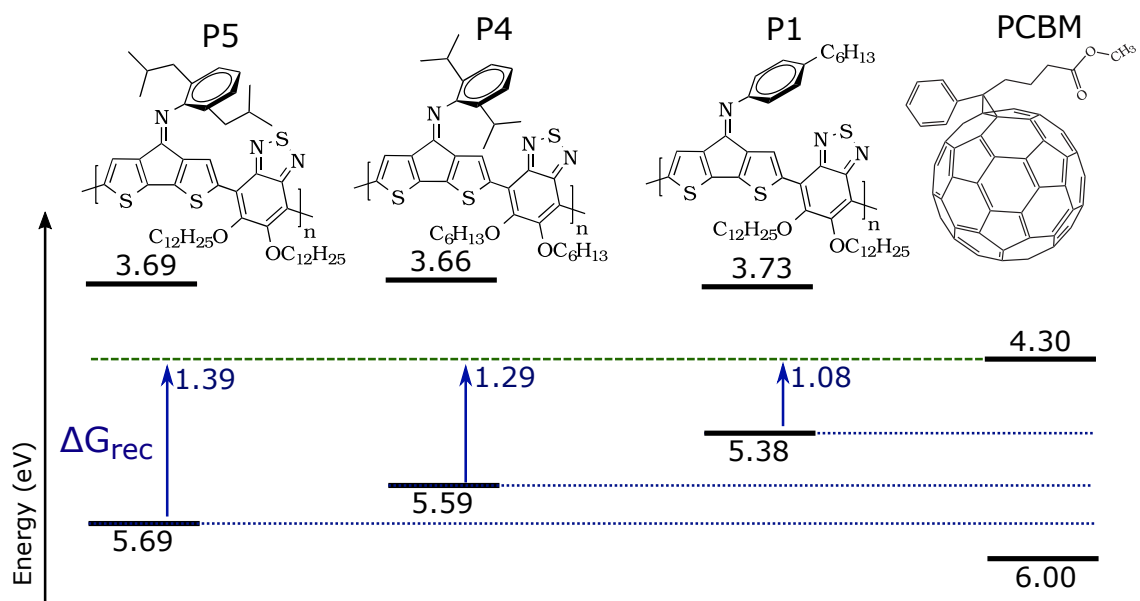


Figure 6.13: Molecular structures of cyclopentadithiophene based polymer donors (P5, P4, and P1) and the fullerene based acceptor (PCBM). Shown are the highest occupied molecular orbital energy level (E_{HOMO}) calculated from the onset of oxidation, and the lowest unoccupied molecular orbital energy level (E_{LUMO}) calculated from the onset of reduction, with comparison of the electrochemical band gaps and LUMO offsets of the donors relative to the PCBM acceptor (E vs vacuum). Also displayed are the driving force for recombination (ΔG_{rec} , blue arrow), equivalent to the free energy offset between donor polymer E_{HOMO} and PCBM acceptor E_{HOMO} .

within these donor-acceptor systems. The applied bias time resolved charge extraction measurement enables the investigation of the influence of ΔG_{rec} on recombination kinetics with this unique series of donor-acceptor systems, even in the presence of poor charge transport/extraction or significant trapping caused by poor/unoptimised bulk heterojunction morphology. The following section therefore presents an investigation of the possible influence of ΔG_{rec} on recombination kinetics. The introduction of two additional donor polymer blend systems (P4 and P5, see Figure 6.13) provide ΔG_{rec} of 1.08, 1.29, and 1.39 eV for P1, P4, and P5 respectively.

New photovoltaic device were fabricated using the P4 and P5 donors blended with PCBM, in addition to the P1 blend device presented in the previous section (see Figure 6.8). All devices have an identical device architecture and comparable active layer thickness of 100 nm. The *JV* response for each of the devices is presented in Figure 6.14 (top), along with a comparison of the UV-Visible absorbance spectra (bottom). While all donor-acceptor blends exhibit peak donor absorbance about 700 nm, both P4 and P5 peaks are shifted to shorter wavelengths due to the increasing relative donor material bandgap. A 700 nm excitation wavelength is used within the following section transient measurements, targeting peak donor absorption of all blends while minimising PCBM absorption.

The *JV* response of each device is displayed in Figure 6.14 (top), with the key performance parameters summarised in Table 6.2. The P1 device exhibits the greatest J_{SC} , while P4 and P5 blend devices exhibit comparable J_{SC} slightly below that of the P1 blend device. Further, all devices exhibit a comparable extracted current density at high reverse bias (on the order of 8.5 mA cm⁻² at -1 V), indicating similar charge generation limited by transport/extraction behaviour. The measured V_{OC} of each device strongly correlates with the ΔG_{rec} of the respective donor-acceptor blend system, increasing from the 570 mV of the P1 blend device through to 785 mV of the P5 blend device. This observation is consistent with the scaling of V_{OC} with ΔG_{rec} as discussed in the previous section. Additionally the *FF* of P4 and P5 blend devices are observed to be low relative to the P1 blend device, resulting in similar η . This may indicate that, although a greater ΔG_{rec} yields an increasing V_{OC} , a corresponding increase in recombination close to open-circuit condition limits achievable device *FF*. Further, the difference in V_{OC} between P4 and P5 of only 35 mV is less than would be expected based on the difference in donor HOMO levels. In the case of equivalent charge densities at open-circuit, this observation could be attributed to differences in trap state density distribution, thereby influencing the the measured V_{OC} . However this observation could also be explained by differences in charge density at open-circuit, caused by a relative difference in recombination kinetics between the two material systems. Transient measurements are performed below to further investigate the bimolecular recombination behaviour of each of these blend devices.

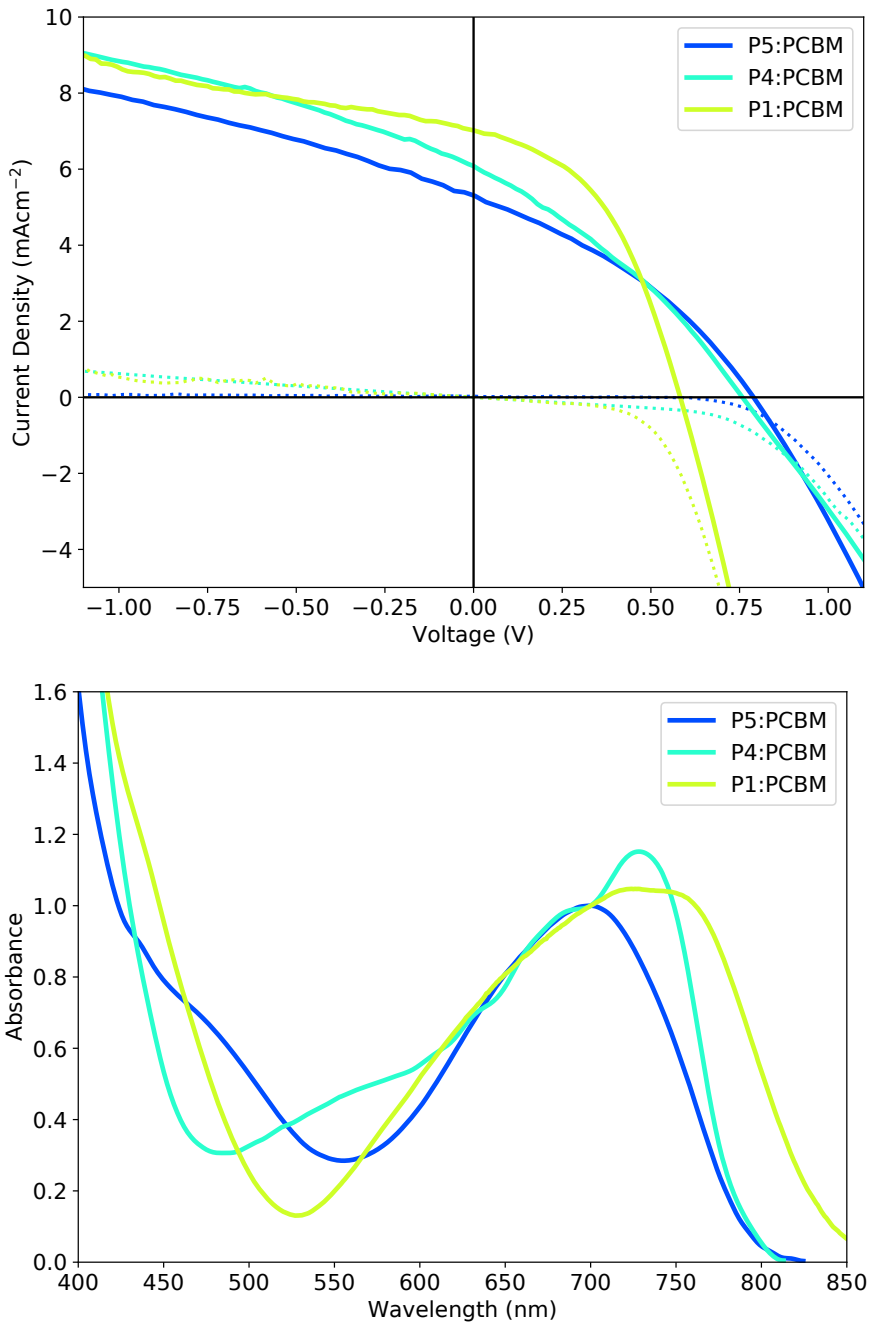


Figure 6.14: **Top:** Current-voltage response of P1, P4, and P5 blend devices at 100 mWcm^{-2} . The response of both with illumination (solid line) and without (broken line) are also displayed. **Bottom:** UV-Visible spectra of each blend device, normalised for absorbance at 700 nm wavelength.

Table 6.2: Summary of device parameters and steady state performance (current-voltage results displayed in Figure 6.14), open circuit voltage V_{OC} , short-circuit current J_{SC} , fill factor FF, and solar conversion efficiency η .

Device	V_{OC} (mV)	J_{SC} (mA cm $^{-2}$)	FF -	η (%)
P1:PCBM	570	7.0	0.46	1.9
P4:PCBM	750	6.1	0.32	1.6
P5:PCBM	785	5.4	0.34	1.5

Time Resolved Charge Extraction and Recombination Kinetics

Applied bias time resolved charge extraction measurements were performed on each of the blend devices at a range of excitation densities, with Figure 6.15 displaying the resulting charge density decay (top) and charge carrier lifetime as a function of charge density (bottom). A power law fit is also displayed on both plots, with the slope corresponding to the empirical reaction order. As ΔG_{rec} is only expected to influence recombination kinetics under conditions of high charge density where close proximity of charge carriers is likely, only the region of delay times from 100 ns to 10 μ s is presented. Beyond this region, diffusion mediated recombination kinetics dominate. Further, an excitation density of 100 μ J cm $^{-2}$ is used to ensure a high initial photogenerated charge density.

The P1, P4, and P5 blend devices exhibit a comparable initial (100 ns excitation-extraction delay) charge density on the order of 5×10^{16} cm $^{-3}$, indicating similar charge photogeneration yield. This is consistent with the findings of Section 6.3.2, where P1, P4, and P5 all have ΔG_{ET} of ~ 0.60 eV. Further, this enables a comparison of recombination kinetics at comparable initial charge densities under identical excitation conditions. The decay in charge density and therefore recombination kinetics however vary greatly between donor-acceptor systems. The charge carrier lifetime has been calculated for each of these devices (Figure 6.15, bottom), and plotted against the ΔG_{rec} of each system in Figure 6.16 at two high charge densities. High charge densities are used to present the region of increased spatial localisation and proximity of the charge carrier populations at the donor-acceptor interface, where recombination is expected to be more strongly influenced by ΔG_{rec} than in the diffusion mediated regime. A dependence of lifetime on ΔG_{rec} is observed, with a decrease in ΔG_{rec} yielding an extension of lifetime and therefore slower relative recombination kinetics for a given charge density. This trend is also observed to be stronger at the lower 4.5×10^{16} cm $^{-3}$ charge density, due primarily to observed differences in empirical reaction order δ between devices (the slopes in Figure 6.15).

The above results indicate that ΔG_{rec} does in fact appear to influence the bimolecular recombination kinetics within these donor-acceptor systems at high charge densities, and is the first time that this behaviour has been experimentally observed in donor-acceptor organic photovoltaic sys-

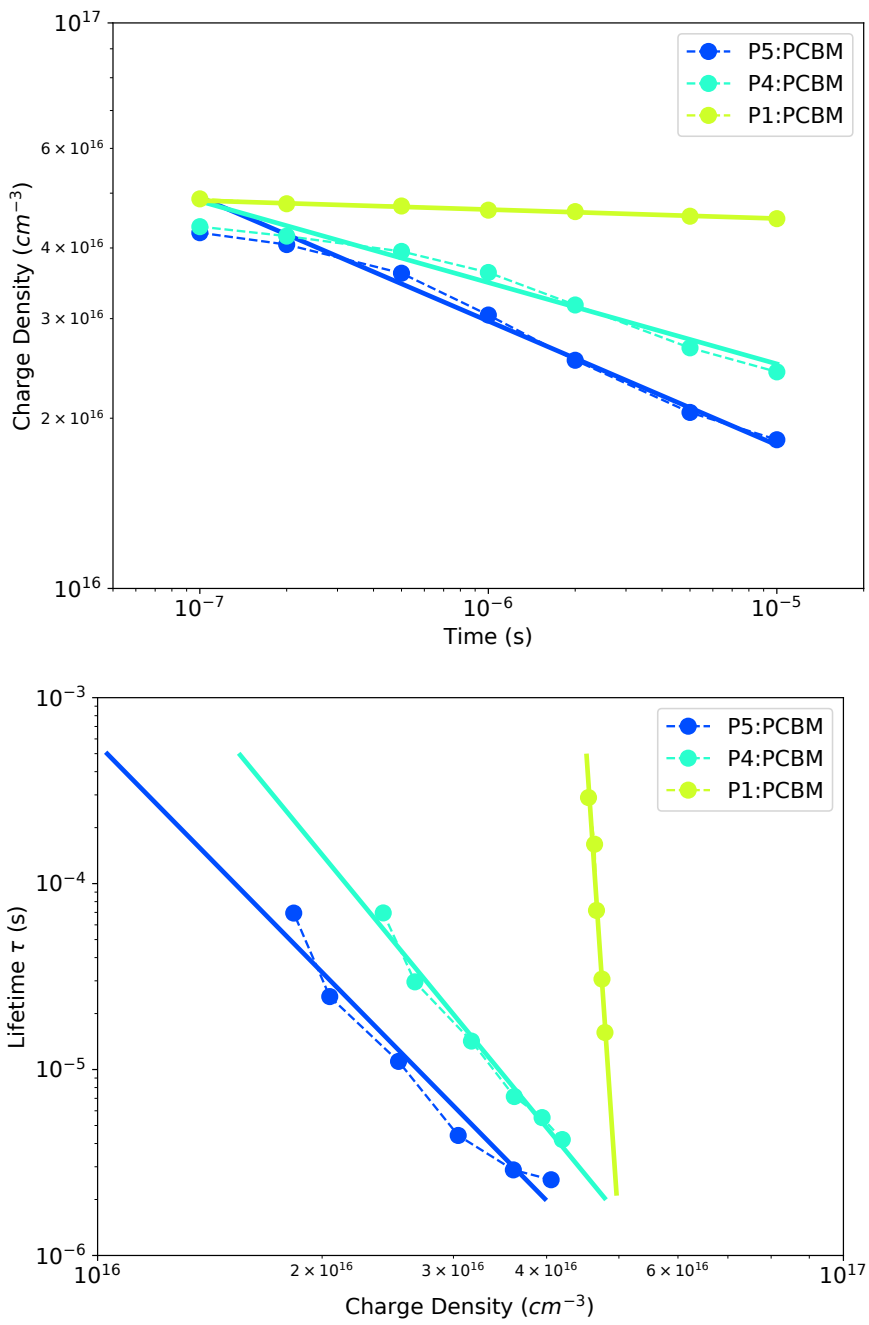


Figure 6.15: **Top:** Charge density decay obtained through applied bias time resolved charge extraction measurements for three donor-acceptor blend devices (as labelled), using an excitation density of $100 \mu\text{Jcm}^{-2}$. **Bottom:** The calculated dependence of charge carrier lifetime on charge density. A power law fit (solid line) to each plot is also displayed in all plots.

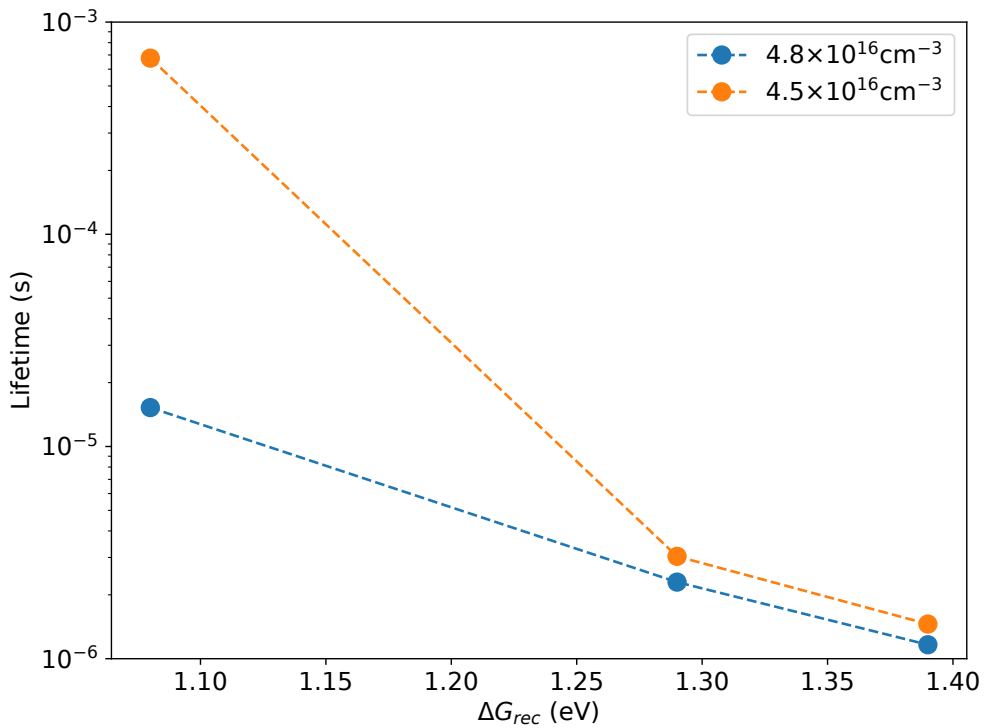


Figure 6.16: Charge carrier lifetime as a function of driving force for recombination ΔG_{rec} at two high charge densities (as labelled), obtained from Figure 6.15 (bottom) for each donor-acceptor blend device.

tems using charge extraction. If the bimolecular recombination electron transfer reaction is within the Marcus inverted region, then ΔG_{rec} should not influence the reaction rate and therefore should not produce the observed dependence of charge carrier lifetime on ΔG_{rec} . This therefore suggests that the reorganisation energy of these systems must be quite large (comparable to ΔG_{rec} and therefore on the order of 1.4 eV) in order to avoid the inverted region. Another possible explanation for these observations is that bimolecular recombination is not limited by interfacial electron transfer, but rather by the influence of trap states, with the degree of influence exhibiting a dependence on ΔG_{rec} . The exact origin of this influence is however unclear, and warrants further investigation. As discussed in the previous section, accurate determination of E_{ch} within these donor-acceptor systems is unreliable. Therefore it would be worthwhile reproducing these measurements with alternate sets of donor-acceptor systems in which E_{ch} can be reliably determined, in order to further investigate the observed influence of ΔG_{rec} .

Additional plots are presented within the Appendix (Figures 8.4 and 8.5), providing an extension to the results already presented within this section, incorporating the additional P2 and P3 polymer donor species under identical measurement conditions. Note that the P2 and P3 polymer donors have a ΔG_{ET} lower than the P1/P4/P5 set of donors, and as such may produce a relative difference in initial charge generation yield. The additional results do however strengthen the trends already highlighted above, where a positive dependence of ΔG_{rec} on empirical reaction order δ is observed

at comparable high charge densities. Further, these results suggest that the observed dependence of δ on ΔG_{rec} is not due to any variation in trap state density (E_{ch}), but rather a direct influence of the energetic driving force between donor and acceptor on recombination kinetics. A possible origin for this observed behaviour may be due to variations in the charge-transfer state energy (correlated with ΔG_{rec}) determining the kinetics of charge-transfer state reformation, which may in turn represent a rate-limiting intermediate step in the bimolecular recombination process at sufficiently high charge densities. The donor-acceptor systems with larger ΔG_{rec} may exhibit an equilibrium between charge separated and charge-transfer states that more strongly favours charge-transfer states. As such, a bias towards recombination through charge-transfer state reformation may provide a possible cause for the relative increase in recombination kinetics observed within these blend devices. However as already discussed, further detailed investigations are required to verify any causal link to charge-transfer state energy and reformation kinetics, as they relate to bimolecular recombination kinetics in these donor-acceptor blend systems.

As discussed in the previous sections, bimolecular recombination appears to exhibit a greater influence on the extraction yield and therefore performance of photovoltaic devices than does any variation in ΔG_{ET} . As ΔG_{rec} is observed to have an influence on recombination kinetics, more emphasis should be placed on optimising ΔG_{rec} of donor-acceptor systems in addition to improving charge photogeneration, thereby reducing bimolecular recombination losses.

6.4 Conclusions

The primary objective of this chapter was to determine the influence of the driving force for electron transfer ΔG_{ET} on charge generation yield in operational donor-acceptor photovoltaic devices, with additional objectives to investigate the influence of material energy levels on device photovoltage V_{OC} , and the influence of the driving force for recombination ΔG_{rec} on recombination processes. Investigations were performed through the use of the newly developed applied bias time resolved charge extraction technique, facilitating accurate investigation of these material systems which exhibit disparate and inefficient charge transport/trapping behaviour. The charge extraction results were compared with previously presented results from the ultrafast transient absorption studies of blend films. This has enabled the validation of optical technique results, and provided a comprehensive investigation of generation and recombination processes in these material systems. Additionally, the time resolved charge extraction measurement proved capable of reliably determining charge generation yields much lower than possible with transient absorption based measurements, and should therefore be generally employed in the investigation of charge photogeneration processes.

The measured charge extraction yields indicate that ΔG_{ET} of 0.18 eV results in less than one third that of donor-acceptor systems with ΔG_{ET} of 0.30 eV or above, while increasing ΔG_{ET} above 0.30 eV does not yield a significant further increase in charge generation yield. Increasing ΔG_{ET}

does however result in a reduction in device V_{OC} for a given charge density (and fixed bandgap), resulting in a net loss in overall device efficiency. For a given ΔG_{ET} , increasing the donor material bandgap and therefore ΔG_{rec} can increase the device V_{OC} without sacrificing charge generation yield. However, increasing ΔG_{rec} was also observed to increase bimolecular recombination kinetics at high charge densities, and is the first time that this has been observed experimentally. This behaviour was further correlated with a reduced device FF and thereby reduced overall η . Further, nanosecond bimolecular recombination was found to have a greater influence on device extraction yield than any variation in ΔG_{ET} , indicating that these recombination processes are crucial in determining the overall photovoltaic device performance.

Chapter 7

Conclusions and Outlook

The primary motivation for the investigations of this thesis was to develop an improved understanding of charge carrier generation and recombination processes in donor-acceptor organic photovoltaic systems, in order to better reconcile material systems design and charge photogeneration behaviour with the performance of operational photovoltaic devices, and thereby provide improved design principals for the development of new donor-acceptor systems and device architectures. To this end, a primary objective was to quantify the influence of the free energy driving force for electron transfer ΔG_{ET} on electron transfer kinetics and charge generation yield in organic photovoltaic systems, with the motivation of reducing ΔG_{ET} as a method for increasing device photovoltage (reduce energy losses) while maintaining a high device current (high charge generation/separation efficiency and yield). Is there a minimum required ΔG_{ET} ? And do increases above this minimum value provide further benefits?

In order to investigate the influence of ΔG_{ET} on charge generation processes, a series of novel cyclopentadithiophenes based polymer donor materials were used, featuring comparable bandgap and a range of ΔG_{ET} relative to the PCBM acceptor from 0.18 to 0.57 eV. These donor polymers were chosen as they exhibit similar solubility, morphology, processability, and sufficiently red-shifted main absorption bands relative to PCBM enabling selective photoexcitation of the donor phase in photovoltaic blends. Ultrafast transient absorption spectroscopy was then used to investigate the charge photogeneration processes within these donor-acceptor systems, capable of monitoring electron transfer kinetics and excited state decay. Models were developed for the interpretation of femtosecond transient absorption kinetics results to obtain a quantitative understanding of electron transfer kinetics and yield (Chapter 3). The results of these investigations indicate that a ΔG_{ET} of 0.18 eV is not sufficient to yield ultrafast charge generation, while driving forces above this value exhibited near-unity electron transfer yield on the femtosecond timescale. Additionally, no increase in electron transfer kinetics or estimated charge generation yield was found with an increase in ΔG_{ET} from 0.30 to 0.57 eV. The initial charge generation yield appears limited by charge-transfer state recombination, rather than the electron transfer kinetics. As such, the driving force for electron transfer should exceed 0.18 eV for the presented donor-acceptor systems, in

order to facilitate near unity electron transfer yield and subsequent high charge carrier generation/separation yield. It is however important to minimise this driving force, as further increases do not provide an increase in initial charge carrier generation yield, but do result in a reduction in achievable device photovoltage, thereby negatively impacting device performance. Future investigations into the charge-transfer state recombination process may provide further insight into the sub-unity charge separation yields observed, as the presented findings indicate this to be an important step within the charge photogeneration process.

The ultrafast transient absorption results alone are unable to provide information on the overall charge generation efficiency of operational photovoltaic devices, and do not provide insight into charge carrier transport, recombination, or trapping behaviour. As such, charge extraction measurements were sought to investigate the charge extraction yield of operational photovoltaic devices, as well as bimolecular recombination kinetics and trap state density distribution as a function of charge density (thereby facilitating a like-for-like comparison between donor-acceptor systems). The performance and suitability a relatively novel switched transient charge extraction technique was assessed using the heavily studied PCDTBT:PCBM and P3HT:PCBM donor-acceptor material systems (Chapter 4). Significant extraction losses were identified, leading to inaccuracy of results under certain measurement conditions, with up to an estimated five fold underestimation of charge density and five fold overestimation charge carrier lifetime. Further, the impact of morphology on charge transport and extraction behaviour in devices incorporating the cyclopentadithiophenes based polymer donors presented issues when using charge extraction techniques for measuring photogenerated charge density.

In response to the identified limitations of existing charge extraction techniques, a new time resolved charge extraction technique was developed using a combination of applied reverse bias and a high impedance switch (Chapter 5). The capabilities and limitations of the developed technique were thoroughly characterised for a range of measurement conditions and device parameters. This technique was then used to accurately determine the origin of, and systematically quantify the observed charge extraction losses, enabling the attribution of operational device performance limitations to the underlying loss mechanisms. The results of these investigations indicate that up to half of photogenerated charge density is lost without the application of an applied reverse bias in time resolved charge extraction measurements, which in turn significantly impacts the calculation of recombination kinetics and trap state density distribution. Additionally, the applied reverse bias is capable of reducing the observed disparity in measurement results obtained for comparable devices with differences in active layer thickness, thereby enabling a more accurate comparison between those devices. Further the applied reverse bias improves the range of measurement conditions over which charge carrier dynamics can be reliably investigated, and is most effective when investigating systems with a low mobility-lifetime product (short lifetime, slow charge transport) by reducing the significant recombination/extraction losses during measurement.

The developed technique was particularly important for the investigation of devices incorporating the cyclopentadithiophenes based polymer donors, which were found to exhibit poor charge transport and extraction behaviour. The influence of morphology on charge generation/recombination was not the focus of this thesis, rather the influence of donor-acceptor system energetics. Use of the developed applied bias charge extraction technique aided in the investigation of these polymer donor systems, helping to overcome morphological extraction limitations. The development of this new technique provides a robust and capable method for investigating nanosecond to millisecond charge carrier dynamics, applicable to a wide range of photovoltaic systems. This technique may additionally benefit from future development regarding the extension of measurable charge density and delay times into the millisecond timescale, through modification of the high impedance currently used. In particular, better alignment with photovoltage decay measurements will enable the improvement of trap state density distribution calculations.

Investigations were performed to quantify the influence of ΔG_{ET} on charge generation yield using the newly developed applied bias time resolved charge extraction technique, with photovoltaic devices incorporating the cyclopentadithiophenes based polymer donors (Chapter 6), providing complimentary results to the purely optical transient absorption studies. The results of these investigations aligned with the conclusions of the ultrafast kinetics findings, where the measured charge extraction yield was found to be influenced by ΔG_{ET} . Devices incorporating the donor-acceptor system with ΔG_{ET} below 0.30 eV produced an initial charge extraction yield under identical excitation conditions less than 40 % that of devices incorporating donor-acceptor systems with ΔG_{ET} of 0.30 or 0.57 eV. Additionally, the measured device photovoltage was found to decrease with an increase in ΔG_{ET} for a given charge density. As such, an increase in ΔG_{ET} from 0.30 to 0.57 eV only yielded an increase in extraction yield of 20 %, while exhibiting a reduction in device photovoltage on the order of 35 %. Although further research is required on additional sets of donor-acceptor systems in order to understand how transferable these results are to alternate material systems, the fundamental insights obtained herein can be used to inform the development of new and improved donor-acceptor photovoltaic systems. A deeper understanding of the factors that determine the magnitude of the observed minimum ΔG_{ET} requires further investigation.

Importantly, it was observed that the relative differences in measured extraction yield between donor-acceptor systems, on the order of 10 to 30 % for a given excitation density, were orders of magnitude less than that observed for variations in excitation density (charge density). These observations strongly indicate that, while the initial charge photogeneration yield can influence the extraction yield of operational devices, bimolecular recombination has a much greater impact on the overall extraction yield and therefore on photovoltaic device performance. Relative differences in the electron transfer yield of donor-acceptor systems due to differences in ΔG_{ET} may be less important than the relative degree of bimolecular recombination.

Further measurements were therefore performed using additional cyclopentadithiophenes based donor-acceptor systems, featuring comparable ΔG_{ET} however with a range of polymer donor bandgaps. This provided a range of free energy driving forces for recombination ΔG_{rec} . Applied bias time resolved charge extraction measurements were used to investigate the influence of ΔG_{rec} on charge carrier lifetime under conditions of identical high charge density. The results indicate that ΔG_{rec} does in fact influence recombination kinetics, where a reduction of ΔG_{rec} yields an extended charge carrier lifetime, and is the first reported observation of such a result obtained using charge extraction. This result may suggest that the reorganisation energy of these donor-acceptor systems is quite high, on the order of 1.4 eV, and as such the determination of reorganisation energy for these systems may help elucidate whether this is in fact the origin of the observed behaviour. Reliable determination of the reorganisation energy of disordered organic systems such as those presented herein is however a difficult and involved task, outside the scope of this thesis, and is therefore left for future investigation.

Alternatively, recombination kinetics within these systems may still be governed by the influence of trap states at high charge densities, however the trap state density appears to have a dependence on ΔG_{rec} . This is in itself interesting, and the origin of such behaviour remains uncertain. Although the trap state density distribution E_{ch} was found to exhibit a small dependence on ΔG_{rec} , accurate determination of E_{ch} within these donor-acceptor systems using the charge extraction approach was found to be unreliable, due to the influence of a highly dispersive charge carrier mobility. As such, future investigations are required to understand the influence of ΔG_{rec} on bimolecular recombination kinetics in operational devices, incorporating an alternative set of donor-acceptor systems with matched ΔG_{ET} , comparable E_{ch} , and a range of ΔG_{rec} (with known reorganisation energy if possible). Although these requirements are difficult to address, bimolecular recombination has shown to produce the largest impact on overall device performance/efficiency, strongly influencing device photocurrent, photovoltage, and fill factor. It is therefore an area that should be the focus of continued research, to more accurately understand and model bimolecular recombination processes, and in turn enable the design of new material systems and devices architectures to minimise the associated losses in device efficiency.

The primary findings of this thesis contribute to our expanding understanding of the fundamental influences of energetic driving forces in charge carrier generation and recombination processes within donor-acceptor photovoltaic systems. Although further investigations into the generality of these findings across different material systems can provide further insight and refine our understanding, the knowledge gained through the presented investigations can be utilised in the development of improved material systems and device architectures, enabling the continued improvement of organic photovoltaic system performance. Additionally, the newly developed charge extraction technique provides the wider photovoltaic community with a robust and capable methodology for investigating the fundamental processes governing charge carrier transport, extraction, and recombination within photovoltaic systems. Finally, a number of interesting questions have been

raised regarding the possible influence of material systems energetics on bimolecular recombination processes, presenting a promising area of future research which has been relatively untouched to date.

The primary findings of Chapters 3 and 6 regarding the influence of the driving force for electron transfer on charge generation kinetics and yield have been published in the Journal of Physical Chemistry C.⁵⁰ The primary findings of Chapters 4 and 5 regarding the first time introduction of an applied bias in time resolved charge extraction measurements, and the elucidation and quantification of extraction losses, have been published in Advanced Energy Materials.¹²⁴

References

- ¹ Harald Hoppe and Niyazi Serdar Sariciftci. Organic solar cells: An overview. *Journal of Materials Research*, 19(7):1924–1945, 2004.
- ² Christoph Winder and Niyazi Serdar Sariciftci. Low bandgap polymers for photon harvesting in bulk heterojunction solar cells. *Journal of Materials Chemistry*, 14(7):1077–1086, 2004.
- ³ Serap Günes, Helmut Neugebauer, and Niyazi Serdar Sariciftci. Conjugated polymer-based organic solar cells. *Chemical reviews*, 107(4):1324–1338, 2007.
- ⁴ Huaxing Zhou, Liqiang Yang, and Wei You. Rational design of high performance conjugated polymers for organic solar cells. *Macromolecules*, 45(2):607–632, 2012.
- ⁵ Peter Wurfel. *Physics of Solar Cells: From Principles to New Concepts*. WILEY-VCH, 2005.
- ⁶ Sophie E. Gledhill, Brian Scott, and Brian A. Gregg. Organic and nano-structured composite photovoltaics: An overview. *Journal of Materials Research*, 20(12):3167–3179, 2005.
- ⁷ Suman Kalyan Pal, Tero Kesti, Manisankar Maiti, Fengling Zhang, Olle Inganäs, Stefan Hellstrom, Mats R. Andersson, Frederic Oswald, Fernando Langa, Tomas Osterman, Torbjörn Pascher, Arkady Yartsev, and Villy Sundstrom. Geminate Charge Recombination in Polymer/Fullerene Bulk Heterojunction Films and Implications for Solar Cell Function. *Journal of the American Chemical Society*, 132:12440–12451, 2010.
- ⁸ C. W. Tang. Two-layer organic photovoltaic cell. *Applied Physics Letters*, 48(2):183–185, 1986.
- ⁹ Peter Peumans and Stephen R Forrest. Separation of geminate charge-pairs at donor–acceptor interfaces in disordered solids. *Chemical Physics Letters*, 398(1):27–31, 2004.
- ¹⁰ A Bruno, LX Reynolds, C Dyer-Smith, J Nelson, and SA Haque. Determining the exciton diffusion length in a polyfluorene from ultrafast fluorescence measurements of polymer/fullerene blend films. *The Journal of Physical Chemistry C*, 117(39):19832–19838, 2013.
- ¹¹ Xu Zhang, Zi Li, and Gang Lu. First-principles simulations of exciton diffusion in organic semiconductors. *Physical Review B*, 84(23):235208, 2011.
- ¹² Michael C Heiber and Ali Dhinojwala. Estimating the Magnitude of Exciton Delocalization in Regioregular P3HT. *The Journal of Physical Chemistry C*, 117(42):21627–21634, 2013.

¹³ Gang Yu, Jun Gao, Jan C Hummelen, Fred Wudl, and Alan J Heeger. Polymer photovoltaic cells: enhanced efficiencies via a network of internal donor-acceptor heterojunctions. *Science-AAAS-Weekly Paper Edition*, 270(5243):1789–1790, 1995.

¹⁴ N. S. Sariciftci, L. Smilowitz, A. J. Heeger, and F. Wudl. Photoinduced Electron Transfer from a Conducting Polymer to Buckminsterfullerene. *Science*, 258(5087):1474–1476, 1992.

¹⁵ Ryan D Pensack and John B Asbury. Barrierless free carrier formation in an organic photovoltaic material measured with ultrafast vibrational spectroscopy. *Journal of the American Chemical Society*, 131(44):15986–15987, 2009.

¹⁶ VI Arkhipov, Paul Heremans, and H Bässler. Why is exciton dissociation so efficient at the interface between a conjugated polymer and an electron acceptor? *Applied Physics Letters*, 82(25):4605–4607, 2003.

¹⁷ Dirk Veldman, Stefan CJ Meskers, and René AJ Janssen. The Energy of Charge-Transfer States in Electron Donor–Acceptor Blends: Insight into the Energy Losses in Organic Solar Cells. *Advanced Functional Materials*, 19(12):1939–1948, 2009.

¹⁸ Hiroyuki Tamura and Irene Burghardt. Potential barrier and excess energy for electron–hole separation from the charge-transfer exciton at donor–acceptor heterojunctions of organic solar cells. *The Journal of Physical Chemistry C*, 117(29):15020–15025, 2013.

¹⁹ Dirk Veldman, Ozlem Ipek, Stefan CJ Meskers, Jörgen Sweelssen, Marc M Koetse, Sjoerd C Veenstra, Jan M Kroon, Svetlana S van Bavel, Joachim Loos, and René AJ Janssen. Compositional and electric field dependence of the dissociation of charge transfer excitons in alternating polyfluorene copolymer/fullerene blends. *Journal of the American Chemical Society*, 130(24):7721–7735, 2008.

²⁰ Koen Vandewal, Abay Gadisa, Wibren D Oosterbaan, Sabine Bertho, Fateme Banishoeib, Ineke Van Severen, Laurence Lutsen, Thomas J Cleij, Dirk Vanderzande, and Jean V Manca. The Relation Between Open-Circuit Voltage and the Onset of Photocurrent Generation by Charge-Transfer Absorption in Polymer: Fullerene Bulk Heterojunction Solar Cells. *Advanced Functional Materials*, 18(14):2064–2070, 2008.

²¹ Markus C Scharber, David Muhlbacher, Markus Koppe, Patrick Denk, Christoph Waldauf, Alan J Heeger, and Christoph J Brabec. Design rules for donors in bulk-heterojunction solar cells-towards 10% energy-conversion efficiency. *Advanced Materials*, 18(6):789, 2006.

²² Cody W Schlenker, Kung-Shih Chen, Hin-Lap Yip, Chang-Zhi Li, Liam R Bradshaw, Stefan T Ochsenbein, Feizhi Ding, Xiaosong S Li, Daniel R Gamelin, Alex K-Y Jen, et al. Polymer triplet energy levels need not limit photocurrent collection in organic solar cells. *Journal of the American Chemical Society*, 134(48):19661–19668, 2012.

- ²³ Edward W Snedden, Andrew P Monkman, and Fernando B Dias. Kinetic studies of geminate polaron pair recombination, dissociation, and efficient triplet exciton formation in PC: PCBM organic photovoltaic blends. *The Journal of Physical Chemistry C*, 116(7):4390–4398, 2012.
- ²⁴ Andrea Maurano, Chris G Shuttle, Rick Hamilton, Amy M Ballantyne, Jenny Nelson, Weimin Zhang, Martin Heeney, and James R Durrant. Transient optoelectronic analysis of charge carrier losses in a selenophene/fullerene blend solar cell. *The Journal of Physical Chemistry C*, 115(13):5947–5957, 2011.
- ²⁵ Jonathan A. Bartelt, David Lam, Timothy M. Burke, Sean M. Sweetnam, and Michael D. McGehee. Charge-Carrier Mobility Requirements for Bulk Heterojunction Solar Cells with High Fill Factor and External Quantum Efficiency above 90%. *Advanced Energy Materials*, 5(15):1500577, 2015.
- ²⁶ Chellappan Vijila, Samarendra P Singh, Evan Williams, Prashant Sonar, Almantas Pivrikas, Bronson Philippa, Ronald White, Elumalai Naveen Kumar, S Gomathy Sandhya, Sergey Gorelik, et al. Relation between charge carrier mobility and lifetime in organic photovoltaics. *Journal of Applied Physics*, 114(18):184503, 2013.
- ²⁷ Jenny Nelson. Diffusion-limited recombination in polymer-fullerene blends and its influence on photocurrent collection. *Physical Review B*, 67(15):155209, 2003.
- ²⁸ Almantas Pivrikas, Helmut Neugebauer, and Niyazi Serdar Sariciftci. Charge carrier lifetime and recombination in bulk heterojunction solar cells. *Selected Topics in Quantum Electronics, IEEE Journal of*, 16(6):1746–1758, 2010.
- ²⁹ Benjamin J Leever, Christopher A Bailey, Tobin J Marks, Mark C Hersam, and Michael F Durstock. In situ characterization of lifetime and morphology in operating bulk heterojunction organic photovoltaic devices by impedance spectroscopy. *Advanced Energy Materials*, 2(1):120–128, 2012.
- ³⁰ Gang Li, Yan Yao, Hoichang Yang, Vishal Shrotriya, Guanwen Yang, and Yang Yang. "Solvent annealing" effect in polymer solar cells based on poly (3-hexylthiophene) and methanofullerenes. *Advanced Functional Materials*, 17(10):1636, 2007.
- ³¹ Carsten Deibel and Vladimir Dyakonov. Polymer–fullerene bulk heterojunction solar cells. *Reports on Progress in Physics*, 73(9):096401, 2010.
- ³² Hideo Ohkita, Steffan Cook, Yeni Astuti, Warren Duffy, Steve Tierney, Weimin Zhang, Martin Heeney, Iain McCulloch, Jenny Nelson, Donal DC Bradley, et al. Charge carrier formation in polythiophene/fullerene blend films studied by transient absorption spectroscopy. *Journal of the American Chemical Society*, 130(10):3030–3042, 2008.
- ³³ Thomas Kirchartz, Florent Deledalle, Pabitra Shakya Tuladhar, James R Durrant, and Jenny Nelson. On the differences between dark and light ideality factor in polymer: fullerene solar cells. *The Journal of Physical Chemistry Letters*, 4(14):2371–2376, 2013.

³⁴ Thomas Kirchartz and Jenny Nelson. Meaning of reaction orders in polymer: fullerene solar cells. *Physical Review B*, 86(16):165201, 2012.

³⁵ Christopher M. Proctor and Thuc-Quyen Nguyen. Effect of leakage current and shunt resistance on the light intensity dependence of organic solar cells. *Applied Physics Letters*, 106:083301, 2015.

³⁶ Dan Credginton, Rick Hamilton, Pedro Atienzar, Jenny Nelson, and James R Durrant. Non-Geminate Recombination as the Primary Determinant of Open-Circuit Voltage in Polythiophene: Fullerene Blend Solar Cells: an Analysis of the Influence of Device Processing Conditions. *Advanced Functional Materials*, 21(14):2744–2753, 2011.

³⁷ Andrea Maurano, Rick Hamilton, Chris G Shuttle, Amy M Ballantyne, Jenny Nelson, Brian O'Regan, Weimin Zhang, Iain McCulloch, Hamed Azimi, Mauro Morana, et al. Recombination dynamics as a key determinant of open circuit voltage in organic bulk heterojunction solar cells: a comparison of four different donor polymers. *Advanced Materials*, 22(44):4987–4992, 2010.

³⁸ Zhenjing Kang, Shan-Ci Chen, Yunlong Ma, Jianbin Wang, and Qingdong Zheng. Push-Pull Type Non-Fullerene Acceptors for Polymer Solar Cells: Effect of the Donor Core. *ACS Applied Materials & Interfaces*, 9(29):24771–24777, 2017.

³⁹ Minh Trung Dang, Lionel Hirsch, and Guillaume Wantz. P3HT: PCBM, best seller in polymer photovoltaic research. *Advanced Materials*, 23(31):3597–3602, 2011.

⁴⁰ Park Sung Heum, Roy Anshuman, Beaupre Serge, Cho Shinuk, Coates Nelson, Moon Ji Sun, Moses Daniel, Leclerc Mario, Lee Kwanghee, and Heeger Alan J. Bulk heterojunction solar cells with internal quantum efficiency approaching 100%. *Nature Photonics*, 3(5):297–302, 2009.

⁴¹ Luyao Lu and Luping Yu. Understanding low bandgap polymer PTB7 and optimizing polymer solar cells based on it. *Advanced Materials*, 26(26):4413–4430, 2014.

⁴² Juliane Kniepert, Ilja Lange, Jan Heidbrink, Jona Kurpiers, Thomas J. K. Brenner, L. Jan Anton Koster, and Dieter Neher. Effect of Solvent Additive on Generation, Recombination, and Extraction in PTB7:PCBM Solar Cells: A Conclusive Experimental and Numerical Simulation Study. *Journal of Physical Chemistry C*, 119:8310–8320, 2015.

⁴³ Jason D Azoulay, Zachary A Koretz, Bryan M Wong, and Guillermo C Bazan. Bridgehead Imine Substituted Cyclopentadithiophene Derivatives: An Effective Strategy for Band Gap Control in Donor-Acceptor Polymers. *Macromolecules*, 46(4):1337–1342, 2013.

⁴⁴ Yankang Yang, Zhi-Guo Zhang, Haijun Bin, Shanshan Chen, Liang Gao, Lingwei Xue, Changduk Yang, and Yongfang Li. Side-Chain Isomerization on an n-type Organic Semiconductor ITIC Acceptor Makes 11.77% High Efficiency Polymer Solar Cells. *Journal of the American Chemical Society*, 138(45):15011–15018, 2016.

- ⁴⁵ Sibel Leblebici, Jiye Lee, Alexander Weber-Bargioni, and Biwu Ma. Dielectric Screening To Reduce Charge Transfer State Binding Energy in Organic Bulk Heterojunction Photovoltaics. *The Journal of Physical Chemistry C*, 121(6):3279–3285, 2017.
- ⁴⁶ Zhi Guo, Doyun Lee, Richard D Schaller, Xiaobing Zuo, Byeongdu Lee, TengFei Luo, Haifeng Gao, and Libai Huang. Relationship between Interchain Interaction, Exciton Delocalization, and Charge Separation in Low-Bandgap Copolymer Blends. *Journal of the American Chemical Society*, 136(28):10024–10032, 2014.
- ⁴⁷ Natalie Banerji. Sub-picosecond delocalization in the excited state of conjugated homopolymers and donor–acceptor copolymers. *Journal of Materials Chemistry C*, 1:3052–3066, 2013.
- ⁴⁸ Tracey M Clarke and James R Durrant. Charge photogeneration in organic solar cells. *Chemical Reviews*, 110(11):6736–6767, 2010.
- ⁴⁹ Stoichko D Dimitrov and James R Durrant. Materials design considerations for charge generation in organic solar cells. *Chemistry of Materials*, 26(1):616–630, 2013.
- ⁵⁰ Brendan Wright, Kenji Sunahara, Akihiro Furube, Andrew Nattestad, Tracey M Clarke, Guillermo C Bazan, Jason David Azoulay, and Attila J Mozer. Driving Force Dependence of Electron Transfer Kinetics and Yield in Low Bandgap Polymer Donor-Acceptor Organic Photovoltaic Blends. *The Journal of Physical Chemistry C*, 119(23):12829–12837, 2015.
- ⁵¹ Bright Walker, Jianhua Liu, Chunki Kim, Gregory C Welch, Jin Keun Park, Jason Lin, Peter Zalar, Christopher M Proctor, Jung Hwa Seo, Guillermo C Bazan, et al. Optimization of energy levels by molecular design: evaluation of bis-diketopyrrolopyrrole molecular donor materials for bulk heterojunction solar cells. *Energy & Environmental Science*, 6(3):952–962, 2013.
- ⁵² MC Scharber and NS Sariciftci. Efficiency of bulk-heterojunction organic solar cells. *Progress in Polymer Science*, 38(12):1929–1940, 2013.
- ⁵³ R. A. Marcus. On the Theory of Oxidation-Reduction Reactions Involving Electron Transfer. I. *The Journal of Chemical Physics*, 24(5):966–978, 1956.
- ⁵⁴ Jean-Luc Brédas, David Beljonne, Jérôme Cornil, J Ph Calbert, Z Shuai, and R Silbey. Electronic structure of π -conjugated oligomers and polymers: a quantum-chemical approach to transport properties. *Synthetic Metals*, 125(1):107–116, 2001.
- ⁵⁵ Claudia Turró, Jeffrey M. Zaleski, Yanna M. Karabatsos, and Daniel G. Nocera. Bimolecular Electron Transfer in the Marcus Inverted Region. *Journal of the American Chemical Society*, 118(25):6060–6067, 1996.
- ⁵⁶ P. Thanasekaran, T. Rajendran, S. Rajagopal, C. Srinivasan, R. Ramaraj, P. Ramamurthy, and B. Venkatachalam. Marcus Inverted Region in the Photoinduced Electron Transfer Reactions of Ruthenium(II)-Polypyridine Complexes with Phenolate Ions. *The Journal of Physical Chemistry A*, 101(44):8195–8199, 1997.

- ⁵⁷ Manoj Kumbhakar, Arpan Manna, Mhejabeen Sayed, Anil Kumar, and Haridas Pal. Observation of the Marcus Inverted Region for Bimolecular Photoinduced Electron-Transfer Reactions in Viscous Media. *The Journal of Physical Chemistry B*, 118(36):10704–10715, 2014.
- ⁵⁸ Yi Zhao and WanZhen Liang. Charge transfer in organic molecules for solar cells: Theoretical perspective. *Chemical Society Reviews*, 41(3):1075–1087, 2012.
- ⁵⁹ JJM Halls, Jérôme Cornil, DA Dos Santos, R Silbey, D-H Hwang, AB Holmes, Jean-Luc Brédas, and RH Friend. Charge-and energy-transfer processes at polymer/polymer interfaces: A joint experimental and theoretical study. *Physical Review B*, 60(8):5721, 1999.
- ⁶⁰ Yi Zhou, Kristofer Tvingstedt, Fengling Zhang, Chunxia Du, Wei-Xin Ni, Mats R Andersson, and Olle Inganäs. Observation of a Charge Transfer State in Low-Bandgap Polymer/Fullerene Blend Systems by Photoluminescence and Electroluminescence Studies. *Advanced Functional Materials*, 19(20):3293–3299, 2009.
- ⁶¹ Safa Shoaei, Tracey M Clarke, Chun Huang, Stephen Barlow, Seth R Marder, Martin Heeney, Iain McCulloch, and James R Durrant. Acceptor energy level control of charge photogeneration in organic donor/acceptor blends. *Journal of the American Chemical Society*, 132(37):12919–12926, 2010.
- ⁶² Steve Albrecht, Koen Vandewal, John R Tumbleston, Florian SU Fischer, Jessica D Douglas, Jean MJ Fréchet, Sabine Ludwigs, Harald Ade, Alberto Salleo, and Dieter Neher. On the efficiency of charge transfer state splitting in polymer: fullerene solar cells. *Advanced Materials*, 26(16):2533–2539, 2014.
- ⁶³ Koen Vandewal, Steve Albrecht, Eric T Hoke, Kenneth R Graham, Johannes Widmer, Jessica D Douglas, Marcel Schubert, William R Mateker, Jason T Bloking, George F Burkhard, et al. Efficient charge generation by relaxed charge-transfer states at organic interfaces. *Nature Materials*, 13(1):63–68, 2014.
- ⁶⁴ VD Mihailescu, LJA Koster, JC Hummelen, and PWM Blom. Photocurrent generation in polymer-fullerene bulk heterojunctions. *Physical Review Letters*, 93(21):216601, 2004.
- ⁶⁵ Charles L. Braun. Electric field assisted dissociation of charge transfer states as a mechanism of photocarrier production. *The Journal of Chemical Physics*, 80(9):4157–4161, 1984.
- ⁶⁶ Jean-Luc Brédas, David Beljonne, Veaceslav Coropceanu, and Jérôme Cornil. Charge-transfer and energy-transfer processes in π -conjugated oligomers and polymers: a molecular picture. *Chemical Reviews*, 104(11):4971–5004, 2004.
- ⁶⁷ Xiong Gong, Minghong Tong, Fulvio G Brunetti, Junghwa Seo, Yanming Sun, Daniel Moses, Fred Wudl, and Alan J Heeger. Bulk Heterojunction Solar Cells with Large Open-Circuit Voltage: Electron Transfer with Small Donor-Acceptor Energy Offset. *Advanced Materials*, 23(20):2272–2277, 2011.

- ⁶⁸ Tae Eui Kang, Han-Hee Cho, Chul-Hee Cho, Ki-Hyun Kim, Hyunbum Kang, Myounghee Lee, Sunae Lee, BongSoo Kim, Chan Im, and Bumjoon J Kim. Photoinduced charge transfer in donor–acceptor (DA) copolymer: fullerene bis-adduct polymer solar cells. *ACS Applied Materials & Interfaces*, 5(3):861–868, 2013.
- ⁶⁹ Koen Vandewal, Zaifei Ma, Jonas Bergqvist, Zheng Tang, Ergang Wang, Patrik Henriksson, Kristofer Tvingstedt, Mats R Andersson, Fengling Zhang, and Olle Inganäs. Quantification of Quantum Efficiency and Energy Losses in Low Bandgap Polymer: Fullerene Solar Cells with High Open-Circuit Voltage. *Advanced Functional Materials*, 22(16):3480–3490, 2012.
- ⁷⁰ Stoichko D Dimitrov, Zhenggang Huang, Florent Deledalle, Christian B Nielsen, Bob C Schroeder, Raja Shahid Ashraf, Safa Shoaei, Iain McCulloch, and James R Durrant. Towards optimisation of photocurrent from fullerene excitons in organic solar cells. *Energy & Environmental Science*, 7(3):1037–1043, 2014.
- ⁷¹ David C Coffey, Bryon W Larson, Alexander W Hains, James B Whitaker, Nikos Kopidakis, Olga V Boltalina, Steven H Strauss, and Garry Rumbles. An optimal driving force for converting excitons into free carriers in excitonic solar cells. *The Journal of Physical Chemistry C*, 116(16):8916–8923, 2012.
- ⁷² Hilary M. Feier, Obadiah G. Reid, Natalie A. Pace, Jaehong Park, Jesse J. Bergkamp, Alan Sellinger, Devens Gust, and Garry Rumbles. Local Intermolecular Order Controls Photoinduced Charge Separation at Donor/Acceptor Interfaces in Organic Semiconductors. *Advanced Energy Materials*, 6(6):1502176, 2016.
- ⁷³ Marius Koch, Romain Letrun, and Eric Vauthey. Exciplex Formation in Bimolecular Photoinduced Electron-Transfer Investigated by Ultrafast Time-Resolved Infrared Spectroscopy. *Journal of the American Chemical Society*, 136(10):4066–4074, 2014.
- ⁷⁴ Alexander J Ward, Arvydas Ruseckas, Mohanad Mousa Kareem, Bernd Ebenhoch, Luis A Serrano, Manal Al-Eid, Brian Fitzpatrick, Vincent M Rotello, Graeme Cooke, and Ifor DW Samuel. The Impact of Driving Force on Electron Transfer Rates in Photovoltaic Donor–Acceptor Blends. *Advanced Materials*, 27(15):2496–2500, 2015.
- ⁷⁵ Stijn Verlaak, David Beljonne, David Cheyns, Cedric Rolin, Mathieu Linares, Frédéric Castet, Jérôme Cornil, and Paul Heremans. Electronic structure and geminate pair energetics at organic–organic interfaces: the case of pentacene/C₆₀ heterojunctions. *Advanced Functional Materials*, 19(23):3809–3814, 2009.
- ⁷⁶ Fiona C Jamieson, Ester Buchaca Domingo, Thomas McCarthy-Ward, Martin Heeney, Natalie Stingelin, and James R Durrant. Fullerene crystallisation as a key driver of charge separation in polymer/fullerene bulk heterojunction solar cells. *Chemical Science*, 3(2):485–492, 2012.

- ⁷⁷ Alexander L Ayzner, Dennis Nordlund, Do-Hwan Kim, Zhenan Bao, and Michael F Toney. Ultrafast Electron Transfer at Organic Semiconductor Interfaces: Importance of Molecular Orientation. *The Journal of Physical Chemistry Letters*, 6(1):6–12, 2014.
- ⁷⁸ Tomohiro Higashino, Tomoki Yamada, Masanori Yamamoto, Akihiro Furube, Nikolai V. Tkachenko, Taku Miura, Yasuhiro Kobori, Ryota Jono, Koichi Yamashita, and Hiroshi Imahori. Remarkable Dependence of the Final Charge Separation Efficiency on the Donor–Acceptor Interaction in Photoinduced Electron Transfer. *Angewandte Chemie International Edition*, 55(2):629–633, 2016.
- ⁷⁹ Artem A. Bakulin, Akshay Rao, Vlad G. Pavelyev, Paul H. M. van Loosdrecht, Maxim S. Pshenichnikov, Dorota Niedzialek, Jérôme Cornil, David Beljonne, and Richard H. Friend. The Role of Driving Energy and Delocalized States for Charge Separation in Organic Semiconductors. *Science*, 335(6074):1340–1344, 2012.
- ⁸⁰ Stoichko D Dimitrov, Artem A Bakulin, Christian B Nielsen, Bob C Schroeder, Junping Du, Hugo Bronstein, Iain McCulloch, Richard H Friend, and James R Durrant. On the energetic dependence of charge separation in low-band-gap polymer/fullerene blends. *Journal of the American Chemical Society*, 134(44):18189–18192, 2012.
- ⁸¹ Raphael Tautz, Enrico Da Como, Christian Wiebeler, Giancarlo Soavi, Ines Dumsch, Nils Fröhlich, Giulia Grancini, Sybille Allard, Ullrich Scherf, Giulio Cerullo, et al. Charge photo-generation in donor–acceptor conjugated materials: influence of excess excitation energy and chain length. *Journal of the American Chemical Society*, 135(11):4282–4290, 2013.
- ⁸² Artem A Bakulin, Stoichko D Dimitrov, Akshay Rao, Philip C Y Chow, Christian B Nielson, Bob C Schroeder, Ian McCulloch, Huib J Bakker, James R Durrant, and Richard H Friend. Charge-Transfer State Dynamics Following Hole and Electron Transfer in Organic Photovoltaic Devices. *The Journal of Physical Chemistry Letters*, 4:209–215, 2013.
- ⁸³ Xiaoyang Zhu and Antoine Kahn. Electronic structure and dynamics at organic donor/acceptor interfaces. *MRS Bulletin*, 35(06):443–448, 2010.
- ⁸⁴ Arne C Morteani, Paiboon Sreearunothai, Laura M Herz, Richard H Friend, and Carlos Silva. Exciton regeneration at polymeric semiconductor heterojunctions. *Physical Review Letters*, 92(24):247402, 2004.
- ⁸⁵ Jean-Luc Brédas, Joseph E Norton, Jérôme Cornil, and Veaceslav Coropceanu. Molecular understanding of organic solar cells: the challenges. *Accounts of chemical research*, 42(11):1691–1699, 2009.
- ⁸⁶ Z Li, X Zhang, and G Lu. Exciton diffusion in disordered small molecules for organic photovoltaics: insights from first-principles simulations. *Journal of Physics: Condensed Matter*, 26(18):185006, 2014.

- ⁸⁷ D Peckus, A Devižis, D Hertel, K Meerholz, and V Gulbinas. Exciton diffusion, annihilation and their role in the charge carrier generation in fluorene based copolymers. *Chemical Physics*, 404:42–47, 2012.
- ⁸⁸ Loren G Kaake, Daniel Moses, and Alan J Heeger. Coherence and uncertainty in nanostructured organic photovoltaics. *The Journal of Physical Chemistry Letters*, 4(14):2264–2268, 2013.
- ⁸⁹ Tak W Kee. Femtosecond Pump–Push–Probe and Pump–Dump–Probe Spectroscopy of Conjugated Polymers: New Insight and Opportunities. *The Journal of Physical Chemistry Letters*, 5(18):3231–3240, 2014.
- ⁹⁰ Sarah Maria Falke, Carlo Andrea Rozzi, Daniele Brida, Margherita Maiuri, Michele Amato, Ephraim Sommer, Antonietta De Sio, Angel Rubio, Giulio Cerullo, Elisa Molinari, et al. Coherent ultrafast charge transfer in an organic photovoltaic blend. *Science*, 344(6187):1001–1005, 2014.
- ⁹¹ Kai Chen, Alex J Barker, Matthew E Reish, Keith C Gordon, and Justin M Hodgkiss. Broadband ultrafast photoluminescence spectroscopy resolves charge photogeneration via delocalized hot excitons in polymer: fullerene photovoltaic blends. *Journal of the American Chemical Society*, 135(49):18502–18512, 2013.
- ⁹² Alex J Barker, Kai Chen, and Justin M Hodgkiss. Distance distributions of photogenerated charge pairs in organic photovoltaic cells. *Journal of the American Chemical Society*, 136(34):12018–12026, 2014.
- ⁹³ Hiroyuki Tamura and Irene Burghardt. Ultrafast charge separation in organic photovoltaics enhanced by charge delocalization and vibronically hot exciton dissociation. *Journal of the American Chemical Society*, 135(44):16364–16367, 2013.
- ⁹⁴ Askat E Jailaubekov, Adam P Willard, John R Tritsch, Wai-Lun Chan, Na Sai, Raluca Gearba, Loren G Kaake, Kenrick J Williams, Kevin Leung, Peter J Rossky, et al. Hot charge-transfer excitons set the time limit for charge separation at donor/acceptor interfaces in organic photovoltaics. *Nature Materials*, 12(1):66–73, 2013.
- ⁹⁵ Arun Aby Paraecattil and Natalie Banerji. Charge Separation Pathways in a Highly Efficient Polymer: Fullerene Solar Cell Material. *Journal of the American Chemical Society*, 136(4):1472–1482, 2014.
- ⁹⁶ Brett M Savoie, Akshay Rao, Artem A Bakulin, Simon Gelinas, Bijan Movaghfar, Richard H Friend, Tobin J Marks, and Mark A Ratner. Unequal partnership: Asymmetric roles of polymeric donor and fullerene acceptor in generating free charge. *Journal of the American Chemical Society*, 136(7):2876–2884, 2014.
- ⁹⁷ K Birgitta Whaley, Aleksey A Kocherzhenko, and Abraham Nitzan. Coherent and Diffusive Time Scales for Exciton Dissociation in Bulk Heterojunction Photovoltaic Cells. *The Journal of Physical Chemistry C*, 118(47):27235–27244, 2014.

- ⁹⁸ Zhiqiang Guan, Ho-Wa Li, Jinfeng Zhang, Yuanhang Cheng, Qingdan Yang, Ming-Fai Lo, Tszy-Wai Ng, Sai-Wing Tsang, and Chun-Sing Lee. Evidence of Delocalization in Charge-Transfer State Manifold for Donor:Acceptor Organic Photovoltaics. *ACS Applied Materials & Interfaces*, 8(33):21798–21805, 2016. PMID: 27482867.
- ⁹⁹ A Pivrikas, NS Sariciftci, G Juška, and R Österbacka. A review of charge transport and recombination in polymer/fullerene organic solar cells. *Progress in Photovoltaics: Research and Applications*, 15(8):677–696, 2007.
- ¹⁰⁰ Zhe Li and Christopher R. McNeill. Transient photocurrent measurements of PCDTBT:PC70BM and PCPDTBT:PC70BM Solar Cells: Evidence for charge trapping in efficient polymer/fullerene blends. *Journal of Applied Physics*, 109:074513, 2011.
- ¹⁰¹ Fabian Etzold, Ian A. Howard, Michael Meister, Ralf Mauer, Tae-Dong Kim, Kwang-Sup Lee, Nam Seob Baek, and Frederic Laquai. Ultrafast Exciton Dissociation Followed by Nongeminate Charge Recombination in PCDTBT:PCBM Photovoltaic Blends. *Journal of the American Chemical Society*, 133:9469–9479, 2011.
- ¹⁰² Timothy M. Burke, Sean Sweetnam, Koen Vandewal, and Michael D. McGehee. Beyond Langevin Recombination: How Equilibrium Between Free Carriers and Charge Transfer States Determines the Open-Circuit Voltage of Organic Solar Cells. *Advanced Energy Materials*, 5(11):1500123–n/a, 2015. 1500123.
- ¹⁰³ W. Shockley and W. T. Read. Statistics of the Recombinations of Holes and Electrons. *Physical Reviews*, 87:835–842, Sep 1952.
- ¹⁰⁴ Tracey M Clarke, Christoph Lungenschmied, Jeff Peet, Nicolas Drolet, and Attila J Mozer. A Comparison of Five Experimental Techniques to Measure Charge Carrier Lifetime in Polymer/Fullerene Solar Cells. *Advanced Energy Materials*, 5(4), 2015.
- ¹⁰⁵ A Pivrikas, G Juška, R Osterbacka, M Westerling, M Viliunas, K Arlauskas, and H Stubb. Langevin recombination and space-charge-perturbed current transients in regiorandom poly (3-hexylthiophene). *Physical Reviews B*, 71(12):125205, 2005.
- ¹⁰⁶ Tobias Hahn, Steffen Tscheuschner, Frank-Julian Kahle, Markus Reichenberger, Stavros Athanasopoulos, Christina Saller, Guillermo C. Bazan, Thuc-Quyen Nguyen, Peter Strohriegl, Heinz Bässler, and Anna Köhler. Monomolecular and Bimolecular Recombination of Electron–Hole Pairs at the Interface of a Bilayer Organic Solar Cell. *Advanced Functional Materials*, 27(1):1604906, 2017.
- ¹⁰⁷ Tracey M Clarke, Jeff Peet, Patrick Denk, Gilles Dennler, Christoph Lungenschmied, and Attila J Mozer. Non-Langevin bimolecular recombination in a silole-based polymer: PCBM solar cell measured by time-resolved charge extraction and resistance-dependent time-of-flight techniques. *Energy & Environmental Science*, 5(1):5241–5245, 2012.

- ¹⁰⁸ R. A. Street. Reply to “Comment on ‘Interface state recombination in organic solar cells’”. *Physics Review B*, 82:207302, 2010.
- ¹⁰⁹ R. A. Street, M. Schoendorf, A. Roy, and J. H. Lee. Interface state recombination in organic solar cells. *Physics Review B*, 81:205307, 2010.
- ¹¹⁰ Carsten Deibel and Alexander Wagenpfahl. Comment on “Interface state recombination in organic solar cells”. *Phys. Rev. B*, 82:207301, Nov 2010.
- ¹¹¹ Stefan D. Oosterhout, Andrew J. Ferguson, Bryon W. Larson, Dana C. Olson, and Nikos Kopidakis. Modeling the Free Carrier Recombination Kinetics in PTB7:PCBM Organic Photovoltaics. *The Journal of Physical Chemistry C*, 120(43):24597–24604, 2016.
- ¹¹² Germà Garcia-Belmonte, Antonio Guerrero, and Juan Bisquert. Elucidating operating modes of bulk-heterojunction solar cells from impedance spectroscopy analysis. *The Journal of Physical Chemistry Letters*, 4(6):877–886, 2013.
- ¹¹³ B Arredondo, B Romero, G Del Pozo, M Sessler, C Veit, and U Würfel. Impedance spectroscopy analysis of small molecule solution processed organic solar cell. *Solar Energy Materials and Solar Cells*, 128:351–356, 2014.
- ¹¹⁴ Li Tao, Zhipeng Huo, Yong Ding, Yi Li, Songyuan Dai, Lu Wang, Jun Zhu, Xu Pan, Bing Zhang, Jianxi Yao, Mohammad K. Nazeeruddin, and Michael Gratzel. High-efficiency and stable quasi-solid-state dye-sensitized solar cell based on low molecular mass organogelator electrolyte. *Journal of Material Chemistry A*, 3:2344–2352, 2015.
- ¹¹⁵ N.W Duffy, L.M Peter, R.M.G Rajapakse, and K.G.U Wijayantha. A novel charge extraction method for the study of electron transport and interfacial transfer in dye sensitised nanocrystalline solar cells. *Electrochemistry Communications*, 2(9):658–662, 2000.
- ¹¹⁶ CG Shuttle, A Maurano, R Hamilton, B O'Regan, JC De Mello, and JR Durrant. Charge extraction analysis of charge carrier densities in a polythiophene/fullerene solar cell: Analysis of the origin of the device dark current. *Applied Physics Letters*, 93(18):3501, 2008.
- ¹¹⁷ Attila J. Mozer, Niyazi Serdar Sariciftci, Almantas Pivrikas, Ronald Österbacka, Gytis Juška, Lutz Brassat, and Heinz Bässler. Charge carrier mobility in regioregular poly(3-hexylthiophene) probed by transient conductivity techniques: A comparative study. *Physics Review B*, 71:035214, 2005.
- ¹¹⁸ Ilja Lange, Juliane Kniepert, Patrick Pingel, Ines Dumsch, Sybille Allard, Silvia Janietz, Ullrich Scherf, and Dieter Neher. Correlation between the Open Circuit Voltage and the Energetics of Organic Bulk Heterojunction Solar Cells. *Journal of Physical Chemistry Letters*, 4:3865–3871, 2013.
- ¹¹⁹ Juliane Kniepert, Ilja Lange, Niels J. van der Kaap, L. Jan Anton Koster, and Dieter Neher. A Conclusive View on Charge Generation, Recombination, and Extraction in As-Prepared

and Annealed P3HT:PCBM Blends: Combined Experimental and Simulation Work. *Advanced Energy Materials*, 4:1301401, 2014.

¹²⁰ C. Deibel, A. Wagenpfahl, and V. Dyakonov. Origin of reduced polaron recombination in organic semiconductor devices. *Physical Review B*, 80:075203, Aug 2009.

¹²¹ Florent Deledalle, Pabitra Shakya Tuladhar, Jenny Nelson, James R Durrant, and Thomas Kirchartz. Understanding the apparent charge density dependence of mobility and lifetime in organic bulk heterojunction solar cells. *The Journal of Physical Chemistry C*, 118(17):8837–8842, 2014.

¹²² A Baumann, J Lorrman, D Rauh, C Deibel, and V Dyakonov. A new approach for probing the mobility and lifetime of photogenerated charge carriers in organic solar cells under real operating conditions. *Advanced Materials*, 24(32):4381–4386, 2012.

¹²³ Claudia M Cardona, Wei Li, Angel E Kaifer, David Stockdale, and Guillermo C Bazan. Electrochemical considerations for determining absolute frontier orbital energy levels of conjugated polymers for solar cell applications. *Advanced materials*, 23(20):2367–2371, 2011.

¹²⁴ Brendan Wright, Yukihiko Nakajima, Tracey M. Clarke, Kouichi Okuda, Heikki Paananen, Attila J. Mozer, and Shogo Mori. Quantifying Recombination Losses during Charge Extraction in Bulk Heterojunction Solar Cells Using a Modified Charge Extraction Technique. *Advanced Energy Materials*, 7(11):1602026, 2017.

¹²⁵ Dan Credgington and James R. Durrant. Insights from Transient Optoelectronic Analyses on the Open-Circuit Voltage of Organic Solar Cells. *Journal of Physical Chemistry Letters*, 3:1465–1478, 2012.

¹²⁶ Christopher M Proctor, Martijn Kuik, and Thuc-Quyen Nguyen. Charge carrier recombination in organic solar cells. *Progress in Polymer Science*, 38(12):1941–1960, 2013.

¹²⁷ Hiroyuki Matsuzaki, Akihiro Furube, Ryuzi Katoh, Samarendra Pratap Singh, Prashant Sonar, Evan Laurence Williams, Chellappan Vijila, Gomathy Sandhya Subramanian, Sergey Gorelik, and Jonathan Hobley. Excited-state dynamics in diketopyrrolopyrrole-based copolymer for organic photovoltaics investigated by transient optical spectroscopy. *Japanese Journal of Applied Physics*, 53(1S):01AB11, 2014.

¹²⁸ Yi-Ming Chang and Leeyih Wang. Efficient Poly(3-hexylthiophene)-Based Bulk Heterojunction Solar Cells Fabricated by an Annealing-Free Approach. *The Journal of Physical Chemistry C*, 112(45):17716–17720, 2008.

¹²⁹ Fiona C Jamieson, Tiziano Agostinelli, Hamed Azimi, Jenny Nelson, and James R Durrant. Field-independent charge photogeneration in PCPDTBT/PC70BM solar cells. *The Journal of Physical Chemistry Letters*, 1(23):3306–3310, 2010.

- ¹³⁰ Yongxi Li, Lian Zhong, Bhoj Gautam, Hai-Jun Bin, Jiu-Dong Lin, Fu-Peng Wu, Zhanjun Zhang, Zuo-Quan Jiang, Zhi-Guo Zhang, Kenan Gundogdu, Yongfang Li, and Liang-Sheng Liao. A near-infrared non-fullerene electron acceptor for high performance polymer solar cells. *Energy Environ. Sci.*, 10:1610–1620, 2017.
- ¹³¹ Elisa Collado-Fregoso, Samantha N. Hood, Safa Shoaei, Bob C. Schroeder, Iain McCulloch, Ivan Kassal, Dieter Neher, and James R. Durrant. Intercalated vs Nonintercalated Morphologies in Donor–Acceptor Bulk Heterojunction Solar Cells: PBTTT:Fullerene Charge Generation and Recombination Revisited. *The Journal of Physical Chemistry Letters*, pages 4061–4068, 2017.
- ¹³² Hideo Ohkita and Shinzaburo Ito. Transient absorption spectroscopy of polymer-based thin-film solar cells. *Polymer*, 52(20):4397–4417, 2011.
- ¹³³ Mário N Berberan-Santos. A luminescence decay function encompassing the stretched exponential and the compressed hyperbola. *Chemical Physics Letters*, 460(1):146–150, 2008.
- ¹³⁴ MN Berberan-Santos, EN Bodunov, and B Valeur. Mathematical functions for the analysis of luminescence decays with underlying distributions 1. Kohlrausch decay function (stretched exponential). *Chemical Physics*, 315(1):171–182, 2005.
- ¹³⁵ Tracey M Clarke, Jeff Peet, Andrew Nattestad, Nicolas Drolet, Gilles Dennler, Christoph Lüngenshmied, Mario Leclerc, and Attila J Mozer. Charge carrier mobility, bimolecular recombination and trapping in polycarbazole copolymer: fullerene (PCDTBT: PCBM) bulk heterojunction solar cells. *Organic Electronics*, 13(11):2639–2646, 2012.
- ¹³⁶ Wei Lin Leong, Sarah R. Cowan, and Alan J. Heeger. Differential Resistance Analysis of Charge Carrier Losses in Organic Bulk Heterojunction Solar Cells: Observing the Transition from Bimolecular to Trap-Assisted Recombination and Quantifying the Order of Recombination. *Advanced Energy Materials*, 1:517–522, 2011.
- ¹³⁷ Germà Garcia-Belmonte, Pablo P Boix, Juan Bisquert, Michele Sessolo, and Henk J Bolink. Simultaneous determination of carrier lifetime and electron density-of-states in P3HT: PCBM organic solar cells under illumination by impedance spectroscopy. *Solar Energy Materials and Solar Cells*, 94(2):366–375, 2010.
- ¹³⁸ Jarvist M Frost, James Kirkpatrick, Thomas Kirchartz, and Jenny Nelson. Parameter free calculation of the subgap density of states in poly (3-hexylthiophene). *Faraday Discussions*, 174:255–266, 2014.
- ¹³⁹ Julien Gorenflo, Michael C. Heiber, Andreas Baumann, Jens Lorrmann, Matthias Gunz, Andreas Kampgen, Vladimir Dyakonov, and Carsten Deibel. Nongeminate recombination in neat P3HT and P3HT:PCBM blend films. *Journal of Applied Physics*, 115:144502, 2014.
- ¹⁴⁰ Guanran Zhang, Tracey M. Clarke, and Attila J. Mozer. Bimolecular Recombination in a Low Bandgap Polymer:PCBM Blend Solar Cell with a High Dielectric Constant. *The Journal of Physical Chemistry C*, 120(13):7033–7043, 2016.

¹⁴¹ Ardalan Armin, G Juška, Bronson Philippa, Paul L. Burn, Paul Meredith, Ron White, and Almantas Pivrikas. Doping-induced screening of the built-in-field in organic solar cells: Effect on charge transport and recombination. *Advanced Energy Materials*, 3, 03 2013.

Chapter 8

Appendix

Ultrafast Transient Absorption Transients A selection of transients are displayed in Figures 8.1 and 8.2 showing the picosecond excited-state kinetics as a function of PCBM blend film concentration and polymer donor species, illustrating distinct differences in transient behaviour, both between PCBM concentrations for a single polymer donor and between respective polymer donors at a single PCBM concentration.

Transient Fitting Models Additional details of excited state transient fitting are presented in Figure 8.3, with a comparison of the final model used (top) to a simplified model without a power law decay of photogenerated polaron signal (middle), as well as an alternative model using an exponential decay to fit the observed polaron decay (bottom). Goodness-of-fit values (χ^2 , lower is better) for each model fitting are also presenting along with the fitting parameter results. The dataset used is that of the P2 blend film at a 70 % PCBM concentration with 532 nm excitation, 1400 nm probe wavelength, and $7 \mu\text{J cm}^{-2}$ excitation density.

These transients exhibit a decay component on a timescale compatible with bimolecular recombination (picosecond to nanosecond) and are best described by a model including a power-law type decay component (Figure 8.3, top). A 30 % reduction in goodness-of-fit is observed without the use of an additional model component to account for the observed polaron decay behaviour. Using an exponential decay in place of a power law (Figure 8.3, bottom) yields a comparable goodness-of-fit and similar resulting electron transfer lifetime (τ_2). However, this model is less physically grounded as non-geminate polaron recombination is known to be a bimolecular process. Further, an exponential decay overestimates the degree of recombination on the picosecond to nanosecond timescale (refer to Chapter 3).

Transient Fitting Models Additional details of excited state transient fitting are presented in Figure 8.3, with a comparison of the final model used (top) to a simplified model without a power law decay of photogenerated polaron signal (middle), as well as an alternative model using an exponential decay to fit the observed polaron decay (bottom). Goodness-of-fit values (χ^2 , lower is better) for each model fitting are also presenting along with the fitting parameter results. The

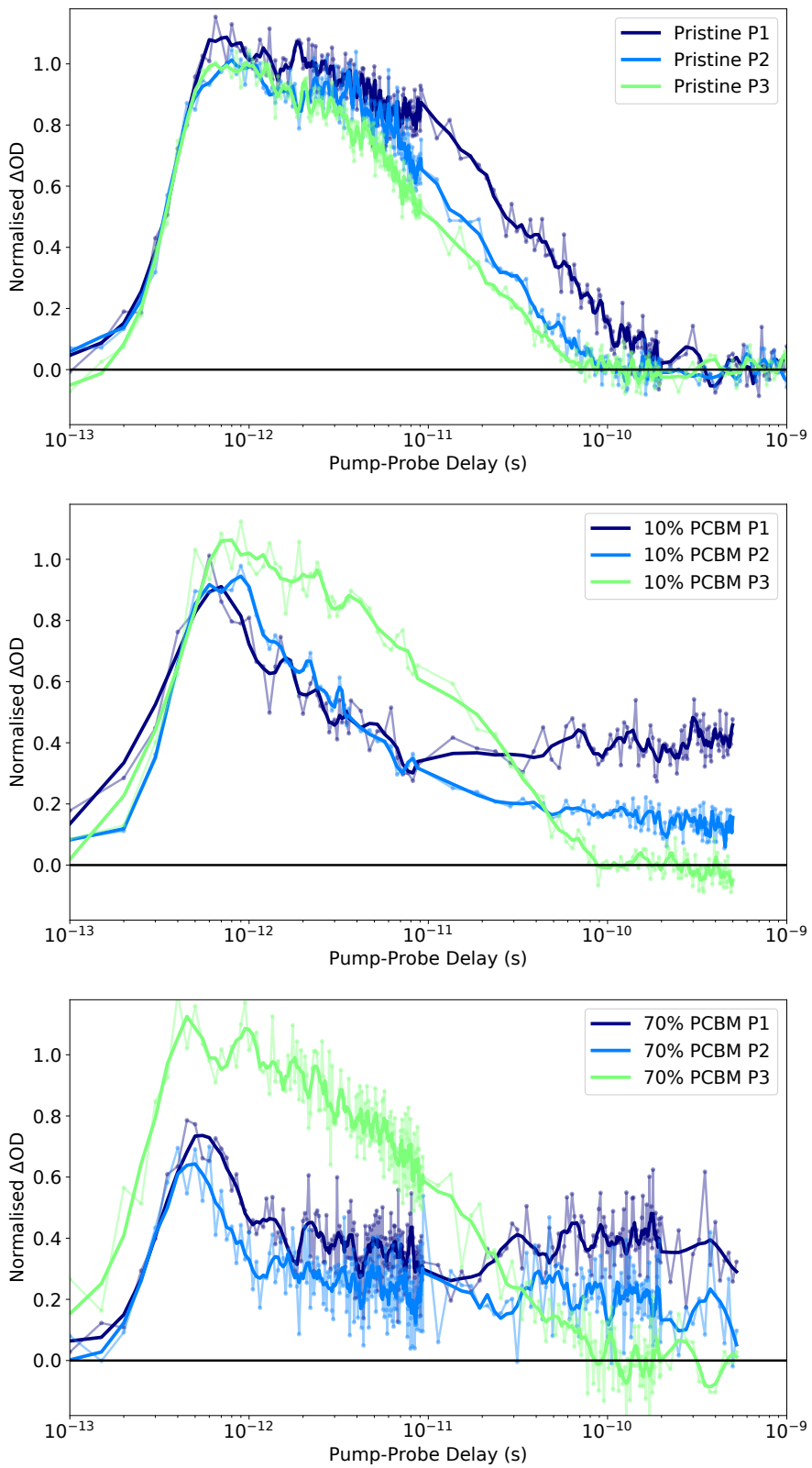


Figure 8.1: Transient absorption transients using a 532 nm excitation and 1400 nm probe wavelength, at a $7 \mu\text{J cm}^{-2}$ excitation density. The plots present the transients of each polymer donor species (as labelled), obtained from films of pristine donor, 10 %, and 70 % PCBM blends. All transients display both raw data and smoothed plot.

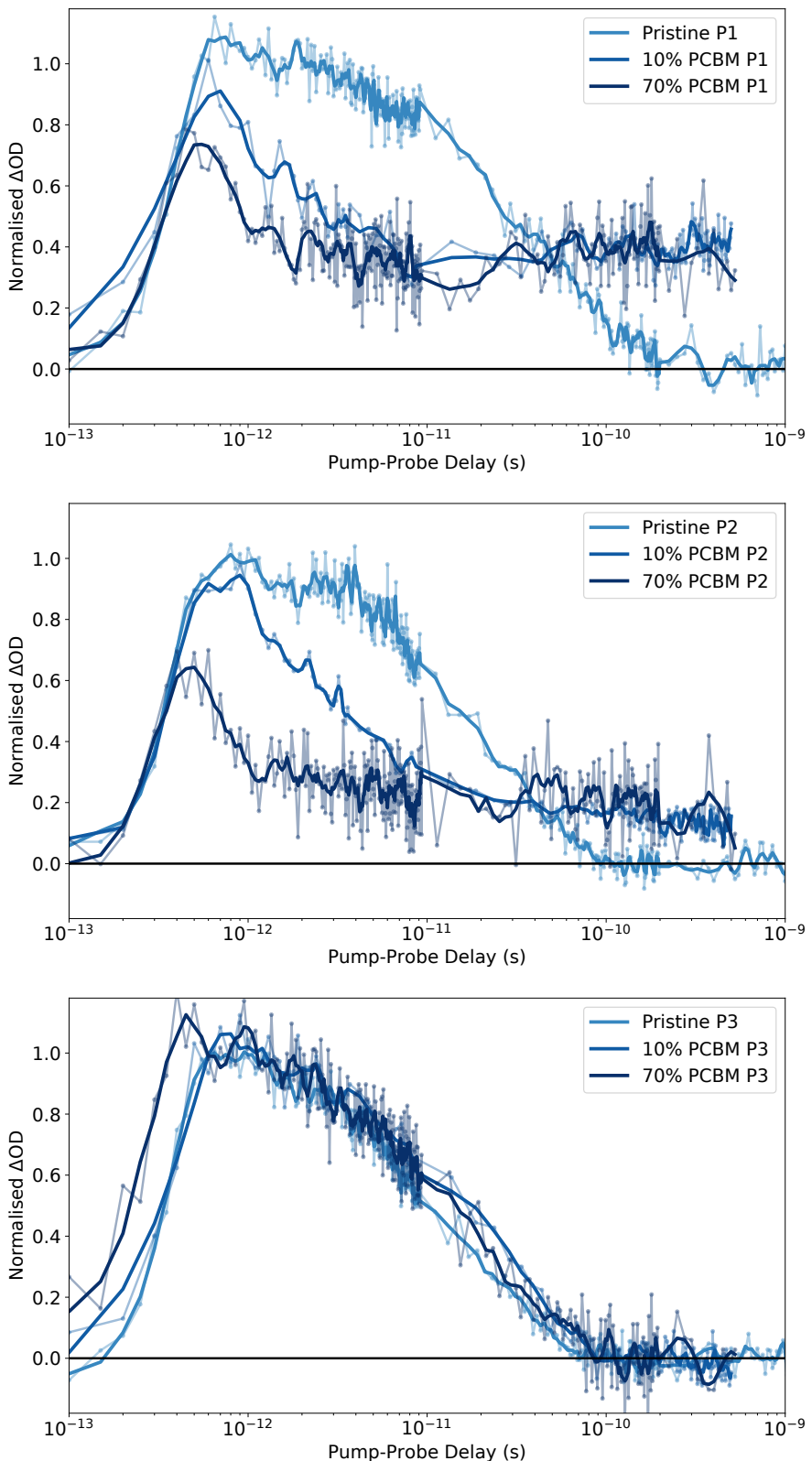


Figure 8.2: Transient absorption transients using a 532 nm excitation and 1400 nm probe wavelength, at a $7 \mu\text{J cm}^{-2}$ excitation density. The plots present the transients of each film blend (as labelled), obtained from each donor species. All transients display both raw data and smoothed plot.

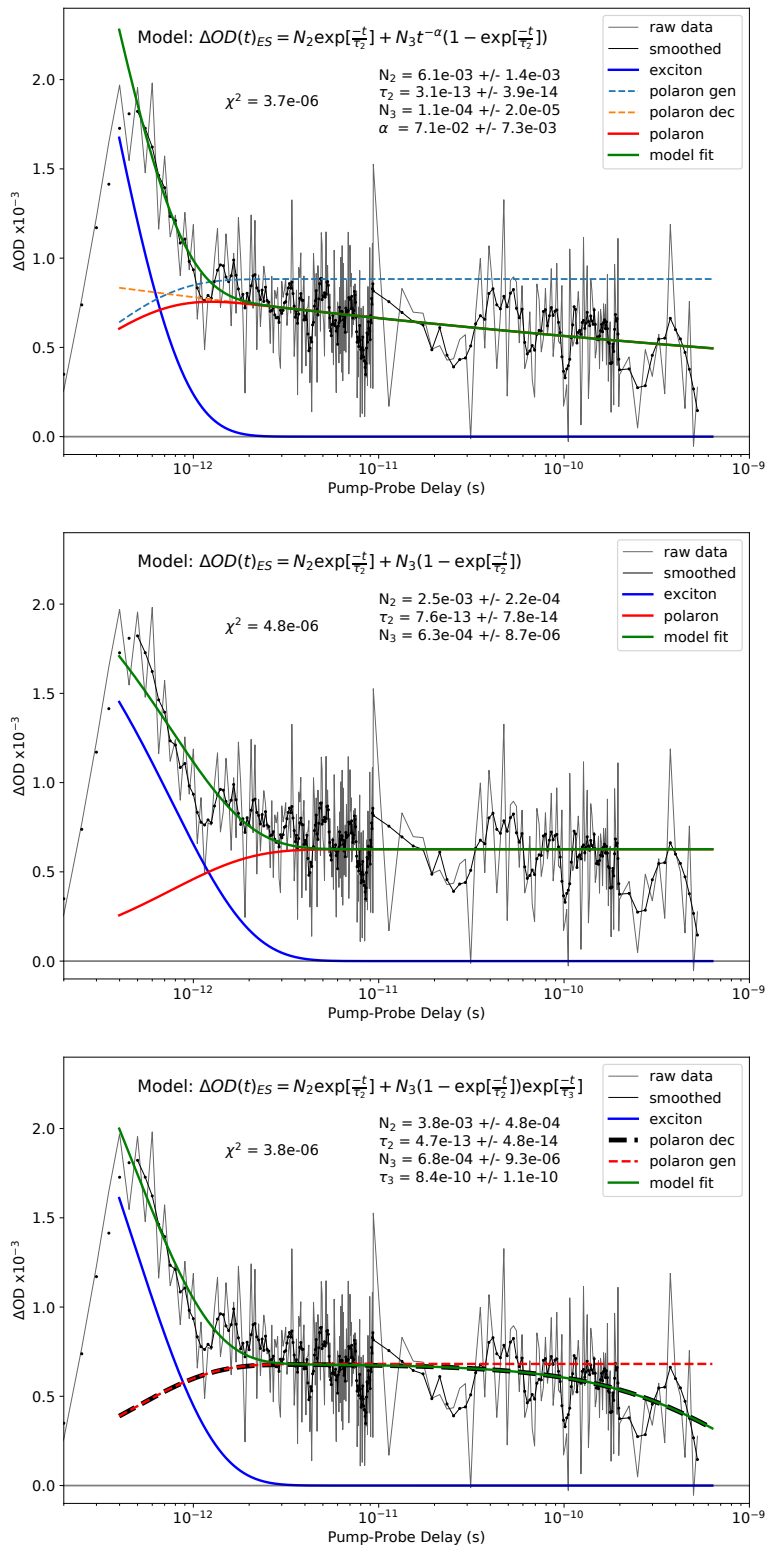


Figure 8.3: Fitting of transient absorption transients (532 nm excitation, 1400 nm probe wavelength, $7 \mu\text{J cm}^{-2}$ excitation density) for a P2 donor blend film with 10 % PCBM. The plots presented include the fitting model used and resulting parameters (inset text), the raw and smoothed transient data, the individual model components, and the final model fitting (as labelled).

dataset used is that of the P2 blend film at a 70 % PCBM concentration with 532 nm excitation, 1400 nm probe wavelength, and $7 \mu\text{J cm}^{-2}$ excitation density.

These transients exhibit a decay component on a timescale compatible with bimolecular recombination (picosecond to nanosecond) and are best described by a model including a power-law type decay component (Figure 8.3, top). A 30 % reduction in goodness-of-fit is observed without the use of an additional model component to account for the observed polaron decay behaviour. Using an exponential decay in place of a power law (Figure 8.3, bottom) yields a comparable goodness-of-fit and similar resulting electron transfer lifetime (τ_2). However, this model is less physically grounded as non-geminate polaron recombination is known to be a bimolecular process. Further, an exponential decay overestimates the degree of recombination on the picosecond to nanosecond timescale (refer to Chapter 3).

Energetics of Recombination Kinetics The plots presented in Figures 8.4 and 8.5 provide an extension of the results presented in Chapter 6, Section 6.3.4, incorporating the additional P2 and P3 polymer donor species. Figure 8.4 displays the extracted charge density decay and corresponding charge carrier lifetime as a function of charge density for each donor blend device, obtained using a $10 \mu\text{J cm}^{-2}$ excitation density and 2 V applied reverse bias. The dependence of calculated empirical reaction order δ on the energetic driving force for recombination ΔG_{rec} is also presented, derived from the preceding plots, and displays a clear influence of recombination kinetics (reaction order δ) on ΔG_{rec} , with an increasing ΔG_{rec} resulting in a reduced δ and therefore increased recombination kinetics at a comparable charge density.

Figure 8.5 displays the photovoltage decay transients and corresponding dependence of photovoltage on extracted charge density for each donor blend device, obtained using a $10 \mu\text{J cm}^{-2}$ excitation density and 2 V applied reverse bias. Both device photovoltage and characteristic of the trap state density distribution E_{ch} are also displayed as a function of ΔG_{rec} , obtained at a charge density of $2 \times 10^{16} \text{ cm}^{-3}$ from the preceding plots. The dependence of photovoltage on ΔG_{rec} matches that already presented and discussed in Chapter 6, Section 6.3.3, however with the additional ΔG_{rec} values provided by all five donor blend devices. The calculated E_{ch} of these devices does not show a strong correlation to ΔG_{rec} , indicating that the trap state density is unlikely the origin of observed dependence of δ on ΔG_{rec} .

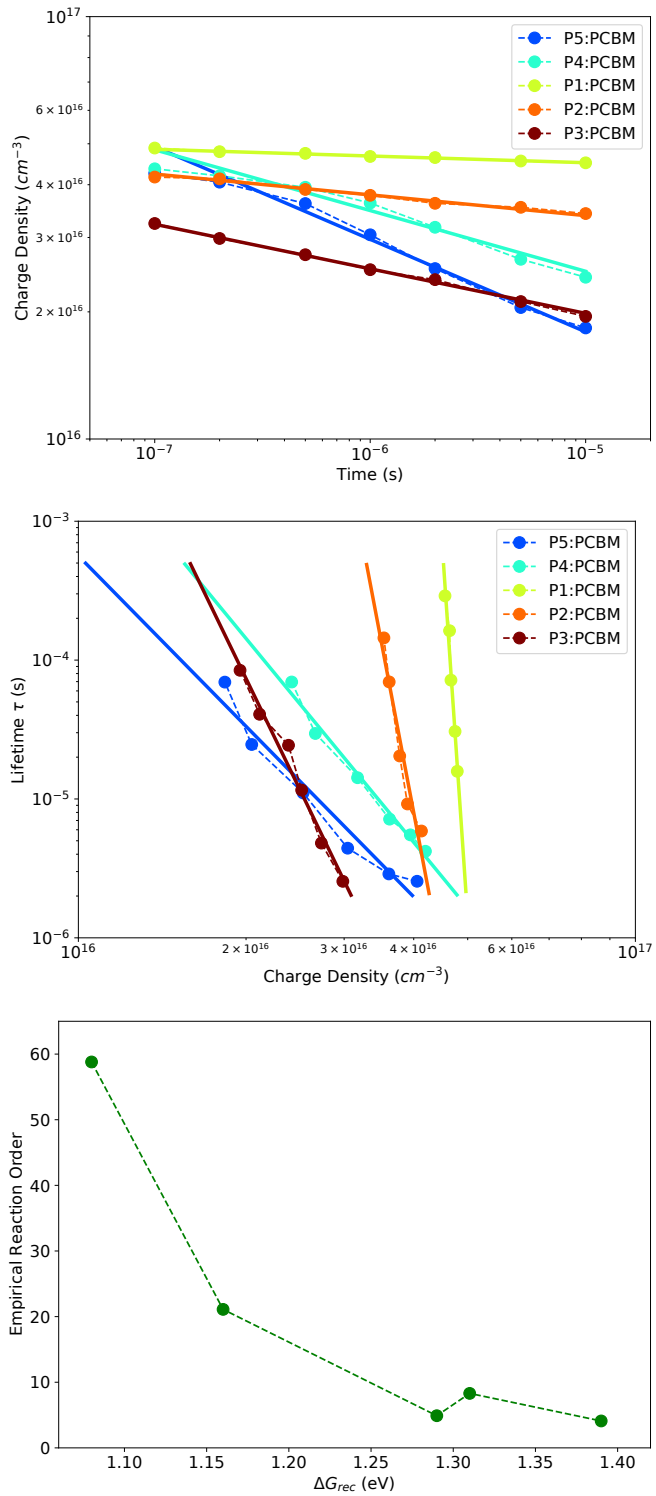


Figure 8.4: Extracted charge density decay (top), charge carrier lifetime (middle), and empirical reaction order as a function of energetic driving force for recombination ΔG_{rec} (bottom), for P1-5 donor blend devices obtained using a $10 \mu\text{J cm}^{-2}$ excitation density and 2 V applied reverse bias.

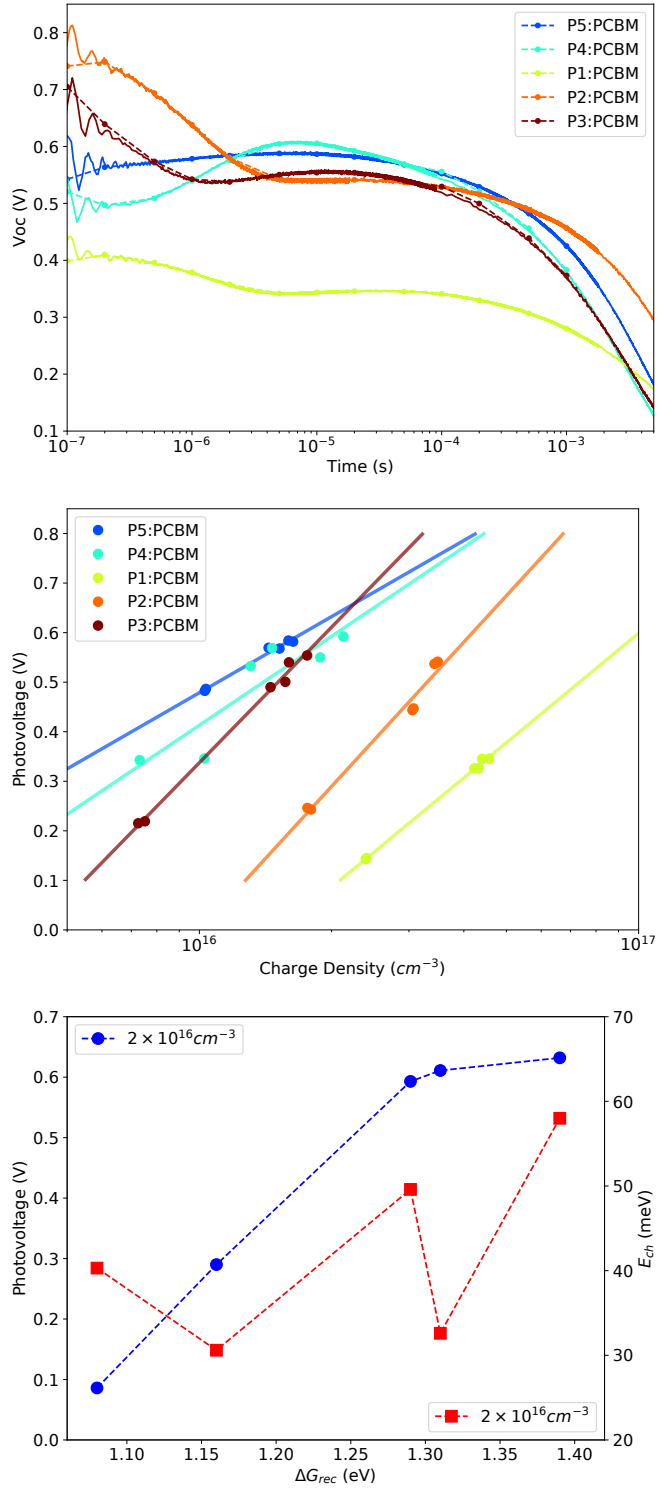


Figure 8.5: Photovoltage decay (top), photovoltage versus extracted charge density (middle), and characteristic trap state density distribution E_{ch} as a function of energetic driving force for recombination ΔG_{rec} (bottom), for P1-5 donor blend devices obtained using a $10 \mu J \text{ cm}^{-2}$ excitation density and 2 V applied reverse bias.